Study of Bluff Body Flow Fields and Aeroelastic Stability using a Discrete Vortex Method.

by

Ian J. Taylor
BSc. (Hons).

A Dissertation submitted to the
Faculty of Engineering, University of Glasgow,
for the degree of Doctor of Philosophy.

University of Glasgow
Department of Aerospace Engineering

May 1999

University of Glasgow.

ABSTRACT.

Study of Bluff Body Flow Fields and Aeroelastic Stability using a Discrete Vortex Method.

by Ian Taylor

A two dimensional discrete vortex method has been developed to simulate the unsteady, incompressible flow field and aerodynamic loading on bluff bodies. The method has been validated successfully on a range of simple bluff geometries, both static and oscillating, and has also been validated on a wider range of problems including static and oscillating suspension bridge deck sections. The results have been compared with experimental data and demonstrate good qualitative and quantitative agreement, and also compare favourably with other computational methods. Most notably, the method has been used to study the aeroelastic stability of a recent bridge deck, with accurate predictions of the critical flutter velocity.

A thorough literature review is presented, considering the nature of bluff body flows and the aeroelastic phenomena associated with the unsteady flow field. Analytical methods are considered for studying these phenomena and other computational methods are reviewed.

The basis of the method is the discretisation of the vorticity field into a series of vortex particles, which are transported in the flow field that they collectively induce. In the method presented herein, the time evolution of the system of particles is calculated by solving the vorticity transport equation in two stages : employing the Biot-Savart law to calculate particle velocities and random walks to simulate flow diffusion. The Lagrangian approach to the calculation avoids the necessity for a calculation grid, and therefore removes some of the problems associated with more traditional grid based methods. These include numerical diffusion and difficulties in resolving small scale vortical structures. In contrast, vortex methods concentrate particles in areas of vorticity, and can provide high quality representations of these small scale structures. Dispensing with a calculation mesh also eases the task of modelling a more arbitrary range of geometries. In particular, vortex methods are well suited to the analysis of moving body problems.

The vortex method presented herein was originally developed to study dynamic stall on pitching aerofoils. The necessary modifications to enable the method to be used as a tool to study bluff body flow fields are presented. These include improvements to the modelling around sharp corners and an empirical procedure to account for three dimensional effects in the wake. Also, a more efficient algorithm for the velocity calculation has been implemented, reducing the computational operation count from $O(N^2)$ to $O(N+N\log N)$. The procedure uses a zonal decomposition algorithm, where the velocity influence of a group of vortex particles can be calculated using a series expansion.

Results of the validation exercise are firstly presented for a range of simple bluff geometries to give confidence in the results before moving on to more complex geometries. These results include the effect of incidence on the aerodynamic loading for a stationary square cylinder, and also a study of the effect on aspect ratio for rectangular cylinders. This includes the limiting case of a flat plate. Vortex lock-in is studied on a square cylinder undergoing a forced transverse oscillation, for a range of frequencies and amplitudes. The results in each of these cases are in good agreement with experimental data. The flutter instability on a recent bridge design and also on the original Tacoma Narrows bridge section are considered. Predictions of the flutter derivatives and of the critical flutter velocity on each section indicate the capability of the method to analyse the stability of bridge sections. A study of flow control devices, which are used to increase structural stability has been made, demonstrating how the vortex method could potentially be used as part of a design process to investigate a range of possible designs. It is anticipated that future work on the vortex method will include a link to a structural solver to give a full aeroelastic model that can be used to analyse the flow around a wide range of geometries.

TABLE OF CONTENTS.

LIST OF FIGURES

NOMENCLATURE.

A_i^*	Torsional degree of freedom flutter derivatives.
A	Area.
$\mathbf{A}$	Coefficient matrix for nascent vortices.
a_{ij}	Coefficients of the nascent vortex values, γ_i.
a_j	Coefficients of series expansion for zonal decomposition.
a	Amplitude of oscillations.
B	Along-wind body dimension; Bridge deck width. Body region in Flow field.
$\mathbf{B}$	Mate of coefficient matrix $\mathbf{A}$.
C_D	Drag coefficient.
C_{Fy}	Aerodynamic force coefficient normal to body.
C_L	Lift coefficient.
C_{Lrms}	RMS lift coefficient.
C_{Lb}	Component of lift coefficient at body oscillation frequency.
C_{LbR}	Real component of CL_b.
C_{LbI}	Imaginary component of CL_b.
C_{L0}	Amplitude of component of lift coefficient at body oscillation frequency.
C_M	Moment coefficient.
C_p	Pressure coefficient.
C_{pb}	Base pressure coefficient.
C_{pmin}	Minimum pressure coefficient on circular cylinder.
C_{prms}	RMS pressure coefficient.
C_s	Smagorinsky constant used in LES simulations.
c	Mechanical damping coefficient of structure.
D	Body dimension.
D_0	Vortex merging parameter.
d	Distance of vortex particle to body surface.
F	Flow region; Contribution to mass flow across surface panel from different sources in flow field.
$\mathbf{F}$	Influence matrix for nascent vortices.
F_L	Lift Force.
$F_{Lh}, F_{L\alpha}$	Components of lift coefficient due to transverse and torsional body displacement respectively.
$F_{Mh}, F_{M\alpha}$	Components of lift coefficient due to transverse and torsional body displacement respectively.
f	Natural response frequency of bridge.
H_i^*	Transverse degree of freedom flutter derivatives.

H	Factor on zone radius beyond which zonal decomposition may be used.
h	Displacement in transverse (plunge) direction. (Vertical degree of freedom.)
I	Unit moment of inertia.
i	Unit imaginary number $\left(=\sqrt{-1}\right)$
K	Reduced frequency. $\left(=\dfrac{B\omega}{U}=\dfrac{B(2\pi n)}{U}\right)$;
	Number of sub-panels on each body panel.
k	Spring stiffness of structure;
	Sub-panel identifier.
L	Lift coefficient at elastic axis;
	Across-wind body dimension.
L_b	Component of lift at body oscillation frequency.
L_0	Amplitude of component of lift at body oscillation frequency.
l	Level of subdivision of flow field in zonal decomposition.
M	Moment coefficient at elastic axis;
	Number of grid point used in Vortex-in-Cell fast algorithm;
	Magnitude of amplitude of active flow control vanes.
m	Mass per unit length.
N	Number of vortex particles in flow field;
	Number of nodes on body surface.
Np	Number of particles in zone.
Nt	Number of terms in series expansion.
n	Frequency.
$\mathbf{n}$	Vector normal to body surface.
P	Pressure.
P_i^*	Along wind degree of freedom (swaying) flutter derivatives.
Re	Reynolds number $\left(=\dfrac{U D}{\nu}\right)$
$\mathbf{r}$	Position vector of point in flow field.
S	Surface in flow field.
S_α	Static unbalance about elastic axis.
St	Strouhal number.
s	Non-dimensional time unit. $\left(=\dfrac{t U}{D}\right)$
$\mathbf{s}$	Vector tangential to body surface.
t	Time.
t_c	Creation time of vortex particle.
U	Flow velocity;
	Real component of complex velocity vector.
$\mathbf{U}$	Velocity vector.

U_c	Critical flutter velocity.
U_r	Reduced velocity.
u	Horizontal component of velocity;
	Local velocity in boundary layer in direction parallel to flat plate.
V	Imaginary component of complex velocity vector.
V	Induced velocity at body surface.
v	Vertical component of velocity.
X	Parameter in determination of critical flutter velocity $\left(= \dfrac{\omega}{\omega_h} \right)$
x	Horizontal co-ordinate in Cartesian frame of reference;
	Horizontal distance along flat plate from front edge.
Y	Non-dimensional distance from surface of flat plate.
y	Body displacement;
	Vertical co-ordinate in Cartesian frame of reference;
	Local distance from surface of flat plate.
Z	Complex co-ordinate on body surface.
Z_c	Complex co-ordinate of centre of zone.
Z_k	Complex co-ordinate of centre of nascent vortices in control zone.
Zn	Normal vector to body surface represented as complex co-ordinate.
z	Complex co-ordinate of point in flow field.
A	Fourier transform of body displacement in torsional degree of freedom.
α	Angle of incidence;
	Angle of incidence of passive flow control vanes;
	Displacement in torsional (pitch) direction. (Torsional degree of freedom.)
β	Constant of decay.
Γ	Circulation (strength) of vortex particle.
$\Gamma(0)$	Initial circulation (strength) of vortex particle.
γ	Vorticity distribution in control zone around body surface.
$\Delta\Gamma$	Drop in circulation of vortex due to circulation decay since creation.
Δt	Timestep.
Δt_c	Age of merged vortex particle.
δ	Thickness of control zone;
	Boundary layer thickness.
δ_1	Displacement thickness of boundary layer on flat plate.
ε	Truncation error in series expansion for zonal decomposition.
ζ	Critical damping ratio.
η	Random walk components for diffusion model.
θ	Momentum thickness of boundary layer on flat plate.
θ_B	Angle from horizontal for start of base region on circular cylinder.
θ_{min}	Angle from horizontal for minimum pressure coefficient on circular cylinder.

ν	Kinematic viscosity.	
Ξ	Fourier transform of body displacement in transverse degree of freedom.	
ρ	Fluid density.	
σ	Core radius.	
Φ_L	Fourier transform of lift coefficient.	
Φ_M	Fourier transform of moment coefficient.	
ϕ	Phase angle.	
Ψ	Vector potential.	
Ω	Rotational velocity.	
ω	Circular frequency	$(=2\pi n)$;
	Vorticity.	
∇	Gradient operator.	
$\nabla.$	Divergence operator.	
$\nabla \times$	Curl operator.	
∇^2	Laplace operator.	$\left(= \dfrac{\partial^2 ()}{\partial x^2} + \dfrac{\partial^2 ()}{\partial y^2} \right)$
$\dfrac{D}{Dt}$	Material derivative	$\left(= \dfrac{\partial ()}{\partial t} + (\mathbf{U}.\nabla)() \right)$

Subscripts

A	Amplitude.
b	Body;
	Control zone region in flow field.
c	Centre of zone;
	Reference co-ordinate of body.
d	Diffusion.
ds	Direct summation.
h	Vertical degree of freedom.
i	Body identifier.
j	Body node identifier;
	Identifier for terms in series expansion of zonal decomposition.
k	Identifier for particles in zone in zonal decomposition algorithm;
	Identifier for nascent vortex particles.
M	Merged vortex particle.
p	Point in space.
s	Vortex shedding.
st	Starting value or condition.
tot	Total CPU for time step.
v	Flow control guide vanes.

w	Wake region in flow field;
	Identifier for vortex particle in wake region.
zd	Zonal decomposition.
0	Amplitude.
∞	Far field boundary;
	Freestream.
α	Torsional degree of freedom.

ACKNOWLEDGEMENTS.

Throughout this project, I have benefited from advice, help and support from numerous people to whom many thanks are due. However, to attempt to mention each individual by name would be impossible and would do a gross injustice to anyone that I should fail to mention. I would rather express a general thank you to everyone in the Department of Aerospace Engineering, University of Glasgow who has helped me in any way, however small, and made the three years so enjoyable.

A special thanks must go to Dr. Marco Vezza who supervised my research throughout the project and also spent many hours proof reading the thesis. I am extremely grateful for his continuous advice, ideas, support and encouragement which have proved to be invaluable.

Thanks also must go to the Engineering and Physical Sciences Research Council who provided funding for the research.

A big thank you to my wife, Shona, who allowed me to indulge myself in my studies for three years. As well as her support and encouragement, she has often kept my feet on the ground and helped me stay in the real world rather than slipping into insanity.

Finally, to the illustrious Kate, I managed it, I've completed the set for you.

CHAPTER 1

INTRODUCTION.

1.0   Background and Objectives.

Knowledge of the flow field around bluff structures, in particular suspension bridge sections, is of major importance in the fields of civil and wind engineering. As modern structures become ever taller, longer and as a result more flexible, aeroelastic phenomenon such as flutter, galloping and vortex induced vibration, arising from the structural response to the aerodynamic forcing, have a greater impact. The loading induced by the unsteady aerodynamics and the structural response to these forces are a major consideration during the design process. The importance of these effects can be demonstrated by using the now famous example of the catastrophic failure of the original Tacoma Narrows suspension bridge in 1940. Prior to this collapse, it was deemed sufficient to consider only the static wind loading on structures derived from time-averaged wind pressures and forces. However, investigation into the Tacoma Narrows failure, combined with many research studies since the event, has confirmed that the response of the bridge to the unsteady wind loading was one of the prime causes of the collapse. It is now well known that the bridge failed due to torsional flutter as depicted in Fig. 1.1 and also discussed in more detail by Billah and Scanlan [1].

Since the Tacoma incident, the analysis of unsteady aerodynamics and its effect on the aeroelastic response of suspension bridges has become a major topic of research. With modern bridge designs placing more challenging demands on the engineer, due to ever longer spans, increased flexibility of the structure and the necessity for lighter materials, an understanding of unsteady aerodynamics is now a design priority. The problems that are experienced by wind engineers in the design and analysis of civil engineering structures are summarised in the introductory remarks to Simiu and Scanlan's well know text on wind engineering, "Wind Effects on Structures" [2] :

"The development of modern materials and construction techniques has resulted in the emergence of a new generation of structures that are often, to a degree unknown in the past, remarkably flexible, low in damping and light in weight. Such structures generally exhibit an increased susceptibility to the action of wind. Accordingly, it has become necessary to develop tools enabling the designer to estimate wind effects with a higher degree of refinement than was previously required."

To illustrate the problem and highlight advances made, the original Tacoma Narrows bridge had a span of 854m, whereas the Great Belt East (Storebelt) bridge, Denmark, opened in June 1998

has a main suspended span of 1624m. Longer span structures are either already under construction or are in the design phase, notably the Akashi Kaikyo bridge in Japan with a span of 1990m and the proposed Messina Straits bridge in Italy with a free span of 3300m. Greater understanding of flutter instability in recent years has led to the potential to increase the critical flutter velocity by the addition of fairings or stabilising guide vanes to the structure. These devices, although attractive due to the increase in structural stability, lead to greater complexity in the design and place further demands on experimental testing to optimise the flow control as well as ensuring the devices produce the desired increase in flutter speed.

The analysis of bridge aerodynamics has advanced rapidly since Tacoma and techniques for predicting the onset of flutter have been established for many years. One of the key analysis techniques for analysing flutter instability employs flutter derivatives, which can be used to derive the critical flutter velocity of a particular bridge design [3]. However, virtually all of this analysis is based on experimental investigations of the unsteady aerodynamics from various wind tunnel tests of the structures. Notwithstanding the rapid advances in computational hardware and the development of many numerical models in recent years, the complex flow field effectively places a limitation on the use of computational methods and analysis tools. Due to the complexity of the unsteady flow field and of the associated non-linear dynamics, there are few numerical models that have demonstrated sufficient accuracy for the results to be reliably used in the analysis of a wide range of bluff body flows, and particularly to investigate flutter on bridge sections. Several numerical models have been shown to be well suited to particular problems and accurately predict the flow field for these specific cases. Despite these developments, many of the computational models lack the generality to be reliably applied to a wide range of cases, and fall short of the accuracy required for a usable and reliable design tool. However, accurate prediction of the flow field using computational methods is becoming increasingly important and attractive, due to the cost and time involved in running and building models for wind tunnel tests. Another beneficial aspect of the numerical treatment of fluid-structure interactions is that it allows detailed information about the flow field to be studied, information that may not be easily extracted from wind tunnel experiments. Hence, it is clear that the development of a numerical model to analyse the unsteady aerodynamic flow field around bridge deck sections, or bluff structures in general, would be a valuable analysis tool for the wind engineer and highlights a significant area of research that has yet to be fully realised.

One of the main complications with developing accurate numerical models, is that not all of these aeroelastic instabilities are completely understood at present due to the complex nature of the flow. There are few theoretical formulations of the aeroelastic effects from first principles, although attempts have been made to develop empirical analytical models. However, many of these models include parameters that need to be derived from existing experimental data and due to the flow complexity, only tend to model the dominant aerodynamic effects. Hence, the

analytical models do not reveal any of the basic physical causes of the instabilities and in many cases, important details of the fluid-structure interaction may be neglected in the analysis.

One numerical technique that has undergone significant development in recent years, and has been shown to be well suited to analysing unsteady and highly separated flow fields, is the discrete vortex method. The numerical technique utilised by vortex methods is based on the discretisation of the vorticity field rather than the velocity field, into a series of vortex particles. These particles are of finite core size, each carrying a certain amount of circulation, and are tracked throughout the flow field that they collectively induce. As such, the model does not require a calculation mesh and provides a very different approach to more traditional grid based computational fluid dynamics methods. More details of the modelling approach are given in later chapters and is reviewed in detail in [4-6]. However, one of the main advantages of vortex methods over grid based approaches is that the Lagrangian nature of the method significantly reduces some of the problems associated with grid methods, such as numerical diffusion and difficulties in achieving resolution of small scale vortical structures in the flow. Vortex particles are naturally concentrated into areas of non-zero vorticity and enable vortex methods to capture these small scale flow structures in more detail.

The research presented herein reports the development and validation of a vortex method with the aim of producing a method that can successfully predict the flow field for a range of bluff bodies and fluid-structure interaction problems. The discussion above highlights the lack of numerical models that give reliable and accurate results over a wide range of cases. To ensure that there can be sufficient confidence in the results obtained from the vortex method, an extensive validation exercise for bluff body flows has been undertaken, starting from simple geometries and building on each result until the prediction of the unsteady aerodynamics of suspension bridge sections can be reliably predicted. The results of these analyses are presented in this thesis and demonstrate the accuracy of the vortex method for a wide range of problems. As the final aim of the research was the investigation of the effect of unsteady aerodynamics on suspension bridges, much of the analysis has concentrated on sharp edged bluff bodies, although for completeness, the method is briefly demonstrated on smooth curvature bodies. Added to the analysis of suspension bridge flutter, the capability of the method is further demonstrated by a study of the effect of flow control devices. The effect of passive and active guide vanes on the flutter instability are analysed using the vortex method, indicating that the method may be used as a design tool to study the unsteady aerodynamic effects on wind engineering structures. As the focus of the research has been primarily on sharp edged bodies, the separation locations of the shear layers are fixed and the resolution of the boundary layers is not as critical as for smooth curvature bodies. The fixed separation, combined with a lack of wake turbulence modelling and some empirical aspects to the model, means that the method developed takes more of an engineering approach to the study of the flow around sharp edged bluff bodies. However, as demonstrated in the results presented herein, the method is shown to be a useful tool for

analysing the flow field and aerodynamic loads on sharp edged bodies and future research is anticipated that will develop a more physical model that could be applied to a wider range of bluff bodies.

1.1   Organisation of Thesis.

Chapter 2 gives a brief survey and review of research that has been conducted into the analysis of bluff body and bridge aerodynamics, along with various numerical methods that have been developed. Some of the more important analytical models that have been developed for analysing the various aeroelastic instabilities, such as vortex induced vibration and galloping, are mentioned. Also, a review of the analysis techniques used for analysing the flutter instability on suspension bridge sections is discussed. Grid based numerical models and discrete vortex methods, both using a number of different modelling approaches, are reviewed and assessed with regard to their suitability for analysing bluff body flow fields.

Chapter 3 outlines the vortex method that has been developed to analyse bluff body flow fields. The method was originally used for the analysis of the dynamic stall phenomena on aerofoils undergoing a pitching motion [7-9]. A brief summary of the numerical implementation is given, followed by a more detailed discussion of the modelling changes that have been implemented to enable successful prediction of bluff body flows.

The results of the validation exercise are presented in Chapter 4. The first part of the chapter gives the results of calculations on various simple geometries, to demonstrate the ability of the method to successfully predict the flow field around bluff bodies. Various key flow parameters are presented for each case to demonstrate the accuracy of the method, both qualitative and quantitative, to give confidence in the predictions on more complex and challenging configurations. In the latter part of the chapter, the results of an analysis on a recent suspension bridge are presented, including an investigation into the flutter stability of the structure. Also, to demonstrate further the capability of the method, a study has been carried out into the effect of flow control devices, both passive and active, on the critical flutter velocity of the bridge.

Finally, Chapter 5 summarises the developments and improvements made to the method, and summarises the results from the validation. Indications are also given as to potential future research and applications of the model.

CHAPTER 2

LITERATURE REVIEW.

2.0   Introduction.

In the field of civil and wind engineering, one of the fundamental design criteria is to produce a structure that can withstand the wind loads to which it will be subjected. However, as most such structures are bluff, the nature of the flow field around the body is highly separated and unsteady. Over many years, much research has been undertaken in an attempt to understand the nature of the complex processes and interactions involved in bluff body flow fields, and there remain aspects that are not fully understood.

Much of the rich array of literature reporting bluff body flows is based on experimental studies. These results have provided a valuable insight into the complex nature of the flow fields under consideration. However, analysis of the problems using mathematical or numerical techniques has proved far more difficult. Much of the problem has been to develop a model that can be generally applied to a wide variety of bluff shapes. As shall be discussed, the nature of the flow field varies from body to body, and also varies depending on the body's orientation to the oncoming flow. Added to this, the inherently unsteady nature of the flow, means that aeroelastic effects and fluid-structure interaction are often present. An important part of the design process is to ensure that the fluid-structure interactions are fully analysed, so that the oscillations can be controlled. Much of this effort is currently based on experimental procedures and various design codes. However, numerical models are being developed that could be potentially used in this process, though many currently lack the generality to analyse the wide range of problems that would be necessary for such a design tool.

The following sections highlight some aspects of the unsteady nature of bluff body flows, and the associated aeroelastic phenomena due to fluid-structure interaction. A number of analytical methods that have been developed for the analysis of these effects will briefly be discussed. In recent years, the rapid advances in both computer hardware and software have made the use of numerical models for unsteady flow analysis much more practicable. Some of the more common techniques, and the results of bluff body analysis along with their limitations, will be reviewed. In particular, the development of vortex methods will be discussed along with some of the techniques used to improve the modelling and efficiency of the calculation.

2.1   Bluff Body Flows.

A body immersed in an oncoming flow can be termed bluff if it generates separated flow over a large proportion of the body surface. On bodies with curved surfaces, such as a circular cylinder, the location of the separation points depends on the Reynolds number, *Re*, and the state of the boundary layers on the body surface. This has been well documented [2, 10-11] and the variation of drag coefficient, C_D, with *Re* is shown in Fig. 2.1. The most notable feature is the "Critical Region", where separation is delayed until further back on the cylinder surface, due to the boundary layers undergoing transition from a laminar to turbulent state. The *Re* at which the Critical Region occurs varies depending on factors such as surface roughness and freestream turbulence. On sharp edged bodies, however, the separation point is likely to be fixed at the corners and will be much less dependant on *Re*, as is demonstrated on the square section cylinder [2 and 12] with the C_D remaining constant over a range of *Re* (Fig. 2.2). However, different aspect ratios of rectangular cylinder, and also varying the angle of incidence of sharp edged bodies, produce a wide range of different flow fields, for which there are many experimental studies [13-19].

One of the main features of bluff body flows is the formation of an organised unsteady wake motion due to periodic vortex shedding from the body although the exact flow structure is also dependent on *Re* (Fig. 2.3). Vortices of opposite sign are formed and shed from alternate sides of the body forming a regular wake pattern termed the "von Karman Vortex Street" after one of the first researchers to discuss the phenomena [20]. Vortex shedding generally occurs at a regular frequency and for each geometry, a constant non dimensional frequency can be obtained from the Strouhal number, *St* (2.1)

$$St = \frac{n_s D}{U} \tag{2.1}$$

The flow pattern around each body is particular to that shape, but in general, the vortex street is a characteristic of the wake in bluff body flows. It is also important to note that the vortex street is dependant also on the *Re* of the flow as illustrated by the change in the wake of the circular cylinder as *Re* is increased [2] (Fig. 2.4). The process involved in the generation of the vortex street is complex and as yet a general model has been difficult to ascertain. However, a key factor in the formation is the interaction of the shear layers shed from each side of the body and various explanations of this process have been proposed [21]. The interaction of the periodic fluctuations in the wake interact with the body, causing an unsteady pressure loading on the structure. This unsteady loading is directly responsible for a particular type of fluid induced body oscillation as will be discussed in the next section.

Many of the models that have been developed are based on the assumption that the von Karman vortex street is an inherently two-dimensional process. However, numerous experiments have demonstrated that a significant proportion of the shed vorticity is transferred from the spanwise component, ω_z, to the streamwise component, ω_x, due to three dimensional wake effects [22-30], along with oblique vortex shedding [22 and 26]. Another problem is that the shedding process itself is not fully two-dimensional, even on sharp edged bodies, as indicated from measurement of the spanwise variation of pressure on the body [14-15, 31-33]. Although the nature of bluff body flows are characterised by unsteady periodic vortex shedding, each body, and even bodies at different orientations, give very different flow fields. This variation in flow field at different angles of incidence can lead to other sources of instability as will be mentioned later.

2.2   Vortex Induced Vibration.

One of the main effects of the vortex street is to induce an oscillating pressure load on the body. When the structure is flexibly mounted, this can result in an oscillatory motion induced by the vortex shedding, usually termed vortex induced vibration (VIV). In most cases the induced motion is in the transverse direction at a frequency equal to *St* arising due to the unsteady lift force. However, in some cases, usually in denser fluids, motion can be induced in the streamwise direction, due to the unsteady drag force, at a frequency of 2*St*. The most noticeable feature of VIV is when the vortex shedding frequency approaches the natural frequency of the body, n_b. Near this frequency, the body oscillation controls the vortex shedding, with the shedding frequency being displaced to the body frequency, an effect termed "lock-in". In the lock-in region, the vortex shedding frequency is constant rather than a function of the freestream velocity (Fig. 2.5).

An extensive review of the phenomena of vortex induced vibration is given by Bearman [34] and also by Parkinson [35-36] and Sarpkaya [37]. Both transverse and streamwise oscillations have been studied in experiments by many researchers on a range of geometries. [13, 31-32, 37-54]. The effect of VIV may be studied using a free oscillation technique, where the body responds to the induced loading, or a forced oscillation, where the body motion is prescribed. An important benefit of forced oscillation experiments is indicated in [34], in that the body motion can be closely controlled. The available experimental evidence from free and forced oscillations suggest that the flow fields are essentially the same. That is, a freely suspended body oscillating at a steady amplitude can be assumed to have the same flow field as that of a body being forced to oscillate at the same amplitude and frequency and *Re*. As the flow can change rapidly in free oscillation experiments, the advantage of the forced oscillation is that flow conditions can be more closely controlled, allowing the effects of various parameters, such as amplitude and frequency, to be investigated in detail.

Although most bluff bodies will exhibit VIV behaviour, a general model from first principles is difficult to derive as each geometry behaves differently, and produces very different flow fields. Corless and Parkinson [55] suggested that VIV can occur on any bluff cylinder with an appreciable afterbody, where the afterbody is defined as the part of the cross section downstream of the separation points, which interacts with the wake structure to give rise to the unsteady pressure loading on the body. Deniz et al [56] and Parkinson [35-36] suggested that one of the most important parameters determining the oscillatory response to vortex shedding is the afterbody length. As the pressure loading on the body occurs principally on the afterbody, geometries with a short afterbody will be only weakly excited. For example, on a D-section cylinder with its flat face upstream and normal to the onset flow, the shear layers will separate at the two sharp corners with the semicircular region forming the afterbody (Fig. 2.6). However, with the flat face downstream, the flow will still tend to separate at or near the corners, depending on *Re*, resulting in very little or no afterbody and hence elicit a negligible VIV response.

Another factor that leads to varying VIV response behaviour is the variation of key flow parameters on different geometries. The base pressure coefficient, C_{pb}, has been shown to be very sensitive to body oscillation, with a considerable increased suction for the circular cylinder through the lock-in region compared to the base pressure on the stationary body [31, 48 and 57]. On the square cylinder, however, C_{pb} tends to exhibit slightly less suction in the lock-in region relative to the stationary value [31 and 41]. C_{pb} is also affected by afterbody length, with rectangular cylinders close to the critical section showing an increase in suction in the lock-in region, contrary to the effect on higher aspect ratio sections [41]. Bearman and Obasaju [31] also noted that the circular cylinder displayed a much greater amplification of the fluctuating surface pressures and also fluctuating C_L than the square. It has also been demonstrated that bodies in motion also exhibit much more spanwise correlation, which is a contributing factor in the variation of the parameters discussed above [2, 31-32, 34 and 46]. The combination of the geometric effects, the variation exhibited by flow parameters and the complex nature of the flow field, serve to demonstrate the problems involved in developing a general model for VIV.

Through the lock-in region, the fluctuating lift and response of a transversely oscillating body are approximately sinusoidal, with the lift leading the body motion by some phase angle, ϕ (2.2).

$$y = y_A \sin(2\pi n_s t)$$
$$C_L = C_{L_A} \sin(2\pi n_s t + \phi)$$

$$(2.2)$$

The phase is important to the response of the body, as VIV can only occur when ϕ is positive. When this is the case, the lift leads the body motion implying that lift is contributing to the motion, the so called "negative damping" condition. For the circular cylinder, the phase tends to

be positive throughout the lock-in region [34, 37, 48 and 58]. For the square section cylinder, the phase is only positive at reduced velocities, U_r (2.3), higher than the resonant point [13, 31, 34 and 44] (Fig. 2.7).

$$U_r = \frac{U}{n_b D} \qquad (2.3)$$

Hence VIV only occurs on the square at the upper end of the lock-in region. Also noticeable in the results from the square cylinder is that the reduced velocity at which ϕ becomes positive increases at higher amplitudes. This was also demonstrated by Obasaju [45], using the measured ϕ from forced oscillation experiments to calculate the variation of the mass-damping parameter with U_r at a fixed amplitude (Fig. 2.8). This analysis gives the value that the mass-damping parameter for a freely oscillating cylinder should take when the vibration amplitude is constant. It is clear from Fig. 2.8 that the cylinder cannot oscillated below the resonance point as the required mass-damping is negative.

2.2.1   Analytical Models for VIV.

As discussed above, the complex nature of the flow field around bodies undergoing VIV, and the differing nature of the response of different geometries, make the development of a general analytical method difficult. Most of the effort to date has been focused on the specific case of the circular cylinder. Although most of the methods developed, with suitable parameter selection, are applicable to other geometries, the circle has been used because of its insusceptibility to galloping. This becomes important in cases of low damping, where the critical velocity of galloping is close to the reduced velocities at which VIV occurs, and the two phenomena cannot be treated separately, as will be discussed later.

For a stationary cylinder, the fluctuating lift force can be approximated by

$$F_L = \tfrac{1}{2}\rho U^2 C_{Ls} \sin(\omega_s t) \qquad (2.4)$$

where

$$\omega_s = 2\pi n_s$$

with $C_{Ls} \approx 0.6$. For a cylinder undergoing oscillatory motion, (2.4) is inadequate, as F_L varies with amplitude until a limiting amplitude is reached. If y is the transverse displacement, then the equation of motion can be written as

$$m\ddot{y} + c\dot{y} + ky = F(y,\dot{y},\ddot{y},t) \qquad (2.5)$$

The crux of developing an analytical model for VIV lies in finding an empirical expression for *F* to fit experimental observations. A variety of approaches have been developed, a number of which are briefly discussed.

One such approach is the Lift-Oscillator method originally proposed by Hartlen and Currie [59]. The equation of motion is rewritten to give the equation of motion

$$\frac{\ddot{y}}{D} + 2\zeta\omega_1 \frac{\dot{y}}{D} + \omega_1^2 \frac{y}{D} = \frac{\rho U^2}{2m} C_L \tag{2.6}$$

where

$$\omega_1^2 = \frac{k}{m}, \text{ and } 2\omega_1\zeta = \frac{c}{m}$$

C_L can be assumed to satisfy the characteristics of a Van der Pol oscillator and is linked to the body velocity by

$$\ddot{C}_L + a_1 \dot{C}_L + a_2 \dot{C}_L^3 + a_3 C_L = a_4 \dot{y} \tag{2.7}$$

with a_i, i=1 to 4, being constants to be derived from experimental observations. Assuming the body motion and the lift force both to be sinusoidal, a frequency ratio can be obtained that gives the steady state amplitude of the response as well as the phase, ϕ. Two of the unknown parameters can be obtained from the pressure oscillations on the stationary body, with the last two being required to fit the experimental data. Reasonably good response amplitudes are predicted by the model through the lock in region although the agreement is generally qualitative rather than quantitative. One of the noticeable aspects of the model is the failure to predict some hysteresis behaviour in the response for low damping cases. Also, Parkinson indicated that the lock-in range may be displaced to the left [35].

The Hartlen-Currie Lift Oscillator model, although giving reasonable predictions of the amplitude response, uses a somewhat heuristic method. The representation of the lift is based on an approach that is dependent more on the similarity between the vortex shedding process and the behaviour of non-linear oscillators than on the underlying physical behaviour of the fluid. Along with the qualitative nature of the results and the need to derive the empirical parameters for each experiment, the original model proved inadequate. An improved model, with more accurate results, was presented by Skop and Griffen [58], where relations were derived for the empirical model parameters from the system parameters that govern the response of the cylinder, such as the physical mass and damping. Results of the analytic model are further discussed and compared with experiment in [48-49] and demonstrate the ability of the model to capture the variation in the response for a range of reduced damping. Also demonstrated by the

models, in agreement with experiment, is the amplification of the aerodynamic force coefficients in the lock-in region due to the increased spanwise correlation of the vortex shedding.

As mentioned above, one of the main criticisms of the Hartlen-Currie model is that there is no systematic attempt to base the model on the known fluid dynamic behaviour, and hence the results cannot be properly interpreted in terms of the fluid phenomena. An alternative model that does attempt to retain as much of the fluid dynamics as possible whilst remaining tractable analytically was developed by Iwan and Blevins [60]. This model introduced a hidden flow variable to describe the vortex shedding process and is derived from considering the momentum within a control volume around the body and part of the wake region. Hence, the model parameters are inferred directly in terms of physical criteria and can be determined from static and forced oscillation experiments, allowing the model to predict the response data. Although the model was formulated from a different basis to the Hartlen-Currie model, the hidden flow variable was also found to be the solution of a Van der Pol type non-linear oscillator, giving some credence to both approaches. The results obtained were similar in nature to the original Hartlen-Currie model [59].

Both models discussed above were for the analysis of elastically mounted rigid cylinders. However, through the use of a mode shape factor and the model scaling principle, the analytical models have been modified to investigate the VIV response of flexible structures such as cables [61-62]. The basis for the model is the assumption that the vortex shedding process is strongly dependent on the local vibration amplitude and only weakly on nearby spanwise elements of the structure. Hence, an essentially 2D model can be used to analyse the response of more complex, inherently 3D structures, although the model may still often be inaccurate for cases with low structural damping. Skop et al [63] introduced a second component to the lift force in the Hartlen-Currie model, represented by a stall term proportional to the body transverse velocity, providing an asymptotic, self limiting response at zero damping, behaviour not predicted by earlier models. This also has the benefit of using a basis for the model that is closer to the fluid dynamics of the problem. The equations of motion are modified to give

$$\ddot{y} + 2\zeta\omega_1\dot{y} + \omega_1^2 y = a\left(C_L - \frac{2\alpha}{\omega_s}\dot{y}\right) \qquad (2.8)$$

where the last term on the RHS is the stall term and α is a constant to be determined from experiments. The maximum amplitude response is well predicted, demonstrating good agreement with experiment.

A third, but less used model is the wake-oscillator model which originates from an attempt to simulate the fluid dynamic effects of a circular cylinder using a torsional oscillator for the "dead air" region behind the cylinder [64]. The lift coefficient can be represented as proportional to the angular displacement of the wake-oscillator with the displacement being assumed to be sinusoidal. Based on knowledge of various parameters defining the flow field around the stationary cylinder, such as the amplitude of lift oscillations, St and the length of the vortex formation region downstream of the body, the response amplitude can be calculated from the equations of motion of the wake-oscillator. Good agreement with experimental data was obtained for the phase angle, lock-in region and the response amplitude of the oscillation. Although some promise is shown by this model, the main drawback, and the reason why the model is less extensively used, is the required knowledge of the wake flow and vortex formation region behind the cylinder. This is more complicated on sharp edged bodies, especially high aspect ratio bodies, where there is more interaction between the downstream corners and the vortex formation as the oscillation amplitude increases, making it more difficult to determine the required wake parameters. Such a model has not been demonstrated on oscillating sharp edged bodies, although some general wake models have been developed for stationary bodies [65].

The principles of the models discussed above were applied to more complex problems such as bridge deck sections by Ehsan and Scanlan [66]. The maximum response amplitude for the section was predicted and linked to the full bridge response using a modal analysis. However, as with the models discussed above, parameter identification is still a problematic area for the analysis. This problem was addressed by Gupta et al [67] by applying a parameter identification technique based on the concepts of invariant imbedding and non-linear filtering theory. The technique still requires a response experiment, but has proved to be less sensitive than previous calculations and has also proved to give good results in turbulent flows. Larsen [68] developed a general Van der Pol oscillator model to analyse the VIV response of a wide range of structures. In previous models, the relationship between structural damping and response did not always match the experimental data. However, Larsen generalised the model by introducing a functional relation between the response and damping, by equating the energy supplied by the vortex shedding process to the energy dissipated by the non-linear restoring force and structural damping. The model is successfully demonstrated on a range of structures.

Practical applications of the VIV models are discussed in Griffin and Ramberg [50], Simiu and Scanlan [2] and also Dyrbye et al [69]. Discussion of the relevance of the models to design codes is also made, along with various methods of suppressing the oscillations such as longitudinal slats or helical strakes. All of the models discussed have proved useful in describing the basic criteria of VIV oscillations. However, the development of a completely successful analytic model, from basic flow principles, that represents the full range of response

behaviour of VIV, is still elusive. All of the models discussed above rely to varying degrees upon empirical parameters derived from experimental data with judicious selection to obtain good agreement with the data. One of the main drawbacks of all of the methods is the lack of detailed flow field information that is provided by the results and the failure to reveal any of the basic physical causes of the instabilities. For this reason, analysis of VIV has predominantly used experimental techniques, however as computational methods become more powerful and practicable, numerical techniques are increasingly being used, as will be discussed later.

2.3   Galloping.

Across-wind galloping is a self excited instability only found on bodies that have some form of asymmetry in the aerodynamic forces associated with the cross flow, whereby a body experiencing a perturbation normal to the cross flow, receives a further force tending to increase the motion. A circular cylinder, with perfect symmetry will not exhibit galloping, though galloping is a common occurrence of on ice-laden cables, where the ice introduces the required asymmetry. For low amplitude motion, it can be shown that the Glauert-Den Hartog (2.9) criteria is a necessary, though not sufficient, condition for galloping [2, 70-71].

$$\left(\frac{d\,C_L}{d\alpha} + C_D \right) < 0 \tag{2.9}$$

Unlike VIV, galloping may exhibit large amplitude oscillations many times the across-wind body dimensions and, depending on the mass damping parameter, usually occurs at frequencies much lower than those of vortex shedding. As a result of the generally low frequency oscillation, the phenomena is governed by essentially quasi-steady forces. This is reflected in the reasonably successful development of an analytical theory for galloping, presented in detail in [2, 35-36, 70-73], based on a quasi-steady analysis of the variation of the aerodynamic forces with angle of incidence on a static body.

The equation of motion can be written in the usual form (2.10).

$$m\ddot{y} + c\dot{y} + ky = \tfrac{1}{2}C_{F_y}\,\rho\,U^2\,D \tag{2.10}$$

The quasi-steady assumptions mean that the lift and drag coefficients, $C_L(\alpha)$ and $C_D(\alpha)$ on an oscillating cylinder at an effective angle of attack α (Fig. 2.9), are assumed to be the same as those on a stationary body at the same angle of attack. Hence, C_{Fy}, can be obtained from the variation of the force coefficients on the stationary body. Since the effective angle of attack is a function of the body and freestream velocity only, C_{Fy} can be expressed as a function of $\dot{y}/U$,

using a seventh order polynomial fit (2.11) suggested by Parkinson [36 and 73].

$$C_{F_y} = A_1\left(\frac{\dot{y}}{U}\right) - A_2\left(\frac{\dot{y}}{U}\right)^2\frac{\dot{y}}{|\dot{y}|} - A_3\left(\frac{\dot{y}}{U}\right)^3 + A_5\left(\frac{\dot{y}}{U}\right)^5 - A_7\left(\frac{\dot{y}}{U}\right)^7 \qquad (2.11)$$

The solution of (2.10) and (2.11) gives the steady state amplitude response of the body and also gives a prediction of the critical velocity of the onset of galloping. Good agreement with experimental data is shown in [73] and various modifications to the method, including modelling the effects of turbulence are presented in [35, 72, 74-80].

2.4   Combined Models for Vortex-Induced Vibration and Galloping.

The analytical galloping theory works very well for cases with reasonably high mass damping where the critical onset velocity for galloping is significantly higher than the resonant velocity of VIV. Parkinson et al [35 and 73] showed that there is good agreement between theory and experiment for amplitude response except in the case where the resonant velocity is closest to the critical onset velocity for galloping (Fig. 2.10). When the resonant velocity and galloping onset get closer, the inertia effects of the body motion become a dominant effect on the fluid dynamics of the system, and the quasi-steady assumption inherent in the galloping theory is violated. At low damping values, galloping and VIV become coupled and almost indistinct. These effects have been demonstrated by numerous researchers [13, 36, 38, 42, 44-45, 55, 81-84]. Luo and Bearman [81] improved the range of applicability of a quasi-steady analysis to lower reduced velocities, by utilising unsteady aerofoil theory on a square cylinder undergoing transverse oscillation. The results are improved by the inclusion of inertia terms in the model, though close to the resonant region, the effects of VIV are not fully captured. A similar result was obtained by Luo et al [85] again by the inclusion of an inertia term in the equation of motion.

Attempts have been made to incorporate an analytical model for VIV within galloping theory, a number of which are reviewed by Parkinson [36]. Among the models discussed are those of Bouclin [86] and Tamura and Shimada [87]. Bouclin used a simple combination of the Hartlen-Currie lift-oscillator model [59] with galloping theory, and solved numerically due to the strong non-linearity of the equations of motion. Good results for the amplitude response were obtained, although the ratio between vortex shedding frequency and body frequency shows some trends that are not observed experimentally. Tamura and Shimada combined the wake-oscillator model of Tamura et al [64] with galloping theory. Numerical methods are again utilised to obtain the amplitude response and good qualitative agreement with experimental results is demonstrated.

Corless and Parkinson [55 and 88] used a slightly modified lift-oscillator model combined with galloping theory and use the method of multiple time scales to obtain an analytical solution for the response of the body. The model is semi-empirical, with a few parameters that are

determined from results of static and a number of forced vibration experiments. Good results are obtained, although the model tends to overpredict the amplitudes in the VIV region. This is improved upon in [88] where the higher order terms of the galloping equations are not neglected in the resonance region. It is also suggested that this model may also indicate the effects of sub-harmonic resonance on the amplitude response.

All of the models described above for VIV and galloping are semi-empirical with model parameters that are defined from experimental results. The semi-empirical approach avoids much of the complexity whilst retaining some of the predictive nature of the model. Despite the relatively successful results obtained thus far by both the VIV and galloping models, they are limited and do not give a detailed picture of the complex flow field and fluid structure interactions.

2.5   Flutter

Like galloping, flutter is a self excited aeroelastic response and can lead to self destructive oscillations. The response can manifest itself as a one degree of freedom (1DOF) torsional rotation, or as the two degree of freedom (2DOF) "classical flutter" where the vertical translation and torsional motion are coupled. Of all civil engineering structures, the suspension bridge in particular is susceptible to the phenomenon of flutter and for this reason, the following discussion will concentrate on the analysis of flutter on bridges. The most notable example is the famous destruction of the Tacoma Narrows bridge in 1940, in which the failure is generally accepted to have been caused by a 1DOF torsional instability [1, 3, 89-90]. Bridges are particularly prone to oscillations due to their prominent exposure to wind and the lightweight, flexible structure, generally leading to low natural frequencies. If the structure is given an initial disturbance, the motion will either decay or diverge depending on whether the energy the oscillation extracts from the flow is less than or exceeds the energy dissipated through mechanical damping. The point at which the motion changes from the decaying to diverging case is the critical flutter condition and occurs at some wind speed termed the "critical flutter velocity".

The analysis of flutter on suspension bridges is analogous to investigations of aerofoil flutter, although the two are sufficiently different such that separate formulations are necessary [2-3, 70, 91-93]. The equations of motion for the bridge deck are essentially the same as for that of a typical aerofoil.

$$m\ddot{h} + S_\alpha\ddot{\alpha} + c_h\dot{h} + k_h h = L_h$$
$$S_\alpha\ddot{h} + I\ddot{\alpha} + c_\alpha\dot{\alpha} + k_\alpha\alpha = M_\alpha$$

(2.12)

Various methods of analysis have been proposed, but the following method by Scanlan et al [3] is now the generally accepted analysis procedure.

The basic model uses the assumption that for small sinusoidal oscillations, the self-excited lift and moment on a bluff body may be treated as linear in the structural displacement and rotation, and in their first two derivatives [2-3 70 and 93]. Most wind engineering analyses use a real form for L_h and M_α [3] rather than the complex form that is usual in aeronautical analysis.

$$L_h = \tfrac{1}{2}\rho U^2 (2B)\left[KH_1^*(K)\frac{\dot{h}}{U} + KH_2^*(K)\frac{B\dot{\alpha}}{U} + K^2 H_3^*(K)\alpha + K^2 H_4^*(K)\frac{h}{B} \right]$$

$$M_\alpha = \tfrac{1}{2}\rho U^2 (2B)^2\left[KA_1^*(K)\frac{\dot{h}}{U} + KA_2^*(K)\frac{B\dot{\alpha}}{U} + K^2 A_3^*(K)\alpha + K^2 A_4^*(K)\frac{h}{B} \right] \quad (2.13)$$

The coefficients A_i^* and H_i^* are termed the "flutter derivatives" or "flutter coefficients". It can be shown that these flutter derivatives are analogous to coefficients derived from the Theodorsen circulation function for inviscid thin aerofoil flutter theory [2-3, 69-70]. However, unlike thin aerofoil theory, the flutter derivatives are usually determined experimentally using two dimensional sectional model tests. Also, whereas galloping theory relies on information that can be obtained from static conditions, the flutter derivatives may only be measured when the body is undergoing oscillatory motion [2 and 69]. It is also important to note that the assumption of sinusoidal motion mean that only oscillations at the harmonic frequencies are analysed and the higher modes are neglected.

Much research has been conducted into the determination of the flutter derivatives using a variety of techniques [89, 91-108]. Sectional model tests are usually used to measure the aerodynamic forces on a body either undergoing a forced sinusoidal oscillation, or from free oscillation tests. In the latter, the body is given an initial displacement and the rate of decay of the oscillation, as well as the oscillation frequency are used to determine the flutter derivatives. A common means to obtain the flutter derivatives from free oscillation experiments is the System Identification technique, in which the frequency and damping of the time history of the bridge deck response are used to obtain the system stiffness and damping which are then used to derive the flutter derivatives [98, 103-105]. Many of these experiments are conducted on 1DOF oscillations, and hence information on the coupling effects of 2DOF oscillations are neglected. More recent studies have developed the techniques allowing a multi-mode analysis of the structure, where the flutter derivatives are derived from a single series of 2DOF oscillations. [97, 100-101, 103-105]. Another method is the "Step-by-Step" method of deriving the flutter derivatives, which allows the effect of each derivative on the instability to be assessed, information which is unclear from the conventional formulation [95-96]. Recent investigations have attempted to obtain general

relations between the flutter derivatives [95] and although some success has been achieved on streamlined bridge sections, the relationships do not hold well on other sections.

The flutter derivatives give a picture of the structural response in the frequency domain, for an assumed small amplitude sinusoidal motion. However, the arbitrary motion of the body in both the h and α directions may be analysed in the time domain using indicial functions, which are related to the flutter derivatives by a Fourier transform. Indicial functions give the circulatory lift response to a step change in the angle of attack of the flow and are analogous to those use in thin aerofoil theory [70, 91-93, 107 and 109]. Indicial functions cannot be derived from theoretical principles, and require experimental data for their determination. It should be noted that although the flutter derivatives may be used to derive the indicial functions, the flutter derivatives are only strictly valid for sinusoidal motion. The results for a typical indicial function obtained for bridge decks, when compared with the equivalent aerofoil Wagner function, clearly demonstrate the dissimilarity between bridge and aerofoil flutter (Fig. 2.11) [70, 89, 91-93 and 107]. The Wagner function describes the initial monotonic increase in unsteady lift following a step change in incidence, whereas the bridge function rises to an initial peak followed by a decay to steady conditions.

In modern long span bridges, the motion in the along wind direction, or swaying motion, is becoming a much more important component of the structural response. The equations of motion (2.13) can be extended to represent the swaying response of the structure, by a third set of flutter derivatives, P_i^* [70, 103, 105 and 110]. These derivatives are generally calculated using quasi-steady relations (2.14)[103, 110-111].

$$P_1^* = -\frac{2}{K}C_D, \quad P_2^* = \frac{1}{K}\frac{dC_D}{d\alpha}, \quad P_3^* = \frac{1}{K^2}\frac{dC_D}{d\alpha} \tag{2.14}$$

Recent experiments have derived P_i^* from a sectional model test that allowed motion in the along wind direction [110]. These results indicate that the above spanwise flutter derivative relations may be somewhat pessimistic in predicting the swaying response, and it is felt that ideally, they should be derived from oscillatory experiments in a similar manner to the vertical and torsional derivatives. Conventionally, the critical flutter velocity is derived from the A_i^* and H_i^* derivatives only. However, recent studies on long span bridges have also demonstrated that the inclusion of the P_i^* derivatives may play a much more vital role in the analysis than previously anticipated. For a recent bridge design, it was found that the critical flutter velocity when using all three DOF was almost halved when compared to the conventional analysis using only A_i^* and H_i^* [112]

The flutter derivatives (2.13) are now generally accepted for analysis of suspension bridge flutter and have proved invaluable in the analysis of the general response of bridge decks. The flutter derivatives can be derived from a two dimensional sectional model that models the bridge in geometry only. Along with the static force coefficients and combined with knowledge of the modal forms of the full bridge, the aeroelastic response of a full three-dimensional model may be predicted [2, 69-70, 106 and 111]. To validate this, flutter derivatives have also been measured on a full three dimensional model and consistency illustrated with those measured on a sectional model [113]. Hence, the flutter derivatives provide a general and useful guide to the stability of particular bridge deck configurations. Investigations on how the cables and towers affect the stability of the structure have also been made [114].

A number of different formulations of the flutter derivatives exist, some of which are discussed in [115] and other alternatives given in [116-118]. The Scanlan convention presented above (2.13) although widely used, suffers from a loss of information at low Ur as each flutter derivative must have zero value approaching zero Ur. An attempt to derive an alternative formulation, that draws on the advantages of each formulation has been made with a reasonable amount of success [115].

A solution to the flutter equations (2.13) to derive the critical flutter velocity can be obtained by assuming h and α have solutions proportional to

$$\frac{h}{B} = \frac{h_0}{B} e^{i\omega t} = \frac{h_0}{B} e^{iKs}$$
$$\alpha = \alpha_0 e^{i\omega t} = \alpha_0 e^{iKs}$$

(2.15)

The solution procedure is discussed in more detail in [2, 69-70 and 119] and is also presented in Appendix F.

Studies have been made to investigate the effects of turbulence and buffeting on the flutter response and critical velocity [2, 69-70, 103, 105, 107, 111, 120-123]. The random effects due to gusting of natural wind may be determined from the flutter derivatives. It has also been shown that turbulence in general does not have a large effect on the flutter derivatives. However, the effect of turbulence is to generally increase the critical flutter velocity, due to the reduction in the spanwise coherence of the flow field across the section. Recent investigations have also modified the models to analyse the aeroelastic behaviour of bridges during construction [69 and 124]. The main effect of the modification is to include modelling for the eccentric ballast often used to damp any oscillatory response of the structure during the construction phase.

Vortex induced oscillation is not as great a problem on bridge structures as flutter, although the phenomenon has been investigated by various researchers [89, 125-127]. Early investigations

of the Tacoma Narrows catastrophe concluded that the cause of the failure was due to motion induced by vortex shedding, although the cause is now known to be 1DOF torsional flutter [1]. Scanlan suggested that when the generally low speed case of VIV occurs, the linear analytic model for flutter may be supplemented at the lock-in condition by the inclusion of a time dependent force term [105]. This was demonstrated in a combined model for flutter and VIV analysis, where the maximum amplitude in the lock-in region, for vertical or torsional motion, may be calculated [128]. However, any undesirable VIV or other instability are often avoided early in the design stage, by altering the structural form to adjust the onset and behaviour of the oscillatory response [105].

With the tendency towards longer span bridges, the aerodynamic stability often requires enhancement by some flow control device that increases the critical flutter velocity of the structure. A common practice is the addition of fairings to the edges of the section [126 and 129], where the fairing adjusts the separation from the leading edge, giving the deck section a more streamlined form. Fairings are particularly useful for improving the behaviour of the notably unstable H-section form used in the original Tacoma Narrows Bridge [126]. An alternative approach is the use of guide vanes or aerodynamic appendages supported from the section, that effectively increase the aerodynamic damping of the bridge. These vanes may be passive with their position relative to the bridge deck remaining constant, or to gain further increase in flutter stability, may be actively controlled. The effect of such appendages on the flutter velocity on a number of deck sections is presented by Cobo del Arco et al [130]. Other studies, both theoretical and experimental are presented in [131 and 132]. Kobayashi [131] indicated that in theory the critical flutter velocity may be increased up to an infinite value. A similar use of guide vanes was also studied by Larsen [133], with the aim of suppressing the vertical oscillations of the Great Belt East bridge due to excitation from vortex shedding.

These models have proved reasonably successful in determining the critical flutter velocity and response of a structure. However, there is still a heavy reliance on experimental input to the models, with the key to these analyses being the extraction of the flutter coefficients from a series of sectional model tests.

2.6   Grid Based Numerical Models.

Most of the analytical models discussed above rely to some extent on measurements of aerodynamic forces, or the derivation of a number of empirical parameters from experiment. However, the development in computer hardware and software means that, increasingly, numerical models are being used to analyse bluff body flows and the structural response in fluid-structure interaction problems. A numerical method that can reliably predict the flow field around

static and oscillating bodies would be a valuable tool early in the design process of a structure. A much wider range of designs could be investigated using the computational model than could feasibly be studied using experimental techniques, leaving wind tunnel tests to simply validate the final design. Many of these numerical models use Eulerian techniques, in which a mesh or grid is used to model the flow field. Recent research and results of analyses for bluff body flows, using some of the more prominent and successful methods, are discussed below.

For low Reynolds numbers, computational results showing good agreement with experimental data have been achieved by numerous researchers [135-141]. In most of these cases, the flow field is assumed to be two dimensional and also to be laminar. Okajima and fellow researchers [135-138] reported calculations on a range of geometries. The variation of the flow field and of key parameters, such as C_D and *St* on different aspect ratio rectangular cylinders was well predicted in [136] (Fig. 2.12). Results for a square cylinder undergoing forced transverse and longitudinal oscillations were presented in [135 and 137]. Good agreement with experiment is shown and the lock-in phenomenon is captured by the computation, although the low *Re* means that the lock-in range is quite large (U_r from approximately 2.0 to 16.0). The results for the longitudinal oscillations are not quite as good due to the failure to predict the two different modes of vortex shedding discussed by Obasaju et al [51-52]. Davis and Moore [139] presented computational results for various rectangular configurations, and good agreement with experiment is demonstrated for the variation of *St* with *Re*. The authors claimed, however, that the effects of increasing *Re*, and hence increasing turbulent diffusion, are partially modelled, somewhat dubiously, by adjusting the amount of numerical diffusion in the calculation. Another interesting use of computational methods for bluff body analysis is the study of wind tunnel blockage and its effect on the aerodynamic characteristics of stationary and oscillating cylinders [138].

Fujiwara et al [140] reported calculations on elastically supported bridge deck sections using a finite difference calculation. The VIV phenomenon is captured by the calculations on some sections, although the amplitude of the body response is overestimated. The response is limited to the vertical degree of freedom, and no analysis of flutter is presented. Sohanker et al [141] modelled the flow around rectangular cylinders at various angles of incidence. The effects of aspect ratio are well predicted, although at incidence the agreement between numerical results and experiment is not as good (Fig. 2.13). In particular, the typical variation of *St*, with a peak at approximately 12° where the shear layer reattaches to the side face, is not captured by the calculations. Similar discrepancies are found in the C_D and C_L results, although comparison is more difficult due to the higher *Re* used in the experimental data.

Although the mean flow field around a bluff body may be two dimensional or the problem may be geometrically two dimensional, there is a significant three dimensionality within the flow even at low *Re* due to turbulent diffusion in each direction. The vortex shedding process itself is not fully two dimensional, as is demonstrated by the spanwise pressure variation in the base region of the body [14-15]. Another example of the three dimensionality of the process often found in wind tunnel studies, is oblique vortex shedding caused by end effects on the model. Also, as *Re* increases, there is more vortex stretching and roll-up giving rise to streamwise vorticity and also breakdown of the vortices due to the turbulent motion.

Hence, one of the most problematic areas for grid based methods is the modelling of turbulence and turbulent diffusion, which has a large effect on the wakes of bluff bodies. A range of methods have been developed to tackle these problems, each of which has a different philosophy and modelling approach. For low *Re*, it is feasible to use a calculation mesh in which all the scales of turbulent motion may be resolved. In this case, the flow field is modelled using direct numerical simulation (DNS), and as all the turbulence scales are resolved, the procedure does not require a turbulence model [134]. Many wind engineering applications are at much higher *Re* than can be modelled successfully by DNS, and hence, DNS has not been widely used for bluff body flow fields. At higher *Re*, the number of grid points required to completely resolve the flow field becomes prohibitive and some model for the small scale turbulent motion needs to be introduced. A natural progression from DNS is large-eddy simulation (LES) where large structures are modelled directly with the small scale structures approximated using some appropriate model. A different approach is to model the flow field using the Reynolds-averaged Navier-Stokes (RANS) equations to model the general fluid motion, together with a turbulence model that simulates only the superimposed turbulent fluctuations, such as the k-ε model.

As discussed above, many practical wind engineering problems are at a high *Re*, at which turbulent diffusion plays a significant role in the flow phenomena and cannot be neglected. Rodi [134] stated that modelling has until recently used the RANS equations together with statistical turbulence models to simulate the effects of all turbulent motion. However, in vortex shedding situations typical of bluff body flows, the unsteady RANS equations are solved to model the vortex shedding motion, and only the superimposed stochastic turbulence fluctuations are simulated by the turbulence model. Much of the research effort for predicting bluff body flow fields has been directed to developing the k-ε eddy viscosity model although other models such as the Reynolds-Stress model have also been investigated. Experience has shown that many of these statistical models do not fully capture the complex flow fields, especially when the flow is dominated by the large scale vortical structures that are experienced in processes like vortex shedding. An alternative approach is LES, where the large scale eddy

structures are resolved, leaving only the small scale turbulent motion to be modelled. However, the main drawback of this procedure is the large computational expense, in terms of both CPU and memory requirements. Brief reviews and some comparisons of the various techniques and modelling strategies, including methods of implementation, are given in [134, 142-143], with numerous computations on bluff bodies reported by various researchers in [144-154].

The k-ε turbulence model relates the Reynolds stresses to mean velocity gradients by the eddy viscosity. The two parameters, k and ε, together define the local state of the turbulence and represent the turbulent kinetic energy, (TKE), and its rate of dissipation respectively. One of the main problems that has been encountered in the k-ε model is the high predicted TKE in regions of stagnation, arising from the modelling assumption that the eddy viscosity is isotropic (Fig. 2.14). The effect that this has on bluff body flow calculations is to cause too much mixing in the separated shear layers, which in turn results in an under prediction of the forces on the body. In some cases, this can also result in the failure to predict any vortex shedding motion in the body wake [152]. Various adjustments to the standard k-ε model have been suggested to improve the results, based on either increasing the rate of TKE dissipation or to inhibit the rate of production [134, 142-143], although the methods used are somewhat empirical. Typical results of calculations for the C_p around a square cylinder are shown in Fig. 2.15. Also, Rodi [134] showed that whereas the modifications are necessary for square cylinder calculations, the length of the separation region behind a surface mounted cube, which is already over-predicted by the standard model, is increased by the changes.

In LES, the time dependent Navier-Stokes equations are solved numerically with only large motions, such as those typical of vortex shedding being resolved leaving only the small scale turbulent motions to be modelled. These small scale motions are typically accounted for in subgrid-scale models (SGS), of which that due to Smagorinsky is often used [134, 142-143 153-154]. In this model, the subgrid-scale eddy viscosity is related to the strain rate of the resolved large scale motion as a velocity scale and to the mesh size as a length scale. This model however introduces an empirical constant, C_s, which has been found not to be universal but dependent on the flow considered, and may also vary from point to point in the flow. Dynamic models are being investigated, where time dependent values of C_s are calculated, though these are currently at an early stage of development and at present tend to be numerically unstable [134]. One of the main disadvantages of LES methods is the large computational expense, with the CPU required being around an order of magnitude higher than the standard k-ε model, although the rapid increase in the speed of modern computational hardware is making the use of LES more realistic.

Near the body surface, wall functions are often necessary due to the high resolution that is required in the mesh to sufficiently resolve the viscous sub-layer at high Re [134]. These

functions use power laws to obtain the near wall velocities and shear stresses, although the application of such functions is questionable in regions of highly separated flow that are typical of bluff bodies. As with the various k-ε models, qualitatively good results have been obtained for the flow field around a square cylinder, with the representative quantities of C_D and *St* also well predicted. The conclusions from these analyses are that the LES models tend to give a better simulation of the details of the flow, compared to RANS models combined with a stochastic turbulence model, due to the extra resolution provided by the calculation. However, as well as the much greater computational requirements, the main drawbacks with LES are that the solutions are not uniformly good, and there can be a large variation between solutions. Postulated reasons for the variation [134], include insufficient resolution on the side faces in the highly separated region where there may be a small reverse flow, and also numerical diffusion due to insufficient grid resolution as the large eddy structures are shed from the body. Yu and Kareem [153-154] demonstrated the use of LES on square and rectangular cylinders. Good results are obtained for the mean force coefficients in each case although aspect ratios less than 1.0 and the effects of incidence are not investigated. Murakami et al [144, 146 and 152] used LES to simulate the flow around a square cylinder undergoing a forced transverse oscillation in the vortex lock-in frequency regime. Reasonably good results for the phase angle between body oscillation and C_L are obtained. Panneer Selvam et al [155] presented an efficient LES model in which a 3D model is used to study the flow around a circular cylinder near the critical *Re*. The method utilises accurate approximations of the convection terms using a finite element model, resulting in less numerical diffusion. A consequence of this is that the reduction in C_D in the critical regime is predicted with a greatly reduced number of grid points compared to other LES results.

Koutmos and Mavridis [151] have developed a two-dimensional procedure that encompasses aspects of both LES and k-ε models. Within these calculations, large scale vortex structures are characterised by their quality, deterministic or random, and by their size. In this hybrid method, the periodic component of the TKE is determined from the periodic velocity components, with the small scale random turbulent fluctuations modelled by a modified k-ε procedure. This mixed model is in general shown to outperform the standard k-ε models and produced results similar in quality to more conventional LES calculations. However, the predicted C_D and *St* for the square cylinder are generally too high, although the calculations are performed in a channel with 19% blockage ratio and appear to be uncorrected.

Numerous studies have highlighted a significant difference between two and three dimensional LES calculations [145, 147, 152-153 and 156]. Tamura and Kuwahara [147 and 156] demonstrated these differences by comparing the results of two and three dimensional calculations on a square cylinder at 15° incidence. In 2D, even with excellent resolution, the reattachment of the shear layer to the side face is not obvious due to strong vortical structures

convecting along the surface. In 3D, with similar resolution, more representative results are obtained and the separation is more stable and clearly defined (Fig. 2.16). The differences can be attributed to the three dimensional dissipation and stretching of the shed vortices. Similar effects have been observed and measured experimentally [25-27]. Comparing both 2D and 3D calculations at various angles of incidence shows that the 3D calculation captures the correct variation of the force coefficients (Fig. 2.17). Similar conclusions were obtained in [152-153], although it is interesting that the difference between 2D and 3D is much less prominent in the results reported by Yu et al [153]. All these results show that accurate prediction of the complex flow fields are becoming practical, although the implied necessity for a fully three dimensional model again adds to the computational effort required for these calculations. A recent estimate was that 20hrs CPU was required on a CRAY super-computer to calculate the flow field during one vortex shedding cycle.

Numerical methods are also now being applied to more complex geometries including bridge deck sections [140, 157-158]. Lee et al, using a k-ε model, and Kuroda both presented calculations of the static force coefficients at a range of angles of incidence for some recent bridge designs. Both sets of calculations were applied to stationary bodies only and onset of flutter using oscillating bodies was not analysed. However, Lee's results for the 2D section static wind loading have been input to a dynamic structural response analysis to assess the displacement of the full structure. Despite the successful predictions for static sections, "CFD, however, is still some distance away from being sophisticated enough to handle the cases of flutter derivatives for the complex shapes of typical bridge sections." (Scanlan [105])

2.7   Discrete Vortex Methods.

An alternative to the grid based numerical methods is a Lagrangian approach, where the principle is based on the tracking of quantities within the flow field rather than calculating these quantities at the nodes of a mesh. Discrete vortex methods use such an approach and are based on the idea that the vorticity within a flow field can be represented, through discretisation, by a series of vortex particles. This principle is not new, with amongst others, Helmholtz and Rosenhead suggesting that in inviscid flows, areas of vorticity could be modelled using a series of vortices of "appropriate circulation and infinitely small cross section" [4]. Following this lead, discretisation of the vorticity field into a distribution of vortex particles embedded in a potential flow has become the basis from which vortex methods have evolved. However, it is the rapid advancement in computer technology that has allowed vortex methods to become a useful analysis tool. Many different models have been developed, and there is now a vast literature available, with comprehensive reviews given in [4-6, 159-161].

The vortex particles used to represent the vorticity are free to move in the flow field in a Lagrangian manner and are tracked numerically in time, hence removing the necessity for a calculation mesh. The velocity field can be ascertained by determining the velocity of each particle. Therefore, given the distribution of vortex particles and the boundary conditions, the flow field is defined. Vortex methods have a number of advantages over grid based methods arising from the Lagrangian approach, such as the necessity for a velocity calculation only at the vortex centres, vortices concentrated only in areas of vorticity and exact treatment of boundary conditions at infinity. Also, the absence of a calculation mesh indicates that vortex methods may be applied to a wide range of geometries, as problems associated with fitting meshes to the body geometry are avoided. However, the advantages have to be measured alongside problems such as the singularities that arise from the use of point vortices, the computational cost being proportional to the square of the number of vortex particles and also the inherent inaccuracies incurred by representing a continuous vorticity distribution by a series of discrete particles. Much literature has been published on attempts to circumvent these disadvantages and will be briefly summarised in the following section, with the reviews [4-6, 159-162] giving a much more detailed discussion.

2.7.1 Theoretical and Numerical Aspects of Discrete Vortex Methods.

The basis of vortex methods stems from a modified representation of the two dimensional incompressible Navier-Stokes equations (2.16). Using the definition of vorticity as the curl of velocity, the conventional velocity-pressure form of the equations can be redefined in a vorticity-stream function form, giving the vorticity transport equations (2.17).

$$\nabla.\mathbf{U} = 0$$
$$\frac{\partial \mathbf{U}}{\partial t} + (\mathbf{U}.\nabla)\mathbf{U} = -\frac{1}{\rho}\nabla P + \nu\nabla^2\mathbf{U} \tag{2.16}$$

$$\nabla^2\Psi = -\omega$$
$$\frac{\partial \omega}{\partial t} + (\mathbf{U}.\nabla)\omega = \nu\nabla^2\omega \tag{2.17}$$

For inviscid flows, these equations state that vorticity is a kinematic property of any given vortex particle, and in viscous flows, they describe how the vorticity created at boundaries is convected and diffused in the flow. It should be noted, that in homogeneous flows, vorticity is created only by the boundaries of fluid regions [4 and 7].

By discretising the vorticity field into a distribution of point vortices, a solution to the 2D Euler equations for inviscid flow is provided by the dynamics of the system. However, the singular

nature of point vortices is potentially a large source of error within vortex methods, especially adjacent to the body surface, where many vortices are in close proximity with each other. The introduction of cut-off functions to represent a distribution of vorticity within some "core radius", σ, around the vortex centre removes the singularity of point vortices. Numerous cut-off schemes have been used and are discussed in more detail in [4-5, 160-161]. It has been pointed out that although the use of cut-off functions removes the singularity problem, they must be regarded as a mathematical rather than a physical artifice [4]. The velocity field induced by a vortex with small but finite size, is quantitatively correct at large distances from the vortex, but only qualitatively correct near the core as the singularity is removed (Fig. 2.18)

The diffusion term, $\nu\nabla^2\omega$ in the vorticity transport equations (2.17), has proved to be problematic for Lagrangian vortex methods. Various methods have been utilised to modify the inviscid model to allow viscous flow calculations : the core expansion technique [5-6, 161 and 163], random vortex method [164-168], particle strength exchange [169-171] and the diffusion velocity method [172-174]. In each of these methods, the vorticity transport equation is split into two parts in an operator splitting technique, with convection and diffusion being solved sequentially rather than simultaneously. All of these models simulate viscous diffusion only, and do not model the effects of turbulent diffusion on the flow field.

The random walk technique has been widely used and is based on the idea that the diffusion equations can be solved in a statistical sense for homogeneous flows where the kinematic viscosity, ν, is assumed to be constant. Each particle is given a random displacement with a Gaussian probability distribution with zero mean and standard deviation $\sqrt{2\nu\Delta t}$. Numerous convergence proofs of the technique have been derived [176-178], also discussed by Puckett in [161], and convergence has been demonstrated practically by Sethian et al [165 and 179]. However, the random walk technique does have a more mathematical rather than physical basis, and should ideally be applied to the case with many overlapping vortex blobs [4]. As the diffusion equation is solved in a statistical sense, if the number of vortex particles in the calculation is increased, the viscous diffusion effects in the flow will be better modelled. Also, the number of particles required to provide sufficient resolution of the flow field will increase as *Re* increases. Along with the effects of turbulent diffusion at high *Re* being neglected, other limitations of the random walk are that at high *Re*, the viscous diffusion component becomes very small, resulting in the calculated flow effectively being inviscid, although this is a problem for all the viscous diffusion models. The core expansion technique, where σ is time varying, has been used to simulate diffusion [5-6, 161 and 163], although Greengard [180] proved that the model converges to a system of equations different to the Navier-Stokes equations. Despite the diffusion being correctly modelled, the convection is calculated from an averaged velocity rather than the local velocity field, although this problem may be redressed by using a

combination of the core expansion method and a vortex splitting technique. In the particle strength exchange scheme, instead of maintaining a constant circulation for each vortex particle, the circulation is modified to account for diffusion. One technique that is often used in this process is the Vortex-in-Cell method, where the circulation is interpolated onto a mesh fitted to the calculation domain. The diffusion equation is solved at each mesh node, and the new vorticity field redistributed to the vortex particles [161 and 181]. The diffusion velocity method uses the gradient of vorticity to generate an extra velocity term, which accounts for the diffusion part of the Navier Stokes equations. The vortices are hence propagated by the convection velocity and diffusion velocity (2.18).

$$u_d = -\frac{\nu}{\omega} \cdot \frac{\partial \omega}{\partial x}, \quad v_d = -\frac{\nu}{\omega} \cdot \frac{\partial \omega}{\partial y} \qquad (2.18)$$

Ogami et al [173] state that the diffusion velocity gives a net flow of vorticity that is proportional to the vorticity gradient, and as such is consistent with the "First Law of Diffusion". Hence, the technique is more based on the physical processes than the previous methods discussed above. However, in the far wake of the body, where particles are greatly dispersed, calculation of the vorticity gradient may be more prone to error. Little velocity is induced between distant vortices, and hence eddies in the wake of a body will stop spreading once the component vortices are sufficiently far apart. Clarke and Tutty [172] found that the diffusion velocity method worked well close to the body, but switched to the random walk method at greater distances from the body.

One of the main disadvantages of vortex methods is that for a flow field of N particles, the velocity calculation requires $O(N^2)$ operations and hence becomes prohibitive at large N. One procedure that can be used to improve computational efficiency is vortex amalgamation or merging [160 and 182]. In this process, two vortices are merged into a single vortex particle to limit the number of particles in the flow, and hence reduce the operation count. This merging process is irreversible and does introduce a small error into the velocity field induced by the newly merged vortex particle. For this reason, merging only takes place if some error tolerance is satisfied, and hence is avoided for particles that have large circulation, that are close to the body surface and for pairs of particles with large inter-vortex spacing. Other more complex techniques have been developed that reduce the operation count from $O(N^2)$ to $O(N \log N)$ or even $O(N)$. These techniques included the Vortex-in-Cell method [5, 160 and 166], Anderson's method of local corrections [183-184], and Multipole Methods [172, 185-188]. Brief reviews are given of each of these techniques in [161 and 189] and will be summarised below.

The Vortex in Cell (VIC) method (or sometimes Cloud in Cell method) aims to reduce the operation count of the velocity calculation, by combining elements of both the Lagrangian and

Eulerian approaches. A fixed mesh is fitted over the domain of the flow field, with the vortex particles representing the discretised vorticity field flowing through the mesh in a Lagrangian manner. The reduction in the operation count is achieved through the use of the mesh to calculate the velocity field. For a flow field containing N particles and using a mesh containing M nodes, the VIC method reduces the operation count to approximately $O(N+M\log M)$. The method of local corrections, was proposed by Anderson [183] and also used by Baden et al [190], and is a variation on the VIC technique. The method is based on the observation that the difference between the velocity induced by a point vortex and a vortex blob is very small at large distances from the vortex centre. The velocity field is calculated from a distribution of point vortices using the VIC method and is then "locally corrected" about the centre of each vortex. The main drawback of these methods is that some of advantages of the vortex method are lost with the need to fit a Eulerian mesh to the flow field. The interpolation to and from the mesh will include areas of the flow where there is little or no vorticity and will also introduce some numerical diffusion into the solution.

Multipole expansions utilise very different techniques to the VIC methods described above, the basic philosophy being to decompose the flow field into a series of zones, each containing a cluster of vortex particles. Provided that a zone is sufficiently far from the point z, at which the velocity is being calculated, then the contribution of the particles in the zone to the velocity, can be found by a Laurent series expansion (2.19) rather than from direct summation of all the particles.

$$\mathrm{U}(z) - i\,\mathrm{V}(z) = \sum_j \frac{a_j}{2\pi i \left(z - Z_c\right)^j} \qquad (2.19)$$

The advantages of this technique are that firstly, the Lagrangian nature of the vortex method is retained and secondly, accurate results can be obtained with a significant reduction in the operation count. The implementation of the method varies from application to application and full descriptions of some of these methods are given in [172, 185-188 and 191]. Typically, multipole expansions give an operation count of $O(N\log N)$ for a flow field of N particles. The Fast Multipole Method (FMM) of Greengard and Rokhlin [185] is claimed to give an operation count of $O(N)$ although this is questioned by Aluru [192] who argues the algorithm may also be $O(N\log N)$ in the worst case. In addition to all the above methods, improved calculation efficiency can be obtained by using parallel computation techniques, examples of which are demonstrated for vortex methods in [186, 193-194].

A significant amount of research has been conducted into the implementation of the boundary conditions on the body surface, where the conditions of no-slip and no-penetration are to be satisfied. Surface singularity distributions, such as vortex sheets are used to satisfy the no-

penetration condition. Between each node that defines the body surface, these distributions are divided into segments, with the circulation of each being either constant, varying linearly or in some other manner. The nodal values of the distribution are determined by solving a set of simultaneous linear equations, and therefore define the surface vorticity distribution. Once vorticity is shed from the body, the existence of wake vorticity in an otherwise potential flow, influences the normal velocity condition at the boundary surface. A common technique is the use of image vortices within the body to cancel the normal velocity for simple geometries such, as circular cylinders, with transformation mappings used to model more complex configurations [4 and 161].

As discussed above for grid based methods, an important aspect of bluff body wakes is the diffusion due to the small scale turbulent fluctuations in the flow. Although there exist numerous turbulence models for grid based methods, the Lagrangian nature of vortex methods mean that a very different modelling approach is required. It has been suggested that the Lagrangian approach may be advantageous and that vortex methods may be better suited to modelling turbulent flow than grid based applications [200-201]. The flow fields predicted by vortex methods are characterised by small scale fluctuations arising from the interactions of the vortex particles, and in a 3D model, these interactions could be sufficiently complex to resemble the nature of turbulent flow provided there is a high enough density of particles to give sufficient resolution of the flow. However, the development of turbulence models applicable to vortex methods is at present not as advanced as with grid based methods and though some theoretical models have been demonstrated, none have as yet been practically applied to vortex method calculations. Using the idea that the limiting factor on modelling the small scale fluctuations in the flow is the resolution provided by the vortex particles, one turbulence modelling approach for vortex methods is a method similar to grid based LES models. The vortex method would be used to model all the large flow structures and the small scale structures modelled using some appropriate turbulence model although the method of application would be very different to grid based methods. This has been demonstrated to an extent by Milane and Nourazar [174] who use a 3D subgrid-scale model to provide the turbulent diffusion component to the flow over a splitter plate calculated by a 2D vortex method. The results are encouraging, though some care is needed in the implementation of the subgrid-scale model as it requires a mesh to be fitted to the computational domain, which may introduce a source of numerical diffusion. Another potential approach, as yet only discussed theoretically is presented by Cottet [228], where the truncation error produced by the core function is analysed and can be used as the starting point for an eddy viscosity model. This method retains the Lagrangian aspect of the model though it remains to be proved as a practical approach to the problem.

Vortex methods have progressed rapidly with a wide variety of techniques leading to improved modelling and calculation efficiency, as indicated in the above discussion. The grid free nature of the method, as well as the concentration of the calculation domain in areas of high vorticity imply that vortex methods are well suited to the analysis of bluff body flow fields. Also, the absence of a calculation grid allows complex body geometries and moving bodies to be modelled fairly easily, with boundary conditions only requiring to be applied relative to the body. In the following section, various results from calculations on bluff body flows using discrete vortex methods are discussed.

2.7.2 Discrete Vortex Method Results.

Successful simulation of the complex flow field around a bluff body presents a challenge for any computational method. However, the discrete vortex method has proved particularly well suited to these highly separated flows [162 and 195] and a range of results are presented for a variety of geometries in [166, 168, 172, 196-207]. Each of these methods uses the theoretical basis that is presented above, although implementation differs in each case as discussed briefly below. It should be noted that virtually all of these methods utilise fast algorithms, generally either VIC or a multipole method, though comparison of the efficiency of the methods will not be discussed here.

A key aspect of vortex methods is how the vorticity is shed form the body surface into the flow with the shedding process being described by two parameters, the strength and position of the new wake vortex being introduced into the flow field. An extensive review and discussion of various techniques that have been used for the introduction of the vortex particles into the flow is given by Sarpkaya [4]. One of the main problems to be addressed is how the newly created vortices are shed from the body surface. Generally, vortices are released at the location of the shear layer separation. A more complex approach is to create vortices at the boundary surface that satisfy the no-slip condition, effectively representing the boundary layer. If the boundary layer is well resolved, the vortices will separate automatically from the surface near to the true separation points [164].

For sharp edged bodies, the separation of the shear layer is often fixed at the corners, and this is taken advantage of in numerous models. However, the highly separated and re-circulatory nature of the flow mean that as well as the primary separation from the upstream corners, there may also be secondary separation at the downstream corners, a phenomenon often neglected in many models. Bergstrom et al [200-201] alternately released vortex particles from the upstream corners of a square cylinder, with the strength of the vortex being determined from the local velocity field at the separation locations (Fig. 2.19). The mean wake velocities and instantaneous

streamlines from the calculation were realistic (Fig. 2.20), although the mean suction pressure on the side faces was too low, and the *St* is overpredicted somewhat. Bienkiewicz et al [202-203] used a similar procedure for releasing vortices at a specified separation point. However, it was noted that a perturbation had to be introduced to the flow in symmetric cases to accelerate the development of oscillatory flow. Good results were obtained for the square cylinder at 0°, though the variation of *St* and C_D with incidence was not well captured (Fig. 2.21). This may be a direct result from the assumption that separation from the downstream corners is only a secondary effect. As the body moves to incidence, one of the shear layers will intermittently, then fully, separate from one of the downstream corners, making the assumption invalid (Fig. 2.22). This may also introduce problems on high aspect ratio bodies, where there will be reattachment on the side faces with the shear layer separating from the downstream corners. The C_D results for varying aspect ratio from Blevins [195] demonstrate this problem (Fig. 2.23).

The separation location needs much more careful treatment in the case of the circular cylinder. Clarke and Tutty [172] allowed the vortex blobs created from the surface vorticity distribution to be convected in the flow, and hence the separation points are automatically determined. However, it was found that some vortex particles with large circulation were released leading to a distorted local velocity field, and so "dynamic vortex creation" was introduced, whereby a vortex that is formed with a strength greater than some maximum, is split into a number of smaller strength particles. Good results were demonstrated on a circular cylinder in impulsively started flow. Smith and Stansby [166] use a model whereby the newly created vorticity on the body surface is shared between a specified number of new vortices that are created at each body node. The variation with time of the surface pressure distribution and the location of the separation point for the starting flow around a circular cylinder was well predicted.

Koumoutsakos et al [170 and 198] investigated the flow around an impulsively started circular cylinder using a very high resolution of particles. The convergence of vortex methods ideally requires that the vortex cores should overlap at all times, however, in practise this is difficult to achieve as the wake convects downstream. To overcome this, the particle locations were redistributed onto a uniform grid whilst interpolating the vorticity distribution to the new positions. This allowed high resolution simulation of the cylinder wake, as the particles are not allowed to disperse too quickly, or conversely, to cluster together. The variation of C_D with time compared well with analytic and experimental results, and a detailed investigation of the development of the flow field was presented although most of the discussion is based on qualitative comparisons with experiment. A similar method was used to investigate rotationally oscillating cylinders by Shiels et al [199], with the results being used to study the mechanism of the reduction in C_D due to the rotational oscillations.

Vortex methods are now being applied to a wider range of problems [167 and 168], including more realistic applications such as the analysis of suspension bridge deck sections [119, 167, 196 and 208], though these results will be discussed in more detail in Chapter 4. In general, the results discussed above demonstrate that discrete vortex methods are particularly well suited to the analysis of a wide range of bluff body flows. Added to this, complex geometries can be modelled relatively easily as the problems of mesh generation are avoided. Many of the problems experienced with grid based methods, such as numerical diffusion and modelling of the near wall flow in highly separated regions, are avoided in vortex methods as the vortex particles tend to be concentrated in areas of high vorticity, leading to good resolution of the vortical flows.

CHAPTER 3

DISCRETE VORTEX METHOD - THEORY AND NUMERICAL MODELLING.

3.0 Introduction.

In this chapter, the theory and numerical implementation of a discrete vortex method is presented and discussed. Much of the model was developed prior to this study and the numerical modelling is presented in more detail by Lin et al [7-9]. Originally, the aim of the method was to study the dynamic stall phenomenon on aerofoil geometries and the model was primarily developed for this application. Hence, much of the modelling lacked the generality required to enable satisfactory analysis of other configurations. Also, it has been found that the original model was somewhat sensitive to a number of input parameters that define aspects of the numerical model. The aim of this research was to develop a model to analyse the flow field around sharp edged bodies. The fixed location of the shear layer separation mean that boundary layer resolution is not as critical as on smooth curvature bodies. Hence, the model developed has taken more of an engineering approach to the analysis, though future research is anticipated that will improve the physical modelling aspects of the method. The discussion presented herein gives a summary of the theory and implementation of the model, but will however focus in more detail on the necessary modifications that have been made to generalise the vortex method and allow an improved analysis of a much wider range of geometries.

3.1 Governing Equations.

Two dimensional incompressible flow is governed by the continuity and full viscous Navier-Stokes equations (3.1) and (3.2) :

$$\nabla . \mathbf{U} = 0 \tag{3.1}$$

$$\frac{\partial \mathbf{U}}{\partial t} + \left(\mathbf{U}.\nabla\right)\mathbf{U} = -\frac{1}{\rho}\nabla P + \nu\nabla\mathbf{U}^2 \tag{3.2}$$

Both ρ and ν are treated as constants as the flow is assumed to be both incompressible and homogeneous. By taking the curl of (3.2), the momentum equation can be reformulated in a velocity-vorticity form which corresponds to the vorticity transport equation (3.3).

$$\frac{\partial \vec{\omega}}{\partial t} + \left(\mathbf{U}.\nabla\right)\vec{\omega} = \nu\nabla\vec{\omega}^2 \tag{3.3}$$

where the vorticity is defined as the curl of the velocity (3.4)

$$\vec{\omega} = \nabla \times \mathbf{U} \qquad \text{with } \vec{\omega} = \mathbf{k}\omega \tag{3.4}$$

Also, by defining a vector potential, $\vec{\Psi}$, such that $\mathbf{U} = \nabla \times \vec{\Psi}$, $\nabla.\vec{\Psi} = 0$ and $\vec{\Psi} = \bar{\mathbf{k}}\Psi$, then the continuity equation may be rewritten as

$$\nabla^2\Psi = -\omega \tag{3.5}$$

The vorticity transport equation (3.3) defines the motion of vorticity in the flow due to convection and diffusion. As the pressure field is not explicitly defined in (3.3), the variation of vorticity at a point in the flow is therefore influenced by the surrounding velocity and vorticity of the flow.

The calculations are subject to boundary conditions (3.6) that implement the no-slip and no-penetration conditions by ensuring that the local velocity of the flow at the body surface is the same as that of the body. Also, the boundary conditions indicate that the flow in the far field is undisturbed by the vorticity shed from the body surface.

$$\begin{aligned}\mathbf{U} &= \mathbf{U}_i \text{ on } S_i \quad \text{and} \quad \mathbf{U} = \mathbf{U}_\infty \text{ on } S_\infty \\ &\text{or} \\ \nabla\Psi &= \nabla\Psi_i \text{ on } S_i \quad \text{and} \quad \nabla\Psi = \nabla\Psi_\infty \text{ on } S_\infty \end{aligned} \tag{3.6}$$

The boundary conditions normal and tangential to the body surface cannot both be applied explicitly as only one component can be specified. Only the normal component is satisfied explicitly although the tangential component is implicitly satisfied due to the representation of the internal kinematics of each solid body. The velocity at a point $\mathbf{r}$ on the surface or within body i can be described by

$$\mathbf{U}_i = \mathbf{U}_{ic} + \Omega_i \times \left(\mathbf{r} - \mathbf{r}_{ic}\right) \tag{3.7}$$

where $\mathbf{r}_{ic}$ is a fixed reference point on the body (Fig. 3.1). This may also be represented in stream function form

$$\nabla^2\Psi_i = -2\Omega_i \qquad \text{in } B_i \tag{3.8}$$

The velocity field is calculated using the Biot-Savart law, which expresses the velocity in terms of the vorticity field. This relationship has been derived by Vezza [209], also discussed in detail by Lin [7], through the application of Greens Theorem to (3.5) for the flow region F (Fig. 3.2) and to (3.8) for the body region B_i. For a point p outside the solid region, the velocity is given by

$$\mathbf{U}_p = \mathbf{U}_\infty + \frac{1}{2\pi} \int_{F_b} \omega \frac{\mathbf{k} \times (\mathbf{r}_p - \mathbf{r})}{\|\mathbf{r}_p - \mathbf{r}\|^2} dF_b + \frac{1}{2\pi} \int_{F_w} \omega \frac{\mathbf{k} \times (\mathbf{r}_p - \mathbf{r})}{\|\mathbf{r}_p - \mathbf{r}\|^2} dF_w$$

$$+ \frac{1}{2\pi} \int_{B_i} 2\Omega_i \frac{\mathbf{k} \times (\mathbf{r}_p - \mathbf{r})}{\|\mathbf{r}_p - \mathbf{r}\|^2} dB_i$$

(3.9)

where $F = F_b \cup F_w$ and $F_b \cap F_w = 0$. Equation (3.9) details the different contributions to the velocity from the freestream, the vorticity in a small zone around the body called the control zone, the vorticity in the remaining flow area or wake zone and the vorticity inside the solid region due to the rotational motion of the body.

3.2   Numerical Implementation.

The governing equations defined in the previous section are for most cases impossible to solve analytically. For this reason, an approximate solution may be obtained numerically through the discretisation of the vorticity field into a series of vortex particles. However, care must be taken that the discretisation gives a true representation of the flow domain. Vorticity is created only at the fluid boundaries in a thin layer close to the body surface and the vorticity in the wake of the body arises through convection and diffusion of the vorticity created at the body surface. In cases of highly separated flow such as that seen on bluff bodies, although the wake region is wide, the vorticity is contained within the regions defined by the separated shear layers emanating from the body surface (Fig. 3.3). Outside of this region, the flow is largely irrotational, and hence only the region containing vorticity need be discretised, demonstrating why vortex methods are particularly well suited to the analysis of bluff body flows.

As the vorticity in the flow originates on the body surface, the discretisation of the vorticity in this region is important to capture well its subsequent evolution. The idea that the vorticity is created in a thin layer around the body surface indicates that the flow can be divided into two zones. The first is the control zone near the body surface in which vorticity is created, and the second is the wake zone which contains the remaining vorticity that is shed from the body surface through convection and diffusion (Fig. 3.4). These two sub-regions of the flow utilise different discretisation procedures.

For a two dimensional body, a polygonal representation of the body surface is created by connecting a series of N nodes, that define the body geometry, with straight lines forming a series of panels. Each panel is further subdivided into K equal length sub-panels. The vorticity in the control zone can be treated as a one dimensional vortex sheet, which is then discretised using a two stage process. First, the vorticity in the control zone, γ, is treated as a quantity that varies

piecewise linearly and continuously along the surface. The values of γ at the node points therefore represent the entire vorticity distribution within the control zone. Secondly, the panel distribution of vorticity is further broken down into vortex blobs, one for each sub-panel. The blob is positioned a distance δ above the middle of the sub-panel. This process is illustrated in Fig. 3.5, and the vortex locations on each panel and sub-panel are given in complex notation by (3.10)

$$z_k = \left(\left(\frac{K-k+0.5}{K} \right) Z_j + \left(\frac{k-0.5}{K} \right) Z_{j+1} \right) + i\delta Z n_j \qquad (3.10)$$

The strength of each nascent vortex particle is obtained from the γ values at the nodes and from the linear variation of γ along each panel (3.11).

$$\Gamma_k = \left(\left(\frac{K-k+0.5}{K} \right) \gamma_j + \left(\frac{k-0.5}{K} \right) \gamma_{j+1} \right) \frac{\left| Z_{j+1} - Z_j \right|}{K} \qquad (3.11)$$

The circulation of each nascent vortex is equivalent to the total vorticity in the control zone above the kth sub-panel. Both (3.10) and (3.11) are for the case where each panel is assumed to be a flat surface, simply connecting each node with a straight line. For high curvature regions, such as aerofoil leading edges, more general forms of these equations are used to model the high curvature of the surface more accurately [7].

The γ values in the creation zone are the solution of the linear system of equations arising from the boundary conditions which are implemented by ensuring zero mass flow through each surface panel. Although this cannot guarantee that the boundary conditions are satisfied at all points on each panel, there will be at least one point on the panel with zero relative normal velocity. The implementation is expressed as

$$F_{js} + F_{ji} + F_{jf} + F_{jv} + F_{jn} = 0 \qquad (3.12)$$

where each term represents the contribution of the mass flow from different sources. The first and second terms are from the motion of the body, with the remaining terms representing the contributions from the freestream, the vortices in the wake and the vortices within the control zone. The total number of equations (3.12) is N for a body with N panels, but only N-1 are independent as there is no source or sink within the body. Hence when N-1 panels satisfy zero mass flow, the mass flow for the final panel will automatically be zero. One advantage of the current discretisation procedure is that the particle density on the panel surface can be increased by simply using more sub-panels between each surface node. Hence, greater resolution of the vorticity field near the body is obtained with little increase in the computational operation count, as the number of panels and hence the number of equations in (3.12) has not increased [7].

A further equation required to make the solution unique is based on the principle of Kelvin's theorem. This states that the rate of change of the circulation in the entire flow field is zero as there is no external source of vorticity. However, Kelvin's theorem is only strictly valid for inviscid flows, and in the case of viscous flow, there is diffusion of vorticity through the body contour. By integrating the pressure gradient along the closed boundary on the body surface, it can be shown that the net increase in vorticity created at the surface is produced at the expense of the vorticity inside the body and does not depend on the diffusion in the outer flow [7]. This arises as the pressure distribution is required to be single valued in the flow field, and therefore requires a zero integral of the pressure gradient around a closed contour. The relationship holds for viscous flow, unlike Kelvin's theorem, due to this single valued pressure requirement. Hence, the resulting circulation condition (3.13) completes the linear system of equations, providing a unique solution

$$\sum_w \Gamma_w + \sum_{j=1}^N \sum_{m=1}^K \left(\Gamma_j\right)_m + 2\Omega_i A_i = \Gamma_{st} \tag{3.13}$$

where the first term is the circulation of the vortices in the wake, the second is the circulation of the vortices in the control zone, the third is the circulation due to the body rotation and the fourth is the initial circulation in the flow field prior to the start of the calculation, which in impulsively started flows will be zero. The second term contains the unknown γ values. Once the system of equations are solved for the $N \gamma$ values, the strengths of the nascent vortices in the control zone are obtained. The relative position of the nascent vortices to the body surface remains fixed at all times, with changes in circulation being reflected in the γ distribution at each time step.

All vortices outside the control zone originate from nascent vortices, with their positions being the result of convection and diffusion at each time step. A wake vortex is created when a nascent particle crosses from the control zone into the wake zone and effectively models the shedding of vorticity from the body. The simulation of vortex convection and diffusion employs an operator splitting technique, where the vorticity transport equation (3.3) is split into a separate convection part (3.14) and diffusion part (3.15), both of which are solved sequentially as proposed by Chorin [164].

$$\frac{\partial \omega}{\partial t} + \left(\mathbf{U}.\nabla\right)\omega = 0 \tag{3.14}$$

$$\frac{\partial \omega}{\partial t} = \nu\nabla^2\omega \tag{3.15}$$

As vorticity forms one of the conserved properties of the particles in inviscid flows, the velocity at the centre of each vortex particle is equal to the velocity of the vorticity transport which is

evaluated from (3.9). This is exact for point vortices though the use of vortex blobs does introduce a truncation error. The diffusion process is modelled using a random walk procedure [164] which satisfies the Gaussian distribution of zero mean and standard deviation $\sqrt{2\nu\Delta t}$ or in non-dimensional form $\sqrt{2\Delta t/Re}$, where Δt is the timestep. At each time step the position of the vortex particles are updated according to (3.16)

$$Z_w(t + \Delta t) = Z_w(t) + U_w(t).\Delta t + \left(\eta_x + i\eta_y\right) \tag{3.16}$$

where the first term on the RHS is the original particle position, the second is the increment due to convection and the third is the increment due to diffusion. U_w is the velocity of the particle and η_x and η_y are the random walk components in the x and y directions respectively. The random walk method provides a relatively simple scheme for modelling viscous diffusion, though it does have limitations as discussed in the previous chapter. The random walk assumes homogeneity with the kinematic viscosity taken to be constant throughout the flow. The model works best when there are many overlapping vortex particles, particularly near to the body surface [4]. Other limitations of the random walk are that high *Re* flows are not correctly modelled. In this case, the viscous diffusion component from the random walk is negligible and the calculated flow field is effectively modelled as if it were inviscid. As with other diffusion models, the random walk does not model the effects of turbulent diffusion at high *Re*. However, other diffusion models have their own limitations and problems, but lack the simple implementation that the random walk offers.

The exchange of vorticity between the control zone and the wake, or the release and absorption of vortex particles from/to the wake are determined by the new vortex positions at the next instant of time, with respect to the surface position. To ensure that the release of the vortex particles from the control zone to the wake is modelled smoothly, the full circulation of the nascent vortex is not released into the wake unless it has moved a distance 2δ from the edge of the control zone, where δ is the control zone thickness (Fig. 3.6). A more general approach to the vorticity release was investigated by Lin [7]. However, for bluff body or highly separated cases, the differences between the two schemes were found to be negligible.

It is likely that a number of wake vortices will at some stage cross the control zone boundary back into the vorticity creation region. These vortices, referred to as absorbed vortices, are removed from the wake and the circulation integrated into the vorticity distribution within the control zone. As well as providing a mechanism to limit the number of vortices contained in the computational domain, the process also helps to stabilise the implementation of the boundary conditions. The procedure for vortex release and absorption is demonstrated in Fig. 3.7.

The calculation of the velocity of a single vortex particle requires the influence of all regions of vorticity in the flow field to be taken into account (3.9). For a flow field containing N particles this leads to an operation count of $O(N^2)$, which becomes prohibitive as N increases. As mentioned above, N can be restricted somewhat by the absorption of wake vortices into the control zone. Another technique implemented in the vortex method for limiting N is to merge particles in the body wake [7]. A pair of vortices are merged if they satisfy a given criteria, such that the induced surface velocity on the body is not affected significantly. For this reason it is preferable to merge vortices that are distant from the body, for which the inter-vortex spacing is small, and whose circulation is small and of the same sign [160].

It is assumed that two vortices located at Z_1 and Z_2, with circulation Γ_1 and Γ_2, are merged into a single vortex with location Z (3.17) and circulation Γ (3.18).

$$Z = \frac{\Gamma_1 Z_1 + \Gamma_2 Z_2}{\Gamma} \qquad (3.17)$$

$$\Gamma = \Gamma_1 + \Gamma_2 \qquad (3.18)$$

The induced velocity at the body surface is given by

$$V(Z_0) = \frac{i\Gamma}{2\pi}\left(\frac{1}{Z_0 - Z}\right) \qquad (3.19)$$

where Z_0 is the nearest node on the body surface, to whichever of Z_1 and Z_2 is nearest to the body. The difference between the induced velocity on the body from the two separate vortices and the single merged vortex is given by ΔV (3.20), and only when this is sufficiently small can the vortices be merged.

$$\Delta V(Z_0) = V(Z_0) - V_1(Z_0) - V_2(Z_0) \qquad (3.20)$$

It can be shown that ΔV may be approximated by (3.21) [210].

$$\Delta V(Z_0) = \frac{|\Gamma_1 \Gamma_2|}{|\Gamma|} \frac{|Z_1 - Z_2|^2}{|D_0 - d_1|^{1.5}|D_0 - d_2|^{1.5}} \qquad (3.21)$$

where d_1 and d_2 are the distance from the vortices to the body surface and D_0 is a parameter that has a large influence close to the body, chosen such that the vortices near the body are less likely to be merged. The vortices are only merged if ΔV is less than some criteria V_{crit} which is defined such that the error on the body surface is minimal. However, sufficient vortex merging takes place to have a significant effect on the reduction in operation count.

The pressure distribution on the body surface can be evaluated by integrating the pressure gradient along the body contour. The pressure gradient expression is derived in [7] and the gradient at node j on the body surface is (3.22)

$$\frac{1}{\rho}\frac{\partial P}{\partial s} = -\mathbf{s}.\frac{D\mathbf{U}_c}{Dt} - \mathbf{n}.(\mathbf{r} - \mathbf{r}_c)\frac{D\Omega}{Dt} + \mathbf{s}.(\mathbf{r} - \mathbf{r}_c)\Omega^2 + v\frac{\partial\omega}{\partial n} \tag{3.22}$$

The first three terms on the RHS are due to the body motion and represent the surface tangential components of the body reference point acceleration, the rotational acceleration and the centripetal acceleration. The final term is the negative rate of vorticity creation at the body surface and is calculated from the vorticity distribution created in the control zone between time t-Δt and t [7, 160 and 210]. The resulting pressure distribution is integrated around the body surface to calculate the aerodynamic forces on the body and the moment about the body reference point.

3.3   Generalisation and Improvement of Model.

The discrete vortex method presented by Lin [7] was developed specifically for the analysis of the dynamic stall phenomenon on pitching aerofoils. As a result, much of the modelling lacked generality and could not be easily applied to other geometries. However, one of the main advantages of the vortex method is the potential to successfully model highly separated flow fields that provide a stiff challenge to alternative grid based methods. Hence, much of the development of the vortex method forming part of this study has been a generalisation of the model to produce a tool to analyse a wider range of problems. Much of this work involved numerous changes to the modelling [211], some of which will be mentioned though not discussed in detail, but the combined effect of all the corrections and improvements has been to provide a robust method capable of analysing a variety of stationary and oscillating bodies.

Some of the problems encountered with the original method arose due to the handling of the wake particle locations relative to the body geometry. As part of the merging calculation, the distance of the particles to the nearest point on the body is required. In the original method, once the particles were downstream of the body, the trailing edge of the aerofoil could automatically be taken as the nearest point to simplify the calculation and improve computational efficiency. However, for bluff body cases where the "trailing edge" can not as easily be defined, the calculation was necessarily modified so that the nearest point on the body for every wake vortex particle is found. This does lead to a little more computational effort at each time step, but has been shown to be a necessary modification.

Problems were also encountered with the check to ascertain whether a wake vortex should be re-absorbed into the control zone. Once the nearest body node to the vortex particle is found, the

normal distance to the adjacent body panel is found depending on whether the particle is upstream or downstream of the node (Fig. 3.8). If the normal distance is found to be less than the control zone width, δ, then the particle will be absorbed. This procedure was adapted for sharp edged bodies with a number of extra checks introduced to avoid the situation demonstrated in Fig. 3.8b. The correct procedure is shown in Fig. 3.8c and indicates the extra criteria, that the particle must be no further from the body node than the sum of the panel length and δ, as well as being inside the control zone. This is applied to every panel, not just sharp corners to ensure vortices "between" panels are merged correctly.

Other small, but important modifications were also made to the method, including the body motion that can now be utilised in the calculations. For the pitching aerofoil, the body velocity modelling was concentrated on the specific case of an aerofoil undergoing angular ramp motions [7]. Analysis can now be made of a much wider range of body motions, from a constant translational or rotational velocity, sinusoidal translation in either the longitudinal or transverse directions as well as sinusoidal pitching motion. Any single one of these or any combination may be applied to the body. Also, a general more complex motion can be applied where the velocity of the body, either translational, rotational or both, is specified at each time step of the calculation. These modifications further add to the improved generality of the discrete vortex method.

3.4   Sharp Corner Modelling.

The vortex method assumes that the vorticity distribution on the body surface, defined by γ, varies linearly over each panel and is also continuous at each body node. This assumption is acceptable over most areas of any body surface, where the surface curvature is not too great and the resultant angle between adjacent surface panels is relatively small. However, where there are corners on the body, special treatment is required as the vorticity distribution will not necessarily be continuous. Lin [7] discussed this with particular reference to the trailing edge of an aerofoil. It is noted that the γ value at each node represents the difference between the velocities at the control zone boundaries and the body surface, with this difference changing little on a low curvature surface due to the gradual changes in the velocity field. At a sharp edge, the changes in the velocity are much greater, and at some sharp corners may even be near to being discontinuous. It is then dubious whether the panels joined by the node at the corner should share the same γ value. Lin modelled the aerofoil trailing edge by effectively extending the control zone downstream of the trailing edge and discretising the nascent vorticity in this region in a process similar to the discretisation of the nascent vorticity [7] (Fig. 3.9). Some success was achieved by this approach, although the extension of the control zone is a feature best suited to aerofoil trailing edges, and also works best at low angles of incidence.

For bluff bodies, or other geometries, where the body includes a sharp corner for which the above approach is not applicable, a new approach is required. One of the fundamental problems with the corner is that one γ value is calculated for each node, and is used to obtain the circulation of the nascent vortices for the panels on each side of the node. However, the vorticity distribution on each side of the corner may be very different, as illustrated schematically in Fig. 3.10. On the front face normal to the oncoming fluid, the flow tends to move up the surface towards the corner, resulting in clockwise vorticity near the surface. On the top face, the separated shear layer from the corner causes a clockwise rotating vortex to form above the surface, and hence the local velocity on the top surface is directed back towards the front corner. The resultant vorticity created at the surface therefore tends to have a counter clockwise component. Although this is a simplified argument, it is clear that using a single γ value at the corner will give a poor prediction of the vorticity field on each side of the corner.

A model has now been incorporated within the vortex method to allow a dual γ value to be used at any specified sharp corners on the body surface. This decouples the circulation of the nascent vortices on the panels each side of the corner. The model has been derived so that any sharp corner can be modelled, ranging from the 90° corner in Fig. 3.10 to the aerofoil trailing edge problem. One problem of introducing the dual γ at the corners, is that the linear system of equations used to calculate the γ distribution now becomes under-determined, with N equations being used to determine $N+n$ unknown γ values, where N is the number of surface nodes and n is the number of sharp corners. For this reason, the procedure to solve the system of equations needs to be modified accordingly.

The coefficients for the system of equations are calculated as described previously, however, the dual γ value for the panels on either side of the sharp corners are accounted for in the coefficients. The system of equations in the original model is shown in (3.23)

$$
\begin{bmatrix} a_{11} + a_{12} + \dots + a_{1N} \\ \vdots \quad \ddots \quad \vdots \\ a_{N1} + a_{12} + \dots + a_{NN} \end{bmatrix}
\begin{bmatrix} \gamma_1 \\ \vdots \\ \gamma_N \end{bmatrix}
=
\begin{bmatrix} F_1 \\ \vdots \\ F_N \end{bmatrix}
\tag{3.23}
$$

$$
\begin{bmatrix} \mathbf{A} \end{bmatrix} \begin{bmatrix} \gamma \end{bmatrix} = \begin{bmatrix} \mathbf{F} \end{bmatrix}
\tag{3.24}
$$

where the a_i are the coefficients of the nascent vortex values, γ_i, and F_i are the sum of the contributions to the mass flow across panel i from different sources (3.12). This is shown in matrix form (3.24), where $\mathbf{A}$ is an $N \times N$ matrix, and γ and $\mathbf{F}$ are both $N \times 1$ matrices. However, the extra γ values arising from the dual value introduced at the sharp corners mean that γ now becomes an $(N+n) \times 1$ matrix, and $\mathbf{A}$ is now a non-square $N \times (N+n)$ matrix.

To solve the under-determined system of equations for the $N+n$ γ values, a pseudo-inverse technique is used [212], which is derived in Appendix D. It should be noted that the solution for γ is not unique, though it is consistent from time step to time step [212]. The pseudo-inverse procedure gives the best approximate solution to the system of equations and furthermore, this best approximation can be proven to be unique. Also, the solution obtained satisfies all the necessary flow criteria and boundary conditions on the body surface. It is difficult to quantify the size of any error that may arise from using the best approximate solution, although tests on a number of calculations with and without the sharp corner model indicate that the error is small. In particular, results from a number of aerofoil calculations using the new model at the trailing edge, show little difference to previous results [7]. The vorticity distribution for the square cylinder is shown in Fig. 3.11. The upstream face (AD) is least affected by the flow in the separated region and the body wake. Hence, any errors arising from the sharp corner model, especially at corners A and D would be noticeable on this face. It is clear in Fig. 3.11 that face AD is not greatly affected by the sharp corner model indicating that the error from the approximate solution to the system of equations is small. There is no limit to the number of sharp corners which may be defined and the success of this approach is demonstrated in Fig. 3.11. A and D are located at the upper and lower front corners respectively (Fig. 3.1), and the difference in the vorticity distribution on either side of A and D is clear. The vorticity on the front face is clearly of opposite sign to that on the initial part of the side faces, with a sudden change across the corner. Comparing the new model with the original case, the improvement in the distribution is noticeable (Fig. 3.11). Downstream of the sharp corners, the region of opposite sign vorticity is much more distinct when the sharp corner modelling is included. Also, the sharp spike in the γ distribution at the corners has been reduced significantly.

Another aspect of the sharp corner modelling that has been incorporated along with the vorticity discontinuities described above, arises from the fact that there is an area of vorticity effectively not discretised between the two panels. Only vorticity directly above a panel is discretised into the nascent vortex particles, as demonstrated in Fig. 3.12. For each node that is flagged as a sharp corner, and for which the vorticity discontinuity is applied, the position of the nascent vortex particles on a few panels each side of the corner are shifted slightly towards the corner region (Fig. 3.13). This gives an improved representation of the vorticity at sharp corners, and in particular improves the modelling of aerofoil trailing edges, utilising a similar philosophy to the model employed by Lin [7]. The procedure used is to stretch the upper boundary of the control zone for the three panels either side of the corner, so that the control zone above these panels continues into the corner region (Fig. 3.13). The location of the nascent vortex particles are then adjusted towards the corner using this skewed control zone. This procedure is not radically different from the original method, but does allow an improved model for sharp corners, especially those of a "trailing edge" type as seen on aerofoils and some bridge deck sections.

3.5 Wake Decay Model.

Numerous computational and experimental investigations into bluff body flow fields have shown that even in predominantly two dimensional flows, there is still a strong three dimensionality within the body wake. Experimental results show that although the vortex street typical of bluff body wakes is an inherently two dimensional process, there is a significant proportion of the vorticity transferred away from the spanwise component, ω_z [22-30]. As the vorticity is shed from the body, vortex stretching effects and also turbulent diffusion processes, redistribute the vorticity into each direction. Lin et al [27] present measurements indicating that the transfer of spanwise vorticity is predominantly to the streamwise component, ω_x, and show that ω_z has been reduced by approximately 20% at a plane one diameter downstream of the cylinder. Other researchers have demonstrated the presence of streamwise vorticity and discuss the complex three dimensional nature of the bluff body wake. Experimental results also demonstrate that the vortex shedding process from a bluff body is not fully two dimensional, as shown by the variation in the spanwise pressure coefficient (Fig. 3.14).

Numerical results also demonstrate that bluff body flows have a significant three dimensional component. As discussed in Chapter 2, Tamura et al [147 and 156] discuss the difference in the predicted flow fields from both two and three dimensional calculations. In two dimensions, even with good grid resolutions, the flow field is not accurately calculated, and the shed vortices tend to contain too much circulation. These results, along with other similar calculations [145, 147, 152 and 153], demonstrate that more representative results are predicted by three dimensional calculations which simulate vortex stretching and dissipation of the circulation in each direction.

Similar problems have been reported by researchers using vortex methods [213-216]. Stansby [213] found that the aerodynamic loading was affected, due to the shed vortices rolling up too tightly in the wake, resulting in an over prediction of suction in the base region. The prime cause was that the three dimensional effects which reduce the circulation were not modelled in the two dimensional calculation. A solution proposed was to apply a simple exponential decay to the circulation of each vortex particle, that would "mathematically" if not physically account for these effects (3.25).

$$\Gamma = \Gamma(0)e^{-\beta t} \tag{3.25}$$

Sarpkaya et al [214] proposed a technique whereby each wake vortex particle loses circulation in an amount proportional to its current strength and position after rediscretisation of the vortex sheet. Basuki et al [215] and Kiya et al [216] also employed an exponential decay technique to account for the three dimensionality in the flow (3.26). Basuki found that the suction pressures on a stalled aerofoil in the separated region were overpredicted and the circulation reduction

technique also helped to overcome this problem. It was also claimed that the circulation reduction technique, to an extent, simulates the three dimensional effects.

Early results using the vortex method on bluff body flows indicated that similar trends were being experienced, with strong vortices being shed from the body resulting in high predicted mean and fluctuating force coefficients. In an attempt to model the three dimensional effects of the wake flow, a circulation reduction, or wake decay technique, has been employed in the vortex method presented herein. The model is similar in nature to that used by Basuki et al [215] and Kiya et al [216] (3.26)

$$\Gamma(t) = \Gamma(0)\left[1 - \exp\left(\frac{-\beta}{t - t_c}\right)\right] \tag{3.26}$$

where t_c is the non-dimensional time at which the vortex was created. It should be noted that this model is an empirical approach to the problem and does not satisfy any physical representation of the flow though the desired effect of transfer of vorticity away from the spanwise component is achieved. Also, the effects of this model are most noticeable on bodies with a large base area such as the square cylinder, with the higher aspect ratio bodies, such as bridge sections, being much less reliant on the model. The decay function chosen gives a gradual initial decay rate that increases with time. Although the exponential decay of (3.25) is simpler, the initial decay rate is too severe and the vorticity is found to dissipate too rapidly (Fig. 3.15). The constant β, was chosen to produce a rate of transfer of circulation from the spanwise direction that is consistent with the experimental results of Lin et al [27]. For simplicity, the same decay constant, β, has been used for all the calculations presented herein. However, for cases such as the oscillating square cylinder, the increased spanwise correlation of the vortex shedding within the vortex lock-in region suggests that these cases may require a different β to produce less wake decay.

One consequence of the model is that the decay of the circulation of the wake vortices, does not conserve circulation in the two dimensional plane. To account for this, the decayed circulation is effectively transferred to the point at infinity [215]. The decayed circulation still plays a part in determining the nascent vortex strengths as it is effectively transferred to the fourth term in the circulation equation (3.13). Hence the conservation of circulation condition becomes (3.27)

$$\sum_w \Gamma_w + \sum_{j=1}^{N} \sum_{m=1}^{K} \left(\Gamma_j\right)_m + 2\Omega_i A_i = \Gamma_\infty \tag{3.27}$$

where Γ_∞ includes the circulation transferred to infinity. Care must be taken with the merging of wake vortices when the wake decay model is implemented. The problem lies with determining the

circulation, initial circulation and the effective creation time for the newly merged vortex, especially when the vortices being merged have been created at significantly different times and are at different stages of the decay process. Two possible approaches may be used to determine these parameters : 1) the rate of vorticity decay is preserved in the merged vortex and 2) the drop in the circulation of the two vortices is maintained in the merged vortex. These two procedures are discussed in detail in Appendix E. Although preserving the rate of decay of circulation introduces less error into the merging process, it is considerably more complex to implement and so the method using the drop in circulation has been used. However, it should be noted that if the two vortices are of a similar age, then the error is minimal. As shown in Appendix E, the newly merged vortex has circulation

$$\Gamma_M(t) = \Gamma_1(t) + \Gamma_2(t) \tag{3.28}$$

where $\Gamma_1(t)$ and $\Gamma_2(t)$ are the circulation of the two vortices being merged. The initial circulation and creation time of the merged vortex are given by (3.29) and (3.30) respectively.

$$\Gamma_M(0) = \Gamma_1(0) + \Gamma_2(0) \tag{3.29}$$

$$\Delta t_{cM} = t - t_c = \frac{\beta}{\ln\left(\dfrac{\Gamma_1(0) + \Gamma_2(0)}{\Delta\Gamma_1 + \Delta\Gamma_2}\right)} \tag{3.30}$$

The vortex decay process is a largely mathematical tool rather than a strictly physical model. However, as found by Basuki et al [215], the reduction in the wake circulation does lower the predicted suction pressures on the body surface, as well as reducing the intensity of fluctuating pressures. The decay model has proved beneficial, allowing simulation of complex flow fields using a two dimensional model rather than the necessity of full three dimensional modelling that grid based methods appear to require [145, 147, 152 and 153]. However, the empirical nature of the model must be remembered at all times, as the vortex decay scheme is only analogous to the complex three dimensional processes within the wake. Future research may be aimed at developing a model that has a more physical basis, but retains the quality of the results obtained.

3.6   Improved Computational Efficiency using a Zonal Decomposition Algorithm.

As discussed earlier, one of the problems with the vortex method is that for a flow field containing N particles, the determination of the velocity field requires a calculation with an operation count of $O(N^2)$. This becomes more and more prohibitive as N increases and is a particular problem for bluff body flows, with the large separated regions and wide wakes demanding high numbers of particles to satisfactorily resolve the flow field. N can be restricted somewhat by the absorption of

wake vortices into the control zone and also by the amalgamation of wake vortices as discussed earlier. More complex techniques are available which are aimed at reducing the operation count of the velocity calculation directly to $O(N\log N)$ or even $O(N)$, rather than restricting N. A number of these techniques are discussed in Chapter 2 and also in more detail in [189]. An algorithm to improve the computational efficiency of the vortex method has been developed and successfully implemented. The procedure for the new velocity calculation and the improvement that has been obtained in the operation count is presented in the next section and also in [189].

The zonal decomposition technique was chosen as the method with which to improve the efficiency of the DVM. The choice of this technique over a VIC method was primarily based on the fact that the Lagrangian nature of the method, and the benefits this brings, is retained. The technique utilised in the DVM uses an adaptive zonal decomposition with square zones. The series expansion for the velocity influence from a zone is similar in form to the FMM, although the interactions between zones and particles are handled very differently. This leads to a much simpler algorithm for the velocity calculation, without any great loss in accuracy when compared to direct summation.

3.6.1 Decomposition of Flow Field into a Hierarchical Structure of Square Zones.

As with many other applications, it was decided to use square zones in the decomposition of the flow field. Clarke et al. [172] used rectangular zones in the zonal decomposition and divided each zone into two, along the longest side, such that each sub-zone contained half the particles of the parent zone. However, it was found that some zones with high aspect ratio were created, which could lead to a large radius around the zone. Consequently there would be less likelihood of using the zonal influence in the velocity calculation thus limiting the benefits of the fast algorithm. High aspect ratio zones are avoided if the zone is divided into half along the longest side, irrespective of the number of particles in each half. This alternative, however, leads to more "dormant" zones that contain no particles, again affecting the performance of the algorithm.

The DVM discretises the vorticity field into two sets of vortex particles, which are termed nascent (contained in a small control zone close to the body) and wake particles. These two sets are joined together into a single set of particles for the purpose of the zonal decomposition. The initial zone is the smallest square that contains all the particles in the flow field. If there are greater than some predetermined number of particles in the wake region, NP_{min} say, then this initial zone can be subdivided into four smaller zones in the order shown in Fig. 3.16. Each of the children of the initial zone are subdivided if they contain greater than NP_{min} particles. The children of these new zones are then subdivided, where appropriate, until no further subdivision can take place. This

procedure is illustrated in Fig. 3.17, along with the resulting hierarchical zonal structure for a typical flow field.

This procedure is similar to that described by Van Dommelen et al. [188], although a much simpler method of numbering the zones is used here. The initial zone containing the flow field is numbered zone 0. The four sub-zones of zone 0 are zones 1 to 4 respectively. If zone 1 can be subdivided, then its children will be zones 5 to 8. In general, the children of a zone k will be numbered $Nz+1$ to $Nz+2$, where Nz zones have previously been created. As the children of each zone are always created in the same order (Fig. 3.16), only the *first* child is recorded when a zone is subdivided. Also, when each zone is created, its parent zone will be recorded. Using this numbering scheme, for any zone, its parent and all of its children can easily be traced. The resulting zonal decomposition, containing all the vortex particles in the flow field, provides an hierarchical structure of zones that can be used as part of a fast algorithm for the velocity calculation in the DVM.

3.6.2 Velocity Calculation using Zonal Decomposition and Series Expansion.

As discussed previously (Chapter 2), the velocity influence of a group of particles contained within a zone can be used, if the velocity is being calculated at a point sufficiently far from the centre of the zone. It is usual to define "sufficiently far" as some specified multiple of the zone radius, where the radius is half the side length of the zone (Fig. 3.18). The velocity influence of a zone, at a point z can be calculated from a truncated series expansion (3.31 - 3.32).

$$U(z) - i\, V(z) = \sum_{j=1}^{Nt} \frac{a_j}{\left(z - Z_c\right)^j} + \varepsilon \qquad (3.31)$$

$$a_j = \frac{1}{2\pi i} \sum_{k=1}^{Np} \Gamma_k \left(z_k - Z_c\right)^{j-1} \quad j = 1, \ldots, Nt \qquad (3.32)$$

The derivation of these formulae is given in Appendix A. The coefficients a_j of the series expansion for each zone, are calculated as the zonal decomposition is being performed. It should be noted that the flow field is only decomposed into the zonal structure if greater than some predetermined number of wake particles are present in the calculation. If there are less than this limit, then the velocity calculation for the whole flow field is performed using direct summation.

If a zone contains Np particles, then the operation for the velocity influence at a point is $O(Np^2)$ using direct summation, compared to $O(Nt)$ using zonal decomposition. It is clear that the larger Np is, then the greater will be the reduction in the operation count for the velocity calculation. For

this reason, the hierarchical nature of the zonal decomposition is utilised with the largest possible zone always being used in the calculation, to give the maximum improvement in the speed of the algorithm. Extra efficiency is achieved by varying the number of terms used in the series expansion, Nt, depending on the distance from the particle to the zone centre. For a zone a long distance from the point of interest, the series will converge after only a few terms. However, for a closer zone, more terms of the expansion will be required to ensure convergence.

The implementation of the algorithm will now be demonstrated by considering the calculation of the velocity for one vortex particle. First consider the distance of the particle from the first zone (zone 1). If the particle is greater than twice the zone radius from the zone centre, then the particle is sufficiently far from the zone, and the influence of the zone can be used in the velocity calculation. However, if the particle is less than the required distance and the zone has no children, then the velocity influence of the zone is calculated from direct summation. If the zone however does have children, then each of the children are considered in the same manner as described above. The procedure is repeated until either a zonal influence can be used, or the lowest level of decomposition is reached, and direct summation is used. If the particle is contained within the zone, and the lowest level has been reached, then the zone's contribution is calculated using direct summation later in the algorithm. Otherwise the zone's children are considered as usual. This continues until all the children and "grandchildren" of zone 1 have been considered. The procedure is then repeated on the remaining zones at the top level (zones 2-4). This algorithm is summarised in the flowchart shown in Fig. 3.19.

The procedure described above gives the induced velocity on a particle from all the particles outside of the zone at the lowest level which contains the particle (Fig. 3.20). Also, as discussed above, the largest possible zones are used to give the velocity influence, and are found by considering the least number of possible zones. The final part of the algorithm is a single pass through each of the childless zones, so that the induced velocity by the particles contained in the zone on each other can be calculated using direct summation. This provides the final contribution to the velocity of each particle.

The FMM algorithm developed by Greengard [185] uses a zone vs. zone interaction, and is claimed to give an operation count of $O(N)$, although Aluru indicates that it is actually nearer $O(N\log N)$ in the worst case [192]. The algorithm implemented in the Vortex Method and described above uses a particle vs. zone interaction, and gives an operation count of $O(N+N\log N)$ (Appendix B). The reason for the use of an apparently slower algorithm was primarily due to the simpler implementation of the method, although as discussed below, the algorithm gives very satisfactory results in terms of the calculation efficiency.

3.6.3   Performance of Algorithm.

Three different test cases were used to assess the performance of the zonal decomposition algorithm. Each test case involved a very different body geometry and resulting flow field. The test cases were as follows :

1.   Static aerofoil at 40 degrees incidence.
2.   Circular cylinder.
3.   Square cylinder at 0 degrees incidence.

In each case, the calculations were performed first using the original velocity calculation via direct summation and then using the zonal decomposition algorithm. The calculations were performed on a Silicon Graphics workstation with a 150MHz IP22 R4400 processor, 16Kb cache size and 64Mb main memory size. The performance of each calculation was obtained by outputting the CPU time taken for the whole timestep as well as the CPU for the velocity calculation. The results are shown in Figs. 3.21 to 3.29 and show the CPU plotted against the total number of vortices (wake and nascent combined) for the timestep and velocity calculations respectively. Typical decomposition of the flow field into the hierarchical zonal structure are shown for the square cylinder in Fig. 3.30.

Comparing first the velocity calculation only for both the direct summation and zonal decomposition algorithms, it is clear for each method that the relationship between the CPU and the number of vortices is very similar in each of the three test cases, especially when direct summation is used (Fig. 3.24). As expected, this shows that the calculation is dominated by the number of vortices contained in the flow field rather than their physical location within the flow field. There is slightly more variation in the zonal decomposition case, as the location of particles will determine whether the series expansion can be used for the velocity calculation. However, a strong relationship between the CPU and number of vortices is clear, irrespective of which model is used.

The operation count for the direct summation method is $O(N^2)$ as discussed above. For the zonal decomposition, analysis of the operation count is a little more complex and is shown to be $O(N+N\log N)$ in Appendix B. A least squares curve fit has been fitted to the CPU timings for both direct summation and zonal decomposition, using the operation counts given above. The curve fits, and the derived constants are shown in Figs. 3.25 and 3.26. Table 3.1 shows the improvement obtained by the zonal decomposition algorithm for the CPU required for one timestep, based on the curve fits to the data.

The factor improvement for the whole timestep is also shown in Fig. 3.27, and is compared with the factor improvement in the velocity calculation only. An extra saving was made in the timestep

by using the zonal structure as part of the vortex merging calculation [7 and 210]. Instead of checking against any vortex in the flow field to find if the merging criteria is satisfied, which can also lead to an $O(N^2)$ calculation, only vortices within the same zone at the lowest level are checked. The CPU taken for the merging calculation using the new and old methods is shown in Fig. 3.28. The breakdown of the timestep into various elements of the calculation is shown in Fig. 3.29. It is clear that the main element of each timestep is the velocity calculation. As discussed above, the merging calculation now uses little CPU. Importantly, the zonal decomposition and sorting of the vortices also takes a relatively small amount of CPU. The speed and accuracy of the algorithm can be optimised by judicious selection of a number of parameters that define the zonal decomposition. The optimisation of these parameters is discussed in Appendix C.

Number of Vortices.	CPU from Direct Summation. (secs.)	CPU from Zonal Decomposition. (secs.)	Factor Improvement.
1000	2.041	1.381	1.478
2000	8.164	3.638	2.244
3000	18.370	6.225	2.951
4000	32.658	9.027	3.618
5000	51.028	11.988	4.257
7500	114.812	19.904	5.768
10000	204.110	28.356	7.198
20000	816.440	65.470	12.470
30000	1836.990	105.890	17.348

Table 3.1

3.6.4 Error Introduced by the Zonal Decomposition Algorithm.

The infinite series expansion that is used in the velocity calculation for the zonal decomposition algorithm gives the correct velocity as shown in Appendix A. However, for practical implementation of the method, the series needs to be truncated after a reasonable number of terms have been evaluated. This truncation introduces an error into the calculation when the contribution of a zone is used. As discussed in Appendix C, the algorithm has been optimised to keep this error low, whilst still retaining the calculation efficiency.

By comparing the velocity calculation of a sample flow field using the zonal decomposition and direct summation, estimates of this error can be obtained. The test case was on a circular cylinder, comparing the results over a single timestep. The velocity magnitudes of all the vortices (nascent and wake) were compared. The maximum error was 9.8791E-4, and the rms error was 1.1546E-4 compared to the direct summation results. The percentage error is shown in Fig. 3.31. In general, the error is very small, and it is clear that the larger percentage errors occur for vortices where the velocity is very small, and arise due to some ill-conditioning when dividing by the velocity from direct summation. Fig. 3.32 shows a comparison of the flow field around a circular cylinder after the first 200 time steps of the calculation, using both the direct summation and zonal decomposition algorithms. Although there are differences between the two flow fields, in general they are very similar, showing that despite the errors now introduced into the calculation, the new algorithm gives comparable results to the original method.

It should be noted that the calculation of the velocity using the zonal influence via a series expansion, is derived from assuming that the vortices in the zone are point vortices (Appendix A). However, the vortex method uses vortex blobs, where a core function is implemented, to avoid singularities arising from point vortices [7 and 210]. Long distances from the vortex locations, the velocity influence of a vortex blob and a point vortex are very similar. This is also discussed in section 2.3, for the method of Local Corrections. This method is "... based upon the observation that the difference between the velocity field due to a point vortex and a vortex blob located at the same point in space becomes very small as one moves away from the centres of the vortices" [183]. As the zonal influence is only used at "long" distances from the zone centre, it is clear that the error arising from assuming that the vortices contained in the zone are point vortices, is small. Draghicescu et al [191] presents an algorithm similar to the FMM, using a Taylor series expansion, which is claimed to be not just restricted to potential type functions but also may be used with any decaying kernel or core function. The method therefore offers the potential to accurately calculate the zonal velocity contribution from a distribution of vortex blobs. Future work could also investigate if this model may improve the results currently obtained from the DVM.

3.7   Summary.

The discrete vortex method developed by Lin et al [7-9] for analysis of the dynamic stall phenomenon on aerofoil sections has been further developed and improved. One of the key improvements in the model is the generalisation to allow the calculation of the flow field about a much wider range of geometries. Also, the generalisation procedure has led to the calculations being more stable, with less variation in the results as input parameters are modified. Also, extra modelling has been incorporated to improve the handling of sharp corners and also to account for

wake three dimensionality in a highly separated flow field. A more efficient algorithm has been developed and incorporated into the vortex method to give a significant reduction in the computational operation count. All of these factors combine to improve the results obtained from the vortex method and to enhance the capability of the method as an analysis tool for a wide range of applications. However, some aspects of the modelling, in particular the empirical model to account for three dimensionality in the wake and the lack of modelling for wake turbulence mean that the model developed takes more of an engineering approach to the problem. Also, the model has been developed and validated for primarily sharp edged bodies, though future research is anticipated that will develop more physical aspects to the method that will allow improved analysis of smooth curvature bodies. In the next section, the results of an extensive validation programme for the vortex method are presented for a range of simple and more complex bluff body flow fields. Combined with the aerofoil results presented by Lin [7], the improved capability of the method is demonstrated.

CHAPTER 4

VALIDATION OF DISCRETE VORTEX METHOD AND RESULTS OF ANALYSIS.

4.0   Introduction.

Previous development of the DVM was directed towards the analysis of the dynamic stall phenomenon on pitching aerofoils. Validation of the method for this problem was conducted by Lin [7] as part of the development of the initial code. However, the DVM offers the potential to analyse a much wider range of geometries and problems. Hence, once the DVM had been generalised and the necessary modelling improvements incorporated, as discussed in Chapter 3, a thorough validation of the method was undertaken, the results of which are presented and summarised within this chapter.

The main goal of the study was to develop the DVM so that it could be successfully used to study the effects of the unsteady aerodynamic loading on suspension bridge deck sections. For this reason, much of the validation exercise was directed towards the study of sharp edged bodies. However, for completeness, a brief study of the circular cylinder is included in the results presented herein to demonstrate the capability of the vortex method on bodies of smooth curvature as well as those with sharp edges. Much of the validation exercise used the square section cylinder, partially due to the simple geometry but also because it has been the subject of numerous experimental studies, from which a large database of results has been generated. The effect of angle of incidence on the flow field around the stationary cylinder is investigated. Also, the flow field around a square undergoing forced transverse oscillations was studied for a range of frequencies and amplitudes. A natural extension of the validation was to investigate the effect of aspect ratio on the flow field, including very thin bodies that give a close approximation to a flat plate. Finally, results are presented for a representative modern bridge deck section. These results include static force coefficients and also the extraction of the flutter derivatives for oscillating cases. The usefulness of the DVM for analysing the flow field for bridge deck sections is demonstrated by a study of the effect of passive and active flow control devices on the stability of a bridge section. These devices serve to increase the critical flutter velocity of the structure giving rise to greater aeroelastic stability.

All of the calculations presented below are performed using an impulsively started flow field. Mean quantities are calculated from the time-dependent data once the flow has settled into a fairly regular oscillatory pattern and the effects of the impulsive start become negligible. In each case, a sufficient number of nascent vortices were used on each surface panel to ensure that the particles overlap and provide an accurate resolution of the vorticity distribution on the body surface.

4.1   Circular Cylinder.

The development of the DVM for the prediction of bluff body flow fields has been developed primarily for the analysis of the effect of unsteady aerodynamics on suspension bridges. For this reason, much of the analysis and validation presented herein is for bodies with sharp corners. However, for completeness, the circular cylinder was briefly studied due to the huge amount of research that this geometry has attracted. Also, the flow field around a circle is much more Reynolds number dependent than that around sharp edged bodies, where the separation is generally defined by the corners, rather than by *Re*. The results presented here are intended only to demonstrate the capability of the DVM to analyse bodies with smooth curvature and capture the *Re* sensitivity of the flow field. However, the results do not constitute a full analysis of the circular cylinder, which should be the subject of further study.

Two calculations are presented for Reynolds numbers of 20,000 and 10^6 respectively. The first is in the sub-critical regime, where the shear layers separate from near the top and bottom of the circle. The second is in the super-critical regime, where the boundary layer undergoes transition from a laminar to turbulent state delaying shear layer separation until further aft on the surface of the circle (Chapter 2). From previous experimental results [2], in the low *Re* case, the effects of turbulence on the wake are starting to become noticeable, although there is generally still a fairly regular vortex street discernible close to the body. At the higher *Re*, a regular vortex street may still be seen in the wake though the regular pattern is more affected by the considerable turbulence within the wake. These effects, as well as the variation of key flow parameters, were investigated using the DVM and assessed against expected behaviour.

4.1.1   Results.

The different *Re* in the DVM were achieved in two ways. The first is to adjust the Reynolds number in the calculation, which effectively controls the amount of viscous diffusion in the flow field using the random walk model discussed in Chapter 3. Secondly, different time steps and vortex core sizes were used in the two calculations, similar to the findings of Walther in the development of a vortex method [167]. For the higher *Re*, a lower time step was used along with a much higher density of vortex particles giving greater resolution of the flow field, and is consistent with techniques used in conventional grid based methods.

Instantaneous snapshots of the flow field predicted by the DVM at various stages of the vortex shedding cycle are presented in Figs. 4.1 to 4.4. The results are presented both as velocity vectors and particle plots showing the distribution of vortex blobs. It should be noted that the wake in the calculation extends a large distance behind the body, but for plotting purposes only, is truncated to around two diameters downstream of the body. In both calculations, the formation of the vortex street is clearly seen, although as expected, in the higher *Re* case the particle plots show that the

wake has a much noisier or random look [2]. In the high Re case the diffusion component calculated from the random walk is negligible, as discussed earlier. The flow field shown in Fig. 4.4 is therefore not a good representation of the flow field as the calculation is effectively based on convection only. Also, the flow structure is not representative as no account is taken of the turbulent diffusion in the wake. The wake decay model provides a means of accounting for these effects and as a result the separation points of the shear layers may be predicted reasonably accurately. However, the empirical nature of model does not satisfy any physical criteria and so the flow structure, in particular the formation of the vortices behind the cylinder, is not representative at high Re.

It is clear from Figs. 4.1 to 4.4 that the DVM predictions give the correct qualitative trends for the separation locations in sub-critical and super-critical flow fields. The most notable feature that distinguishes the two calculations is that the separation of the shear layer is further aft in the high Re prediction, giving rise to the narrower wake that is a characteristic of the super-critical regime, despite the high Re case is not a good representation of the flow as discussed above. The quantitative accuracy of the predictions can be assessed by comparison of various key flow parameters with data extracted from wind tunnel experiments. Results from the DVM predictions are compared with experimental data in Table 4.1.

Parameter.	Re = 20,000		Re = 1×10^6	
	ESDU [10]	DVM	ESDU [10]	DVM
C_D	1.200	1.295	0.338	0.392
C_{pb}	-1.200	-1.253	-0.386	-0.5460
θ_b	83.31°	91.20°	128.62°	132.00°
C_{pmin}	-1.296	-1.512	-2.118	-2.672
θ_{min}	70.12°	72.00°	83.59°	86.40°

Table 4.1.

Due to the large amount of wind tunnel results that are available in the literature, the results are only compared with data taken from ESDU [10], which gives representative data for the parameters under investigation. The four parameters, C_{pb}, θ_b, C_{pmin} and θ_{min}, are derived from the mean C_p distribution around the cylinder, as demonstrated using a typical C_p distribution in Fig. 4.5. The parameter C_{pmin} is the minimum value of C_p on the cylinder surface with θ_{min} being the angle from the horizontal at which the minimum pressure occurs. C_{pb} is the mean base pressure and θ_b is the angle at which the base region starts. Both the ESDU data and the DVM results assume that the surface of the cylinder is smooth. The DVM data is taken from mean C_p results over the upper half of the cylinder only though it should be noted that the lower half gives very similar results. The C_{pb} from the DVM is calculated from the mean pressure between θ_b on the upper and lower surface respectively.

The agreement between the DVM results and the ESDU data is generally very good, with the effect of *Re* on the separation locations being well predicted, although the C_D in the high *Re* case is a little high. Another discrepancy in the results is the higher predicted suction for C_{pmin} from the DVM results. However, the location of the separation and the minimum pressure are well predicted. The mean C_p distribution from the DVM for each *Re* is compared with ESDU data in Fig. 4.6, illustrating the agreement between the results. A notable difference is that the predicted C_{pb} is low when compared to experiment. In general the results demonstrate the DVM is capable of capturing the variation of the flow field with *Re*, in particular the much later separation of the shear layers in the super-critical regime combined with a much lower C_D and suction in the base region. However, once again it is noted that the results of the high *Re* cases are affected by the negligible diffusion component from the random walk and also the lack of wake turbulence modelling. The circular cylinder results are only presented to indicate future capability of the method. The model has been developed with the goal of analysing the flow field and aerodynamic loads on sharp edged bodies, which due to the fixed separation locations, are less sensitive than smooth curvature bodies to some of the modelling assumptions. It is anticipated that future research will address these issues and that a full validation of the circular cylinder will be the subject of a future investigation.

4.2   Static Square Section Cylinder.

The flow field around the static square section cylinder has been the subject of many experimental and numerical studies as discussed in Chapter 2. Despite the simple geometry, it provides a useful and challenging test case for the validation of the DVM. As the angle of incidence of the oncoming flow is varied, there is a significant variation in the resulting flow field around the body, with one of the shear layers intermittently interacting with a downstream corner and eventually re-attaching to a side face completely. Successful prediction of this variation in the flow field and the associated static force coefficients for the square cylinder would provide a useful validation of the DVM and would give confidence in results on more complex geometries. The effect of varying the angle of incidence from 0° to 45° is presented in this analysis and the results are non-dimensionalised with respect to the length of the side face, *L*. The calculations were performed at a Reynolds number of 20,000, with a time step of 0.02 and with the nascent vortex particles being created 0.0025*L* from the surface. The corners of the square are labelled as shown in Fig. 4.7.

4.2.1   General Flow Field Visualisation.

Figures 4.8 and 4.9 show the flow field around the square section cylinder at two different angles of incidence. In each case, the flow at various stages of the vortex shedding cycle are shown, using the distribution of particles from the DVM, accompanied by velocity vector plots to give more clarity to the predicted flow field. In general, the qualitative prediction of the flow

fields are good. The alternate vortex shedding from the body, giving rise to a classical vortex street, can clearly be seen in the 0° case (Fig. 4.8). At 15° incidence, the shear layer separating from the front lower corner of the body, is clearly shown to be reattaching on the lower side face (Fig. 4.9). The effect that this reattachment has on the mean force coefficients will be discussed in more detail in the next section. The differences in the wake structure between the two cases can clearly be discerned, with noticeably weaker vortex shedding in the 15° case.

4.2.2   Mean Aerodynamic Force Coefficients : C_D and C_L.

Sample time histories for the lift and drag coefficients are shown in Fig. 4.10. The impulsive nature of the start to the calculation can clearly be seen. However, the flow settles down, in a relatively short period of time, to the expected fairly regular oscillatory cycle induced by the vortex street typical of bluff body flow fields.

The mean aerodynamic force coefficients, C_L and C_D at angles of incidence ranging from $\alpha=0°$ to 45° are shown in Fig. 4.11 and 4.12 compared with experimental data [14, 16-17, 203, 217-219]. A summary of some of these results is compared in Table 4.2 with data from various other computational methods and experiments. The correct variation of both C_L and C_D with incidence is predicted by the DVM and there is good quantitative agreement with the various experimental data. The selected alternative numerical methods, in particular, do not capture the variation in the lift and drag, at the higher angles of incidence.

As the angle of incidence increases, the mean C_D reduces, primarily due to the shear layer that is shed from corner D intermittently contacting corner C (Fig. 4.7). Eventually, when α is approximately 15°, this shear layer reattaches completely to form a separation bubble on face DC. The shear layer that originally separated from D, now separates from C, and hence gives rises to a narrower wake and a lower mean C_D. Further increases in α simply lead to an increase in the width of the wake, producing the gradual increase in C_D between 15° and 45°. The vortex method predicts this trend well, although the minimum C_D is predicted at 15° rather than the 12-13° indicated in the experimental data. As shown above, the attached shear layer can clearly be seen at the higher incidence (Fig. 4.9).

The variation of C_L with incidence can also be explained by the reattachment of the shear layer to face DC. The separation bubble causes higher local suction pressures than those on face AB, and hence give rise to a negative lift coefficient, with a maximum at 15° when the shear layer is fully reattached. As the angle of incidence increases further, the separation bubble becomes smaller, reducing the high local suction pressures on face DC which leads to a gradual increase in C_L. The results obtained from the vortex method again compare well with experimental data. A feature of the accuracy of the variation of the mean C_D and C_L with incidence demonstrate that the DVM would be a useful tool for analysing galloping at high reduced velocities.

Authors	Angle (degrees)	Reynolds Number	Mean C_L	Mean C_D
DVM	0	2.0e+4	0.019	2.38
	15		-0.80	1.59
Lee [14] (experiment)	0	1.76e+5	0.021	2.04
	15		-0.72	1.58
Norberg [17] (experiment)	0	1.3e+4	0	2.15
	15		-0.68	1.80
Naudascher et al [218] (experiment)	0	1.06e+5	0	2.00
	15		-0.54	1.59
Blevins [195] (vortex method)	0	1.0e+4 - 1.0e+5	-	1.56
Koutmos et al [151] (2D CFD)	0	14285	-	2.37
Murakami et al [152] (2D CFD)	0	1.0e+5	0	2.09
Tamura et al [147] (2D CFD)	0	1.0e+4	0	2.4
	15		-1.2	2.3
Tamura et al [147] (3D CFD)	0	1.0e+4	0	2.2 - 2.3
	15		-0.84	1.74

Table 4.2 - Comparison of Mean Force Coefficients.

4.2.3   Mean Base Pressure Coefficient : C_{pb}.

The mean base pressure coefficient was calculated as the average of the pressure coefficient at the mid and quarter points on the leeward face of the body. This is consistent with many other researchers, although some base pressure measurements are taken from the centre of the leeward face only. However, as the pressure in the base region on the square cylinder is reasonably constant, comparisons can be made with each set of data. The variation of mean base pressure with incidence is shown in Fig. 4.13. The results from the DVM show good qualitative and quantitative agreement with experimental data, though there is slightly too much suction at the lower angles of incidence, consistent with the slight over prediction of C_D at low incidence.

Previous researchers have shown that the base pressure is directly related to the amount of vorticity shed from each side of the body [14 and 18], which is in turn related to the distance required from the leeward face for vortex formation. Bearman and Trueman [18] indicated that the greater the distance that the vortices are formed from the body, the less suction there will be in the base region. Hence, from the over prediction of the suction in the base region at low

incidence, it can be deduced that the DVM predicts vortex formation somewhat closer to the body than occurs in practice (Fig. 4.8).

4.2.4 Mean Moment Coefficient : C_M.

The moment coefficient about the centre of the square against incidence is presented in Fig. 4.14, compared with experimental data [17 and 220]. As shown in Fig. 4.7, a positive moment is taken to act in the clockwise direction. Reasonable agreement is shown, with the correct trend of C_M being shown with incidence. The minimum predicted moment occurs between 20-25°, which is a little higher than shown in the experiment. However, the results suggest that the vortex method may be a useful tool for analysing torsional oscillation of structures.

4.2.5 Strouhal Number.

Spectral analysis was performed on the lift coefficient time history, to obtain the Strouhal number, St :

$$St = n_s L/U \tag{4.1}$$

Due to the impulsive start to the calculation, the analysis was performed on a number of complete oscillation cycles of the lift history, after the flow had stabilised. A spectral analysis was also performed on the pressure coefficient time history at the centre of the upper side face. In addition, the location of the stagnation point on the windward face was also analysed. The value of St obtained from each of these methods was found to be consistent, and only the results from spectral analysis of the lift coefficient time history are presented below.

The variation of St with incidence is shown in Fig. 4.15, along with selected experimental data. Also, a summary of some of the results is compared with data from various other computational methods and experiments in Table 4.3. The DVM results compare well with data from other researchers. The 3D CFD results of Tamura and Kuwahara [147] fail to accurately predict the correct variation of St at incidence, although this code did give good results for the mean lift and drag coefficients (Table 4.2).

The correct trends are predicted with a gradual increase in St until a peak is reached at approximately 20°. This is a little higher than experimental values, although a wide range of results has been presented by various researchers. The DVM overpredicts to some degree the vortex shedding frequency at the higher angles of incidence. However, the strength of the vortex shedding and the resulting oscillation in the lift distribution is much weaker at the higher angles of incidence, hence giving rise to a wide range of values for St.

An interesting feature to note between 0° and 12° incidence, is that some researchers show a steady increase in *St* from 0° incidence, whereas others show a decrease in *St* before increasing to the peak value at approximately 13°. The reason for this behaviour is unclear, however in general terms a decrease in the width of the wake can be linked to an increase in *St*. The reattachment of the shear layer to the lower side face is the angle at which the wake is narrowest, and corresponds to the maximum *St* at 13°. In the cases where *St* initially decreases, the increase in the cross body dimension probably has most effect on the wake width, causing a wider wake. Whereas the gradual increase in *St* is probably more dependant on the intermittent reattachment of the shear layer at corner C (Fig. 4.7). The wide range of results demonstrate the sensitivity of *St* to the flow field, and emphasise the good quantitative agreement between the DVM and experiment.

Authors	Angle (degrees)	Reynolds Number	*St*
DVM	0	2.0e+4	0.1278
	15		0.1467
Lee [14] (experiment)	0	1.76e+5	0.1214
	15		0.1424
Norberg [17] (experiment)	0	1.3e+4	0.1322
	15		0.1466
Obasaju [16] (experiment)	0	4.74e+4	0.1269
	15		0.1427
Koutmos et al [151] (2D CFD)	0	14285	0.178 [1]
Murakami et al [152] (2D CFD)	0	1.0e+5	0.132
Tamura et al [147] (2D CFD)	0	1.0e+4	0.103
	15		0.129
Tamura et al [147] (3D CFD)	0	1.0e+4	0.13
	15		0.18

Table 4.3 - Strouhal Number from Various Authors.

4.2.6   Pressure Coefficient on Body Surface : C_p.

The pressure coefficient around the body for the 0° case is shown compared with experimental data [14, 31, 219 and 221], and with other computations [142, 152-154 and 222] in Fig. 4.16. The results are plotted against distance along the body surface, from the centre of the windward

---

[1] Calculation in channel, with high blockage of 19%. Results appear to be uncorrected for blockage.

face and moving clockwise around the body, as shown in Fig. 4.7. The pressure coefficient is normalised using the pressure at the stagnation point as the reference pressure. The pressure coefficient at 10° incidence is shown in Fig. 4.17.

In general, good agreement is shown with experimental data, although the high suction on the leeward face is a symptom of the slightly high prediction of C_D at 0°. The results also demonstrate a favourable comparison with selected results from various 2D and 3D CFD calculations (Fig. 4.16b). The 2D results show significant differences to the experimental data, most notably in the results of Murakami et al [152]. The 2D results of Yu and Kareem [154] show much better agreement, though on the side face of the square, the prediction is outside the range of pressures seen in the experiments. These discrepancies in the 2D results can be attributed to the lack of modelling of the 3D effects in the wake, such as the development of streamwise component of vorticity, ω_x, due to the vortex stretching and roll up of the spanwise von Karman vortices as discussed earlier. The vortex decay calculation was included in the DVM to account for these 3D effects (see Chapter 3).

The results from the vortex method compare well with those calculated from full 3D methods, which typically use $O(10^5)$ grid points, and in general, the 3D results are in much better agreement with the data. Despite the scatter in the predictions, most are within the range of the experiment results. One discrepancy is the high base pressure on the leeward face from the 3D calculation of Murakami et al [152], and the resulting mean drag coefficient is likely to be lower than experiment. Although the 3D results demonstrate good agreement with the data it is likely that such a detailed analysis using a full 3D model would require significantly higher computational effort than the 2D vortex model. [2]

The predicted mean pressure coefficient at 10° incidence also compares well with experimental data. The results demonstrate that the effects of higher angles of incidence on the pressure distribution are successfully predicted by the DVM. Notably, the displacement of the stagnation point along the windward face, and the effects of the reattaching shear layer at corner C have been captured.

4.2.7   RMS Fluctuating Pressure Coefficients.

The rms lift coefficient for the 0° case was calculated to be 1.369. This compares well with experimental data, with various researchers giving values ranging between, 1.20 and 1.35 [14-15, 31 and 46].

---

[2] Conference presentation of [149] estimated that the calculation of one vortex shedding cycle, using 3D CFD method, with $O(10^6)$ grid points required approximately 20hrs CPU on a Cray super-computer. This is compared to the DVM which typically requires 1.5hrs for calculation of one shedding cycle on an Silicon Graphics Indigo workstation or 20 minutes on a DEC Alpha (Section 2.1).

The rms pressure fluctuations around the body surface are shown in Fig. 4.18 compared with various experimental data and with results from other computations. The vortex method results compare well with experiments and, on the side faces in particular, lie in the middle of a fairly wide range of results. The reduction of the fluctuations on the leeward face is also successfully predicted. The results from the 2D CFD calculations give the poorest agreement with experiment, especially on the side face of the square. In general, the 3D calculations show good agreement with experiment and lie within the range exhibited in the data. The poor agreement in the 2D CFD results can again be attributed to the methods not taking account of the transfer of vorticity from the von Karman component arising from the 3D effects in the body wake. This is consistent with the results from the DVM, in that the predicted rms pressure fluctuations, particularly on the leeward face, were poor prior to the addition of the wake decay model.

4.3   Rectangular Section Cylinders.

The DVM has also been validated for rectangular section cylinders at 0° incidence for aspect ratios ranging from 0.25 to 3.0. The calculations were again performed at a Reynolds number of 20,000, with a time step of 0.02. As far as possible, the length of the surface panels were the same as in the square cylinder calculations to ensure consistency in the results. As mentioned above, the crosswind body dimension is used to non-dimensionalise the force coefficients and *St*. The aspect ratio is defined as *B/L* where *B* is the length of the side parallel to the freestream velocity and *L* is the cross wind body dimension. As the calculations are presented for 0° incidence, only the variation of mean C_D and *St* are shown below.

4.3.1   Mean Drag Coefficient : C_D.

The variation of C_D with aspect ratio is shown compared with experimental data and other computations in Fig. 4.19. In general, good agreement is shown with the effect of aspect ratio on the results being well predicted by the DVM. The results also compare favourably with other computations. The most notable effect of aspect ratio on C_D is in the range *B/H*=0 to 1. A maximum value is reached at around *B/H*=0.62, the so called "critical section". At aspect ratios lower than the critical section, the vortex formation is relatively unaffected by the two leeward corners of the body. As the aspect ratio is increased towards the critical section, there is effectively a reduction between the base region and the vortex formation, resulting in an increased suction in the base region and hence a higher C_D [17-18]. Increasing the aspect ratio from the critical section, the influence of the leeward corners on the shear layers moves the vortex formation further downstream, leading to a reduction in the suction in the base region and hence a reduced C_D. The aspect ratio of the critical section is shown by the DVM to be between 0.6 and 0.7 and the C_D at this section is well predicted.

It is notable that the DVM gives a much better prediction of this trend than the vortex methods of both Blevins [195] and Bienkiewicz and Kutz [203]. In both of these cases, the peak C_D at the critical section is not predicted. Each of these two results shows a gradual increase in C_D as the aspect ratio reduces. The CFD results of Okajima et al [136], using a laminar model and neglecting the effects of turbulence, do predict the correct variation of C_D with aspect ratio, both qualitatively and quantitatively. However, the peak C_D at the critical section is underpredicted.

4.3.2   Strouhal Number : *St*

The variation of Strouhal number with aspect ratio is shown in Fig. 4.20, compared with experimental data and other computations. The results from the DVM show good agreement with the data and compare well with the other computations. The Strouhal number behaves differently to C_D at aspect ratios less than 1.0, with a gradual decrease in *St* as aspect ratio increases. The reason for this is that the dominant effect on *St* is the wake width.

At low aspect ratio, the width of the wake is generally constant as the shear layers separate from the front two corners of the body. Hence varying aspect ratio when *B/H* is less than 1.0 has little effect on *St*. Between aspect ratios of *B/H*=2.0 and 3.0, the shear layers separating from the windward corners reattach to the side faces of the body, resulting in a much narrower wake and a correspondingly higher vortex shedding frequency. Various experimental results show that this reattachment is intermittent, resulting in a "double" *St* for some aspect ratios between 2.0 and 3.0. The higher *St* corresponds to the case where the flow reattaches and the lower value is effectively a continuation of the decrease in *St* with aspect ratio.

This phenomena is well predicted by the DVM and is not demonstrated in the results of Bienkiewicz and Kutz [203], where the results are only given up to an aspect ratio of 2.0. The "double" Strouhal number is clearly seen in the experimental results of Norberg [17] and Otsuki et al [13]. The laminar CFD results of Okajima et al [136] are in good agreement with the data and also demonstrate the increase in *St* between aspect ratios of 2.0 and 2.5, although the increase is a little more gradual than some experimental results.

4.4   Flat Plate Calculations.

A natural extension of the effect of aspect ratio is to investigate the limiting case of the flat plate. The modelling of the DVM requires that the geometry under consideration is a closed body and so an infinitely thin flat plate cannot be modelled. However, a good approximation can be obtained by using a very thin rectangular cylinder where the aspect ratio is $O(10^2)$. In this study, aspect ratios of 100 and 200 were used to study the flat plate flow field and ascertain the limits of the DVM.

One of the reasons for studying the flat plate is that the nascent vortex particles may move in any direction due to the convection velocity and diffusion processes. This could mean a particle moving away from the body or towards and even into the interior of the body. In the latter case, the particle is simply re-absorbed into the surface vorticity distribution and is included in the γ distribution for the next time step. However, for the flat plate, there is a much higher probability that a vortex particle could travel through the body to the other side, whereby it would remain as a wake particle and as such would introduce a spurious disturbance and significant error to the predicted flow field. The most severe test for the model where such errors may occur are when the flat plate is normal to the freestream flow. Representative results for the instantaneous flow field are given in Fig. 4.21 and 4.22 for aspect ratios of 100 and 200 respectively. The resulting flow fields demonstrate the ability of the DVM to predict the flow field and no evidence of vortices crossing the body was found in either calculation. Both predictions show the typical flow field with the shear layer separating from each end of the plate, forming a wide wake with a fairly stagnant base region, corresponding with the description of the flow by Simiu and Scanlan [2]. At high *Re*, large vortical structures do not form in the wake, although the shear layers consist of a series of smaller vortices that are alternately shed from each end of the plate. The predicted values of C_D and *St* are shown in Table 4.4 along with representative values derived from experiment [2 and 12]. Reasonably good agreement with the experimental data is demonstrated. It can be seen from comparing the results with the C_D and *St* results for the varying aspect ratio rectangles that the DVM and experimental results are consistent with the values shown in Figs. 4.19 and 4.20. The results presented in Table 4.4 correspond to an aspect ratio of zero and are consistent with the variation of the two quantities as the aspect ratio of the cylinder is reduced.

	Drag Coefficient, C_D	Strouhal Number, *St*
DVM - Aspect ratio = 100	2.238	0.167
DVM - Aspect ratio = 200	2.277	0.170
Experimental Results.	1.96-2.01	0.14-0.15

Table 4.4

Calculations have also been performed on a flat plate at 0° incidence to the freestream flow. In this case, there is no separated region and the quality of the results can be assessed by studying the nature of the predicted boundary layer on the surface of the plate. For such an analysis, the results from the DVM were compared with the standard Blasius profile for a laminar boundary layer [11]. By suitable non-dimensionalisation of the velocity distribution and thickness of the boundary layer, it can be shown that the resultant profile at each location on the flat plate will be the same. The scale factors used for the velocity and distance from the surface are the freestream velocity and the boundary layer thickness, δ, approximated by (4.2), respectively [11].

$$Y = y\sqrt{\frac{U_\infty}{\nu x}} \qquad (4.2)$$

The DVM results are shown in Fig. 4.23, for both the 100 and 200 aspect ratio cases at various locations between 30% and 70% along the flat plate and compared to the theoretical Blasius profile. The DVM predictions are generally in good agreement with theoretical results although at the higher time steps, the results are less accurate. This is to be expected as the higher time step gives a prediction more representative of lower *Re* and the derivation of the Blasius profile was based on the assumption that *Re* is very large. Analytic values for the boundary layer thickness, displacement thickness and momentum thickness can also be derived [11]. The boundary layer thickness is defined as the distance from the surface where the local velocity is equal to $0.99U_\infty$. Displacement thickness δ_1 and the momentum thickness, θ, are defined in (4.3) and the analytic expressions are given in (4.4) [11]. The definitions in (4.3) are used to calculate the respective results from the DVM calculations. Comparison of these results with the analytic values are shown in Fig. 4.24. Reasonable agreement is demonstrated though the results again show that the best agreement is obtained for the low time step cases.

Boundary Layer thickness :   Distance, δ, from surface at which $u=U_\infty$.   (4.3a)

Displacement thickness :

$$\delta_1 = \int_{y=0}^{\infty}\left(1 - \frac{u}{U_\infty}\right)dy \qquad (4.3b)$$

Momentum thickness :

$$\theta = \int_{y=0}^{\infty}\frac{u}{U_\infty}\left(1 - \frac{u}{U_\infty}\right)dy \qquad (4.3c)$$

Boundary Layer thickness :

$$\delta \approx 5.0\sqrt{\frac{\nu x}{U_\infty}} \qquad (4.4a)$$

Displacement thickness :

$$\delta_1 = 1.7208\sqrt{\frac{\nu x}{U_\infty}} \qquad (4.4b)$$

Momentum thickness :

$$\theta = 0.664\sqrt{\frac{\nu x}{U_\infty}} \qquad (4.4c)$$

Although the flat plate could have presented significant problems for the DVM due to the requirement for a closed body, the results demonstrate that no such difficulties were encountered in this study. The successful prediction of the flat plate flow has significant implications when

considering the modelling of bridge deck sections, many of which have struts for structural rigidity or appendages that support fairings or other such control devices. The flat plate results indicate the potential of the DVM to model these problems without any significant modelling changes to the method and further extend the capability of the method as an analysis tool.

4.5 Square Cylinder undergoing Transverse Oscillations.

The flow fields around bluff bodies with square cross section undergoing forced transverse oscillations have been computed using the DVM. The body forcing is sinusoidal in nature with a fixed amplitude, usually presented as an amplitude ratio, a/L, as demonstrated in Fig. 4.7. The period of the body oscillation is represented non-dimensionally as a reduced velocity, U_r, defined as $U/n_b L$. Results are presented for oscillations in the transverse direction with a range of amplitude ratios from 0.05 to 0.25, with reduced velocities typically between 4.0 and 11.0. All calculations were performed using input data that is consistent with the calculations for the static square cylinder discussed above.

The strong dependency of the flow field on the amplitude ratio and reduced velocity results in a division into three distinct flow regimes, namely vortex lock-in, below lock-in and above lock-in. Above lock-in, the flow approaches quasi steady form as the dominance of the forcing oscillation diminishes. Below lock-in, the flow is dominated by the effects of the imposed oscillation and, depending on amplitude, the concentrated vorticity which is generated at the shedding frequency can lead to a complete suppression of the natural vortex shedding mode. Lock-in is defined as the reduced velocity range around the resonant frequency (*St* of the stationary cylinder, shown to be 0.128 from earlier results) when the natural vortex shedding frequency transfers to the body frequency. The increased spanwise correlation of the vortex shedding within the vortex lock-in region suggests that there is less three dimensionality in the wake near the body. As a result, the decay model within the DVM may require an adjustment to the decay constant, β, to account for these effects. However, the constant β that was used for the stationary cylinder was also used for the oscillating cylinder to ensure consistency in the modelling.

4.5.1 Analysis of Lift History.

The DVM results for the time history of the lift coefficient at various amplitudes and reduced velocities demonstrate clearly the different flow regimes discussed above, and also show interesting features of the flow field. Sample lift histories are shown in Fig. 4.25 for the 0.10 amplitude ratio case, at four different reduced velocities. For the case below vortex lock-in, with reduced velocity U_r=5.0, the lift history is quite irregular with a significant modulation of the amplitude. This arises as both the natural vortex shedding frequency and the body frequency are significantly different (stationary square *St* corresponds to a reduced velocity of 7.8), and each has a significant effect on the lift history. As the body frequency becomes closer to the natural

shedding frequency, but still in the region below lock-in, the characteristic beating due to two slightly different forcing frequencies is clearly demonstrated in the case with U_r=6.75. The beating frequency is approximately equal to the difference between the body and shedding frequencies.

In the lock-in range, the lift history is close to sinusoidal, with only one dominant frequency present and with very little modulation of the amplitude of the lift coefficient. This is clearly demonstrated in the results from U_r=8.0. The upper end of the lock-in range is much less distinct than the lower end, as the higher reduced velocity has less effect on the shedding frequency due to the lower energy oscillations of the body. This results in a range of reduced velocities where the flow condition is moving in and out of the resonant vortex lock-in. The lift history for U_r=8.3 clearly demonstrates this effect. The first part of the time history, up to non-dimensional time of approximately 120, demonstrates results typical of the vortex lock-in region, that is high amplitude and fairly regular lift oscillations. The later part of the time history is more representative of results above vortex lock-in : the lift amplitude has reduced significantly, and increased in irregularity as the vortex shedding and body frequencies become distinct. However, the lift is much more regular and sinusoidal when compared to the case below lock-in due to the lesser effect of the body forcing oscillation. This is consistent with a flow which is increasingly quasi-steady in nature above lock-in at higher reduced velocities.

4.5.2   Vortex Shedding Frequency Measurements.

Spectral analysis was performed on the lift histories with the results being used to ascertain the reduced velocity range at which vortex lock-in occurs for each amplitude ratio. Away from lock-in, the vortex shedding frequency and the body frequency can be seen as two distinct peaks in the frequency analysis. At vortex lock-in, the shedding frequency is modulated to the body frequency, and a single peak is seen in the frequency analysis. Both of these phenomena are demonstrated in the results of the DVM calculations, samples of which are given in Fig. 4.26.

The vortex shedding frequency, n_s, is estimated from these power spectra, and is shown, divided by the body frequency, n_b, plotted against U_r in Fig. 4.27. The straight lines in the figures show the ratio between St for the stationary body and n_b. Outside of vortex lock-in, the ratio n_s/n_b should be approximately on this line. In the lock-in region, the ratio becomes equal to unity as the shedding frequency is transferred to the body frequency. This is clearly demonstrated in the results from the DVM. Compared with experimental data [13 and 31], the region of vortex lock-in is well predicted for both the 0.1 and 0.15 amplitude ratios. The most noticeable feature of the results is the wider lock-in range as amplitude ratio increases. Again, this effect is well predicted by the DVM.

4.5.3   General Flow Field Visualisation.

The flow field around the oscillating body is presented (Fig. 4.28 and 4.29) at different stages of the oscillatory cycle, for the reduced velocities U_r=6.0, below vortex lock-in, and U_r=8.0, in vortex lock-in. The results are shown as velocity vectors and in general provide good qualitative representations of the flow field. Compared to the results on a static square (section 4.2) a much greater modulation of the wake is clearly discernible.

In the U_r=8.0 case, the vortex shedding frequency is quite clearly the same as the body frequency demonstrating the vortex lock-in phenomena. This is apparent from Figs. 4.29a and 4.29e, where the body is at the same stage of the oscillation cycle. In both cases, a vortex is forming close to the rear face, due to the shear layer that is shed from the lower side face. If the same comparison is made between Figs. 4.28a and 4.28e, it is clear that vortex shedding occurs at a different frequency to the body oscillation, as illustrated by the dissimilar stages of the shedding cycle.

4.5.4   RMS Lift Coefficient, C_{Lrms}.

The variation of the rms lift coefficient, C_{Lrms}, with U_r over a range of amplitudes is compared with experimental data [38-39] in Fig. 4.30. The variation of C_{Lrms} can be explained by considering the different flow regimes. At low U_r, below lock-in, concentrated vorticity is generated and shed at the body frequency, resulting in the natural vortex shedding mode being suppressed. This leads to a reduction in the fluctuating lift force on the body, an effect which is magnified with increasing oscillation amplitude. In the lock-in region, C_{Lrms} gradually increases until the maximum value is reached at the resonance point. Just above lock-in, the sharp decrease in the C_{Lrms} corresponds with the separation of the vortex shedding and body frequencies. An interaction occurs between the vortex formation and the rear corners on the square which reduces the strength of the vortex, producing the decrease in C_{Lrms}. As U_r is increased further, the flow approaches a quasi steady form, with C_{Lrms} gradually approaching the value found on the stationary body (equal to 1.37 in the DVM and 1.12 in Lu, Chen et al [39][3]).

The results from the DVM demonstrate the variation discussed above and show generally good agreement with experimental data. It should be noted that some of the discrepancies can be attributed to the differences in the range of U_r for which lock-in is assumed. For example, the 0.25 amplitude ratio case has a lock-in range of approximately U_r=5.5 to 12.0 in the experiments [31 and 38], whereas the DVM lock-in range is from 4.5 to 9.0. The variation in experimental results is larger at the upper end of the lock-in range due to the lower frequency oscillation. This explains to some degree why the biggest discrepancy in the DVM results is at the upper end of lock-in. Also, it can be shown that the lock-in is somewhat sensitive to Reynolds number, with a larger range of U_r expected at lower values. The *Re* employed in the DVM was chosen to be

---

[3]Various experimental data shows that C_{Lrms} is generally within the range 1.20 to 1.35 (section 4.2.7).

representative of all the experimental data being used for comparison but differs from each dataset to some degree. The results for the lowest amplitude ratio, 0.05, are more difficult to interpret as only a very small lock-in region was predicted at $U_r \approx 7.5$. Also, the vortex shedding is more dominant making the effects of body oscillation sometimes difficult to detect.

4.5.5   Pressure Coefficient and Fluctuating Pressure Distribution on Body Surface.

The surface pressure coefficient, C_p, around the body is shown in Fig. 4.31 for various reduced velocities, at an amplitude ratio of 0.25. For reference C_p around a stationary square at $0°$ incidence is shown in Fig. 4.16. In each figure, the corners of the body are indicated (Fig. 4.7). Two of the three results shown are in the vortex lock-in region (U_r=7.5 and 7.75) with the third (U_r=8.5) just above lock-in. The DVM results exhibit the correct trends as U_r is varied when compared with the experimental data [31].

The C_p varies only slightly through the resonance region, however one noticeable feature is the significantly increased suction on the side faces when compared to the C_p on the stationary body. During lock-in, the vortices shed from the body are stronger due to the effect of the body oscillation, giving rise to the higher suction on the side faces. Above lock-in, the C_p on the side faces reverts to values closer to those seen on the static body, although there is a significant reduction in the base suction. Lu and Chen et al [39] found a similar effect with a reduction in the drag coefficient at reduced velocities just above lock-in. A conjectured reason for this effect is the significant interference of vortices forming from the side faces with the rear corners of the body at reduced velocities just above lock-in. This interference tends to move the vortex formation further downstream, reducing the base suction.

The rms fluctuating pressure on the body surface, C_{prms}, is shown in Fig. 4.32 for various reduced velocities at an amplitude ratio of 0.1. For reference, the results from the static body are shown in Fig. 4.18. It should be noted that the measurements of fluctuating pressure have not been corrected to account for acceleration effects (due to the pressure transducer not being mounted flush to the cylinder surface), though the errors are only expected to be significant at low reduced velocities [31]. However, previous comparisons between various experimental data have indicated that there can be a wide variation in the C_{prms} results (Fig. 4.18). Allowing for the wide scatter of data, the DVM results exhibit the correct trends with reduced velocity. For instance, in the lock-in region, C_{prms} is noticeably greater, with a maximum at the resonance point.

Below lock-in, C_{prms} is generally reduced slightly, as the flow is dominated by the body motion. The results towards the rear corners of the body (B and C) do however show a tendency for increased C_{prms}. The relative angle of incidence of the freestream flow as the body oscillates, causes the shear layer to begin to reattach to one of the side faces of the body. Before full

reattachment, however, there is be a significant interaction between the shear layer and the rear corner, leading to the higher C_{prms} in this region. Above lock-in, the C_{prms} begins to approach the results seen on the static model. The reduced velocities for the above lock-in case used in the DVM are different from the experimental values due to differences in the upper lock-in boundary (see section 4.5.1). The results of calculations just above lock-in are used (U_r=8.5 and U_r=9.0) which demonstrate the change in C_{prms} as the flow state changes.

4.5.6   Phase Angle and Frequency-Response Component of Lift.

The phase angle, ϕ, is defined as the angle by which the lift force leads the body displacement. From this definition, the lift is capable of sustaining free oscillations of a spring mounted cylinder, when ϕ is within the range $0° < \phi < 180°$, the so called negative damping condition. The characteristic distribution for ϕ with varying U_r is demonstrated in the results from the DVM shown in Fig. 4.33. The most noticeable feature is the sudden increase from negative to positive phase angle through the lock-in region. It is clear that positive ϕ required for vortex induced oscillations only occurs once the reduced velocity is above the resonance point. This is also demonstrated in free oscillation experiments [13 and 44]. The slope of the phase angle distribution also tends to decrease with increasing amplitude, giving further indication of the increased lock-in range at higher amplitude.

The results from the DVM demonstrate good agreement with experimental data (Fig. 4.34), although these data show a wide variation, highlighting the sensitive nature of the unsteady flow field. In addition, variations in the experimental flow conditions, such as *Re*, and variations in the static *St*, may have had a strong effect on the results obtained from the oscillatory tests. However, the DVM results are within the range of experimental data, with the only discrepancy being the smaller predicted lock-in range at higher amplitudes discussed earlier. A favourable comparison can also be made with results obtained from a 3D CFD method [152] at amplitude ratios of 0.10 and 0.25.

The component of the lift history at the body frequency, or "frequency-response" component, may be expressed as

$$L_b(t) = L_0 \cos\left(2\pi n_b t + \phi\right) \tag{4.5}$$

The amplitude of the frequency-response component, L_0, may be non-dimensionalised to give the frequency-response component of the lift coefficient

$$C_{Lb}(t) = C_{L0} \cos\left(2\pi n_b t + \phi\right) \tag{4.6a}$$

where

$$C_{L0} = \frac{L_0}{\frac{1}{2}\rho U^2 L} \qquad (4.6b)$$

is the amplitude of the frequency response component of the lift coefficient. C_{Lb} can be written in complex notation

$$C_{Lb}(t) = \text{Re}\left[\left(C_{LbR} + iC_{LbI}\right)e^{i2\pi n_b t}\right] \qquad (4.6c)$$

The complex components, C_{LbR} and C_{LbI}, can obtained from (4.7)

$$\begin{aligned} C_{LbR} &= C_{L0}\cos\phi \\ C_{LbI} &= C_{L0}\sin\phi \end{aligned} \qquad (4.7)$$

It may be noted that the condition for vortex induced oscillation is for C_{LbI} to be positive.

Comparisons of the frequency response amplitude, C_{L0}, with various experimental data are shown in Fig. 4.35. The most noticeable feature of the results is the approximate correspondence of the peak C_{L0} with the resonance point, and the increasing peak value with amplitude. The DVM results demonstrate good agreement with experiment, although the wide range of data should again be noted. Another feature to be noted is the C_{L0} values below lock-in tend to be higher than those above lock-in. This is indicative of the body oscillation having a more dominant effect on the lift force at the higher frequencies.

Good agreement between the DVM results for C_{LbI} and experiments have also been obtained (Fig. 4.36). Again, comparison is affected by the large variation in different experimental results. The results show that the value of U_r at which C_{LbI} becomes positive increases with amplitude as found in experiments. Allowing for differences in the experimental results, the reduced velocity at which C_{LbI} becomes positive is also well predicted.

4.6   H-Section Cylinder.

The detailed investigation of the unsteady aerodynamic loading and aeroelastic response of bridge deck sections became important after the failure of the Tacoma Narrows bridge in 1940. The problems arose due to the fundamentally unstable aerodynamic nature of the bridge cross section along with the lightweight and flexible structure. Prior to the collapse the bridge had been nicknamed "Galloping Gertie" due to its unstable nature and there were many reports of the bridge undergoing plunging oscillations due to VIV response. However, as discussed by Billah and Scanlan [1], the ultimate catastrophic failure was due to torsional flutter response (Fig. 1.1) and not due to vertical response to VIV as was originally assumed at the time of the failure. Since the Tacoma failure, the H-section cylinder which formed the bridge deck has been the subject of many experimental and numerical analyses to study the unsteady

aerodynamics of the section. Due to the availability of data, the H-section forms a natural step in the validation of the DVM, from the simple geometric bodies discussed above to the study of modern bridge deck sections.

4.6.1   Static H-Section Cylinder.

The section used in this study is a simplified Tacoma geometry, with the cylinder having an aspect ratio of 5. Instantaneous snapshots of the flow field around the cylinder at 0° and 6° incidence (positive angle in clockwise direction) are given in Figs. 4.37 and 4.38 respectively. The figures demonstrate the complex flow field, with vortices shed from both the upstream and downstream vertical faces of the section. The formation of the vortex street is clearly discerned in the wake of the body. Also clearly demonstrated is the strong vortex formed behind the front plate of the H-section and the reattachment of this vortex onto the middle part of the section. The strength of this vortex has a significant effect on the variation of the mean aerodynamic force coefficients with incidence as is discussed below.

Static force coefficients for the section at a range of incidence between -10° to +10° are presented in Fig. 4.39 and results at 0° are presented in Table 4.5. The crosswind dimension is used to non-dimensionalise St and C_D, with the along-wind or body width used for C_L and C_M. In general, good agreement is demonstrated with the experimental data [90]. C_D is generally slightly overpredicted although the correct trend is observed in the DVM results.

	C_D ($\alpha=0°$)	C_{Lrms} ($\alpha=0°$)	$dC_L/d\alpha \mid_{\alpha=0°}$ (rad)	$dC_M/d\alpha\mid_{\alpha=0°}$ (rad)	St ($\alpha=0°$)
Experiment : Schewe [90] $Re = 8.1\times10^5$	1.24	0.227	6.9	-0.77	0.11
Larsen : Vortex Method [119, 196]. $Re = 10^5$	1.40	0.37	N/A	N/A	0.11
DVM $Re = 10^5$	1.31	0.337	6.50	-0.473	0.113

Table 4.5

The C_L and C_M results are good, especially at the low angles of incidence. However, the non-linearity in the experimental data at higher angles is not captured. At the higher angles of incidence, the shear layer is likely to separate completely from the front face leading to the a reduction in both C_L and C_M that is seen in the experimental data. In the DVM results, it is likely that the shear layer does not separate completely and closes in on the body, and hence the linear

region continues beyond the experimental region. A possible cause is an overproduction of vorticity in the DVM calculation although further investigation is necessary to address this discrepancy. Comparing parameters at 0° incidence with experiment and also with results obtained from a vortex method by Larsen et al [119 and 196] again serve to demonstrate the quality of the predictions obtained. The results given in Table 4.5 in particular show that the gradient of C_L and C_M are well predicted and the results compare favourably with those of Larsen. The negative gradient of C_M is responsible for the torsional flutter instability of the H-section.

4.6.2 Oscillating H-Section and Flutter Analysis.

To study the flutter characteristics of the H-section, a series of calculations were performed with the body undergoing forced sinusoidal transverse and torsional oscillations. Both sets of calculations were performed for a range of U_r with the amplitude ratio (with respect to the body width) of the transverse oscillations being 0.025 and the amplitude of the torsional oscillations being 3°. These results are used to derive the flutter coefficients and hence, obtain the critical flutter velocity of the section. The method of the extraction of the flutter coefficients and calculation of the flutter velocity is briefly discussed in Appendix F. The flutter coefficients are compared with experimental data [3] and results from calculations by Larsen [119] in Figs. 4.40 and 4.41. The experimental data for $A_1{}^*$ and $A_3{}^*$ is assumed to be negligible. In general, good agreement is demonstrated with the experimentally derived data and also show a favourable comparison with the vortex method results of Larsen.

The flutter derivatives of most interest in this case are $A_2{}^*$ and $H_1{}^*$, which represent the aerodynamic damping in the torsional and vertical degrees of freedom respectively. A slight peak in the $H_1{}^*$ results at $U_r{\approx}2.0$ is caused by the effects of vortex lock-in for the vertical degree of freedom influencing the flutter derivative and are similar to the results reported by Larsen [196] (Fig. 4.40a). For 1DOF torsional flutter, the critical flutter velocity may be calculated directly from the $A_2{}^*$ flutter derivative, as shown in Appendix F, using (4.8).

$$\left(A_2^*\right) = \frac{2I\zeta_\alpha}{\rho B^4} \tag{4.8}$$

The most important aspect of the $A_2{}^*$ derivative is the reversal in sign at higher U_r, and as such is the prime reason for the torsional instability of the H-section (Fig. 4.41b). The equation (4.8) represents the point at which the total damping (mechanical plus aerodynamic) of the system is zero. At reduced velocities higher than this, a negative damping condition arises and the structure becomes fundamentally unstable. It is clear that the flutter criteria in (4.8) can only occur at positive values of $A_2{}^*$ and hence the reversal in sign is an inherent characteristic of the flutter instability in the torsional DOF. The $A_2{}^*$ derivative shows good agreement with the experimental data. There was some indication from the results, between reduced velocities 3 to

4, of a lock-in phenomena predicted by the DVM. It is not clear if this is a physical or numerical phenomenon and further investigation of these results is required.

The structural properties of the original Tacoma Narrows bridge were taken to be $I=177.73\times10^3$kgm^2/m, $\zeta_\alpha=0.005$ and $B=12$m [119] and using this data in (4.8) indicates that the critical flutter velocity corresponds to when $A_2^*=0.07$. By linearly interpolating from the DVM results, the critical flutter velocity occurs at a reduced velocity of 3.88 or using the structural data, a flutter speed of 9.31ms^{-1}. If a quadratic curve is fitted to the DVM results, the flutter speed is calculated to be 10.31ms^{-1}. Both of these results compare well to the experimentally derived flutter speed of 8.31ms^{-1} as given by Billah et al [1]. The DVM predictions also compare favourably to the vortex method results of Larsen where a flutter speed of 11.5ms^{-1} is calculated [119]. It should be noted that although the flutter instability occurs at a speed of 8.31ms^{-1}, the bridge eventually failed at a wind speed of approximately of 19ms^{-1}.

4.7   Study of Great Belt East Suspension Bridge.

The successful validation of the DVM presented above gives confidence in the method when applied to the analysis of suspension bridge deck sections. To investigate the capability of the DVM for the analysis of the flow field around a representative geometry, a study of the Great Belt East Suspension bridge was undertaken. The bridge forms part of the link between the islands of Funen and Zealand in Denmark [133, 223-226] and the bridge configuration along with the cross section of the main suspended span is illustrated in Fig. 4.42. The Great Belt East bridge with a main span of 1624m, opened in June 1998, and will form the longest single span until the completion of the Akashi Kaikyo bridge in Japan. Therefore, with the bridge being one of the major recent projects in the fields of suspension bridge aerodynamics and wind engineering, it has been the subject of numerous studies, both experimental and numerical, giving a significant data base which can be used to assess the DVM predictions. All of the analysis presented herein is performed on the main suspended span (Fig. 4.42b).

4.7.1   Analysis of Static Section.

A series of calculations on the static section were performed at a range of angles of incidence from -10° to +10°. Instantaneous flow field distributions are given in Figs. 4.43 and 4.44. In the 10° case, the vortices under the body and towards the downstream lower corner show a significant increase in strength when compared to the 0° case and in turn lead to an increase in the lift and moment coefficients. Most modern long span suspension bridge designs, as in this case, utilise a streamlined box section to ensure that the increase in the force coefficients with incidence is not so dramatic to produce a fundamentally unstable design.

In the 0° case, the flow along the upper surface is virtually fully attached and exhibits little separation. The prime reason for this is that the geometric model used in the DVM is a simplified cross section and more complex features, such as crash barriers and cable supports that would disturb the flow, are not modelled. An initial attempt was made to model the crash barriers on the extremities of the upper surface and the effect on the flow field is clearly seen in Fig. 4.45. In this case, there is a significant separation on the upper surface caused by the barriers. Each barrier is modelled by the addition of a flat plate of representative height and thickness at the approximate location. Hence, care must be taken as the "plates" are treated as a solid geometry, and porosity effects are neglected. However, the results demonstrate the effect of barriers and give a indication of potential future developments of the code.

The static force coefficients for the section are presented in Fig. 4.46, compared with experimental results from a section model test [225] and also with results from a finite difference grid based numerical method [158]. C_L and C_M are non-dimensionalised using the along wind body dimensions, B, and B^2 respectively, whereas C_D is non-dimensionalised using the crosswind dimension, L. The results presented by Kuroda [158] also use a simplified deck section with the barriers omitted. Results at 0° incidence are also presented in Table 4.6 along with vortex method results on the Great Belt section from Larsen and Walther [119, 167 and 196], who again model a simplified geometry without any crash barriers.

	$C_D(\alpha=0°)$	$C_L(\alpha=0°)$	$dC_L/d\alpha \mid_{\alpha=0°}$ (rad)	$C_M(\alpha=0°)$	$dC_M/d\alpha\mid_{\alpha=0°}$ (rad)
Experiment [133, 225-226]	0.57	0.067	4.37	0.028	1.17
DVM	0.3544	0.127	6.58	0.0519	1.34
Kuroda - Finite difference [158]	0.4811	-0.1792	7.567	0.0345	1.135
Larsen and Walther - Vortex Method [119 and 196].	0.430	0.000	4.13	0.027	1.15
Walther - Vortex Method [167].	0.4022-0.5855	-0.0571-0.0545	3.214-7.060 (Mean = 4.699)	0.0262-0.0418	0.6807-1.1723 (Mean = 0.9325)

Table 4.6

In general the results compare well with the experiment, in particular C_L and C_M, and show favourable comparison with the alternative numerical methods. The results of Larsen et al [119 and 196] are based on and summarise the results presented in Walther [167]. As can be seen in

Fig. 4.46, Walther's results show a range of values for the force coefficients at each angle of incidence, obtained by use of different parameters in the vortex method. The variation is obtained through variations in the time step and by adjusting the maximum circulation of the wake vortex particles. The range of the results for these parameters, for both the mean force coefficients and the gradients at $\alpha=0°$ are summarised in Table 4.6. Although the data presented by Larsen appears to be more accurate than the DVM, it is not clear which of Walther's results were used to obtain this data. It is clear from Fig. 4.46 that the results of the DVM are comparable with the other predictions in terms of their qualitative and quantitative agreement with experiment.

C_D at 0° is underpredicted somewhat, as also indicated in Larsen's results. However, Larsen suggests that a possible explanation for this discrepancy is the lack of modelling of the crash barriers and parapets in the calculations, elements that were included in the wind tunnel model. It is suggested [119 and 196] that simple calculations of the effect of freestream wind on each barrier or parapet would lead to a contribution to the C_D of approximately 0.162. This increment applied to the DVM results clearly brings the results more in line with the experiment. It is interesting to note that at positive incidence, the C_D predicted by the DVM is higher than the experimental results. In this case, flow is more likely to separate from the "leading edge" of the structure, with the barrier near the front of the section now likely to be located within the vortex generated at the "leading edge". Hence, the barriers are less likely to have a significant effect on the C_D at positive incidence. At negative incidence, the barriers still play are large role in determining the location of the separation and this can be seen in the underprediction of C_D.

The same calculations are performed using the DVM, but including the approximate barrier modelling discussed above and the results are compared to experiment and DVM without barriers in Fig. 4.47. It should again be noted that the model is a crude approximation as the barriers in the DVM are assumed to be solid and impermeable, contrary to the real structure. This is clearly noticeable in the results at 0° where C_D is now overpredicted compared to experiment. The discussion above is backed up to an extent by these results. C_D at positive incidence is still in good agreement with the data and has changed only slightly relative to the DVM without barriers. At negative incidence, where the barriers continue to play a large part in determining the location of separation, the results are significantly affected by the inclusion of the barriers, with C_D now overpredicted by the DVM. Similar effects can be seen on the C_L, where the results at positive incidence are not greatly affected, whereas the results at negative incidence demonstrate a considerable change. Again the differences with experiment may be attributed to the barriers being modelled as a solid plate. The results demonstrate the potential to incorporate detailed structural features within the DVM analysis.

The numerical results of Kuroda [158] were also obtained using a model with the barriers omitted, though the C_D seems to show good agreement with the experimental data. Kuroda attributes the poor agreement with the data for C_L at negative angles of incidence to the lack of

modelling of the barriers. At negative incidence, it is claimed that the flow will be fully attached to the upper surface of the section and will hence lead to a lower C_L than the experiment where the barriers cause a significant separation. Although this argument is plausible, the good agreement of C_D with the data despite the lack of modelling of barriers detracts from the quality of these predictions.

4.7.2   Analysis of Oscillating Section.

On flexible long span bridges, 2DOF flutter is often encountered and careful design of the section is essential to ensure that the critical flutter velocity is within the relevant design criteria. A common method of analysing flutter on bridge sections is by means of the flutter derivatives discussed in Chapter 2. These derivatives are usually extracted from sectional model tests in a wind tunnel, using numerous techniques from either free or forced oscillation experiments. The DVM has been used to derive the flutter derivatives for the Great Belt East main suspended span from a series of calculations of the section undergoing forced sinusoidal oscillations. The simulations involved separate vertical and torsional motion about the axis at mid-chord of the section (Fig. 4.42) at a range of reduced velocities from U_r=4.0-15.0 using the simplified section omitting the crash barriers. The amplitudes were $0.04B$ and $4°$ for the vertical and torsional cases respectively. The flutter derivatives were extracted from the DVM results using the method outlined in Appendix F.

The calculated flutter derivatives are compared with experimental data [98, 124 and 225] in Fig. 4.48. Comparison is also made with flutter derivatives calculated by Walther [167], also using a vortex method modelling the section undergoing 1DOF forced oscillations. The experimental data was derived from wind tunnel tests with smooth freestream flow, using a system identification technique. It should also be noted that this technique requires the body to be excited in both the vertical and torsional directions simultaneously unlike the DVM calculations which employed forced oscillations in each direction separately. This may account for some of the differences between the results. However, good agreement with the data is obtained for all of the derivatives, although generally, in wind engineering, the derivatives A_4^* and H_4^* are assumed to be zero as they are of little significance for practical flutter predictions. An interesting point to note with the Great Belt flutter derivatives is that A_2^* does not exhibit the change in sign that is characteristic for 1DOF torsional flutter as demonstrated for the H-section cylinder in [1-2] and in section 4.6.2. The derivative A_2^* represents the aerodynamic damping in the torsional direction and "negative damping" criteria necessary for torsional flutter only occurs at positive A_2^*. Hence, as A_2^* remains negative over the whole range of reduced velocity, the flutter oscillation for this section is likely to be a 2DOF coupled flutter in both the vertical and torsional directions.

Favourable comparison with the results of Walther [167] are also obtained. As with the static results presented in [167] and discussed above, for each reduced velocity, a range of flutter

derivatives are obtained, depending on the amplitude of the oscillation used in the calculation. It is clear from Fig. 4.48 that the DVM results demonstrate better agreement with the experimental data and show less scatter than those of Walther.

Structural Property	Great Belt East : Main Suspended Span.
Mass / unit length : m (Kg/m)	22.74×10^3
Mass moment of inertia / unit length : I (Kgm^2/m)	2.47×10^6
Frequency of response in vertical direction : f_h (Hz)	0.099
Frequency of response in torsional direction : f_α (Hz)	0.272
Relative-to-critical damping ratio : ζ	0.002

Table 4.7

The critical flutter velocity may be derived from the flutter derivatives using the method outlined by Simiu and Scanlan [2] also discussed by Larsen [119] and extended in Appendix F to incorporate the final two derivatives A_4^* and H_4^* in the calculation. The structural properties of the bridge section used in the analysis are given in Table 4.7 taken from [133 and 196]. Flutter velocity predictions from the DVM analysis are presented in Table 4.8 compared with results from a wind tunnel sectional model test [133 and 225] and predictions by Larsen et al [196]. The flutter derivatives used by Larsen are essentially those presented by Walther [167] and are shown in Fig. 4.48. Noting the scatter of these flutter derivatives, it is not clear which of these results have been used to derive the critical flutter velocity. The DVM results are presented for two cases, the first using only the traditional derivatives A_i^* and H_i^* for i=1-3 and the second also including the final two derivatives, A_4^* and H_4^*. The DVM predictions give an excellent prediction of the critical flutter velocity and the results are certainly comparable with Larsen's results. The accuracy of these results indicates that the DVM is a useful analysis tool for design studies of long span bridges.

Data	Critical Flutter Velocity U_c (ms^{-1})
Full Aeroelastic Model [133]	70-75
Taut Strip Model [133]	72
Wind Tunnel Sectional Model [133, 224-225]	74.2
DVM - A_i^* and H_i^* i=1-3 only	74.997
DVM - A_i^* and H_i^* i=1-4	71.632
Larsen - Vortex method [196]	74.0

Table 4.8

The discussion above only considers the motion of the bridge deck in the vertical and torsional degrees of freedom. Recent studies have suggested that the response of the bridge in the swaying or along-wind direction may also have an important influence on the stability of the structure [112]. It was found on a recent bridge design that if only the vertical and torsional flutter derivatives (H_i^* and A_i^*) were used in the analysis, a flutter velocity of approximately 130ms^{-1} was obtained. However, including the swaying flutter derivatives (P_i^*) into the analysis reduced the flutter velocity to between 70ms^{-1} and 80ms^{-1} [112]. Clearly, on longer span bridges with greater flexibility in the along-wind direction, analysis of the P_i^* derivatives may become more important in the future. Although the DVM has not been used to analyse the swaying derivatives, there is no reason why the method may not be used in such an analysis by modelling a forced oscillation in the along-wind degree of freedom. Future development of the DVM may include an investigation of the potential of the method to derive the P_i^* derivatives.

4.8   Control of Flutter Oscillations.

There have been a number of studies into how the structural stability of suspension bridges may be improved. For "bluff" cross sections, the use of fairings as demonstrated in [126 and 129] gives a significant improvement in stability. However, for "streamlined" sections such as that of the Great Belt East bridge studied in the previous section, the critical flutter velocity may be increased by the addition of guide vanes that act as flow control devices. Such devices are studied in [130-132] indicating the effects of both passive and actively controlled devices. Typical arrangements and applications of these devices are given in Fig. 4.49. The system is based on the idea that the movements of the bridge deck are constantly monitored with the angle of the controlling guide vanes adjusted accordingly to generate stabilising aerodynamic forces and effectively increasing the aerodynamic damping to counteract any tendency to motion. Typical results of the application of such devices as presented in [131-132] are given in Fig. 4.50. It is essential that the guide vanes be located far enough from the bridge deck as is practical to ensure operation outside of the bridge shear layers. Typically the vanes have a chord length that is around 10% of the deck section width. The actively controlled vanes are given an oscillatory motion with the same frequency as the bridge section but out of phase, with the vanes at the leading and trailing edges of opposite phase. It is claimed by Ostenfeld and Larsen [132] that the critical flutter velocity is increased by up to 50% and as suggested by Kobayashi et al, may theoretically be increased up to an infinitely high speed [131].

Although these devices add considerable complexity to the bridge design, from a structural stability point of view, they are attractive. However, testing the effect of the guide vanes in a wind tunnel would involve a significant amount of effort to model even just the passive configuration accurately. The actively controlled guide vanes would present further problems with the modelling of the control and actuation system. Such an experimental study with reasonable results is presented in [131]. To demonstrate the capability of the DVM to be used

as part of a bridge design system, a brief study into the effect of passive and active control vanes on the flutter stability has been carried out. As part of the study, various configurations of passive and active control vanes have been applied to the Great Belt East main suspended span to investigate their effect on the flutter criteria (Fig. 4.51). As this is only a study of the effect of the vanes, a basic elliptical cross section is used. For more practical applications and to optimise the flow control, a more complex aerofoil section may be required. Each of the vanes has chord length 10% of the bridge section width. The effect on the flutter velocity of passive vanes at different angles, and of active vanes at different phase angles, were studied using the DVM. In the calculations, the bridge was given a forced sinusoidal oscillation in either the transverse or torsional DOF and for the passive calculations, the vanes were oscillated with the same amplitude and frequency. To demonstrate the active vanes, the control surfaces were given a forced motion that simulates the displacements that would be activated by the controller. The prescribed displacements of the vanes are given by (4.9). An example of the relative motions of the bridge deck and the two guide vanes is given in Fig. 4.52.

$$\text{Bridge torsional motion :} \quad \alpha(t) = \alpha_0 \sin\left(\frac{2\pi t}{U_r}\right)$$

$$\text{Vane motion :} \quad \alpha_v(t) = M\alpha_0 \sin\left(\frac{2\pi t}{U_r} + \phi\right)$$

$$(4.9)$$

Varying performance of the flow control vanes can be achieved by using different values for the amplitude factor, M, and the phase relative to the bridge section, ϕ. In each calculation, the downstream vane is in opposite phase to the upstream vane as demonstrated by Ostenfeld et al [132]. Using this procedure, simulations may be performed relatively simply and without the need to implement control theory, yet the effect of the active vanes on the flutter criteria can still be assessed.

Five different configurations of guide vanes were used, two of which were passive and three using active vanes each with different phase angles as summarised below :

1)	Passive vanes	: $\alpha = 0°$
2)	Passive vanes	: $\alpha = 4°$
3)	Active vanes	: $M = -2, \phi = 0°$
4)	Active vanes	: $M = -2, \phi = 60°$
5)	Active vanes	: $M = -2, \phi = 90°$

The effect on the flutter derivatives for the passive vanes compared to those of the bridge section without vanes is shown in Fig. 4.53 and 4.54. In general, the vanes do not give rise to any large changes in the flutter derivatives. The most notable effect is a reduction in the magnitude of both H_2^* and A_2^*. However, the changes are only minor, suggesting that the critical flutter velocity

will only be affected very slightly. The flutter velocity for each configuration is calculated using the structural properties given in Table 4.7 using the assumption that the addition of the vanes have no effect on the mass and stiffness of the structure. This assumption may be a little unrealistic but allows an investigation of how the aerodynamic properties of the bridge are affected by the flow control devices. The results are given in Table 4.9.

Configuration.	Critical Flutter Velocity (ms^{-1})
Wind Tunnel Sectional Model -No vanes [133, 224-225].	74.2
DVM calculation - No vanes.	71.632
Passive Vanes - α=0°	68.199
Passive Vanes - α=4°	70.8563

Table 4.9

As expected, the passive guide vanes do not have a large effect on the critical flutter velocity and in fact very slightly reduce the stability of the bridge. This result agrees with the findings of the studies in Ostenfeld et al [132] and Kobayashi [131] as demonstrated in Fig. 4.50. The passive vanes effectively corresponds to the case with M=1 and ϕ=0°. The analysis from [131] gives reducing flutter velocity for ϕ=0° as M increases.

The active control of the guide vanes in this study are only modelled in the cases where the structure is undergoing a torsional oscillation. Hence, no results are presented for A_1^* and H_1^* and the variation in the remaining flutter derivatives due to the actively controlled vanes are shown in Fig. 4.53 and 4.54. As with the passive vanes, there is relatively little change to A_3^* and H_3^*. However, for ϕ=60° and 90° there is a marked change to the A_2^* and H_2^* derivatives. In particular, H_2^* changes from negative to positive at a higher reduced velocity. The ϕ=0° case gives results similar to the bridge deck without vanes.

Configuration.	Critical Flutter Velocity (ms^{-1})
Wind Tunnel Sectional Model -No vanes [133, 224-225].	74.2
DVM calculation - No vanes.	71.632
Active Vanes - M=-2, ϕ=0°	65.50
Active Vanes - M=-2, ϕ=60°	108.154
Active Vanes - M=-2, ϕ=90°	N/A [4]

Table 4.10

---

[4] No Flutter velocity found.

The reduction in flutter velocity for the $\phi=0°$ case is to be expected from the results of Kobayashi [131] (Fig. 4.50b). Also, as $\phi=0°$, the oscillation of the vanes is in phase with the bridge deck as in the passive case, although the amplitude is double that of the bridge deck. The two cases where $\phi>0°$ show a significant change in the flutter velocity, and in the $\phi=90°$ calculation, no flutter velocity was found even when the aerodynamic derivatives were extrapolated beyond the range of reduced velocities used in the calculations (Table 4.10). Again, this agrees with the studies presented in [131-132] (Fig. 4.50) from which it was found that, as M increases, the flutter velocity tends to infinity for a phase of 90°, or even less at the higher amplitude factors. For $\phi=60°$, the flutter velocity has been increased by approximately 51% in agreement with the previous studies (increase of $\approx50\%$ claimed in [132]). However, as calculations were only performed for U_r of 6.0 to 14.0, this result was obtained by extrapolating the flutter derivatives to higher U_r. The flutter velocity obtained must therefore be treated cautiously. Despite this, the result does demonstrate the effect of the actively controlled guide vanes and indicates the capability of the method to study varying design configurations of bridge sections to assess their aeroelastic stability. It is clear that the effect of the passive and active flow controlling guide vanes as predicted by the DVM is in agreement with the results presented in previous studies.

4.9   Summary.

The results presented in this chapter for a wide range of test cases, demonstrate that the DVM is a useful tool for the analysis of bluff body flow fields. The successful prediction of the effects of incidence and aspect ratio on stationary rectangular cylinders, as well as the results on a transversely oscillating square cylinder, show quantitative agreement with experiment over a wider range of cases than the results from many other published numerical methods.

The method has also successfully been applied to static and oscillating bridge deck sections. The mean force coefficients are in good agreement with data and the calculated flutter derivatives have been used to give an accurate prediction of the critical flutter velocity of the bridge sections studied. These results, along with the study of the effect of active and passive flow control devices, demonstrate the capability and power of the DVM for use in the analysis of unsteady aerodynamic effects on suspension bridge decks. Also, the DVM may be used to assess the aeroelastic stability of a wide range of preliminary bridge deck section designs and configurations. Although wind tunnel experiments are still a vital part of the design process, the capability of the DVM to give a relatively quick turnaround time for setting up a model and obtaining results would enable more cost effective assessments covering a potentially wider range of designs than is currently practicable in the wind tunnel.

CHAPTER 5

CONCLUDING REMARKS.

Within this final chapter, the development and application of the DVM for predicting the flow field around bluff bodies, described in the previous chapters, is summarised. The chapter is split into two sections, the first provides a summary of the research presented in this thesis. Modifications that have been implemented to develop the DVM are summarised, as are the results from the analysis of a range of bluff body calculations. The second section indicates areas of future development and research in which the capability of the DVM could be further improved.

5.0   Summary.

A vortex method was developed by Lin [7] for the analysis of the dynamic stall phenomenon on pitching aerofoils. This method has been modified and developed to allow analysis of any general closed two-dimensional geometry. In particular, the model has been generalised with the particular aim of analysing the flow field around sharp edged bluff bodies.

Major improvements to the DVM include the incorporation of a fast algorithm to reduce the operation count from $O(N^2)$ to nearer $O(N+N\log N)$, hence giving a significant improvement in the calculation efficiency. Developments also include the addition of a sharp corner model to give a more accurate representation of the local vorticity distribution near the corners. An empirical circulation decay model has been incorporated into the DVM to provide a means of simulating the three-dimensional effects in the body wake such as vortex stretching. Although this model has had a beneficial effect on the results, the empirical nature means that it does not satisfy any physical representation of the flow. The wake decay, combined with the focus of the research being to analyse the flow around sharp edged bodies, has meant the approach to the analysis was to develop a useful, engineering model.

An extensive validation of the DVM has been carried out on simple bluff body geometries and good agreement with experimental data has been obtained. The results demonstrate the capability of the method to analyse a wide range of bluff body flow fields. The variation of the flow field at different static angles of incidence is well predicted, as is the effect of the body aspect ratio on the flow. Comparison with experimental data is demonstrated in both cases for a number of key flow parameters such as the mean aerodynamic loads and Strouhal number. The aspect ratio study also included successful prediction of the flow around a flat plate, both normal and parallel to the freestream flow. The degree of quantitative agreement between the predicted and experimental results, over this wide range of test cases, compared very favourably with that from

other published computational results, where the agreement is much more selective. Although much of the analysis with the DVM was of sharp edged bodies, a brief study of a circular cylinder demonstrated the capability of the method on a wide range of stationary geometries.

The flow field around a square cylinder undergoing a forced transverse oscillation was studied, to investigate the effects of vortex lock-in. This aeroelastic effect was captured, and the effect of both frequency and amplitude on the results were in good agreement with experimental data. The phase angle, ϕ, between the body displacement and the lift coefficient, C_L, was extracted from the results and was in concordance with the experimental data. Also, the results gave favourable comparison with results from other computations.

The DVM has also been validated on stationary bridge deck sections, using the H-section of the original Tacoma Narrow bridge and a more recent streamlined section used in the main span of the Great Belt East Bridge. Good agreement with published data is obtained for the mean force coefficients and their gradient at $\alpha=0°$. The results are also of comparable quality to other published computational results. The ability of the DVM to model more complex geometries is demonstrated by the inclusion of crash barriers in some of the calculations on the Great Belt East section. The correct qualitative effect on the results is demonstrated, though care must be taken as the barriers are modelled as solid objects whereas there is some porosity in the real case.

Calculations on the H-section and Great Belt East main section undergoing forced 1DOF oscillations in the transverse and torsional directions, demonstrate that the DVM is capable of analysing the aeroelastic stability of bridge sections. Flutter derivatives are extracted from the calculations and are in good agreement with those derived from sectional model tests. The results obtained are at least as accurate as the only other prediction of flutter derivatives that has been found in published literature. The critical flutter velocity for the Great Belt section calculated from the predicted flutter derivatives is found to within a few percent of the value found from experiment. The capability of the method is further demonstrated through a study into the effect of flow control devices on the stability of the bridge section. Both active and passive guide vanes are modelled and the change in the critical flutter velocity gives qualitative agreement with results from previous studies of such devices.

5.1   Future Research and Developments.

A much more detailed analysis of the circular cylinder should be undertaken to add to the validation that has been presented in this thesis. The DVM has shown the potential to capture the variation in the flow field at both sub-critical and super-critical Reynolds numbers (Chapter 4). However, a much more detailed analysis is required to fully develop physical relations between the input parameters of the DVM and *Re*. The engineering approach to some of the modelling means that prior to full validation of the circular cylinder, a number of aspects of the method

would require further investigation and improvement. In particular, the resolution of the boundary layers is more critical on smooth curvature bodies and the problematic aspects of the modelling of both viscous diffusion and wake turbulence at high *Re* need to be addressed. These modelling improvements would add to the range of geometries to which the DVM could be applied, and would also demonstrate the capability of the method on bluff geometries other than those with sharp corners.

The circulation decay model implemented to account for three-dimensional effects in the body wake, despite giving good results, is more of a mathematical tool and is not based completely on the real physical behaviour of the fluid. Future investigations may include the development of a more physical model to account for the three-dimensional effects in the wake although it is not clear as to what form such a model will take.

At present, a turbulence model is not incorporated within the DVM. The low numerical diffusion of a grid free technique, along with a high particle density in the calculation means that a lot of the small scale structures within the flow would be captured. An investigation along these lines to improve the capability of the DVM to model turbulence should be the subject of future research. Such a model may take a form similar to the grid based LES method, although it would require a careful implementation to retain beneficial aspects of the vortex method. Other theoretical models more appropriate for vortex methods and very different to grid based approaches are also worthy of investigation.

The calculation efficiency of the DVM has been significantly improved from $O(N^2)$ to nearer $O(N+N\log N)$ with the incorporation of a fast algorithm. However, further improvement may be obtained from the Fast Multipole Method of Greengard and Rokhlin et al [185 and 187] which is claimed to be $O(N)$. The benefits of this algorithm will become more significant as the number of particles in the flow field is increased beyond the typical number used in the current analysis. A more significant improvement in calculation efficiency could be obtained through the use of parallel computational techniques.

The DVM has been used to investigate the flutter instability of a recently designed bridge deck section. Although the results obtained have demonstrated good agreement with the experimental data, for the DVM to be used with increased confidence as a design tool, further validation needs to be carried out on more existing bridge sections. A validation study of a range of bridge sections that essentially encompass a variety of designs should be conducted in the future. Future studies could also include the calculation and validation of the flutter derivatives in the swaying or along-wind degree of freedom. Most analyses currently assume that the flutter is primarily dependent on the transverse and torsional degrees of freedom, though recent studies have shown the along-wind response may have a significant effect on the critical flutter velocity [112]. Future

modelling enhancements may include linking the DVM to a structural solver to enable the response of a structure to the unsteady aerodynamic flow field to be calculated.

In conclusion, the DVM has been developed to model the flow field around simple sharp edged bluff body geometries and bridge deck sections. An extensive validation of the method has been carried out demonstrating the capability of the method to predict aerodynamic loads for a wide range of problems. Good agreement with experimental data has been obtained and the results demonstrate favourable comparison with other published computational results. The quantitative agreement with experiment demonstrates that the DVM can be applied successfully to a wide range of bluff body flow fields and can be used to analyse the aeroelastic stability of suspension bridge deck sections.

REFERENCES

1. BILLAH, K.Y. and SCANLAN, R.H., 1991, "Resonance, Tacoma Narrows Bridge Failure, and Undergraduate Physics Textbooks." American Journal of Physics, Vol. 59, No. 2, pp. 118-124

2. SIMIU, E. and SCANLAN, R.H., 1986, "Wind Effects on Structures : An Introduction to Wind Engineering." 2nd Edition, John Wiley and Sons.

3. SCANLAN, R.H. and TOMKO, J.J., 1971, "Airfoil and Bridge Deck Flutter Derivatives." Journal of the Engineering Mechanics Division, ASCE, Vol. 97, pp. 1717-1737.

4. SARPKAYA, T., 1989, "Computational Methods with Vortices - The 1988 Freeman Scholar Lecture." Journal of Fluids Engineering, Vol. 111, pp. 5-52.

5. LEONARD, A., 1980, "Vortex Methods for Flow Simulation." Journal of Computational Physics, Vol. 37, pp. 289-335.

6. LEONARD, A., 1985, "Computing Three-Dimensional Incompressible Flows with Vortex Elements." Annual Review of Fluid Mechanics, Vol. 17, pp. 523-559.

7. LIN, H., 1997, "Prediction of Separated Flows Around Pitching Aerofoils using a Discrete Vortex Method." Ph.D. Thesis, Department of Aerospace Engineering, University of Glasgow, Scotland, UK.

8. LIN, H. and VEZZA, M., 1996, "A Pure Vortex Method for Simulating Unsteady, Incompressible, Separated Flows around Static and Pitching Aerofoils." Proceedings of 20th ICAS Conference, Sorrento, Italy.

9. LIN, H., VEZZA, M. and GALBRAITH, R.A.McD., 1997, "Discrete Vortex Method for Simulating Unsteady Flow Around Pitching Aerofoils." AIAA Journal, Vol. 35, No. 3, pp. 494-499.

10. ESDU, 1980, "Mean Forces, Pressures and Flow Field Velocities for Circular Cylindrical Structures : Single Cylinder with Two-dimensional Flow." Engineering Sciences Data Item Number 80025.

11. SCHLICHTING, H., 1968, "Boundary Layer Theory." 6th Edition, pub. McGraw-Hill.

12. SCRUTON, C., 1981, "An Introduction to Wind Effects on Structures." Engineering Design Guides 40, Oxford University Press.

13. OTSUKI, Y., WASHIZU, K., TOMIZAWA, H. and OHYA, A., 1974, "A Note on the Aeroelastic Instability of a Prismatic Bar with Square Section." Journal of Sound and Vibration, Vol. 34, No. 2, pp. 233-248.

14. LEE, B.E., 1975, "The Effect of Turbulence on the Surface Pressure Field of a Square Prism." Journal of Fluid Mechanics, Vol. 69, Part 2, pp. 263-282.

15. VICKERY, B.J., 1966, "Fluctuating Lift and Drag on a Long Cylinder of Square Cross-Section in a Smooth and in a Turbulent Stream." Journal of Fluid Mechanics, Vol. 25, Part 3, pp. 481-494.

16. OBASAJU, E.D., 1983, "An Investigation of the Effects of Incidence on the Flow Around a Square Section Cylinder." Aeronautical Quarterly, Vol. 34, pp. 243-259.

17. NORBERG, C., 1993, "Flow Around Rectangular Cylinders : Pressure Forces and Wake Frequencies." Journal of Wind Engineering and Industrial Aerodynamics, Vol. 49, No. 1-3, pp. 187-196.

18. BEARMAN, P.W. and TRUEMAN, D.M., 1972, "An Investigation of the Flow Around Rectangular Cylinders." Aeronautical Quarterly, Vol. 23, pp. 229-237.

19. KNISELY, C.W., 1990, "Strouhal Numbers of Rectangular Cylinders at Incidence : A Review and New Data." Journal of Fluids and Structures, Vol. 4, pp. 371-393.

20. VON KARMAN, T., 1912, "Über den Mechanismus des Widerstandes den ein bewegter Koerper in einer Fluessugkeit erfaehrt." Nachricht der Koeniglichen Gesellschafet der Wissenschaft, Göttingen.

21. GERRARD, J.H., 1966, "The Mechanics of the Formation Region of Vortices behind Bluff Bodies." Journal of Fluid Mechanics, Vol. 25, pp. 401-413.

22. WILLIAMSON, C.H.K., 1996, "Vortex Dynamics in the Cylinder Wake." Annual Review of Fluid Mechanics, Vol. 28, pp. 477-539.

23. WEI, T. and SMITH, C.R., 1986, "Secondary Vortices in the Wake of Circular Cylinders." Journal of Fluid Mechanics, Vol. 169, pp. 513-533.

24. BAYS-MUCHMORE, B. and AHMED, A., 1993, "On Streamwise Vortices in Turbulent Wakes of Cylinders." Physics of Fluids, Vol. A-5, No. 2, pp. 387-392.

25. BEARMAN, P.W., 1997, "Near Wake Flows Behind Two- and Three-Dimensional Bluff Bodies." Journal of Wind Engineering and Industrial Aerodynamics, Vol. 69-71, pp. 33-54.

26. WILLIAMSON, C.H.K., 1997, "Advances in our Understanding of Vortex Dynamics in Bluff Body Wakes." Journal of Wind Engineering and Industrial Aerodynamics, Vol. 69-71, pp. 3-32.

27. LIN, J.-C., VOROBIEFF, P. and ROCKWELL, D., 1995 "Three-Dimensional Patterns of Streamwise Vorticity in the Turbulent Near-Wake of a Cylinder." Journal of Fluids and Structures, Vol. 9, pp. 231-234.

28. WU, J., SHERIDAN, J., SORIA, J. and WELSH, M.C., 1994, "An Experimental Investigation of Streamwise Vortices in the Wake of a Bluff Body." Journal of Fluids and Structures, Vol. 8, pp. 621-635.

29. WU, J., SHERIDAN, J., WELSH, M.C., HOURIGAN, K. and THOMPSON, M., 1994, "Longitudinal Vortex Structures in a Cylinder Wake." Physics of Fluids, Vol. 6, No. 9, pp. 2883-2885.

30. HAYAKAWA, M. and HUSSAIN, F., 1989, "Three-Dimensionality of Organized Structures in a Plane Turbulent Wake." Journal of Fluid Mechanics, Vol. 206, pp. 375-404.

31. BEARMAN, P.W. and OBASAJU, E.D., 1982, "An Experimental Study of Pressure Fluctuations on Fixed and Oscillating Square-Section Cylinders." Journal of Fluid Mechanics, Vol. 119, pp. 297-321.

32. WILKINSON, R.H., 1981, "Fluctuating Pressures on an Oscillating Square Prism. Part 2 : Spanwise Correlation and Loading." Aeronautical Quarterly, Vol. 32, No. 2, pp. 111-125.

33. WILKINSON, R.H., CHAPLIN, J.R. and SHAW, T.L., 1974, "On the Correlation of Dynamic Pressures on the Surface of a Prismatic Bluff Body." Flow-Induced Structural Vibrations, ed. E. Naudascher, Springer Verlag, Berlin, pp. 471-487.

34. BEARMAN, P.W., 1984, "Vortex Shedding from Oscillating Bluff Bodies." Annual Review of Fluid Mechanics, Vol. 16, pp. 195-222.

35. PARKINSON, G.V., 1974, "Mathematical Models of Flow-Induced Vibrations of Bluff Bodies." Flow-Induced Structural Vibrations, ed. E. Naudascher, Springer Verlag, Berlin, pp. 81-127.

36. PARKINSON, G.V., 1989, "Phenomena and Modelling of Flow-Induced Vibrations of Bluff Bodies." Progress in Aerospace Science, Vol. 26, pp. 169-224.

37. SARPKAYA, T., 1979, "Vortex Induced Oscillations - A Selective Review." Journal of Applied Mechanics ASME, Vol. 46, pp. 241-258.

38. BEARMAN, P.W. and LUO, S.C., 1988, "Investigation of the Aerodynamic Instability of a Square-Section Cylinder by Forced Oscillation." Journal of Fluids and Structures, Vol. 2, pp. 161-176.

39. LU, P.C., CHEN, R.H., CHENG, C.M. and HUANG, J.H., 1996, "Aerodynamics of a Vibrating Square Prism in Homogenous Turbulent Flows." Journal of the Chinese Institute of Engineers, Vol. 19, No. 3, pp. 353-361.

40. LU, P.C., CHENG, C.M. and KAO, C.R., 1997, "The Effects of Turbulence on Mean Flow past Fixed and Oscillating Rectangular Prisms." Journal of the Chinese Institute of Engineers, Vol. 20, No. 6, pp. 615-622.

41. NAKAMURA, Y. and HIRATA, K., 1989, "Critical Geometry of Oscillating Bluff Bodies." Journal of Fluid Mechanics, Vol. 208, pp. 375-393.

42. NAKAMURA, Y. and HIRATA, K., 1991, "Pressure Fluctuations on Oscillating Rectangular Cylinders with the Long Side Normal to the Flow." Journal of Fluids and Structures, Vol. 5, pp. 165-183.

43. NAKAMURA, Y. and MATSUKAWA, T., 1987, "Vortex Excitation of Rectangular Cylinders with a Long Side Normal to the Flow." Journal of Fluid Mechanics, Vol. 180, pp. 171-191.

44. NAKAMURA, Y. and MIZOTA, T., 1975, "Unsteady Lifts and Wakes of Oscillating Rectangular Prisms." Journal of the Engineering Mechanics Division, ASCE, Vol. 101, pp. 855-871.

45. OBASAJU, E.D., 1983, "Forced Vibration Study of the Aeroelastic Instability of a Square-Section Cylinder Near Vortex Resonance." Journal of Wind Engineering and Industrial Aerodynamics, Vol. 12, pp. 313-327.

46. WILKINSON, R.H., 1981, "Fluctuating Pressures on an Oscillating Square Prism. Part 1 : Chordwise Distribution of Fluctuating Pressure." Aeronautical Quarterly, Vol. 32, No. 2, pp. 97-110.

47. GOSWAMI, I., SCANLAN, R.H. and JONES, N.P., 1993, "Vortex-Induced Vibration of Circular Cylinders. 1 : Experimental Data." Journal of Engineering Mechanics, Vol. 119, No. 11, pp. 2270-2287.

48. GRIFFIN, O.M., SKOP, R.M. and KOOPMANN, G.H., 1973, "The Vortex-Excited Resonant Vibrations of Circular Cylinders." Journal of Sound and Vibration, Vol. 31, No. 2, pp. 235-249.

49. GRIFFIN, O.M. and KOOPMANN, G.H., 1977, "The Vortex-Excited Lift and Reaction Forces on Resonantly Vibrating Cylinders." Journal of Sound and Vibration, Vol. 54, No. 3, pp. 435-448.

50. GRIFFIN, O.M. and RAMBERG, S.E., 1982, "Some Recent Studies of Vortex Shedding with Application to Marine Tubulars and Risers." Journal of Energy Resources Technology, Vol. 104, pp. 2-13.

51. OBASAJU, E.D., ERMSHAUS, R. and NAUDASCHER, E., 1990, "Vortex-Induced Streamwise Oscillations of a Square-Section Cylinder in a Uniform Stream." Journal of Fluid Mechanics, Vol. 213, pp. 171-189.

52. OBASAJU, E.D., ERMSHAUS, R. and NAUDASCHER, E., 1992, "Further Results on the Flow-Induced Streamwise Vibration of Cylinders." Journal of Fluids and Structures, Vol. 6, pp. 51-66.

53. LOW, H.T., CHEW, Y.T. and TAN, K.T., 1989, "Fluid Forces on a Cylinder Oscillating in Line with a Uniform Flow." Ocean Engineering, Vol. 16, No. 3, pp. 307-318.

54. BEARMAN, P.W., GARTSHORE, I.S., MAULL, D.J. and PARKINSON, G.V., 1987, "Experiments on Flow-Induced Vibration of a Square-Section Cylinder." Journal of Fluids and Structures, Vol. 1, pp. 19-34.

55. CORLESS, R.M. and PARKINSON, G.V., 1988, "A Model of the Combined Effects of Vortex-Induced Oscillation and Galloping." Journal of Fluids and Structures, Vol. 2, pp. 203-220.

56. DENIZ, S. and STAUBLI, T, 1997, "Oscillating Rectangular and Octagonal Profiles : Interaction of Leading- and Trailing-Edge Vortex Formation." Journal of Fluids and Structures, Vol. 11, pp. 3-31.

57. BEARMAN, P.W. and CURRIE, I.G., 1979, "Pressure Fluctuation Measurements on an Oscillating Circular Cylinder." Journal of Fluid Mechanics, Vol. 91, pp. 661-677.

58. SKOP, R.A. and GRIFFIN, O.M, 1973, "A Model for the Vortex-Excited Resonant Response of Bluff Cylinders." Journal of Sound and Vibration, Vol. 27, No. 2, pp. 225-233.

59. HARTLEN, R.T. and CURRIE, I.G., 1970, "Lift-Oscillator Model of Vortex-Induced Vibration." Journal of Engineering Mechanics Division, ASCE, Vol. 96, No. EM5, pp. 577-591.

60. IWAN, W.D. and BLEVINS, R.D., 1974, "A Model for Vortex Induced Oscillation of Structures." Journal of Applied Mechanics ASME, Vol. 41, pp. 581-586.

61. IWAN, W.D., 1975, "The Vortex Induced Oscillation of Elastic Structural Elements." Journal of Engineering for Industry, Vol. 97, pp. 1378-1382.

62. SKOP, R.A. and GRIFFIN, O.M, 1975, "On a Theory for the Vortex-Excited Oscillations of Flexible Cylindrical Structures." Journal of Sound and Vibration, Vol. 41, No. 3, pp. 263-274.

63. SKOP, R.A. and BALASUBRAMANIAN, S., 1997, "A New Twist on an Old Model for Vortex-Excited Vibrations." Journal of Fluids and Structures, Vol. 11, pp. 395-412.

64. TAMURA, Y. and MATSUI, G., 1979, "Wake-Oscillator Model of Vortex-Induced Oscillation of Circular Cylinder." Wind Engineering, Proceedings of the 5th International Conference, Fort Collins, Colorado, USA, July 1979, ed. J.E. Cermak, Vol. 2, pp. 1085-1094.

65. HANGAN, H. and VICKERY, B.J., 1997, "A Wake Model for Two-Dimensional (Sharp-Edged) Bluff Bodies." Proceedings of 9th International Symposium on Wind Engineering, 9-13 January 1995, New Delhi, India. Journal of Wind Engineering and Industrial Aerodynamics, Vol. 72, pp. 47-60.

66. EHSAN, F. and SCANLAN, R.H., 1990, "Vortex-Induced Vibrations of Flexible Bridges." Journal of Engineering Mechanics, Vol. 116, No. 6, pp. 1392-1411.

67. GUPTA, H., SARKAR, P.P. and MEHTA, K.C., 1996, "Identification of Vortex-Induced-Response Parameters in Time Domain." ASCE Journal of Engineering Mechanics, Vol. 122, No. 11, pp. 1031-1037.

68. LARSEN, A., 1995, "A Generalized Model for Assessment of Vortex-Induced Vibrations of Flexible Structures." Journal of Wind Engineering and Industrial Aerodynamics, Vol. 57, No. 2-3, pp. 281-294.

69. DYRBYE, C. and HANSEN, S.O., 1996, "Wind Loads on Structures" John Wiley and Sons. (English edition.)

70. DOWELL, E.H., CURTESS, H.C., SCANLAN, R.H. and SISTO, F., 1989, "A Modern Course in Aeroelasticity." 2nd Edition, Kluwer Academic Publishers.

71. BLEVINS, R.D., 1977, "Flow-Induced Vibration." pub. Van Nostrand Reinhold Company.

72. NOVAK, M., 1969, "Aeroelastic Galloping of Prismatic Bodies." Journal of the Engineering Mechanics Division, ASCE, Vol. 95, pp. 115-142.

73. PARKINSON, G.V. and SMITH, J.D., 1964, "The Square Prism as an Aeroelastic Non-Linear Oscillator." Quarterly Journal of Mechanics and Applied Mathematics, Vol. 17, Pt. 2, pp. 225-239.

74. NOVAK, M., 1971, "Galloping and Vortex Induced Oscillations of Structures." Proceedings of 3rd International Conference of Wind Effects on Buildings and Structures, Tokoyo, pp. 799-809.

75. NOVAK, M., 1972, "Galloping Oscillations of Prismatic Structures." Journal of the Engineering Mechanics Division, ASCE, Vol. 98, pp. 27-46.

76. LANEVILLE, A. and PARKINSON, G.V., 1971, "Effects of Turbulence on Galloping of Bluff Cylinders." Proceedings of 3rd International Conference of Wind Effects on Buildings and Structures, Tokoyo, pp. 787-797.

77. LINDNER, H., 1992, "Simulation of the Turbulence on Galloping Vibrations." Journal of Wind Engineering and Industrial Aerodynamics, Vol. 41-44, pp. 2023-2034.

78. NAKAMURA, Y. and TOMONARI, Y., 1977, "Galloping of Rectangular Prisms in a Smooth and in a Turbulent Flow." Journal of Sound and Vibration, Vol. 52, No. 2, pp. 233-241.

79. NAKAMURA, Y., 1993, "Bluff-Body Aerodynamics and Turbulence." Journal of Wind Engineering and Industrial Aerodynamics, Vol. 49, pp. 65-78.

80. NOVAK, M. and TANAKA, H., 1974, "Effect of Turbulence on Galloping Instability." Journal of the Engineering Mechanics Division, ASCE, Vol. 100, pp. 27-47.

81. LUO, S.C. and BEARMAN, P.W., 1990, "Predictions of Fluctuating Lift on a Transversely Oscillating Square-Section Cylinder." Journal of Fluids and Structures, Vol. 4, pp. 219-228.

82. OLIVARI, D., 1983, "An Investigation of Vortex Shedding and Galloping Induced Oscillation on Prismatic Bodies." Journal of Wind Engineering and Industrial Aerodynamics, Vol. 11, pp. 307-319.

83. WAWZONEK, M.A. and PARKINSON, G.V., 1979, "Combined Effects of Galloping Instability and Vortex Resonance." Wind Engineering, Proceedings of the 5th International Conference, Fort Collins, Colorado, USA, July 1979, ed. J.E. Cermak, Vol. 2, pp. 673-684.

84. WASHIZU, K., OHYA, A., OTSUKI, Y., and FUJII, K., 1978, "Aeroelastic Instability of Rectangular Cylinders in a Heaving Mode." Journal of Sound and Vibration, Vol. 59, No. 2, pp. 195-210.

85. LUO, S.C., CHEW, Y.T. and GOH, E.Y., 1995, "Unsteady Fluid Force Acting on Oscillating Square-Section Cylinder." ASCE Journal of Engineering Mechanics, Vol. 121, No. 1, pp. 176-180.

86. BOUCLIN, D.N., 1977, "Hydroelastic Oscillations of Square Cylinders." M.A.Sc. Thesis, University of British Columbia, Vancouver, Canada.

87. TAMURA, Y. and SHIMADA, K., 1987, "A Mathematical Model for the Transverse Oscillations of Square Cylinders." Proceedings of International Conference on Flow-Induced Vibrations, Windermere, United Kingdom, pp. 267-275.

88. CORLESS, R.M. and PARKINSON, G.V., 1993, "Mathematical Modelling of the Combined Effects of Vortex-Induced Vibration and Galloping. Part II." Journal of Fluids and Structures, Vol. 7, pp. 825-848.

89. SCANLAN, R.H., 1982, "Developments in Low-Speed Aeroelasticity in the Civil Engineering Field." AIAA Journal, Vol. 20, No. 6, pp. 839-844.

90. SCHEWE, G., 1989, "Nonlinear Flow-Induced Resonances of an H-Shaped Section." Journal of Fluids and Structures, Vol. 3, pp. 327-348.

91. SCANLAN, R.H. and BUDLONG, K.S., 1974, "Flutter and Aerodynamic Response Considerations for Bluff Objects in a Smooth Flow." Flow-Induced Structural Vibrations, ed. E. Naudascher, Springer Verlag, Berlin, pp. 339-354.

92. SCANLAN, R.H., BELIVEAU, J-G. and BUDLONG, K.S., 1974, "Indicial Aerodynamic Functions for Bridge Decks." Journal of the Engineering Mechanics Division, ASCE, Vol. 100, pp. 657-672.

93. SCANLAN, R.H., 1993, "Problematics in Formulation of Wind-Force Models for Bridge Decks." Journal of Engineering Mechanics, Vol. 119, No. 7, pp. 1353-1375.

94. SCANLAN, R.H., JONES, N.P. and SINGH, L., 1997, "Inter-Relations among Flutter Derivatives." Journal of Wind Engineering and Industrial Aerodynamics, Vol. 69-71, pp. 829-837.

95. MATSUMOTO, M., DAITO, Y., YOSHIZUMI, F., ICHIKAWA, Y. and YABUTANI, T., 1997, "Torsional Flutter of Bluff Bodies." Journal of Wind Engineering and Industrial Aerodynamics, Vol. 69-71, pp. 871-882.

96. MATSUMOTO, M., KOBAYASHI, Y. and SHIRATO, H., 1996, "The Influence of Aerodynamic Derivatives on Flutter." Journal of Wind Engineering and Industrial Aerodynamics, Vol. 60, No. 1-3, pp. 227-239.

97. MATSUMOTO, M., SHIRAISHI, N., SHIRATO, H., SHIGETAKA, K. and NIIHARA, Y., 1993, "Aerodynamic Derivatives of Coupled/Hybrid Flutter of Fundamental Structural Sections." Journal of Wind Engineering and Industrial Aerodynamics, Vol. 49, pp. 575-584.

98. POULSEN, N.K., DAMSGAARD, A. and REINHOLD, T.A., 1992, "Determination of Flutter Derivatives for the Great Belt Bridge." Journal of Wind Engineering and Industrial Aerodynamics, Vol. 41, No. 1-3, pp. 153-164.

99. HUSTON, D.R., 1987, "Flutter Derivatives from 14 Generic Bridge Deck Sections." Bridges and Transmission Line Structures, Proceedings of the Sessions at Structures Congress 1987, Orlando, FL, USA, 17-20 Aug. 1987, pp. 281-291.

100. IWAMOTO, M. and FUJINO, Y., 1995, "Identification of Flutter Derivatives of a Bridge Deck from Free Vibration Data." Journal of Wind Engineering and Industrial Aerodynamics, Vol. 54-55, pp. 55-63.

101. JAIN, A., JONES, N.P. and SCANLAN, R.H., 1996, "Coupled Aeroelastic and Aerodynamic Response Analysis of Long-Span Bridges." Journal of Wind Engineering and Industrial Aerodynamics, Vol. 60, No. 1-3, pp. 69-80.

102. LI, Q.C. and LIN, Y.K., 1995, "New Stochastic Theory for Bridge Stability in Turbulent Flow. II." ASCE Journal of Engineering Mechanics, Vol. 121, No. 1, pp. 102-116.

103. SARKAR, P.P., JONES, N.P. and SCANLAN, R.H., 1994, "Identification of Aeroelastic Parameters of Flexible Bridges." Journal of Engineering Mechanics, Vol. 120, No. 8, pp. 1718-1742.

104. SARKAR, P.P., JONES, N.P. and SCANLAN, R.H., 1992, "System Identification for Estimation of Flutter Derivatives." Journal of Wind Engineering and Industrial Aerodynamics, Vol. 41-44, pp. 1243-1254.

105. SCANLAN, R.H., 1997, "Some Observations on the State of Bluff-Body Aeroelasticity." Journal of Wind Engineering and Industrial Aerodynamics, Vol. 69-71, pp. 77-90.

106. SCANLAN, R.H., 1978, "The Action of Flexible Bridges Under Wind, I : Flutter Theory." Journal of Sound and Vibration, Vol. 60, No. 2, pp. 187-199.

107. SCANLAN, R.H., 1996, "Aerodynamics of Cable-Supported Bridges." Journal of Constructional Steel Research, Vol. 39, No. 1, pp. 51-68.

108. HAILI, L. and SHAOZHONG, X., 1997, "A Method for Identification of Aerodynamic Derivatives from Free Vibration Data." Proceedings of 2nd European and African Conference on Wind Engineering, Genova, Italy, 22-26 June 1997, pp. 1593-1600.

109. BRAR, P.S., RAUL, R. and SCANLAN, R.H., 1996, "Numerical Calculation of Flutter Derivatives via Indicial Functions." Journal of Fluids and Structures, Vol. 10, pp. 337-351.

110. SINGH, L., JONES, N.P., SCANLAN, R.H. and LORENDEAUX, O., 1996, "Identification of Lateral Flutter Derivatives of Bridge Decks." Journal of Wind Engineering and Industrial Aerodynamics, Vol. 60, No. 1-3, pp. 81-89.

111. SCANLAN, R.H., 1987, "Interpreting Aeroelastic Models of Cable-Stayed Bridges." Journal of Engineering Mechanics, Vol. 113, No. 4, pp. 555-575.

112. BEITH, J., 1998, Personal Communication, Civil Engineering Consultant, Halcrow Crouch, Glasgow.

113. ZASSO, A., CIGADA, A. and NEGRI, S., 1996, "Flutter Derivatives Identification Through Full Bridge Aeroelastic Model Transfer Function Analysis." Journal of Wind Engineering and Industrial Aerodynamics, Vol. 60, No. 1-3, pp. 17-33.

114. TANAKA, H., YAMAMURA, N. and TATSUMI, M., 1992, "Coupled Mode Flutter Analysis Using Flutter Derivatives." Journal of Wind Engineering and Industrial Aerodynamics, Vol. 42, No. 1-3, pp. 1279-1290.

115. ZASSO, A., 1996, "Flutter Derivatives : Advantages of a New Representation Convention." Journal of Wind Engineering and Industrial Aerodynamics, Vol. 60, No. 1-3, pp. 35-47.

116. JENSEN, A.G. and HOFFER, R., 1997, "Flat Plate Flutter Derivatives : An Alternative Formulation." Proceedings of 2nd European and African Conference on Wind Engineering, Genova, Italy, 22-26 June 1997, pp. 1521-1528.

117. JENSEN, A.G., 1997, "Fluid Dynamic Derivatives : Marine and Wind Engineering Approaches." Journal of Wind Engineering and Industrial Aerodynamics, Vol. 69-71, pp. 777-793.

118. FALCO, M., CURAMI, A. and ZASSO, A., 1992, "Nonlinear Effects in Sectional Model Aeroelastic Parameters Identification." Journal of Wind Engineering and Industrial Aerodynamics, Vol. 41-44, pp. 1321-1332.

119. LARSEN, A., 1997, "Advances in Aeroelastic Analysis of Suspension and Cable-Stayed Bridges." Proceedings of 2nd European and African Conference on Wind Engineering, Genova, Italy, 22-26 June 1997, pp. 61-75.

120. LAROSE, G.L. and LIVESEY, F.M., 1997, "Performance of Streamlined Bridge Decks in Relation to the Aerodynamics of a Flat Plate." Journal of Wind Engineering and Industrial Aerodynamics, Vol. 69-71, pp. 851-860.

121. SCANLAN, R.H. and JONES, N.P., 1990, "A Minimum Design Methodology for Evaluating Bridge Flutter and Buffeting Response." Journal of Wind Engineering and Industrial Aerodynamics, Vol. 36, No. 2, pp. 1341-1353.

122. SCANLAN, R.H., 1978, "The Action of Flexible Bridges Under Wind, II : Buffeting Theory." Journal of Sound and Vibration, Vol. 60, No. 2, pp. 201-211.

123. THORBEK, L. and HANSEN, S.O., 1997, "Coupled Buffeting Response of Suspension Bridges." Proceedings of 2nd European and African Conference on Wind Engineering, Genova, Italy, 22-26 June 1997, pp. 1489-1496.

124. LARSEN, A., 1997, "Prediction of Aeroelastic Stability of Suspension Bridge During Erection." Proceedings of 9th International Symposium on Wind Engineering, 9-13 January 1995, New Delhi, India. Journal of Wind Engineering and Industrial Aerodynamics, Vol. 72, pp. 265-274.

125. KOBAYASHI, H., BIENKIEWICZ, B. and CERMAK, J.E., 1988, "Mechanism of Vortex-Excited Oscillations of a Bridge Deck." Journal of Wind Engineering and Industrial Aerodynamics, Vol. 29, pt. 2, pp. 371-378.

126. HUSTON, D.R., BOSCH, H.R. and SCANLAN, R.H., 1988, "The Effects of Fairings and of Turbulence on the Flutter Derivatives of a Notably Unstable Bridge Deck." Journal of Wind Engineering and Industrial Aerodynamics, Vol. 29, No. 1-3, pp. 339-349.

127. OWEN, J.S., VANN, A.M., DAVIES, J.P. and BLAKEBOROUGH, A., 1996, "The Prototype Testing of Kessock Bridge : Response to Vortex Shedding." Journal of Wind Engineering and Industrial Aerodynamics, Vol. 60, No. 1-3, pp. 91-108.

128. SCANLAN, R.H., 1998, "Bridge Flutter Derivatives at Vortex Lock-In." Journal of Structural Engineering, Vol. 124, No. 4, pp. 450-458.

129. NAGAO, F., UTSUNOMIYA, H., ORYU, T. and MANABE, S., 1993, "Aerodynamic Efficiency of Triangular Fairing on Box Girder Bridge." Journal of Wind Engineering and Industrial Aerodynamics, Vol 49, pp. 565-574.

130. COBO DEL ARCO, D. and BENGOECHEA, A.C.A., 1997, "Some Proposals to Improve the Wind Stability Performance of Long Span Bridges." Proceedings of 2nd European and African Conference on Wind Engineering, Genova, Italy, 22-26 June 1997, pp. 1577-1584.

131. KOBAYASHI, H. and NAGAOKA, H., 1992, "Active Control of Flutter of a Suspension Bridge." Journal of Wind Engineering and Industrial Aerodynamics, Vol. 41-44, pp. 143-151.

132. OSTENFELD, K.H. and LARSEN, A., 1992, "Bridge Engineering and Aerodynamics." Aerodynamics of Large Bridges, ed. A. Larsen, Proceedings of the 1st International Symposium, Copenhagen, Denmark, 19-21 February 1992, pp. 3-22.

133. LARSEN, A., 1993, "Aerodynamic Aspects of the Final Design of the 1624m Suspension Bridge Across the Great Belt." Journal of Wind Engineering and Industrial Aerodynamics, Vol. 48, pp. 261-285.

134. RODI, W., 1997, "Comparison of LES and RANS Calculations of the Flow around Bluff Bodies." Journal of Wind Engineering and Industrial Aerodynamics, Vol. 69-71, pp. 55-75.

135. OKAJIMA, A. and KITAJIMA, K., 1993, "Numerical Study on Aeroelastic Instability of Cylinders with a Circular and Rectangular Cross Section." Journal of Wind Engineering and Industrial Aerodynamics, Vol. 46 and 47, pp. 541-550.

136. OKAJIMA, A., UENO, H. and SAKAI, H., 1992, "Numerical Simulation of Laminar and Turbulent Flows around Rectangular Cylinders." International Journal for Numerical Methods in Fluids, Vol. 15, No. 9, pp. 999-1012.

137. OKAJIMA, A., YI, D., KOBE, M. and UENO, H., 1994, "Numerical and Experimental Studies on Fluid Dynamic Forces of an Oscillating Rectangular Prism." Proceedings of 1994 Pressure Vessels and Piping Conference, Part 4, Minneapolis, MN, USA, 19-23 Jun. 1994, ASME PVP-Vol. 273, pp. 257-264.

138. OKAJIMA, A., YI, D., SAKUDA, A. and NAKANO, T., 1997, "Numerical Study of Blockage Effects on Aerodynamic Characteristics of an Oscillating Rectangular Cylinder." Journal of Wind Engineering and Industrial Aerodynamics, Vol. 67-68, pp. 91-102. Proceedings of the 2nd International Conference on Computational Wind Engineering (CWE 96), Fort Collins, Colorado, USA, 4-8 Aug 1996.

139. DAVIS, R.W. and MOORE, E.F., 1982, "A Numerical Study of Vortex Shedding from Rectangles." Journal of Fluid Mechanics, Vol. 116, pp. 475-506.

140. FUJIWARA, A., KATAOKA, H. and ITO, M., 1993, "Numerical Simulation of Flow Field Around an Oscillating Bridge using Finite Difference Method." Journal of Wind Engineering and Industrial Aerodynamics, Vol. 46-47, pp. 567-575.

141. SOHANKAR, A., NORBERG, C. and DAVIDSON, L., 1997, "Numerical Simulation of Unsteady Low-Reynolds Number Flow around Rectangular Cylinders at Incidence." Journal of Wind Engineering and Industrial Aerodynamics, Vol. 69-71, pp. 189-201.

142. LEE, S., 1997, "Unsteady Aerodynamic Force Prediction on a Square Cylinder using k-e Turbulence Models." Journal of Wind Engineering and Industrial Aerodynamics, Vol. 67-68, pp. 79-90. Proceedings of the 2nd International Conference on Computational Wind Engineering (CWE 96), Fort Collins, Colorado, USA, 4-8 Aug 1996.

143. MURAKAMI, S., 1997, "Overview of Turbulence Models Applied in Computational Wind Engineering (CWE)-1997." Proceedings of 2nd European and African Conference on Wind Engineering, Genova, Italy, 22-26 June 1997, pp. 3-24.

144. MURAKAMI, S., MOCHIDA, A. and SAKAMOTO, S., 1997, "CFD Analysis of Wind-Structure Interaction for Oscillating Square Cylinders." Proceedings of 9th International Symposium on Wind Engineering, 9-13 January 1995, New Delhi, India. Journal of Wind Engineering and Industrial Aerodynamics, Vol. 72, pp. 33-46.

145. SAKAMOTO, S., MURAKAMI, S. and MOCHIDA, A., 1993, "Numerical Study on Flow Past 2D Square Cylinder by Large Eddy Simulation : Comparison Between 2D and 3D Computations." Journal of Wind Engineering and Industrial Aerodynamics, Vol. 50, No. 1-3, pp. 61-68.

146. SAKAMOTO, S., MURAKAMI, S., KATO, S. and MOCHIDA, A., 1993, "Unsteady Pressure Field Around Oscillating Prism Predicted by LES." Journal of Wind Engineering and Industrial Aerodynamics, Vol. 46-47, pp. 551-556.

147. TAMURA, T. and KUWAHARA, K., 1990, "Numerical Study of Aerodynamic Behaviour of a Square Cylinder." Journal of Wind Engineering and Industrial Aerodynamics, Vol. 33, No. 1-2, pp. 161-170.

148. TAMURA, T., ITOH, Y., WADA, A. and KUWAHARA, K., 1995, "Numerical Study of Pressure Fluctuations on a Rectangular Cylinder in Aerodynamic Oscillation." Journal of Wind Engineering and Industrial Aerodynamics, Vol. 54-55, pp. 239-250.

149. TAMURA, T., MIYAGI, T. and KITAGISHI, T., 1997, "Numerical Prediction of Unsteady Pressures on a Square Cylinder with Various Corner Shapes." Proceedings of 2nd European and African Conference on Wind Engineering, Genova, Italy, 22-26 June 1997, pp. 815-822.

150. DARGENT, C., GRAZZINI, F., GEORGE, J. and DARTUS, D., 1996, "Numerical Simulation of the Vortex Shedding Around a Square Cylinder." Proceedings of the 4th

International Conference on Air Pollution, Toulouse, France, 28-30 Aug. 1996, pp. 257-266.

151. KOUTMOS, P. and MAVRIDIS, C., 1997, "A Computational Investigation of Unsteady Separated Flows." International Journal of Heat and Fluid Flow, Vol. 18, No. 3, pp. 297-306.

152. MURAKAMI, S. and MOCHIDA, A., 1995, "On Turbulent Vortex Shedding Flow past 2D Square Cylinder Predicted by CFD." Journal of Wind Engineering and Industrial Aerodynamics, Vol. 54-55, pp. 191-211.

153. YU, D. and KAREEM, A., 1997, "Numerical Simulation of Flow Around Rectangular Prism." Journal of Wind Engineering and Industrial Aerodynamics, Vol. 67-68, pp. 195-208. Proceedings of the 2nd International Conference on Computational Wind Engineering (CWE 96), Fort Collins, Colorado, USA, 4-8 Aug 1996.

154. YU, D. and KAREEM, A., 1996, "Two-Dimensional Simulation of Flow around Rectangular Prisms." Journal of Wind Engineering and Industrial Aerodynamics, Vol. 62, No. 2-3, pp. 131-161.

155. PANNEER SELVAM, R., TARINI, M.J. and LARSEN, A., 1997, "Three-Dimensional Simulation of Flow Around Circular Cylinder using LES and FEM." Proceedings of 2nd European and African Conference on Wind Engineering, Genova, Italy, 22-26 June 1997, pp. 831-838.

156. TAMURA, T., OHTA, I. and KUWAHARA, K., 1990, "On the Reliability of Two-Dimensional Simulation for Unsteady Flows around a Cylinder-Type Structure." Journal of Wind Engineering and Industrial Aerodynamics, Vol. 35, No. 1-3, pp. 275-298.

157. LEE, S., LEE, J.S. and KIM, J.D., 1997, "Prediction of Vortex-Induced Wind Loading on Long-Span Bridges." Journal of Wind Engineering and Industrial Aerodynamics, Vol. 67-68, pp. 267-278. Proceedings of the 2nd International Conference on Computational Wind Engineering (CWE 96), Fort Collins, Colorado, USA, 4-8 Aug 1996.

158. KURODA, S., 1997, "Numerical Simulation of Flow Around a Box Girder of a Long Span Suspension Bridge." Journal of Wind Engineering and Industrial Aerodynamics, Vol. 67-68, pp. 239-252. Proceedings of the 2nd International Conference on Computational Wind Engineering (CWE 96), Fort Collins, Colorado, USA, 4-8 Aug 1996.

159. SARPKAYA, T., 1992, "Brief Reviews of Some Time-Dependent Flows." Journal of Fluids Engineering, Vol. 114, pp. 283-298.

160. SPALART, P.R., 1988, "Vortex Methods for Separated Flows." NASA TM 100068.

161. PUCKETT, E.G., 1993, "Vortex Methods : An Introduction and Survey of Selected Research Topics." Incompressible Computational Fluid Dynamics, ed. M.D. Gunzberger and R.A. Nicolaides, Cambridge University Press.

162. KAMEMOTO, K., 1995, "On Attractive Features of the Vortex Methods." Computational Fluid Dynamics Review -1995 pp. 334-353, ed. Hafez and Oshima, pub. J. Wiley.

163. KUWAHARA, K. and TAKAMI, H., 1973, "Numerical Studies of Two-Dimensional Vortex Motion by a System of Points." Journal of the Physical Society of Japan, Vol. 34, pp. 247-253.

164. CHORIN, A.J., 1973, "Numerical Study of Slightly Viscous Flow." Journal of Fluid Mechanics, Vol. 57, pp. 785-796.

165. SETHIAN, J.A. and GHONIEM, A.F., 1988, "Validation Study of Vortex Methods." Journal of Computational Physics, Vol. 74, pp. 283-317.

166. SMITH, P.A. and STANSBY, P.K., 1988, "Impulsively Started Flow Around a Circular Cylinder by the Vortex Method." Journal of Fluid Mechanics, Vol. 194, pp. 45-77.

167. WALTHER, J.H., 1994, "Discrete Vortex Method for Two-Dimensional Flow Past Bodies of Arbitrary Shape Undergoing Prescribed Rotary and Translational Motion." AFM-94-11, Ph.D. Thesis, Department of Fluid Mechanics, Technical University of Denmark.

168. WALTHER, J.H. and LARSEN, A., 1997, "Two Dimensional Discrete Vortex Method for Application to Bluff Body Aerodynamics." Journal of Wind Engineering and Industrial Aerodynamics, Vol. 67-68, pp. 183-193. Proceedings of the 2nd International Conference on Computational Wind Engineering (CWE 96), Fort Collins, Colorado, USA, 4-8 Aug 1996.

169. DEGOND, P. and MAS-GALLIC, S., 1989, "The Weighted Particle Method for Convection-Diffusion Equations : Part 1 the Case of an Isotropic Viscosity." Mathematics of Computation, Vol. 53, No. 188, pp. 485-507.

170. KOUMOUTSAKOS, P. and LEONARD, A., 1995, "High-Resolution Simulations of the Flow Around an Impulsively Started Cylinder using Vortex Methods." Journal of Fluid Mechanics, Vol. 296, pp. 1-38.

171. KOUMOUTSAKOS, P., LEONARD, A. and PEPIN, F., 1994, "Boundary Conditions for Viscous Vortex Methods." Journal of Computational Physics, Vol. 113, pp. 52-61.

172. CLARKE, N.R. and TUTTY, O.R., 1994, "Construction and Validation of a Discrete Vortex Method for the Two-Dimensional Incompressible Navier-Stokes Equations." Computers Fluids, Vol. 23, No. 6, pp. 751-783.

173. OGAMI, Y. and AKAMATSU, T., 1991, "Viscous Flow Simulation using the Discrete Vortex Model - The Diffusion Velocity Method." Computers and Fluids, Vol. 19, No. 3/4, pp. 433-441.

174. STRICKLAND, J.H., KEMPKA, S.N. and WOLFE, W.P., 1996, "Viscous Diffusion of Vorticity Using the Diffusion Velocity Concept." European Series in Applied and Industrial Aerodynamics : Proceedings Vol. 1 - Vortex Flows and Related Numerical Methods.

175. MILANE, R.E. and NOURAZAR, S., 1995, "On the Turbulent Diffusion Velocity in Mixing Layer Simulated Using the Vortex Method and the Subgrid Scale Vorticity Model." Mechanics Research Communications, Vol. 22, No. 4, pp. 327-333.

176. BEALE, J.T. and MAJDA, A., 1982, "Vortex Methods I : Convergence in Three Dimensions." Mathematics of Computation, Vol. 39, No. 159, pp. 1-27.

177. BEALE, J.T. and MAJDA, A., 1982, "Vortex Methods II : Higher Order Accuracy in Two and Three Dimensions." Mathematics of Computation, Vol. 39, No. 159, pp. 29-52.

178. ROBERTS, S., 1985, "Accuracy of the Random Vortex Method for a Problem with Non-Smooth Initial Conditions." Journal of Computational Physics, Vol. 58, pp. 29-43.

179. SETHIAN, J.A., 1987, "On Measuring the Accuracy of the Vortex Method : Using a Random Method to Model Stable and Unstable Flow." Lecture Notes in Mathematics 1360 - Vortex Methods, (ed. C. Anderson and C. Greengard), pp. 83-95.

180. GREENGARD, C., 1985, "The Core Spreading Vortex Method Approximates the Wrong Equation." Journal of Computational Physics, Vol. 61, pp. 345-348.

181. COTTET, G.H., and MAS-GALLIC, S., 1990, "A Particle Method to Solve the Navier-Stokes System." Numerical Mathematics, Vol. 57, pp. 805-827.

182. SPALART, P.R., LEONARD, A. and BAGANOFF, D., 1983, "Numerical Simulation of Separated Flows." NASA TM 84328.

183. ANDERSON, C.R., 1986, "A Method of Local Corrections for Computing the Velocity Field Due to a Distribution of Vortex Blobs." Journal of Computational Physics, Vol. 62, pp. 111-123.

184. BADEN, S.B, 1987, "Very Large Vortex Calculations in Two Dimensions." Lecture Notes in Mathematics 1360 - Vortex Methods, (ed. C. Anderson and C. Greengard), pp. 96-120

185. GREENGARD, L. and ROKHLIN, V., 1987, "A Fast Algorithm for Particle Simulations." Journal of Computational Physics, Vol. 73, pp. 325-348.

186. GREENGARD, L. and GROPP, W.D., 1990, "A Parallel Version of the Fast Multipole Method." Computers Math. Applic., Vol. 20, No. 7, pp. 63-71.

187. CARRIER, J., GREENGARD, L. and ROKHLIN, V., 1988, "A Fast Adaptive Multipole Algorithm for Particle Simulations." SIAM Jl Sci. Stat Comput, Vol. 9, pp. 669-686.

188. VAN DOMMELEN, L. and RUNDENSTEINER, E.A., 1989, "Fast, Adaptive Summation of Point Forces in the Two-Dimensional Poisson Equation." Journal of Computational Physics, Vol. 83, pp. 126-147.

189. TAYLOR, I.J. and VEZZA, M., 1997, "Application of a Zonal Decomposition Algorithm, to Improve the Computational Operation Count of the Discrete Vortex Method Calculation." Dept. of Aerospace Engineering, University of Glasgow, G.U. Aero Report No. 9711, Glasgow, Scotland, UK.

190. BADEN, S.B. and PUCKETT, E.G., 1990, "A Fast Vortex Method for Computing 2D Viscous Flow." Journal of Computational Physics, Vol. 91, pp. 278-297.

191. DRAGHICESCU, C.I. and DRAGHICESCU, M., 1995, "A Fast Algorithm for Vortex Blob Interactions." Journal of Computational Physics, Vol. 116, pp. 69-78.

192. ALURU, S., 1996, "Greengard's N-Body Algorithm is not Order N." SIAM Journal of Scientific Computing, Vol. 17, No. 3, pp. 773-776.

193. PRINGLE, G.J., 1994, "Numerical Study of Three Dimensional Flow using Fast Parallel Particle Algorithms." PhD. Thesis, Department of Mathematics, Napier University, Edinburgh.

194. SETHIAN, J.A., BRUNET, J.-P., GREENBERG, A. and MESIROV, J.P., 1992, "Two-Dimensional, Viscous, Incompressible Flow in Complex Geometries on a Massively Parallel Processor." Journal of Computational Physics, Vol. 101, pp. 185-206.

195. BLEVINS, R.D., 1989, "Application of the Discrete Vortex Method to Fluid-Structure Interaction." Proceedings of Flow Induced Vibration, 1989 ASME Pressure Vessels and Piping Conference, Honolulu, HI, USA, 23-27 July, 1989, pub. ASME, Pressure Vessels and Piping Division. Vol. 154, pp. 131-140.

196. LARSEN, A. and WALTHER, J.H., 1997, "Aeroelastic Analysis of Bridge Girder Sections Based on Discrete Vortex Simulations." Journal of Wind Engineering and Industrial Aerodynamics, Vol. 67-68, pp. 253-265. Proceedings of the 2nd International Conference on Computational Wind Engineering (CWE 96), Fort Collins, Colorado, USA, 4-8 Aug 1996.

197. KAWAI, H., 1993, "Vortex Induced Vibration of Circular Cylinder." Journal of Wind Engineering and Industrial Aerodynamics, Vol. 46-47, pp. 605-610.

198. LEONARD, A. and KOUMOUTSAKOS, P., 1993, "High Resolution Vortex Simulation of Bluff Body Flows." Journal of Wind Engineering and Industrial Aerodynamics, Vol. 46-47, pp. 315-325.

199. SHIELS, D., LEONARD, A. and STAGG, A., 1996, "Computational Investigation of Drag Reduction on a Rotationally Oscillating Cylinder." European Series in Applied and Industrial Aerodynamics : Proceedings Vol. 1 - Vortex Flows and Related Numerical Methods.

200. BERGSTROM, D.J. and WANG, J., 1995, "Simulation of Flow Over a Square Cylinder Using the Discrete Vortex Method." Proceedings of the 1995 ASME/JSME Fluids Engineering and Laser Anemometry Conference and Exhibition, Hilton Head, SC, USA, 13-18 August 1995, pub. ASME Fluids Engineering Division, Vol. 216, pp. 109-114.

201. BERGSTROM, D.J. and WANG, J., 1997, "Discrete Vortex Method of Flow Over a Square Cylinder." Journal of Wind Engineering and Industrial Aerodynamics, Vol. 67-68, pp. 37-49. Proceedings of the 2nd International Conference on Computational Wind Engineering (CWE 96), Fort Collins, Colorado, USA, 4-8 Aug 1996.

202. BIENKIEWICZ, B. and KUTZ, R.F., 1990, "Applying the Discrete Vortex Method to Flow about Bluff Bodies." Journal of Wind Engineering and Industrial Aerodynamics, Vol. 36, pp. 1011-1020.

203. BIENKIEWICZ, B. and KUTZ, R.F., 1993, "Aerodynamic Loading and Flow Past Bluff Bodies using Discrete Vortex Method." Journal of Wind Engineering and Industrial Aerodynamics, Vol. 46-47, pp. 619-628.

204. CHUA, K., LISOSKI, D., LEONARD, A. and ROSHKO, A., 1990, "A Numerical and Experimental Investigation of Separated Flow Past an Oscillating Flat Plate." International Symposium on Non Steady Fluid Dynamics, Fluids Engineering Division, ASME, Vol. 92, pp. 455-464.

205. INAMURO, T., ADACHI, T. and SAKATA, H., 1993, "Simulation of Aerodynamic Instability of Bluff Body." Journal of Wind Engineering and Industrial Aerodynamics, Vol. 46-47, pp. 611-618.

206. SHIRATO, H. and MATSUMOTO, M., 1997, "Unsteady Pressure Evaluation on Oscillating Bluff Body by Vortex Method." Journal of Wind Engineering and Industrial Aerodynamics, Vol. 67-68, pp. 349-359. Proceedings of the 2nd International Conference on Computational Wind Engineering (CWE 96), Fort Collins, Colorado, USA, 4-8 Aug 1996.

207. SHIRATO, H., MATSUMOTO, M. and SHIRAISHI, N., 1993, "Unsteady Aerodynamic Force Characteristics on 2-D Oscillating Bluff Body." Journal of Wind Engineering and Industrial Aerodynamics, Vol. 46-47, pp. 629-637.

208. LARSEN, A. and WALTHER, J.H., 1997, "Discrete Vortex Simulations of Flow Around Five Generic Bridge Deck Sections." Paper presented at the 8th US National Conference on Wind Engineering, John Hopkins University, Baltimore, Maryland, USA, 5-7 June 1997.

209. VEZZA, M., 1992, "A New Vortex Method for Modelling Two-Dimensional, Unsteady Incompressible, Viscous Flows." Dept. of Aerospace Engineering, University of Glasgow, G.U. Aero Report No. 9245, Glasgow, Scotland, UK.

210. LIN, H and VEZZA M, 1994 "Implementation of a Vortex Method for the Prediction of Separated Incompressible Flows." Dept. of Aerospace Engineering, University of Glasgow, G.U. Aero Report No. 9425, Glasgow, Scotland, UK.

211. TAYLOR, I.J., 1996, "Development and Validation of a Discrete Vortex Method for the Prediction of Separated Incompressible Flows Around Bluff Bodies." Dept. of Aerospace Engineering, University of Glasgow, G.U. Aero Report No. 9622, Glasgow, Scotland, UK.

212. EDWARDS, H.M., 1995, "Linear Algebra." pub. Birkhauser, Boston.

213. STANSBY, P.K., 1985, "A Generalized Discrete-Vortex Method for Sharp-Edged Cylinders." AIAA Journal, Vol. 23, No. 6, pp. 856-861.

214. SARPKAYA, T. and SCHOAFF, R.L., 1979, "Inviscid Model of Two-Dimensional Vortex Shedding by a Circular Cylinder." AIAA Journal, Vol. 17, No. 11, pp. 1193-1200.

215. BASUKI, J. and GRAHAM, J.M.R., 1987, "Discrete Vortex Computation of Separated Airfoil Flow." AIAA Journal, Vol. 25, No. 11, pp. 1409-1410.

216. KIYA, M., SASAKI, K. and ARIE, M., 1982, "Discrete-Vortex Simulation of a Turbulent Separation Bubble." Journal of Fluid Mechanics, Vol. 120, pp. 219-244.

217. ESDU, 1971, "Fluid Forces, Pressures and Moments on Rectangular Blocks." Engineering Sciences Data Item Number 71016.

218. NAUDASCHER, E., WESKE, J.R. and FEY, B., 1981, "Exploratory Study on Damping of Galloping Vibrations." Journal of Wind Engineering and Industrial Aerodynamics, Vol. 8, pp. 211-222.

219. IGARASHI, T., 1984, "Characteristics of the Flow Around a Square Prism." Bulletin of the JSME, Vol. 27, No. 231, pp. 1858-1865.

220. NAKAMURA, Y. and MIZOTA, T., 1975, "Torsional Flutter of Rectangular Prisms." Journal of the Engineering Mechanics Division, ASCE, Vol. 101, pp. 125-142.

221. HASAN, M.A.Z., 1989, "The Near Wake Structure of a Square Cylinder." International Journal of Heat and Fluid Flow, Vol. 10. No. 4, pp. 339-348.

222. DENG, G.B., PIQUET, J., QUEUTEY, P. and VISONNEAU, M., 1994, "2-D Computations of Unsteady Flow past a Square Cylinder with Baldwin-Lomax Model." Journal of Fluids and Structures, Vol. 8, pp. 663-680.

223. TOLSTRUP, C., 1992, "The Fixed Link Across the Great Belt." Aerodynamics of Large Bridges, ed. A. Larsen, Proceedings of the 1st International Symposium, Copenhagen, Denmark, 19-21 February 1992, pp. 249-254.

224. LARSEN, A. and GIMSENG, N.J., 1992, "Wind Engineering Aspects of the East Bridge Tender Project." Journal of Wind Engineering and Industrial Aerodynamics, Vol. 41-44, pp. 1405-1416.

225. REINHOLD, T.A., BRINCH, M. and DAMSGAARD, A., 1992, "Wind Tunnel Tests for the Great Belt Link." Aerodynamics of Large Bridges, ed. A. Larsen, Proceedings of the 1st International Symposium, Copenhagen, Denmark, 19-21 February 1992, pp. 255-267.

226. LARSEN, A. and JACOBSEN, A.S., 1992, "Aerodynamic Design of the Great Belt East Bridge." Aerodynamics of Large Bridges, ed. A. Larsen, Proceedings of the 1st International Symposium, Copenhagen, Denmark, 19-21 February 1992, pp. 269-283.

227 COURCHESNE, J. and LANEVILLE, A., 1979, "A Comparison of Correction Methods Used in the Evaluation of Drag Coefficient Measurements for Two-Dimensional Rectangular Cylinders." Journal of Fluids Engineering, Vol. 101, pp. 506-510.

228 COTTET, G-H., 1996, "Artificial Viscosity Models for Vortex and Particle Methods." Journal of Computational Physics, Vol. 127, pp. 299-308.

APPENDIX A

DERIVATION OF SERIES EXPANSION FOR ZONAL DECOMPOSITION.

Consider a zone D, containing N_p point vortices, with strengths/circulation Γ_k, at positions given by the complex co-ordinates $z_k = x_k + iy_k$, $k = 1, 2 \ldots N_p$. The velocity $\mathbf{U}(z)$ induced by the particles contained in D, at an arbitrary point, $z = x + iy$, outside zone D, is obtained from the Biot-Savart law using,

$$\mathbf{U}(z) = \frac{i}{2\pi} \sum_{k=1}^{Np} \frac{(z - z_k)\Gamma_k}{|z - z_k|^2}$$

Now $\mathbf{U}(z) = u + iv$, where

$$u = -\frac{1}{2\pi} \sum_{k=1}^{Np} \frac{(y - y_k)\Gamma_k}{|z - z_k|^2} \quad , \quad v = \frac{1}{2\pi} \sum_{k=1}^{Np} \frac{(x - x_k)\Gamma_k}{|z - z_k|^2} \tag{A.1}$$

Taking the conjugate of the velocity and substituting from (A.1), we can write

$$\mathbf{U}^*(z) = u - iv$$

$$= -\frac{1}{2\pi} \sum_{k=1}^{Np} \frac{\Gamma_k}{|z - z_k|^2} \left[(y - y_k) + i(x - x_k) \right]$$

$$= -\frac{1}{2\pi i} \sum_{k=1}^{Np} \frac{\Gamma_k}{|z - z_k|^2} \left[i(y - y_k) - (x - x_k) \right]$$

$$\Rightarrow \mathbf{U}^*(z) = \frac{1}{2\pi i} \sum_{k=1}^{Np} \frac{\Gamma_k}{|z - z_k|^2} (z - z_k)^* \tag{A.2}$$

Using $|z|^2 = z.z^*$ for any complex z, then (A.2) can be rewritten

$$\mathbf{U}^*(z) = \frac{1}{2\pi i} \sum_{k=1}^{Np} \frac{\Gamma_k}{(z - z_k)} \tag{A.3}$$

Taking some arbitrary point, Z_m, within D (centre of D say), rewrite the positions of all the vortex particles in D relative to Z_m.

i.e. $\quad z_k{}' = z_k - Z_m$

then substituting in (A.3)

$$\Rightarrow \mathbf{U}^*(z) = \frac{1}{2\pi i} \sum_{k=1}^{Np} \frac{\Gamma_k}{(z - z_k{}' - Z_m)}$$

$$= \frac{1}{2\pi i} \sum_{k=1}^{Np} \frac{\Gamma_k}{(z - Z_m)} \left(1 - \frac{z_k{}'}{(z - Z_m)}\right)^{-1} \tag{A.4}$$

(†) Provided $z_k{}' < (z - Z_m)$ for all k, then (A.4) can be expanded as a power series of the form

$$(1 - x)^{-1} = 1 + x + x^2 + x^3 + \ldots + x^n + \ldots$$

Hence,

$$\mathbf{U}^*(z) = \frac{1}{2\pi i} \sum_{k=1}^{Np} \frac{\Gamma_k}{(z - Z_m)} \left[1 + \frac{z_k{}'}{(z - Z_m)} + \left(\frac{z_k{}'}{(z - Z_m)}\right)^2 + \ldots + \left(\frac{z_k{}'}{(z - Z_m)}\right)^{Nt} + R_{Nt}\right]$$

$$= \frac{1}{2\pi i (z - Z_m)} \left[\sum_{k=1}^{Np} \Gamma_k + \frac{1}{(z - Z_m)} \sum_{k=1}^{Np} \Gamma_k z_k{}' + \frac{1}{(z - Z_m)^2} \sum_{k=1}^{Np} \Gamma_k (z_k{}')^2 + \ldots \right.$$
$$\left. \ldots + \frac{1}{(z - Z_m)^{Nt}} \sum_{k=1}^{Np} \Gamma_k (z_k{}')^{Nt} + R_{Nt}\right]$$

$$\Rightarrow \mathbf{U}^*(z) = \frac{1}{2\pi i (z - Z_m)} \sum_{j=1}^{Nt} \frac{a_j}{(z - Z_m)^{j-1}} + R_{Nt}$$
$$\text{where} \quad a_j = \sum_{k=1}^{Np} \Gamma_k (z_k - Z_m)^{j-1} \tag{A.5}$$

and R_{Nt} is the error due to truncation of the infinite geometric series after N_t terms. The above shows the derivation of the series coefficients and the zonal expansion formula, with (A.5) being equivalent to equations (3.33) and (3.34). Zonal decomposition is only used if a zone is sufficiently far from the point at which the velocity is being calculated. This ensures that the condition (†) for the series expansion is satisfied.

APPENDIX B

OPERATION COUNT OF ZONAL DECOMPOSITION ALGORITHM.

The analysis of the operation count of the zonal decomposition algorithm is very complex. Hence, to simplify the analysis, the case of N vortices homogeneously distributed over a square domain will be considered. The flow domain is continuously subdivided (as shown in Fig. B.1) until the lowest level is comprised of zones that contain n particles. The number of zones at the lowest level is given by N/n. The number of zones at any level of subdivision, l, for a uniform distribution of vortices and uniform subdivisions, is given by 4^l. Therefore the number of levels of subdivision is given by

$$l = \log_4\left(\frac{N}{n}\right) \tag{B.1}$$

The total computational time required for one time step in the calculation is dominated by the velocity calculation. The dominant two factors in the velocity calculation for a domain containing N particles are the contributions from direct summation and zonal decomposition. Only the operation count of these two factors will be considered to simplify the analysis further.

Consider the contribution first from direct summation. For any single vortex, the contribution from direct summation will be due to, at most, the 9 neighbouring zones (including the zone that contains the particle). As each zone contains n particles and there are N particles, the total CPU required for the direct summation contribution is t_{ds}, where

$$t_{ds} \propto 9nN$$
$$\text{i.e} \quad t_{ds} = aN \tag{B.2}$$

where a is a constant that is derived from the number of zones contributing to the direct summation, the number of particles in each zone and the floating point operation speed of the processor.

For the contribution from series expansion due to the influence of distant zones, the analysis is more complex. Consider the worst case, where a series expansion is required to be evaluated at every zone at the lowest level, except the 9 neighbouring zones, i.e.$(N/n-9)$ zones. To evaluate the series expansion at the lowest level, each level and each branch of the quadtree must be evaluated. The number of operations to perform this calculation will be proportional to the number of levels, l as shown in (B.1). These are the main factors affecting the operation count

of the zonal contribution to the velocity. Hence, the CPU required to evaluate the influence of distant zones on a single vortex using series expansion, t_{zd}, is approximately given by

$$t_{zd} \propto Nt\left(\frac{N}{n} - 9\right).cl \tag{B.3}$$

where c is a constant that is derived from the number of "traverses" around the quadtree. (B.3) gives the worst case, where the series expansion is used for every zone at the lowest level, except the neighbours. In general, only p zones will be required, where $p<(N/n-9)$. The total CPU required for the zonal contribution is then given by

$$t_{zd} \propto N.Nt.p.c\log_4\left(\frac{N}{n}\right)$$

$$t_{zd} \propto N.Nt.p.c\frac{\log\left(\frac{N}{n}\right)}{\log(4)} \quad , \quad \text{using} \quad \log_4(a) = \frac{\log(a)}{\log(4)} \tag{B.4}$$

$$t_{zd} = Nb\log N \tag{B.5}$$

where b is a constant that is derived from the number of zones whose series expansion is used, the number of terms in the series expansion and the floating point operation speed of the processor. Note that the dominant factor in the logarithm in (B.4) is the number of particles N, therefore t_{zd} can be approximated using an operation count $O(N\log N)$.

Although this is a very simplified analysis of the zonal decomposition algorithm, it is clear that the total CPU required for the velocity calculation is approximately given by

$$t_{tot} = aN + bN\log N \tag{B.6}$$

giving an algorithm that is of $O(N+N\log N)$. A curve of the form shown in (B.6), has been fitted to the CPU timings from the zonal decomposition algorithm, and is shown in Fig. 3.27, along with the derived constants. The curve is shown to give a reasonable fit to the data, giving some validation to the somewhat simplified analysis discussed above.

APPENDIX C

OPTIMISATION OF PARAMETERS IN THE ZONAL DECOMPOSITION ALGORITHM.

The main parameters that affect the speed and accuracy of the algorithm are :

1. Np - Minimum number of vortices in a zone, such that the zone can be further subdivided.

2. Nt - Number of terms in series expansion.

3. H - Series expansion can be used only when the distance of the vortex from the zone centre is greater than H multiplied by the zones radius.

These parameters have been optimised to obtain the best combination of calculation efficiency and accuracy. The results of this analysis are shown in Figs. C.1-C.3. The results are very much as expected. Increasing H means that only distant zones can be used in the calculation, leading to a larger contribution to the velocity via direct summation and hence an increase in the CPU. However, as the zones used are distant, the series is more likely to converge giving a reduction in the error as H increases (Fig. C.1).

The CPU also increases as Nt increases, as more calculations are clearly required to evaluate more terms in the series expansion (Fig. C.2). As Nt increases, the series is more likely to converge and so the error is reduced. The series is also likely to converge much more quickly if the vortex is further from the zone, and this observation can be used to obtain extra efficiency in the calculation [193]. For example, if a vortex is 4 times the zone radius from the zone centre, the series may converge in around 10 terms say, whereas a vortex that is only 3 times the zone radius from the zone centre, may require 15 terms. As a result, the algorithm uses a varying number of terms in the series expansion, depending on the distance of the vortex from the zone centre.

The variation of CPU and error with Np is a little more complex. If Np is small, there are a large number of small zones, each containing a relatively small number of vortices. Each velocity calculation will therefore require a contribution from a large number of zones, with the series expansion giving a small saving in operation count over direct summation as each zone contains a small number of particles. Hence, for small Np, the CPU will be high. Also, the small zones mean that vortices will satisfy the distance from zone centre criteria, but will still be a small distance from the zone, and may affect the series convergence leading to an increase in the error. For large Np, although when a zone is used in the velocity calculation a large saving in operation count is made, each vortex will have to be further from the zone before the zonal contribution

can be used. Hence, there is likely to be a larger contribution from direct summation and a resulting increase in CPU. However, this does mean that when series expansion is used, the series is more likely to be converged, and so the error is reduced. These effects can be observed in Fig. C.3.

The optimised code requires a balance to be struck between all of these parameters to obtain maximum efficiency for the desired calculation accuracy. The final optimised parameters are:

$Np = 200$

$H = 2.0$

Nt : Varying from 8 to 13 depending on the distance to the zone centre.

These parameters were used in all the calculation results that are presented herein.

APPENDIX D

SOLUTION OF UNDER-DETERMINED SYSTEM OF LINEAR EQUATIONS USING A PSEUDO-INVERSE METHOD.

The vorticity distribution on the body surface is assumed to be continuous, with the γ distribution at the body nodes being used to define the vortex strengths on the panels either side of the node. However, the new sharp corner model uses a dual γ value at the corner node so that a discontinuity can be introduced to the vorticity distribution. Hence the vortex strengths on the panels adjacent to the corner may be calculated from different γ values. This is discussed in more detail in Chapter 3.

Where there is only one γ value for each node and the surface vorticity distribution is assumed to be continuous, then the linear system of equations is (D.1)

$$A\gamma = F \tag{D.1}$$

where $\mathbf{A}$ is an $N \times N$ matrix containing the coefficients of the unknown γ values, which are stored in the $N \times 1$ matrix, γ, where N is the number of nodes on the body surface. $\mathbf{F}$ is the influence matrix containing the contributions to the nascent vorticity from the body motion and wake vorticity. When the vorticity discontinuities are introduced, (D.1) becomes an under-determined system of equations, with more unknowns than equations. In this case, $\mathbf{A}$ is now an $N \times (N+n)$ matrix, and γ is an $(N+n) \times 1$ matrix. Hence a new solution procedure is required to determine the unknown γ values from the linear system of equations. Such a procedure can be found by utilising the mate of matrix $\mathbf{A}$ and is presented below.

For a matrix $\mathbf{A}$, of size $N \times M$, an $M \times N$ matrix $\mathbf{B}$ can be defined such that $\mathbf{B}$ will be called the **mate** of $\mathbf{A}$ if the following four conditions are satisfied [212].

      1) $\mathbf{ABA} = \mathbf{A}$
      2) $\mathbf{BAB} = \mathbf{B}$
      3) $(\mathbf{AB})^T = \mathbf{AB}$
      4) $(\mathbf{BA})^T = \mathbf{BA}$

Also, it should be noted that $\mathbf{B}$ is unique, and that if $\mathbf{B}$ is the mate of $\mathbf{A}$, then $\mathbf{A}$ is also the mate of $\mathbf{B}$. The mate is often called the "pseudo-inverse", the "generalised inverse" or the "Moore-Penrose inverse".

From condition 1) above,

$$\mathbf{ABA} = \mathbf{A}$$
$$\mathbf{ABAA^T} = \mathbf{AA^T}$$
$$\mathbf{AB} = \mathbf{AA^T(AA^T)^{-1}} \quad (=\mathbf{I}) \tag{D.2}$$
$$\mathbf{B} = \mathbf{A^T(AA^T)^{-1}} \tag{D.3}$$

Hence the mate of $\mathbf{A}$ can be found from (D.3). It should also be noted that the mate $\mathbf{B}$ is analogous to the inverse of $\mathbf{A}$ for any matrix $\mathbf{A}$, even if the matrix is not square and has no defined inverse. This can be seen in (D.2) where the product of $\mathbf{A}$ and its mate $\mathbf{B}$ is equal to the identity matrix $\mathbf{I}$. Note that the matrix $\mathbf{AA^T}$ is of Rank N and therefore the inverse exists for the case when $N<M$.

Using the principle of the matrix mate, and taking $M=N+n$, so that $N<M$, a solution to the under-determined system of equations defined in (D.1) may be found as follows. Transforming γ so that

$$\gamma = \mathbf{B}\phi \quad \text{where } \mathbf{B} \text{ is } M \times N, \text{ and } \phi \text{ is } N \times 1.$$

then from (D.1),

$$\mathbf{AB}\phi = \mathbf{F}$$

using (D.3)

$$\mathbf{AA^T(AA^T)^{-1}}\phi = \mathbf{F}$$

so that

$$\phi = \mathbf{F}$$

Hence,

$$\gamma = \mathbf{B}\phi = \mathbf{BF}$$

and the unknown γ can be found from

$$\gamma = \mathbf{A^T(AA^T)^{-1}F} \tag{D.4}$$

Note that

$$\mathbf{A}\gamma = \mathbf{AA^T(AA^T)^{-1}F} = \mathbf{F}$$

as required. It should be noted that the resultant γ distribution is not unique but it is consistent in time. It can also be shown that it gives a unique best approximate solution to the system of equations and also gives the minimum norm solution [212].

APPENDIX E

VORTEX MERGING CALCULATION TO ENSURE CONSISTENT WAKE DECAY PROCESS.

In the vortex merging scheme, the position of the merged vortex is derived from the position and circulation of the two vortices being merged, with the circulation of the merged vortex being the sum of the circulation. However, the process is complicated by the inclusion of the wake decay model within the vortex method. As part of the merging process, the newly merged vortex must decay at a rate that is consistent with the two vortices being merged. To continue the decay process consistently the age and initial circulation of the merged vortex needs to be carefully calculated, accounting for the fact that the two vortices being merged are often decaying at different rates due to their different creation times. Two approaches may be used to maintain the consistency in the vorticity decay process :

1) The circulation of the vortices as well as the rate of decay of circulation should be preserved.

2) The drop in the circulation of each particle from their initial values should be maintained.

The first approach is likely to introduce less error into the calculations but leads to a more complicated procedure to obtain the creation time of the vortex. Whereas the second approach is slightly less accurate, it is much easier to implement within the vortex method. The method for obtaining the initial circulation $\Gamma(0)$ and the creation time, t_c, defined as the time at which the particle is shed from the body into the wake, of the merged vortex using both procedures is discussed below.

The circulation of a vortex particle is decayed using (E.1) as discussed in Chapter 3.

$$\Gamma(t) = \Gamma(0)\left[1 - \exp\left(\frac{-\beta}{t - t_c}\right)\right] \tag{E.1}$$

The age of the vortex can be defined as Δt_c where

$$\Delta t_c = t - t_c \tag{E.2}$$

Procedure 1)

To maintain the circulation and the rate of decay of circulation of the two particles being merged, the conditions (E.3) and (E.4) respectively must hold for the merged particle.

$$\Gamma_M(t) = \Gamma_1(t) + \Gamma_2(t) \tag{E.3}$$

$$\frac{d\Gamma_M(t)}{dt} = \frac{d\Gamma_1(t)}{dt} + \frac{d\Gamma_2(t)}{dt} \tag{E.4}$$

where the subscript M refers to the merged particle and the subscripts 1 and 2 refer to the two particles that are to be merged.

Using (E.1) in (E.3) and (E.4), then

$$\Gamma_M(0)\left[1 - \exp\left(\frac{-\beta}{\Delta t_{cM}}\right)\right] = \Gamma_1(0)\left[1 - \exp\left(\frac{-\beta}{\Delta t_{c1}}\right)\right] + \Gamma_2(0)\left[1 - \exp\left(\frac{-\beta}{\Delta t_{c2}}\right)\right] \tag{E.5}$$

$$-\Gamma_M(0)\frac{\beta}{\Delta t_{cM}^2}\exp\left(\frac{-\beta}{\Delta t_{cM}}\right) = -\Gamma_1(0)\frac{\beta}{\Delta t_{c1}^2}\exp\left(\frac{-\beta}{\Delta t_{c1}}\right) - \Gamma_2(0)\frac{\beta}{\Delta t_{c2}^2}\exp\left(\frac{-\beta}{\Delta t_{c2}}\right) \tag{E.6}$$

Substituting for $\Gamma_M(0)$ from (E.6) in (E.5), then

$$\Delta t_{cM}^2 \exp\left(\frac{\beta}{\Delta t_{cM}}\right)\left[1 - \exp\left(\frac{-\beta}{\Delta t_{cM}}\right)\right] = \frac{\Gamma_1(0)\left[1 - \exp\left(\frac{-\beta}{\Delta t_{c1}}\right)\right] + \Gamma_2(0)\left[1 - \exp\left(\frac{-\beta}{\Delta t_{c2}}\right)\right]}{\dfrac{\Gamma_1(0)\exp\left(\dfrac{-\beta}{\Delta t_{c1}}\right)}{\Delta t_{c1}^2} + \dfrac{\Gamma_2(0)\exp\left(\dfrac{-\beta}{\Delta t_{c2}}\right)}{\Delta t_{c2}^2}} = C$$

$$\Delta t_{cM}^2\left[\exp\left(\frac{\beta}{\Delta t_{cM}}\right) - 1\right] = C \tag{E.7}$$

To find the age of the merged vortex, (E.7) needs to be solved using some iterative scheme. Once Δt_{cM} and hence t_{cM} are found, then the initial circulation can be found from (E.1). However, with large numbers of vortex particles in the wake and a large number of potential merging calculations, the necessity for an iterative scheme for each merged vortex particle would be computationally expensive. For this reason, a simpler procedure has been implemented to define the creation time and initial circulation of the merged vortex.

Procedure 2)

A simpler scheme is to preserve the circulation and also the drop in circulation of the two vortices. The conditions (E.8) and (E.9) are the necessary conditions for the merged particle.

$$\Gamma_M(t) = \Gamma_1(t) + \Gamma_2(t) \tag{E.8}$$

$$\Delta\Gamma_M = \Delta\Gamma_1 + \Delta\Gamma_2 \qquad\qquad (E.9)$$

where

$$\Delta\Gamma_i = \Gamma_i(0) - \Gamma_i(t) \qquad\qquad (E.10)$$

The problem again is to find $\Gamma_M(0)$ and t_{cM}. Using (E.1) and (E.10),

$$\Delta\Gamma_i = \Gamma_i(0) - \Gamma_i(0)\left[1 - \exp\left(\frac{-\beta}{\Delta t_{ci}}\right)\right]$$

$$\Delta\Gamma_i = \Gamma_i(0)\exp\left(\frac{-\beta}{\Delta t_{ci}}\right) \qquad\qquad (E.11)$$

Using (E.11) in (E.9)

$$\Gamma_M(0)\exp\left(\frac{-\beta}{\Delta t_{cM}}\right) = \Gamma_1(0)\exp\left(\frac{-\beta}{\Delta t_{c1}}\right) + \Gamma_2(0)\exp\left(\frac{-\beta}{\Delta t_{c2}}\right) \qquad (E.12)$$

Substituting for $\Gamma_M(0)$ from (E.12) in (E.8) and using the vorticity decay function from (E.1), we have

$$\exp\left(\frac{\beta}{\Delta t_{cM}}\right)\left[\Gamma_1(0)\exp\left(\frac{-\beta}{\Delta t_{c1}}\right) + \Gamma_2(0)\exp\left(\frac{-\beta}{\Delta t_{c2}}\right)\right]\left[1 - \exp\left(\frac{-\beta}{\Delta t_{cM}}\right)\right] = \Gamma_1(t) + \Gamma_2(t)$$

$$\qquad\qquad (E.13)$$

from (E.11)

$$\left(\Delta\Gamma_1 + \Delta\Gamma_2\right)\left[\exp\left(\frac{\beta}{\Delta t_{cM}}\right) - 1\right] = \Gamma_1(t) + \Gamma_2(t)$$

$$\exp\left(\frac{\beta}{\Delta t_{cM}}\right) = \frac{\Delta\Gamma_1 + \Delta\Gamma_2 + \Gamma_1(t) + \Gamma_2(t)}{\Delta\Gamma_1 + \Delta\Gamma_2}$$

and using (E.10)

$$\Delta t_{cM} = \frac{\beta}{\ln\left(\dfrac{\Gamma_1(0) + \Gamma_2(0)}{\Delta\Gamma_1 + \Delta\Gamma_2}\right)} \qquad\qquad (E.14)$$

where Δt_{cM} gives the age of the merged vortex, so that the creation time can be determined using (E.2). The initial circulation of the merged vortex can be found using Δt_{cM} and (E.1), however from combining (E.1) and (E.8)

$$\Gamma_{M}(0)\left[1-\exp\left(\frac{-\beta}{\Delta t_{cM}}\right)\right]=\Gamma_{1}(t)+\Gamma_{2}(t) \tag{E.15}$$

and using (E.14)

$$1-\exp\left(\frac{-\beta}{\Delta t_{cM}}\right)=1-\left(\frac{\Delta\Gamma_{1}+\Delta\Gamma_{2}}{\Gamma_{1}(0)+\Gamma_{2}(0)}\right) \tag{E.16}$$

Substituting from (E.16) in (E.15)

$$\Gamma_{M}(0)\left[\frac{\Gamma_{1}(0)+\Gamma_{2}(0)-\Delta\Gamma_{1}-\Delta\Gamma_{2}}{\Gamma_{1}(0)+\Gamma_{2}(0)}\right]=\Gamma_{1}(t)+\Gamma_{2}(t)$$

and using (E.10), it can be shown that

$$\Gamma_{M}(0)=\Gamma_{1}(0)+\Gamma_{2}(0) \tag{E.17}$$

Hence, using (E.14) and (E.17), the creation time, t_{cM}, and the initial circulation, $\Gamma_{M}(0)$, of the merged vortex can be found, such that the total circulation and the drop in circulation of the two original particles is maintained. This procedure is relatively straightforward to implement within the existing merging scheme and does not lead to a significant increase the computational operation count. Although the procedure is slightly less accurate than the first procedure in giving a consistent decay cycle, it should be noted that when the ages of the two merged vortex particles are similar, the rate of decay of the circulation will also be approximately preserved.

APPENDIX F

EXTRACTION OF FLUTTER DERIVATIVES AND CALCULATION OF CRITICAL FLUTTER VELOCITY.

F.1   Extraction of Flutter Derivatives.

As discussed in Chapter 2, for small amplitude oscillations, the unsteady lift and moment coefficients may be treated as linear in the structural transverse and torsional displacements and their first derivatives. In wind engineering, the commonly used expression for the linearised form of the lift and moment coefficients, developed by Scanlan and co-workers [2-3] is given in (F.1).

$$L_h = \tfrac{1}{2}\rho U^2 (2B)\left[KH_1^*(K)\frac{\dot{h}}{U} + KH_2^*(K)\frac{B\dot{\alpha}}{U} + K^2 H_3^*(K)\alpha + K^2 H_4^*(K)\frac{h}{B}\right]$$

$$M_\alpha = \tfrac{1}{2}\rho U^2 (2B)^2\left[KA_1^*(K)\frac{\dot{h}}{U} + KA_2^*(K)\frac{B\dot{\alpha}}{U} + K^2 A_3^*(K)\alpha + K^2 A_4^*(K)\frac{h}{B}\right]$$

<div align="right">(F.1)</div>

where K is defined as a reduced frequency

$$K = \frac{B\omega}{U} = \frac{B(2\pi n)}{U} \tag{F.2}$$

The coefficients of the displacements and their first derivatives, H_i^* and A_i^*, i=1-4, are the flutter derivatives, which can be used to determine the critical flutter velocity of a structure. The unsteady C_L and C_M predicted by the DVM on bodies undergoing a steady forced oscillation, in either the transverse or torsional degree of freedom, have been used to derive the flutter derivatives numerically. The technique used is briefly described below.

The Fourier transforms of the C_L and C_M may be represented by

$$\Phi_L(\omega) = F_{Lh}(\omega)\Xi(\omega) + F_{L\alpha}(\omega)\Lambda(\omega)$$

$$\Phi_M(\omega) = F_{Mh}(\omega)\Xi(\omega) + F_{M\alpha}(\omega)\Lambda(\omega)$$

<div align="right">(F.3)</div>

where $\Xi(\omega)$ and $\Lambda(\omega)$ are the Fourier transforms of the transverse and torsional displacements respectively. The four F functions in (F.3) represent the components of the lift and moment coefficients due to the transverse or torsional motion respectively. These can be calculated from (F.4) using the assumption that the motion is harmonic and takes the solution forms given by (F.8).

$$F_{Lh}(\omega) = \tfrac{1}{2}\omega^2 \rho B^2 \left(H_4^*(\omega) + iH_1^*(\omega) \right)$$

$$F_{L\alpha}(\omega) = \tfrac{1}{2}\omega^2 \rho B^3 \left(H_3^*(\omega) + iH_2^*(\omega) \right)$$

$$F_{Mh}(\omega) = \tfrac{1}{2}\omega^2 \rho B^3 \left(A_4^*(\omega) + iA_1^*(\omega) \right)$$

$$F_{M\alpha}(\omega) = \tfrac{1}{2}\omega^2 \rho B^4 \left(A_3^*(\omega) + iA_2^*(\omega) \right)$$

(F.4)

The DVM calculations were all performed using a forced sinusoidal oscillation in a single DOF, either transverse or torsional. This results in one or other of the displacement Fourier transforms in (F.3) being zero for each of the calculations, hence the flutter derivatives can be extracted directly from (F.3) and (F.4).

F.2   Calculation of Critical Flutter Velocity.

The critical flutter velocity can be obtained from the flutter derivatives. However, different procedures are used depending on whether the flutter instability is a single DOF or two DOF response. The following sections briefly describe the procedures used in both cases.

F.2.1   Two Degree of Freedom Flutter.

The method for calculating the critical velocity from the flutter derivatives is outlined in detail by Simiu and Scanlan [2], in which the derivatives $H_4{}^*$ and $A_4{}^*$ are both assumed to be zero. The procedure briefly outlined below is based on this method but is extended to include these final two derivatives. Similar derivations of this method are given by Dyrbye et al [69] and Walther [167].

The critical flutter velocity of a structure can be found from the flutter derivatives and the system equations of motion (F.5).

$$m\ddot{h} + c_h \dot{h} + k_h h = \tfrac{1}{2}\rho\, U^2 (2B)\left[KH_1^*(K)\frac{\dot{h}}{U} + KH_2^*(K)\frac{B\dot{\alpha}}{U} + K^2 H_3^*(K)\alpha + K^2 H_4^*(K)\frac{h}{B} \right]$$

$$I\ddot{\alpha} + c_\alpha \dot{\alpha} + k_\alpha \alpha = \tfrac{1}{2}\rho\, U^2 (2B)^2\left[KA_1^*(K)\frac{\dot{h}}{U} + KA_2^*(K)\frac{B\dot{\alpha}}{U} + K^2 A_3^*(K)\alpha + K^2 A_4^*(K)\frac{h}{B} \right]$$

(F.5)

By using a non-dimensional time (F.6), the equations of motion can be rewritten as (F.7).

$$s = \frac{Ut}{B}$$

also

(F.6)

$$\Rightarrow \quad (\dot{\ }) = \frac{d}{dt}(\ ) = \frac{d}{ds}(\ )\frac{ds}{dt} = (\ )' \frac{U}{B}$$

$$\frac{h''}{B} + 2\zeta_h K_h \frac{h'}{B} + K_h^2 \frac{h}{B} = \frac{\rho B^2}{m} \left[K H_1^*(K) \frac{h'}{B} + K H_2^*(K)\alpha' + K^2 H_3^*(K)\alpha + K^2 H_4^*(K)\frac{h}{B} \right]$$

$$\alpha'' + 2\zeta_\alpha K_\alpha \alpha' + K_\alpha^2 \alpha = \frac{\rho B^4}{I} \left[K A_1^*(K)\frac{h'}{B} + K A_2^*(K)\alpha' + K^2 A_3^*(K)\alpha + K^2 A_4^*(K)\frac{h}{B} \right]$$

(F.7)

At the critical flutter velocity, the transverse and torsional frequencies are usually coincident and as a harmonic oscillation is assumed, the solutions to (F.7) can be assumed to have the forms

$$\frac{h}{B} = \frac{h_0}{B}\exp(i\omega t) = \frac{h_0}{B}\exp(iKs)$$

$$\alpha = \alpha_0 \exp(i\omega t) = \alpha_0 \exp(iKs)$$

(F.8)

Using these solution forms in (F.7) gives

$$\frac{h_0}{B}\left[-K^2 + 2\zeta_h K_h Ki + K_h^2 - \frac{\rho B^2}{m}K^2 H_1^*(K)i - \frac{\rho B^2}{m}K^2 H_4^*(K) \right] - \alpha_0 \left[\frac{\rho B^2}{m}K^2 H_2^*(K)i + \frac{\rho B^2}{m}K^2 H_3^*(K) \right] = 0$$

$$\frac{h_0}{B}\left[\frac{\rho B^4}{I}K^2 A_1^*(K)i - \frac{\rho B^4}{I}K^2 A_4^*(K) \right] + \alpha_0 \left[-K^2 + 2\zeta_\alpha K_\alpha Ki + K_\alpha^2 - \frac{\rho B^4}{I}K^2 A_2^*(K)i - \frac{\rho B^4}{I}K^2 A_3^*(K) \right] = 0$$

(F.9)

Defining an unknown X as

$$X = \frac{\omega}{\omega_h}$$

(F.10)

and setting the determinant of the coefficients of h_0/B and α_0 respectively in (F.9) to zero, results in a fourth order complex polynomial in X, the real and imaginary parts of which are given in (F.11).

$$\text{real} \quad : \quad R_4 X^4 + R_3 X^3 + R_2 X^2 + R_1 X + \frac{K_\alpha^2}{K_h^2} = 0$$

$$\text{imag} \quad : \quad I_4 X^4 + I_3 X^3 + I_2 X^2 + I_1 X = 0$$

(F.11)

where

$$R_4 = 1 + \frac{\rho B^4}{I}A_3^* + \frac{\rho B^2}{m}H_4^* - \frac{\rho^2 B^6}{mI}H_1^* A_2^* + \frac{\rho^2 B^6}{mI}A_3^* H_4^* + \frac{\rho^2 B^6}{mI}A_1^* H_2^* - \frac{\rho^2 B^6}{mI}H_3^* A_4^*$$

$$R_3 = 2\zeta_h \frac{\rho B^4}{I}A_2^* + 2\zeta_\alpha \frac{\rho B^2}{m}\frac{K_\alpha}{K_h}H_1^*$$

$$R_2 = -\frac{K_\alpha^2}{K_h^2} - 4\zeta_h\zeta_\alpha \frac{K_\alpha}{K_h} - 1 - \frac{\rho B^4}{I}A_3^* - \frac{\rho B^2}{m}\frac{K_\alpha^2}{K_h^2}H_4^*$$

$$R_1 = 0$$

and

$$I_4 = \frac{\rho B^4}{I} A_2^* + \frac{\rho B^2}{m} H_1^* + \frac{\rho^2 B^6}{mI} A_3^* H_1^* + \frac{\rho^2 B^6}{mI} A_2^* H_4^* - \frac{\rho^2 B^6}{mI} A_4^* H_2^* - \frac{\rho^2 B^6}{mI} A_1^* H_3^*$$

$$I_3 = -2\zeta_\alpha \frac{K_\alpha}{K_h} - 2\zeta_h - 2\zeta_h \frac{\rho B^4}{I} A_3^* - 2\zeta_\alpha \frac{\rho B^2}{m} \frac{K_\alpha}{K_h} H_4^*$$

$$I_2 = -\frac{\rho B^4}{I} A_2^* - \frac{\rho B^2}{m} \frac{K_\alpha^2}{K_h^2} H_1^*$$

$$I_1 = 2\zeta_h \frac{K_\alpha^2}{K_h^2} + 2\zeta_\alpha \frac{K_\alpha}{K_h}$$

The solution for the unknown flutter frequency, ω, will in general of the form $\omega = \omega_1 + i\omega_2$ and will represent either a decaying ($\omega_2 > 0$) or a divergent ($\omega_2 < 0$) oscillation. The critical flutter condition can be found from the point at which the solution is purely imaginary, that is when $\omega_2 = 0$, so that $\omega = \omega_1$. The two quartic polynomials in (F.11) are solved at different values of frequency and the roots of the real and imaginary parts are plotted against reduced velocity, U_r ($= 1/K$), as shown in Fig. F.1. The point at which the roots of the two equations cross, (U_{rc}, X_c) defines the flutter condition. This gives the frequency of the flutter instability, ω, and combined with appropriate structural parameters, the critical flutter velocity can be found from (F.12).

$$U_c = U_{rc} \, n_h B X_c$$

$$\text{where} \quad n_h = \frac{\omega_h}{2\pi}$$

    (F.12)

F.2.2   Single Degree of Freedom Flutter.

For a single degree of freedom flutter instability in the torsional DOF, the equation of motion is as shown in (F.5). However, using the solution forms given in (F.8), for a single DOF oscillation, equation (F.9) simplifies to

$$I\left[K_\alpha^2 - K^2 + 2\zeta_\alpha K_\alpha K i\right] = \rho B^4 K^2 A_3^*(K) + \rho B^4 K^2 A_2^*(K) i$$

    (F.13)

The critical wind speed at which 1DOF torsional flutter occurs is identified at the point at which the structural damping and the aerodynamic damping are balanced. This condition can be obtained from (F.13) by setting the two damping terms (imaginary parts) equal to each other and by also taking K_α to be approximately equal to K. Hence, a critical value of A_2^* can be obtained, at which the damping terms are balanced and which can be used to derive the wind speed for the onset of flutter (F.14).

$$\left(A_2^*\right)_c = \frac{2I\zeta_\alpha}{\rho B^4}$$

    (F.14)

By plotting A_2^* against reduced velocity, the reduced velocity which corresponds to the critical flutter velocity, (U_{rc}), corresponds to the reduced velocity at which $(A_2^*)_c$ occurs (Fig. F.2).
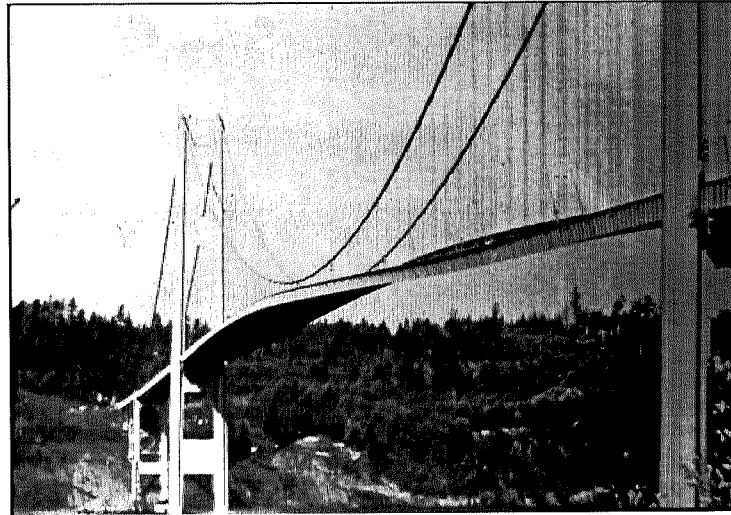
a) Oscillation Prior to Collapse.

b) View along Main Span Demonstrating Torsional Oscillation of Bridge.
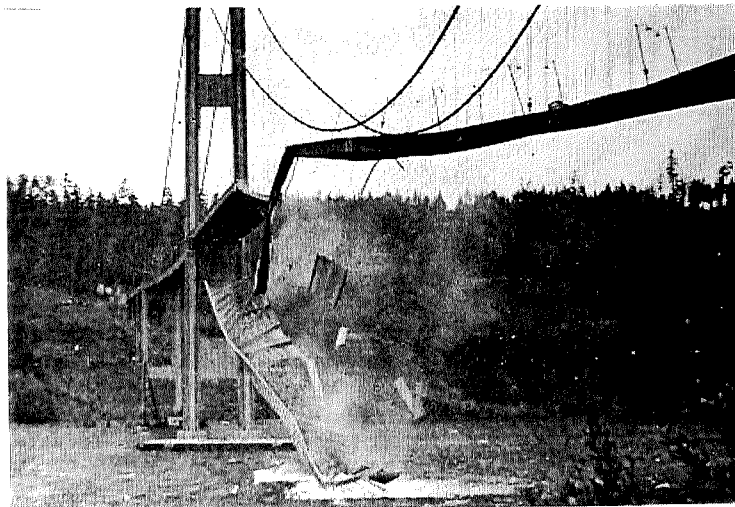
c) Final Collapse.

Fig. 1.1 - Failure of Original Tacoma Narrows Suspension Bridge due to Flutter in Torsional Degree of Freedom.
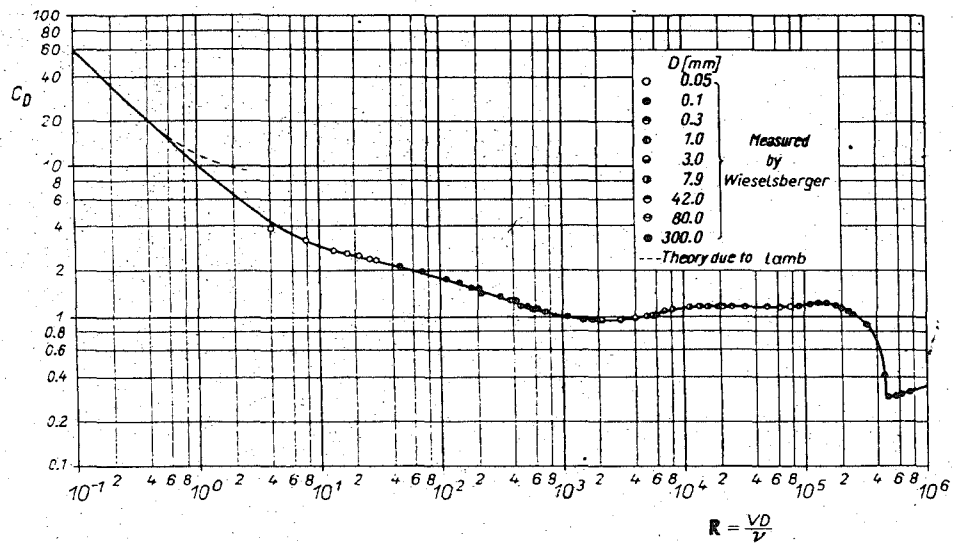
Fig. 2.1 - Variation of Drag Coefficient with Reynolds Number on a Smooth Circular Cylinder.

(from Schlichting, 1968 [11])
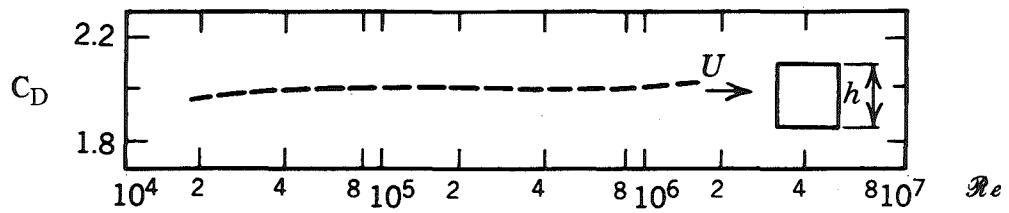
Fig. 2.2 - Variation of Drag Coefficient with Reynolds number on Square Cylinder.

(from Simiu and Scanlan, 1986 [2])
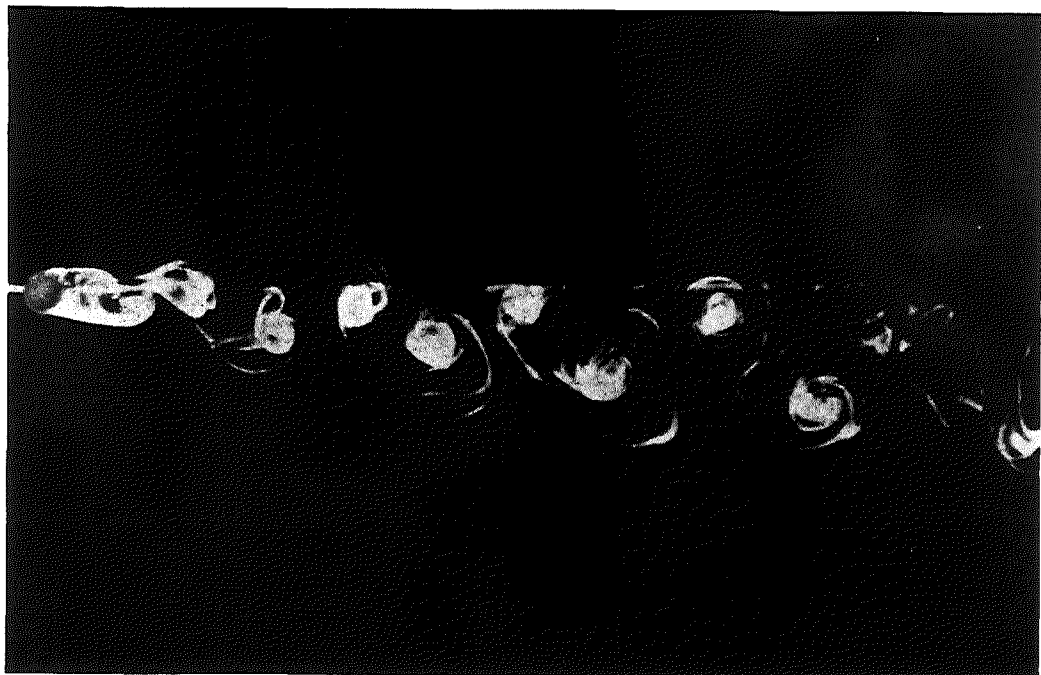
Fig. 2.3 - Vortex Street in Wake of a Circular Cylinder.

(from Simiu and Scanlan, 1986 [2])

$\mathscr{R}e \cong 1$ $\mathscr{R}e \cong 20$

$30 \leq \mathscr{R}e \leq 5000$ VON KARMAN VORTEX TRAIL

$5000 \leq \mathscr{R}e \leq 200000$ $\mathscr{R}e \geq 200000$
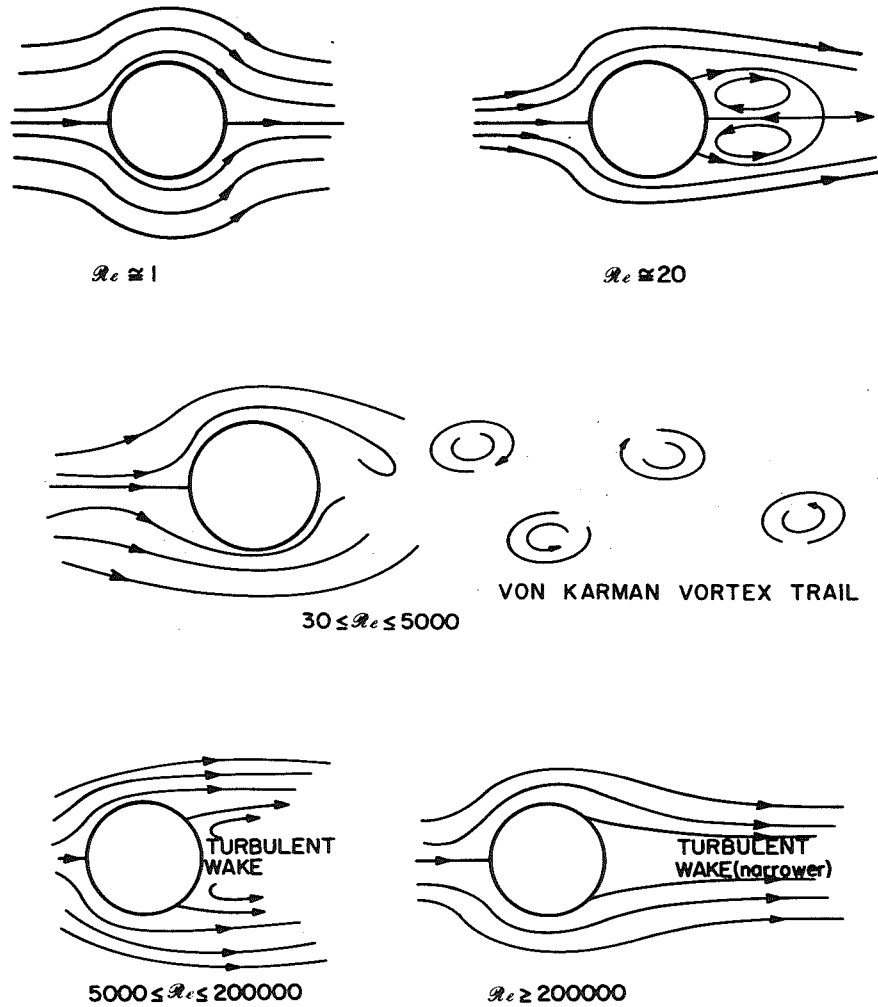
Fig. 2.4 - Variation of Wake and Vortex Street of Circular Cylinder with Reynolds Number.
(from Simiu and Scanlan, 1986 [2])
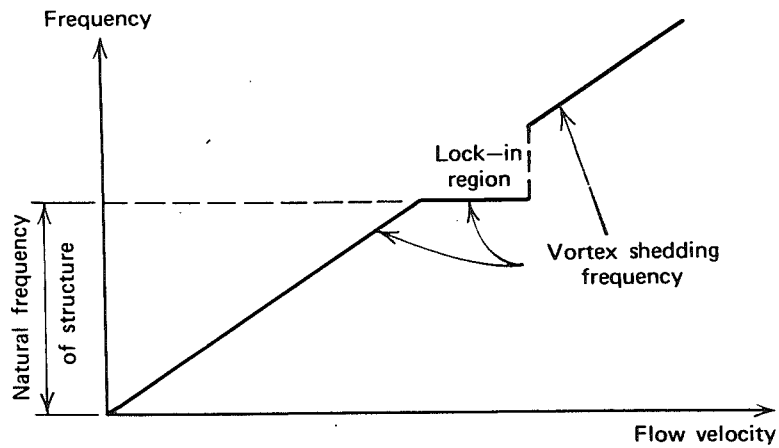
Fig. 2.5 - Evolution of Vortex Shedding Frequency with Flow Velocity over an Elastic Structure.
(from Simiu and Scanlan, 1986 [2])
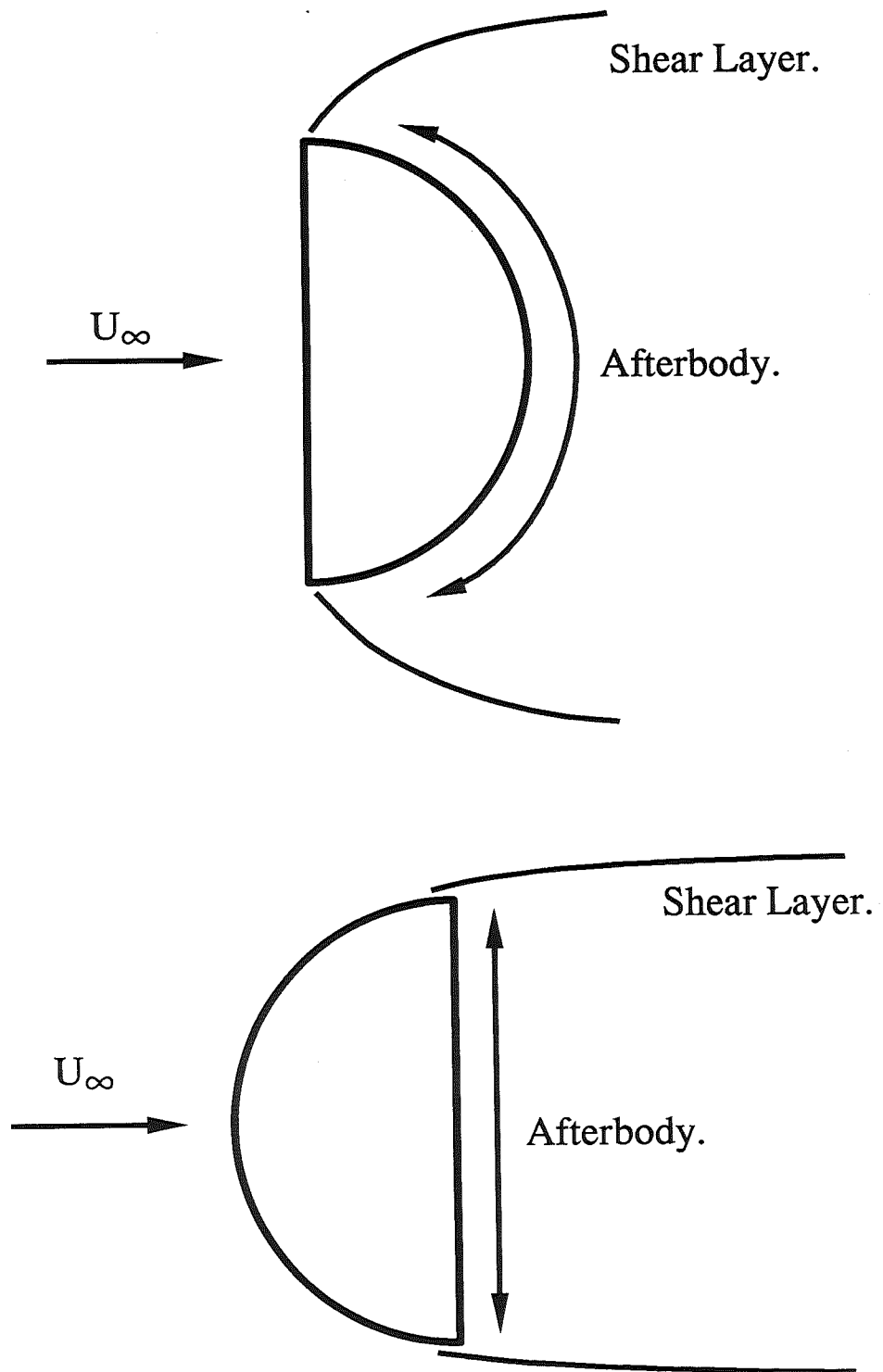
Fig. 2.6 - Effect of afterbody on Structural Response due to Vortex Induced Vibration.

⊙, A/D = 0.05; ×, A/D = 0.10; △, A/D = 0.25.

RESONANCE
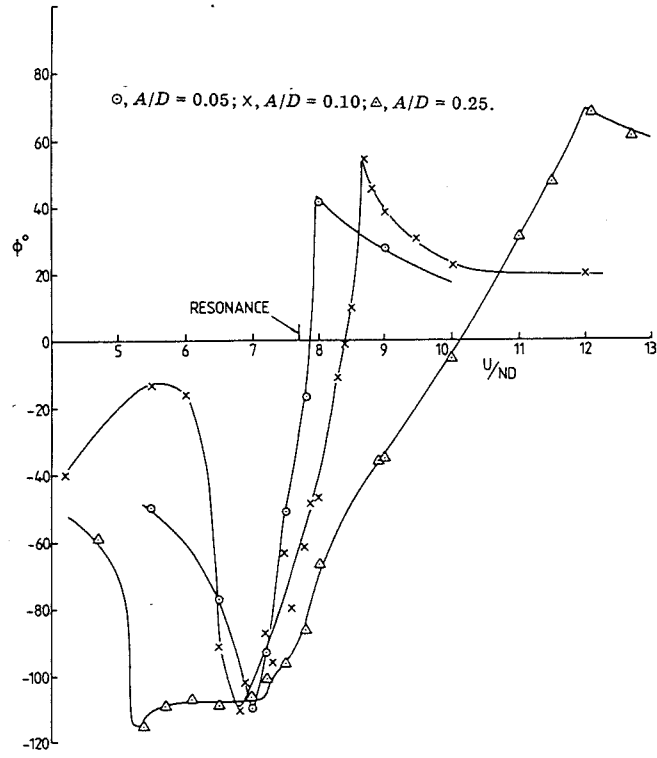
a) Square Cylinder (from Obasaju, 1983 [45])
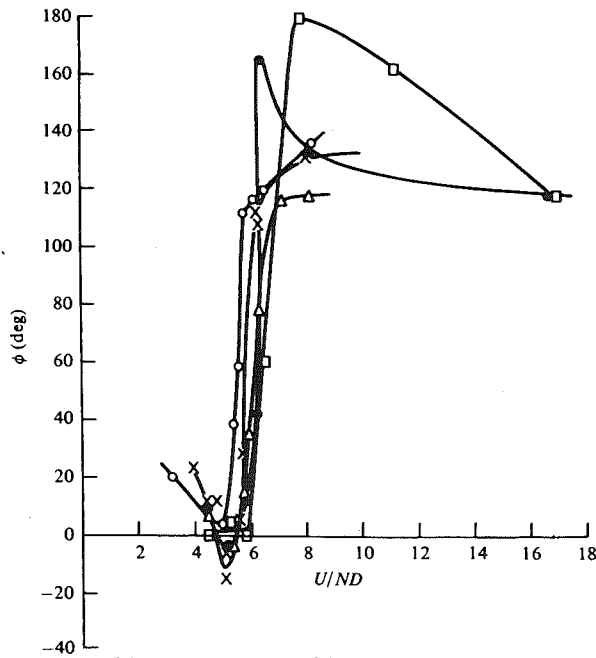
o, $A/D = 0\cdot11$; ×, $A/D = 0\cdot22$; △, $A/D = 0\cdot44$; ●, $A/D = 0\cdot89$; □, $A/D = 1\cdot33$.

b) Circular Cylinder.

(from Bearman and Currie 1979 [57])

Fig. 2.7 - Phase Angle between Lift Coefficient and Cylinder Displacement : Variation with Reduced Velocity.
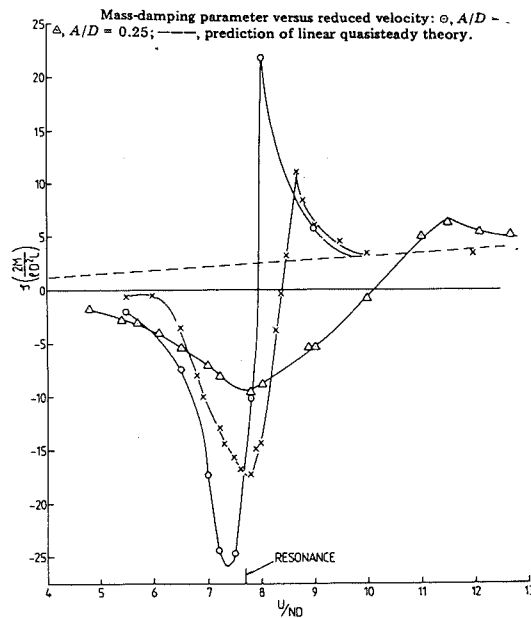
Fig. 2.8 - Variation of Mass-Damping parameter with Reduced Velocity.

(from Obasaju, 1983 [45])

C_{Fy} is effective cross–wind force on body.

Body motion in upwards direction with velocity, $\dot{y}$.

Effective angle of attack, α

given by $\alpha = \tan^{-1}(\dot{y}/U_\infty)$
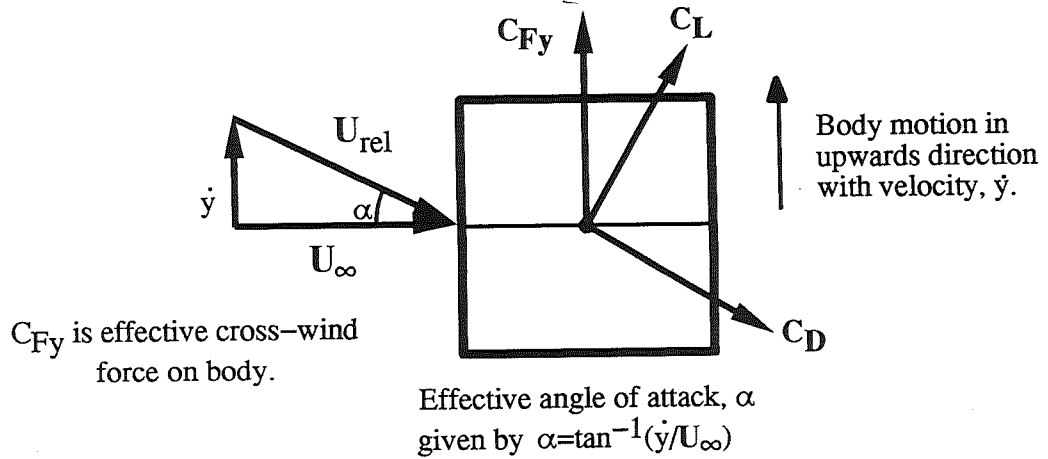
Fig. 2.9 - Relative Angle of Incidence for Cylinder Undergoing Transverse Oscillations.
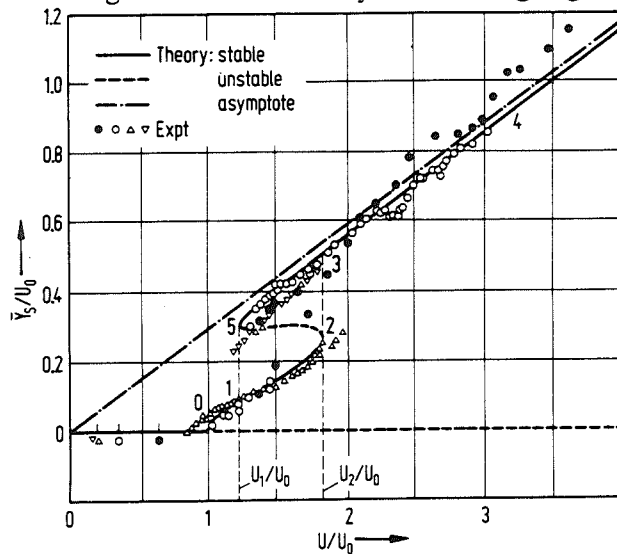
Fig. 2.10 - Amplitude Response Predicted by Quasi-Steady Galloping Theory.

(from Parkinson, 1974 [35])
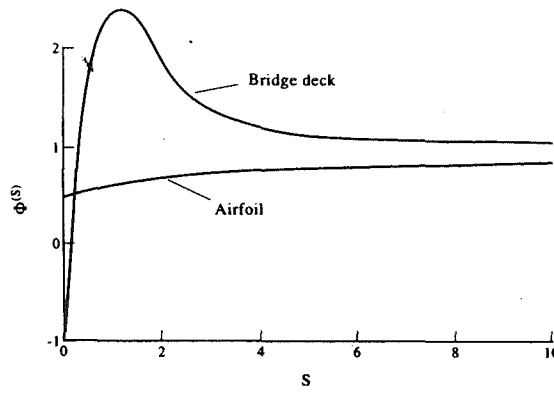
Fig. 2.11 - Comparison of Wagner-type Indicial functions for Aerofoil and Bridge Deck. (from Scanlan, 1996 [107])

a) Comparison between computed and experimental results of C_D and C_{pb}.

b) Comparison between computed and experimental results of *St*.
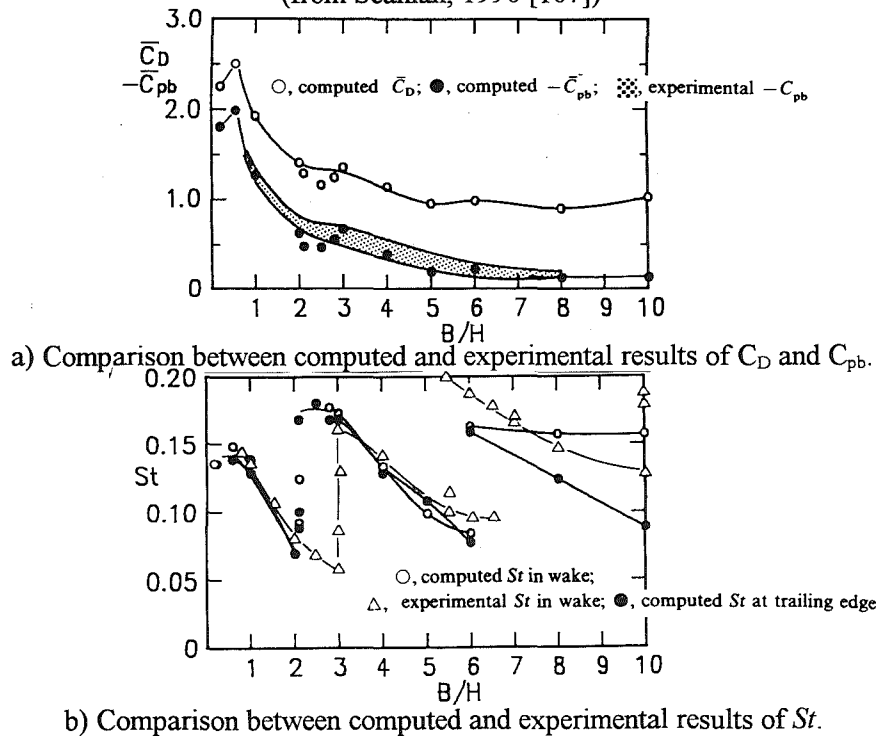
Fig. 2.12 - Variation of Flow Parameters with Aspect Ratio. (from Okajima et al, 1992 [136])

a) *St*

b) C_L

c) C_D
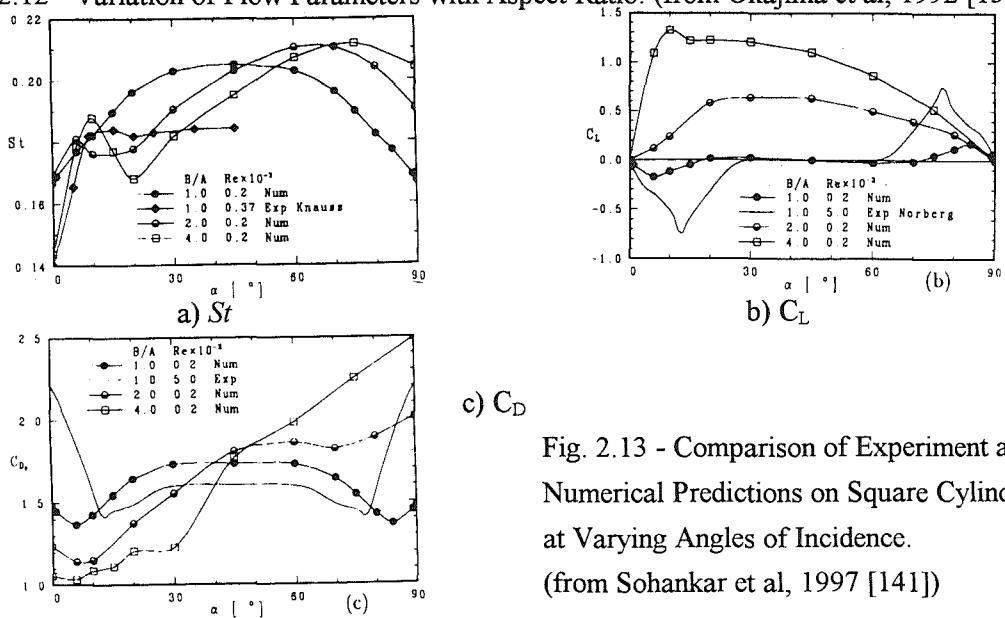
Fig. 2.13 - Comparison of Experiment and Numerical Predictions on Square Cylinder at Varying Angles of Incidence.

(from Sohankar et al, 1997 [141])

(1) Wind tunnel experiment   (2) standard k-ε model
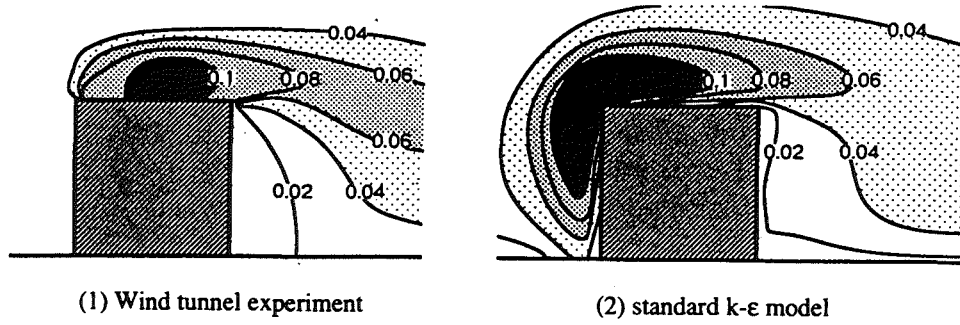
Fig. 2.14 - Over-Production of Turbulent Kinetic Energy by the Standard k-ε Model.
(from Murakami, 1997 [143])

(a) s/D
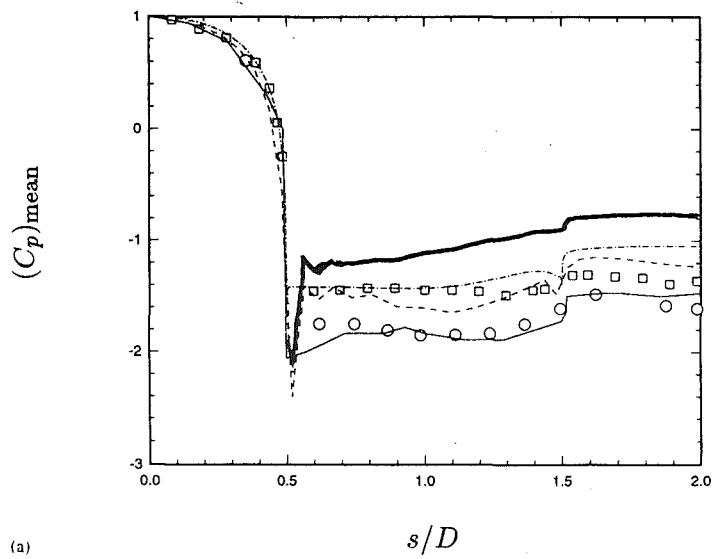
a) Mean Pressure Coefficient around Cylinder.

s/D
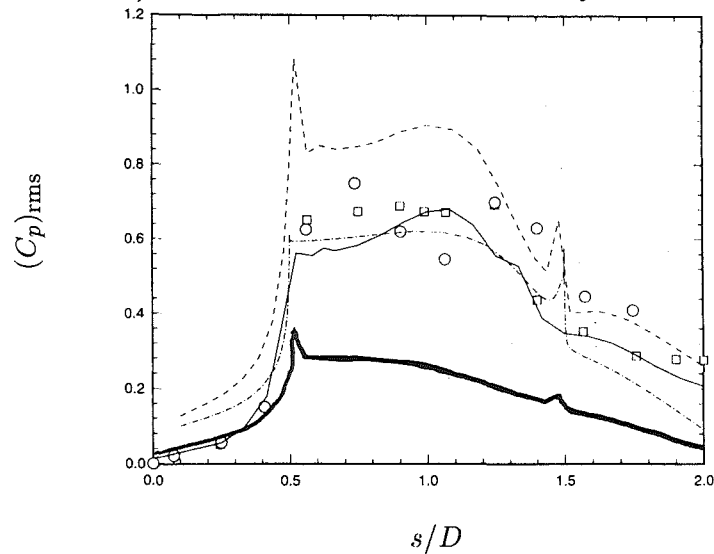
b) RMS Fluctuating Pressure Coefficient.

Fig. 2.15 - Predicted Pressure Coefficient Distributions Around Surface of Square Cylinder
using k-ε and LES. (from Lee, 1997 [142])

Computations: LES ▬ Murakami et al. [16];
k ε models - - - - RNG (case REF), · · · · standard (case SQ), ━●━ low Re (case LX3). Experiments: (a) (□)
(Lyn et al. [15], [○] Bearman et al. (Re = 2.0 × 10⁴) [24], (b) (□) Bearman et al. (Re = 2.0 × 10⁴) [24], (○)
Lee [25] (Re = 1.76 × 10⁵).
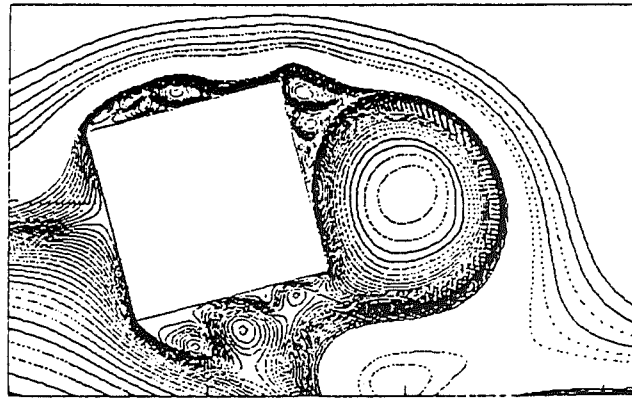
a) 2D Computational Streamlines.
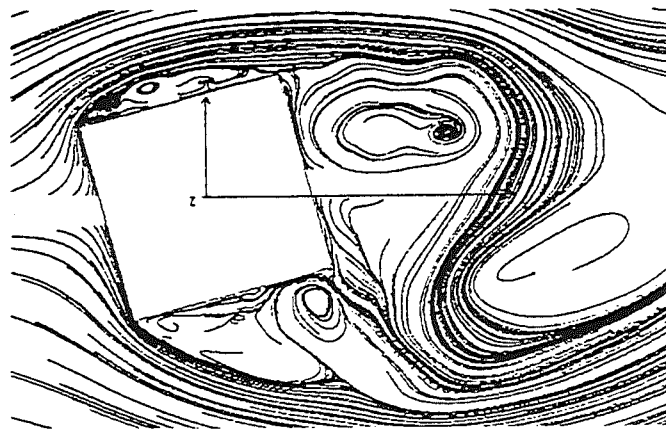
b) 3D Computational Streamlines on a Sectional Plane.

Fig. 2.16 - Comparison of 2D and 3D Computations on Square Cylinder at 15° Incidence.
(from Tamura et al, 1990 [147])
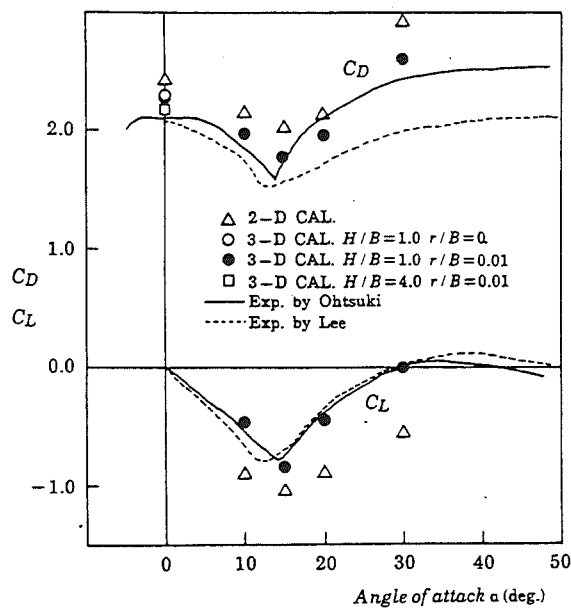
Fig. 2.17 - Variation of Aerodynamic Forces with Incidence on Square Cylinder : Comparison of
2D and 3D Computations. (from Tamura et al, 1990 [156])

$$\frac{\omega(r/\sigma)}{\Gamma/(\pi\sigma^2)}$$

Rankine core
Lamb core
Core in use

$$\frac{u(r/\sigma)}{\Gamma/(2\pi\sigma)}$$

Point vortex
Rankine core
Lamb core
Core in use
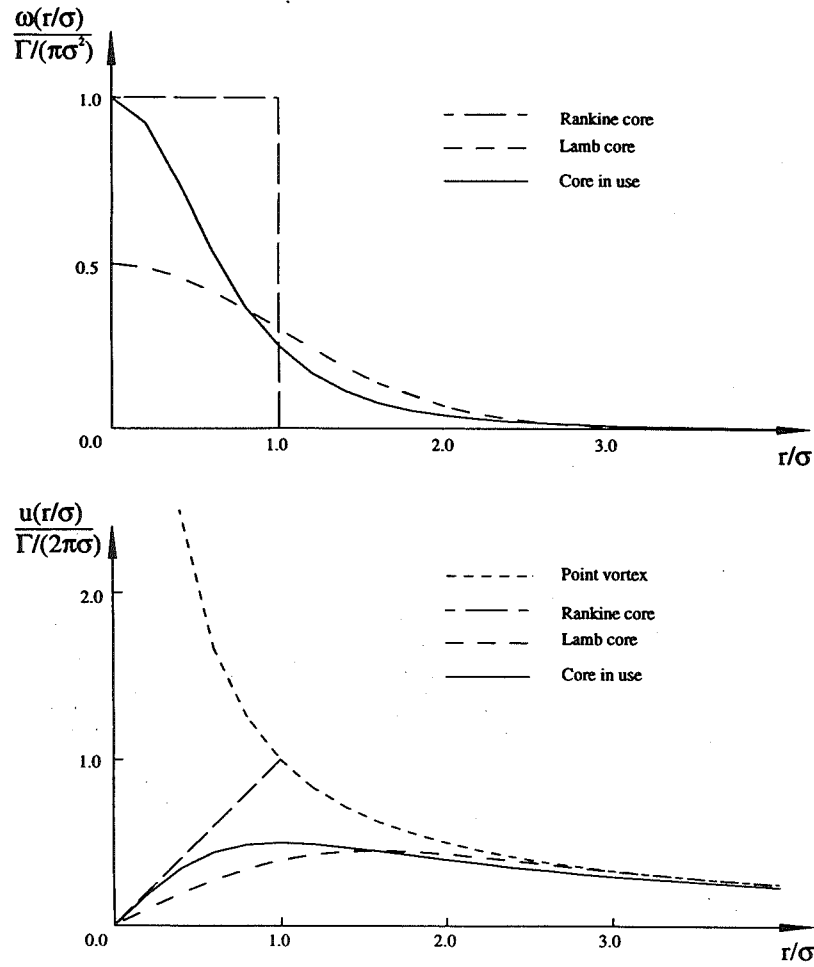
Fig. 2.18 - Vorticity and Velocity Distributions for Various Core Functions.

(from Lin, 1997 [7])
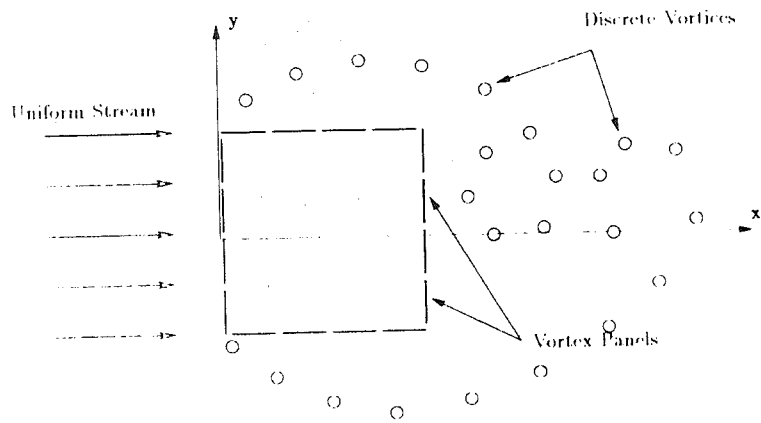
Fig. 2.19 - Schematic Diagram of Vortex Particle Release from Upstream Corners on Square Cylinder.

(from Bergstrom et al, 1997 [201])
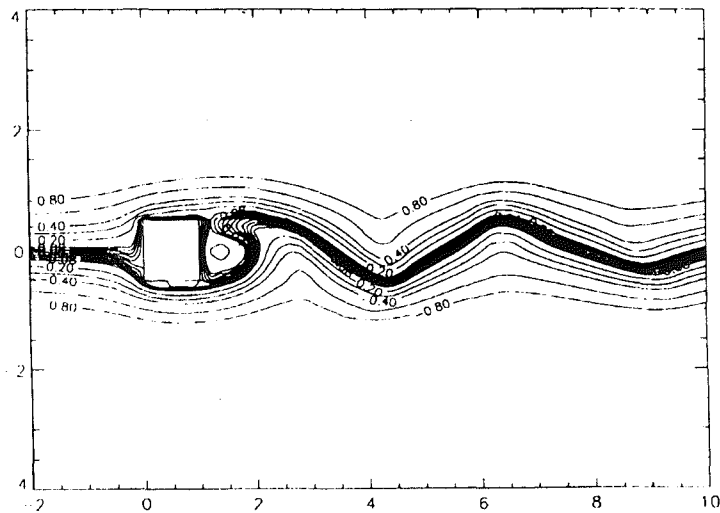
Fig. 2.20 - Streamlines of Flow Field for Square Cylinder Predicted by a Vortex Method.
(from Bergstrom et al, 1997 [201])

a) Mean Lift and Drag Coefficients.

b) Strouhal Number.
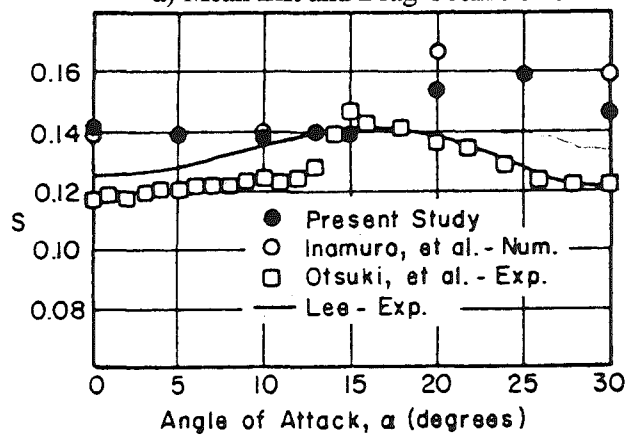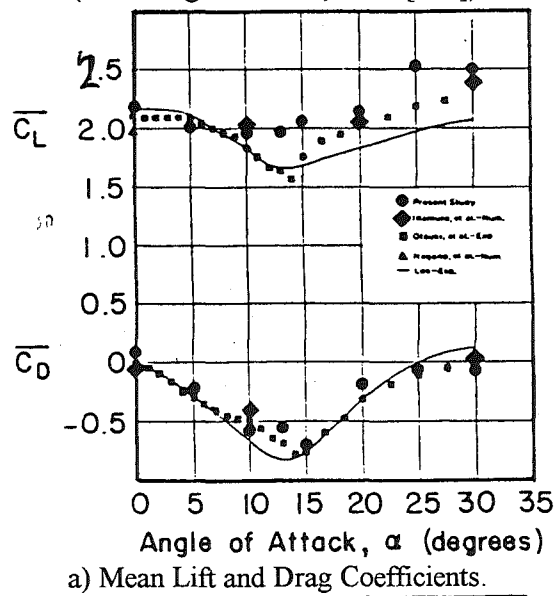
Fig. 2.21 - Comparison of Experiment and Computational Results on a Square Cylinder at
Varying Angles of Incidence. (from Bienkiewicz et al, 1990 [202])

U_∞

0° — Shear layer separates
from front two corners.

U_∞

α

>15° — Shear layer forms
closed separation on side
face and separates from rear corner.
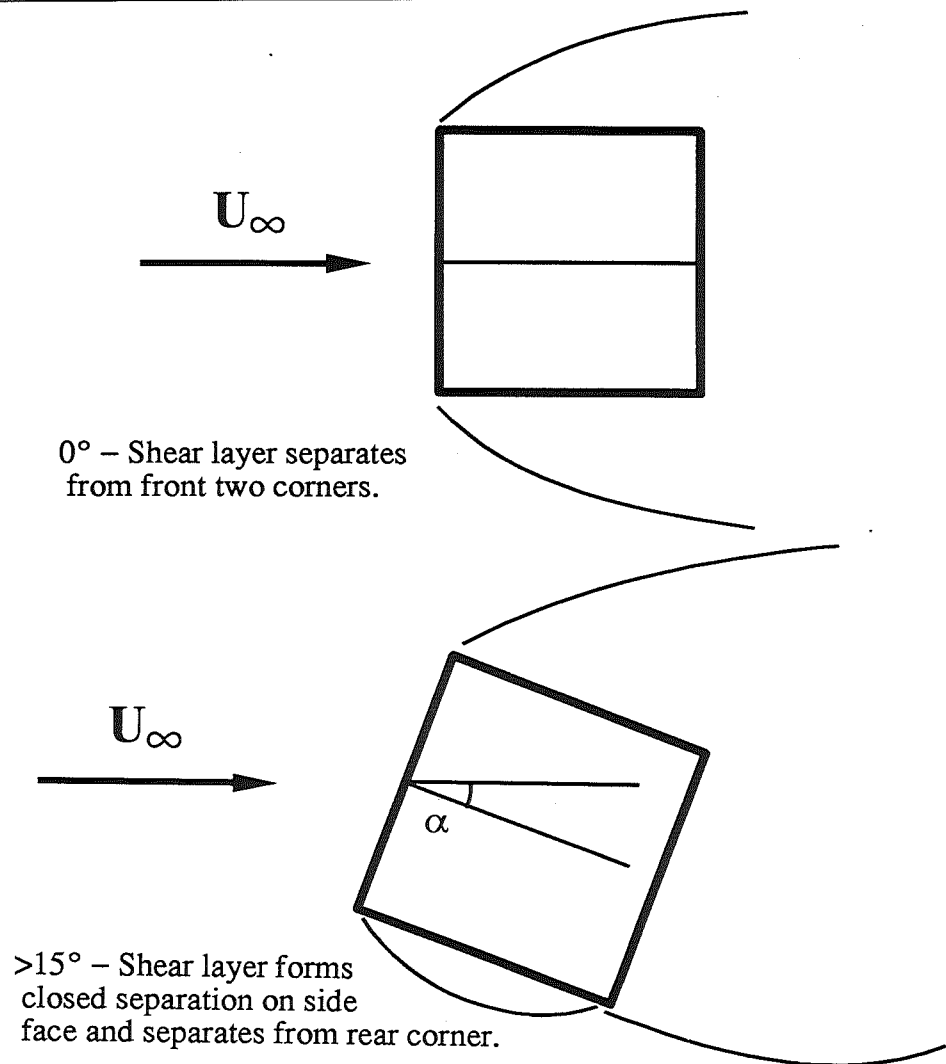
Fig. 2.22 - Schematic of Reattachment of Shear Layer to Side Face of Square Cylinder at Higher
Angles of Incidence.

EXP. DATA

DISCRETE VORTEX METHOD

NAGANO [11] DVM CALC.

DRAG COEFFICIENT, C_D
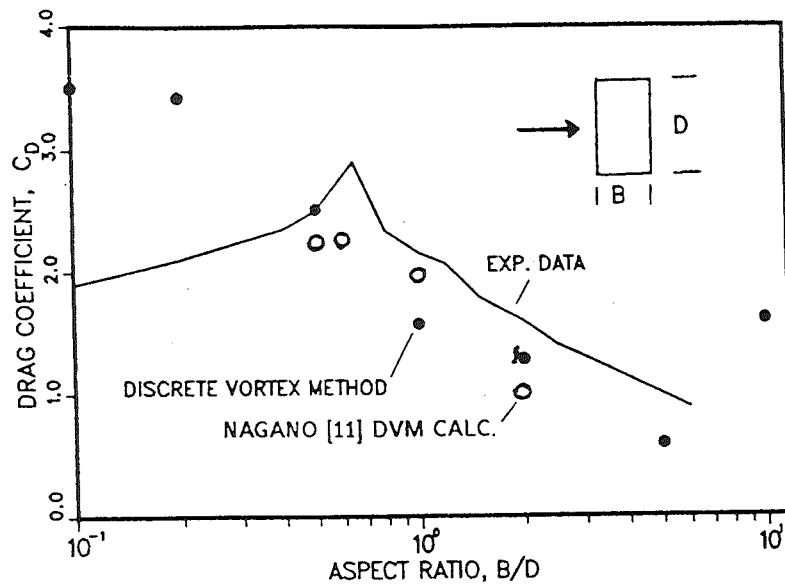
ASPECT RATIO, B/D

Fig. 2.23 - Variation of Drag Coefficient with Aspect Ratio - Comparison of Experiment and
Computational Results. (from Blevins, 1989 [195])
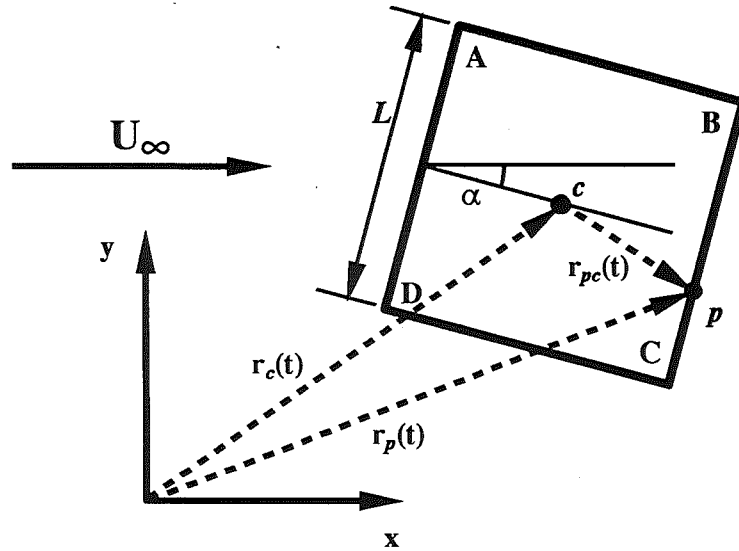
Fig. 3.1 - Body Orientation and Reference Coordinate System.
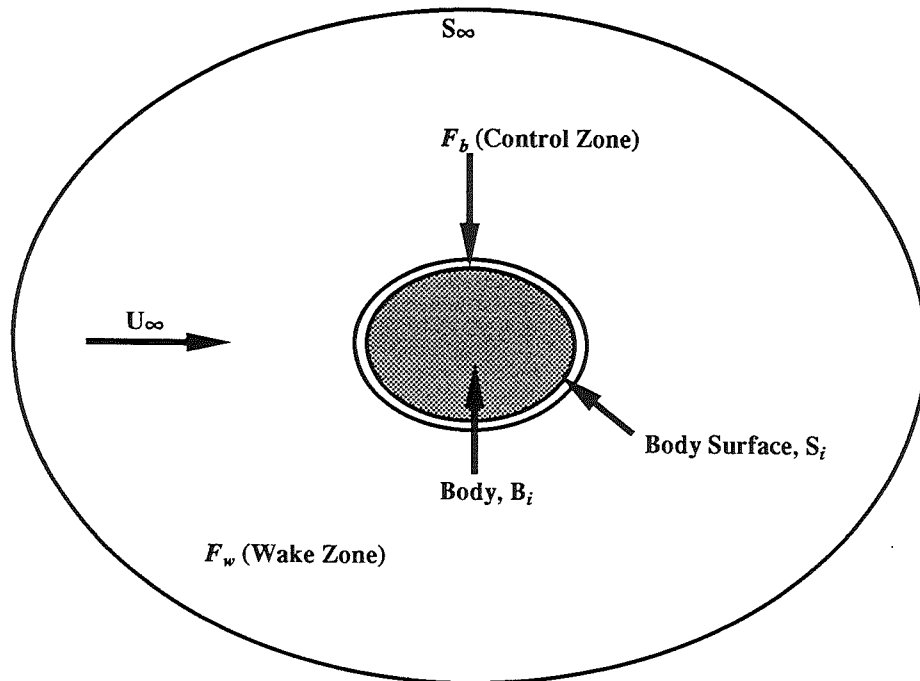
Fig. 3.2 - Flow Domain.
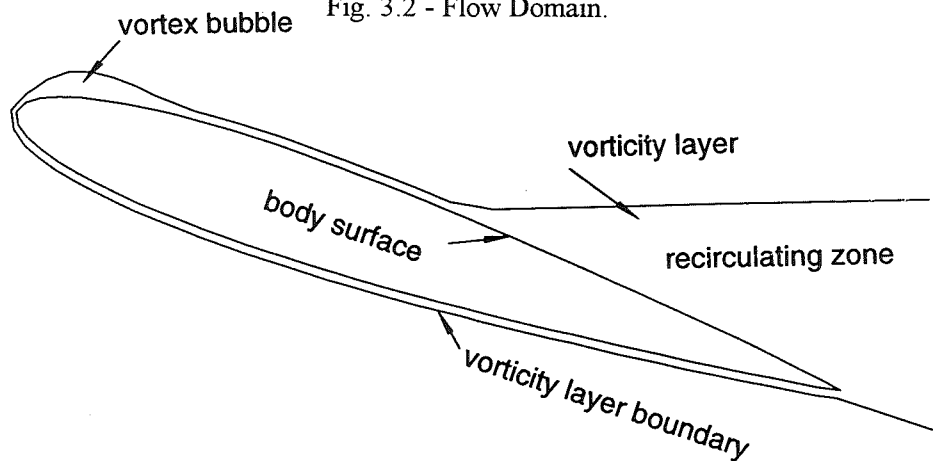
Fig. 3.3 - Illustration of Vorticity Layer and Wake in Separated Flows (from Lin 1997 [7]).

Wake Zone. · Vorticity Boundary.

Control Zone
Boundary.

Surface.
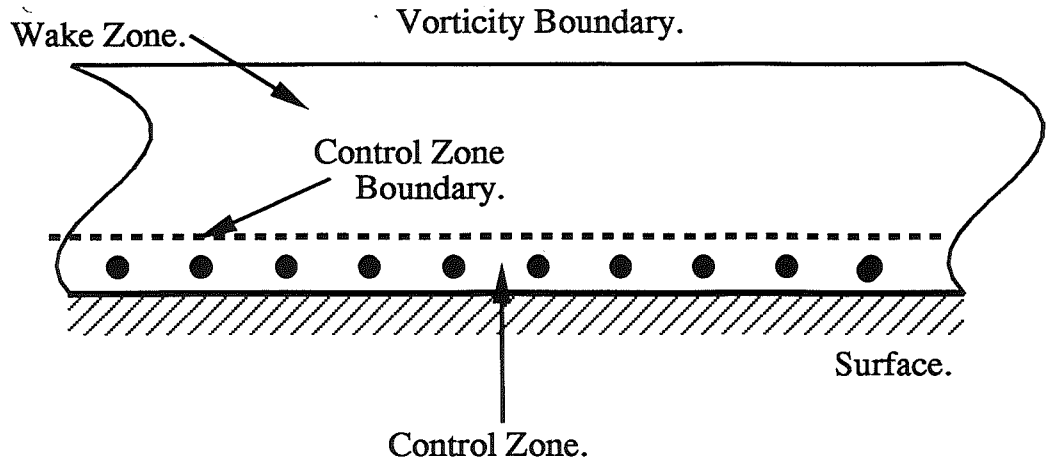
Control Zone.

Fig. 3.4 - Schematic Diagram of Control Zone and Wake Zone for Vorticity Discretisation in Flow Field.

γ_{j+1}

Discretisation of Vorticity on Panel j, between nodes j and j+1.

γ_j

Z_{j+1}

δ

| k=K | k=K−1 | k=2 | k=1 | Z_j |

Panel length, l_j
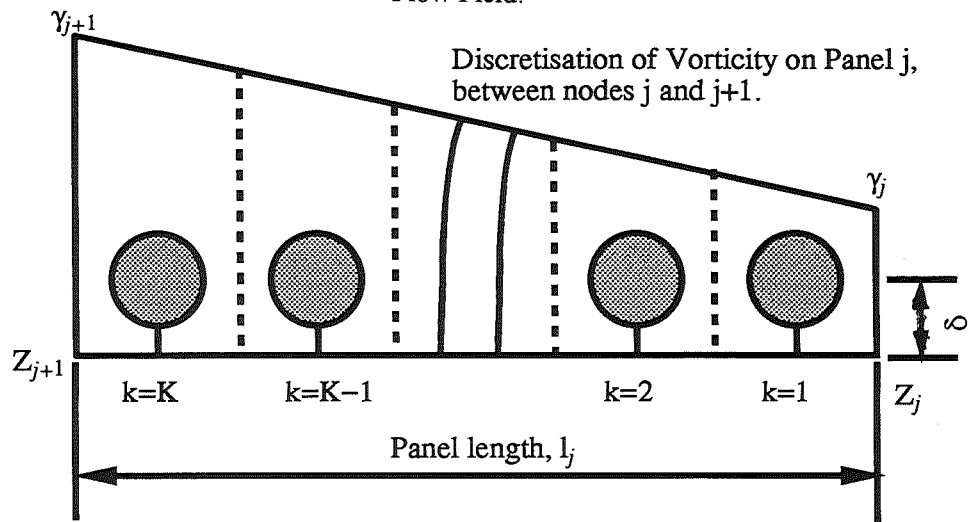
Fig. 3.5 - Discretisation of Vorticity into Vortex Blobs in Control Zone.

B

"Release zone" boundary.

A

2δ

x

δ

Control zone boundary.

Surface. Nascent Vortices.
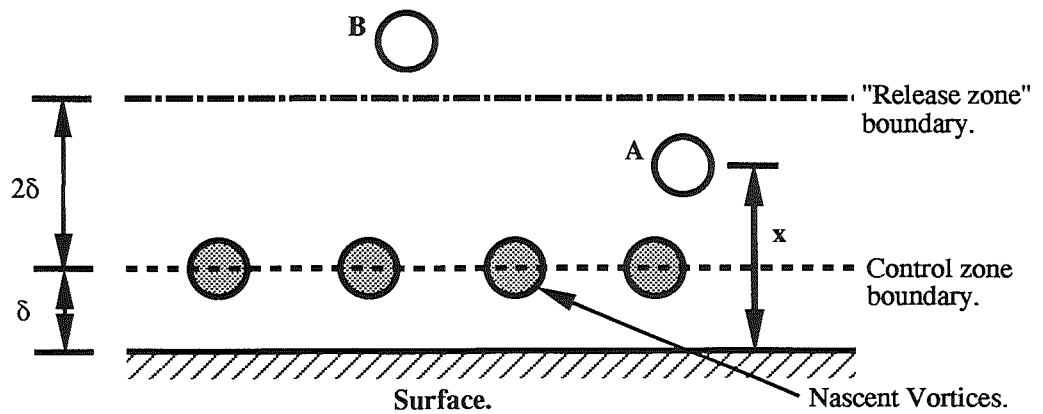
Vortex A : Circulation released to wake = $\Gamma_w(x-\delta)/2\delta$

Remaining circulation reabsorbed into control zone.

Vortex B : Full circulation Γ_w released into wake as outside "release zone".

Γ_w– Circulation of vortex. δ – Control zone thickness.

Fig. 3.6 - Schematic Diagram of Partial Release of Vortex Particles from Control Zone into Wake.

Wake Vortices.

Control zone
boundary.

δ

Surface

Initial position of nascent vortices and wake vortices.

Position incremented for convection and diffusion.
Vortices released into wake or reabsorbed into control zone.

Nascent vorticity re–discretised. Includes vorticity reabsorbed
into control zone.
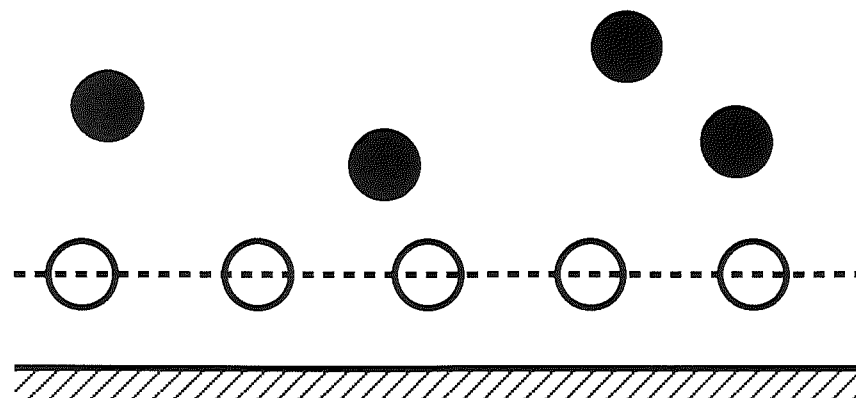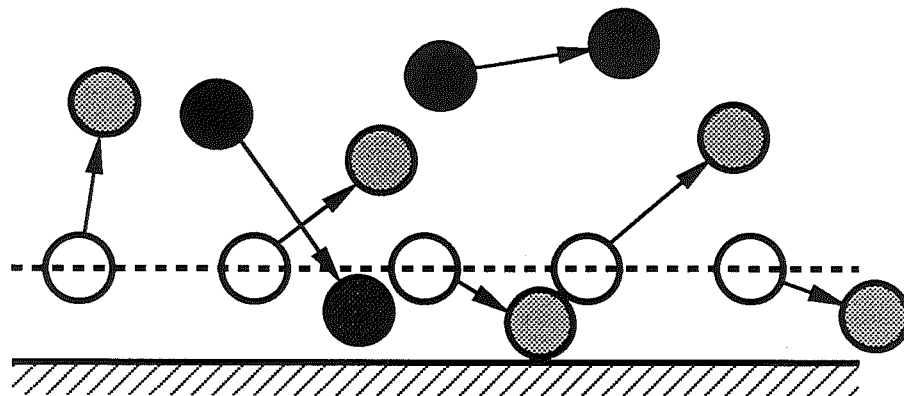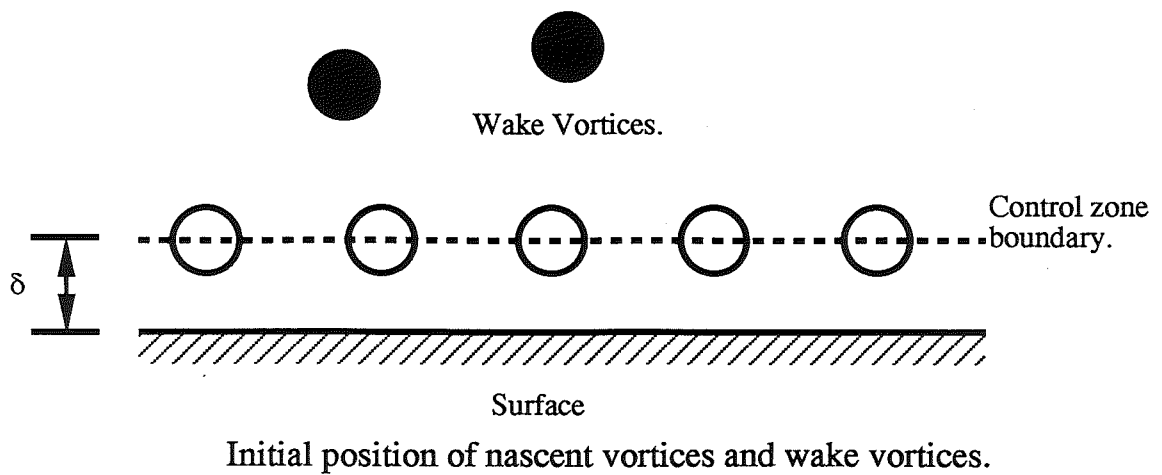
Fig. 3.7 - Transport of Vorticity between Control Zone and Wake through Vortex Release and
Absorption.

Upstream of N

Control zone.

Downstream of N

Both vortices nearest node N.
Absorbed if d < δ.

Vortex in "upstream" region
check against panel N.
Vortex in "downstream" region
check against panel N-1.

N+1

N

N-1
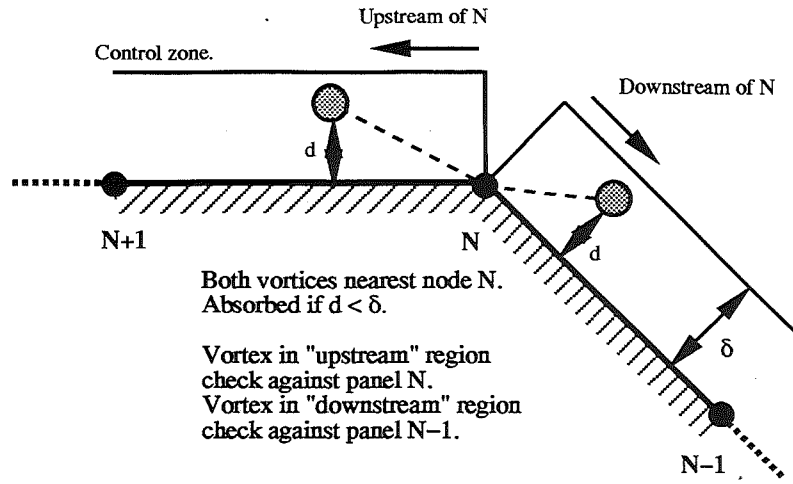
a) Criteria for Checking if Vortex Particles Absorbed.

P

d

Control zone.

N+1

N

Vortex P is incorrectly absorbed as
normal distance to panel N-1, d, is
less than control zone thickness, δ.

δ

N-1
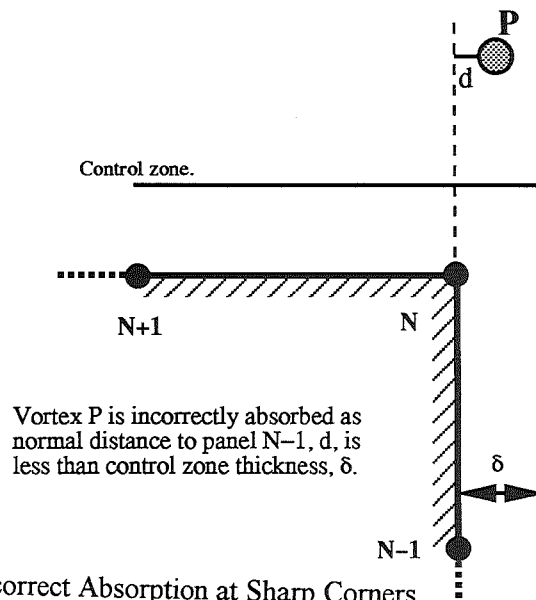
b) Incorrect Absorption at Sharp Corners.

P

d1

δ

Control zone.

N+1

N

New calculation : vortex P is absorbed
to panel N-1 if d1<δ **and** d2<L
where L is panel length plus δ.
Control zone is effectively "rounded"
at corner as shown.

δ

L

d2

N-1
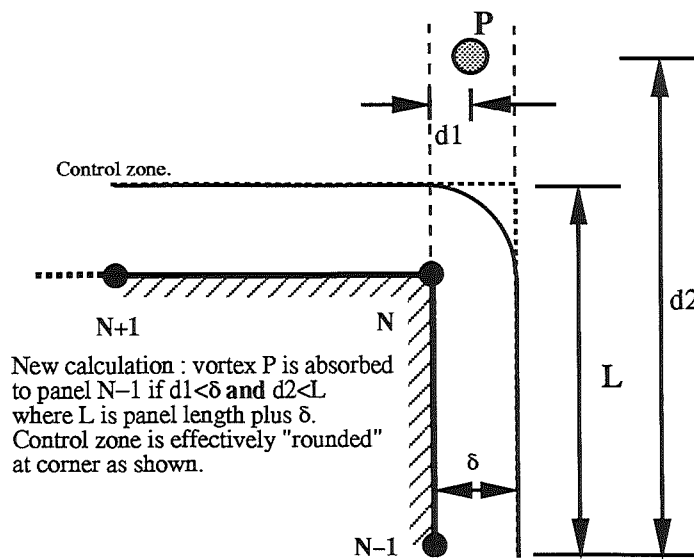
c) Modification to Check for Absorption at Sharp Corners.

Fig. 3.8 - Modification of Vortex Absorption Calculation for Sharp Corners and Regions
Between Panels.
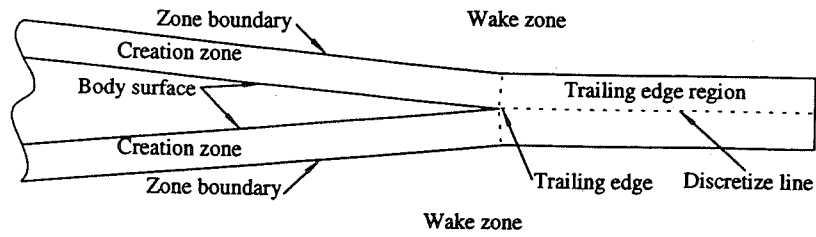
Fig. 3.9 - Discretisation of Vorticity at Aerofoil Trailing Edge (from Lin 1997 [7]).
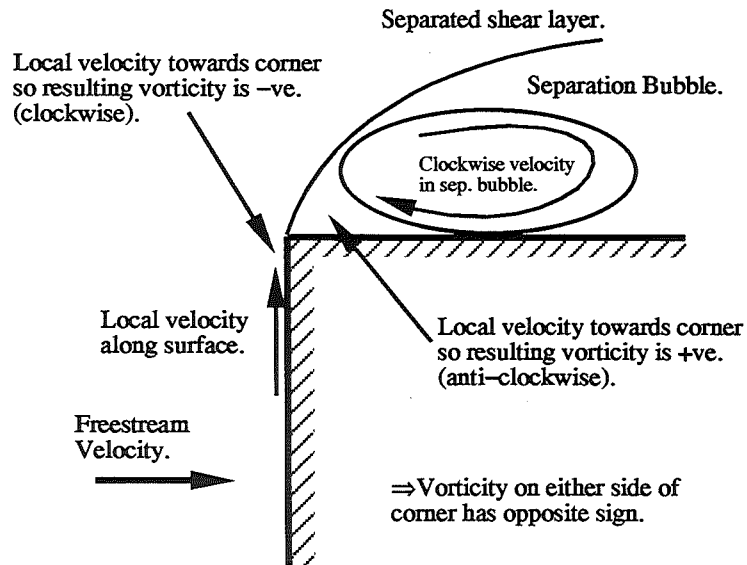
Fig. 3.10 - Schematic of Velocity and Vorticity Distribution Near Upstream Corners of a Square Cylinder.
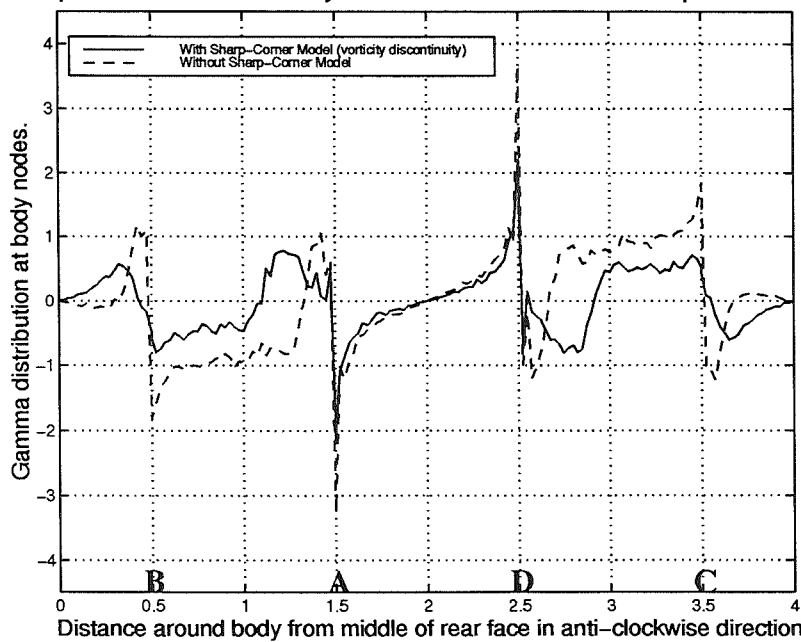
Fig. 3.11 - Vorticity Distribution around Square Cylinder. (Shortly after start of Calculation.)

Nascent Vortex particles
discretise vorticity directly
above sub-panel.

Vorticity in region between
sub-panels at sharp corner
is not discretised.

Body Surface.
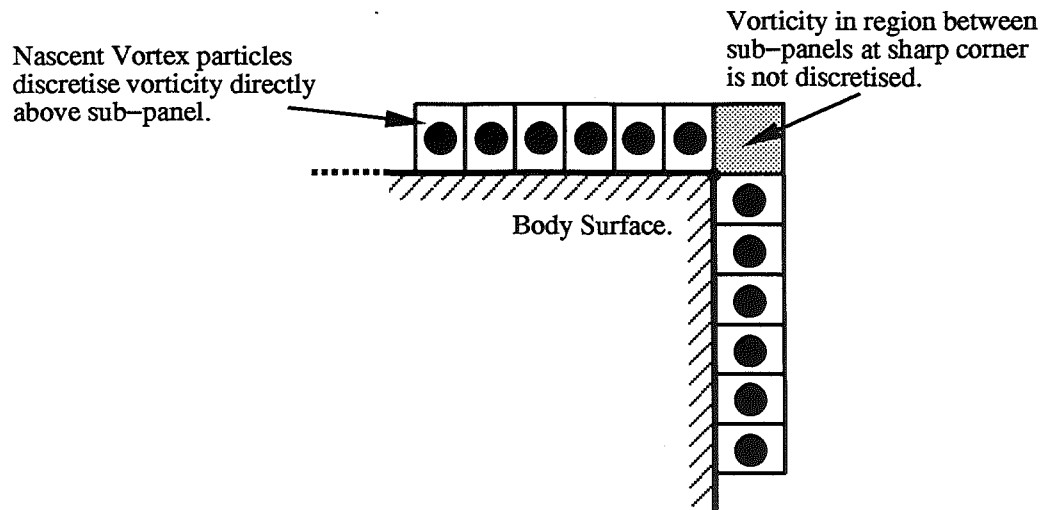
Fig. 3.12 - Region of Vorticity Omitted from Discretisation of Nascent Vorticity at Sharp
Corners.

Body Surface.

Sub-panels skewed towards
corner to discretise nascent
vorticty in region around
the sharp corner.
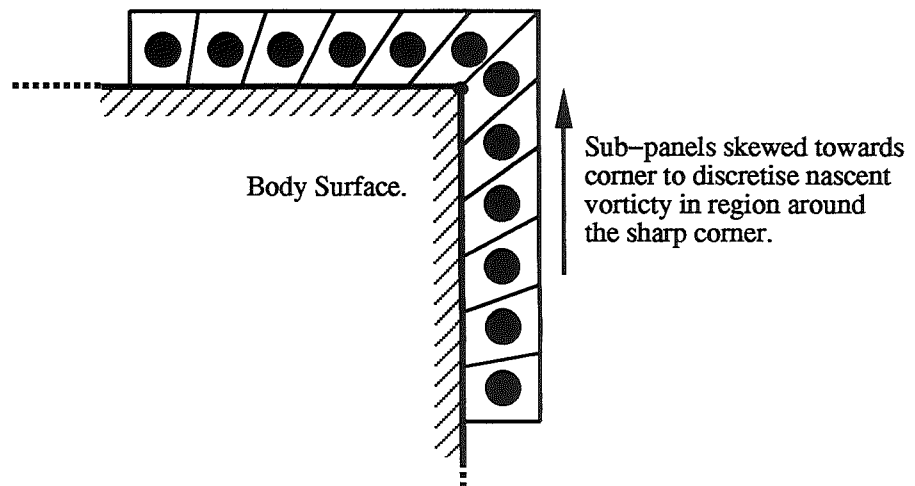
Fig. 3.13 - Modification of Discretisation to Include Nascent Vorticity at Sharp Corners.

SMOOTH
STREAM

TURBULENT
STREAM

r_{AB}/D
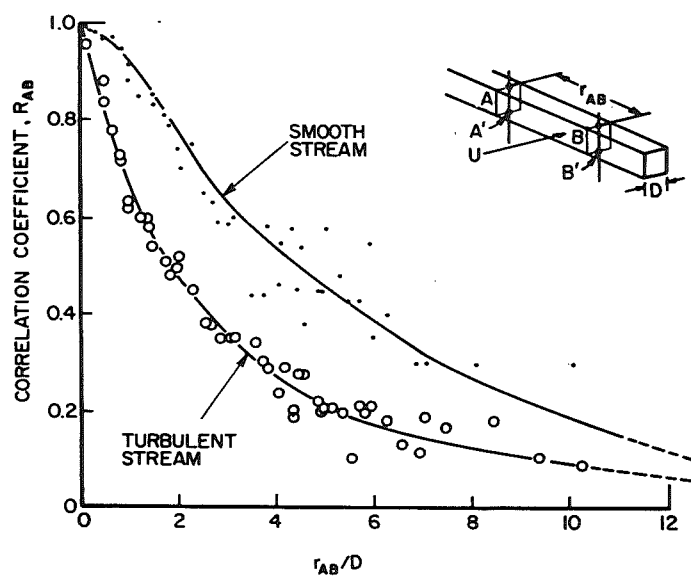
Fig. 3.14 - Spanwise Correlation of the Fluctuating Pressure Difference across the Centre Line of

a Square Cylinder (from Simiu and Scanlan 1986 [2]).
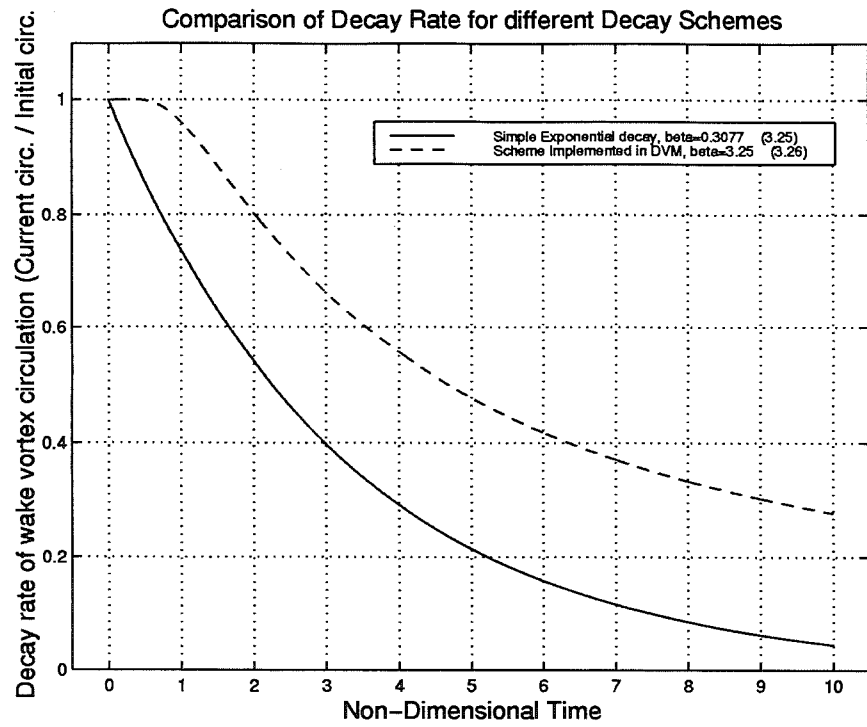
Fig. 3.15 - Comparison of Decay Rates for Different Vorticity Decay Schemes.
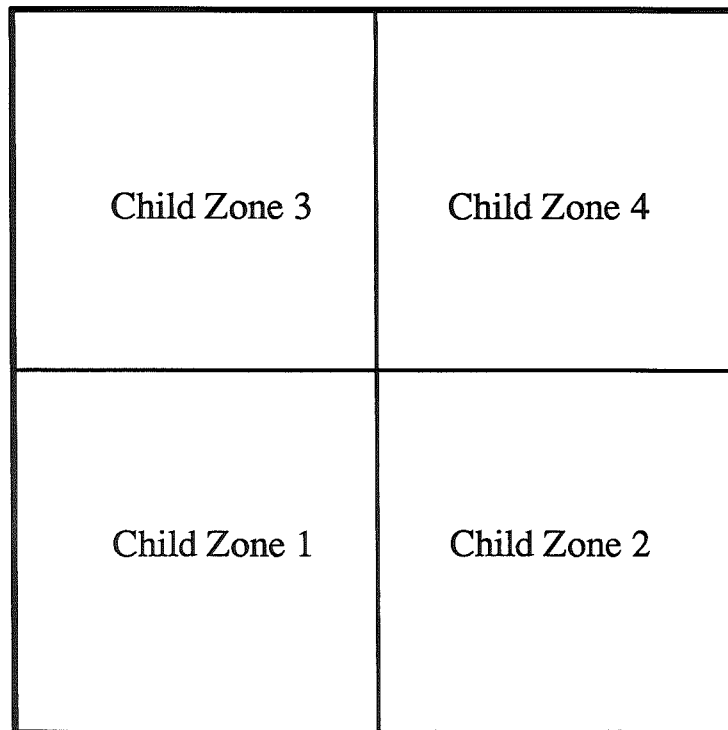
Division of Parent Zone into
Four Child Zones in Order Shown.

Fig. 3.16 - Numbering of Child Zones in Zonal Decomposition Algorithm.
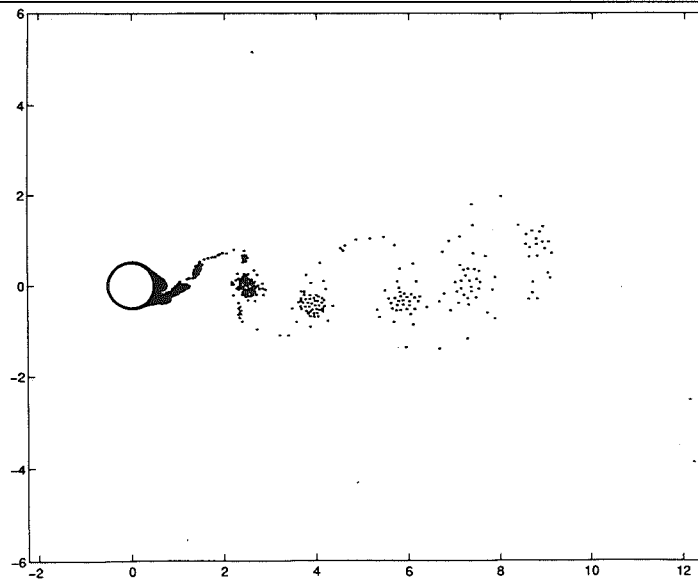
a) Initial Flow Field.
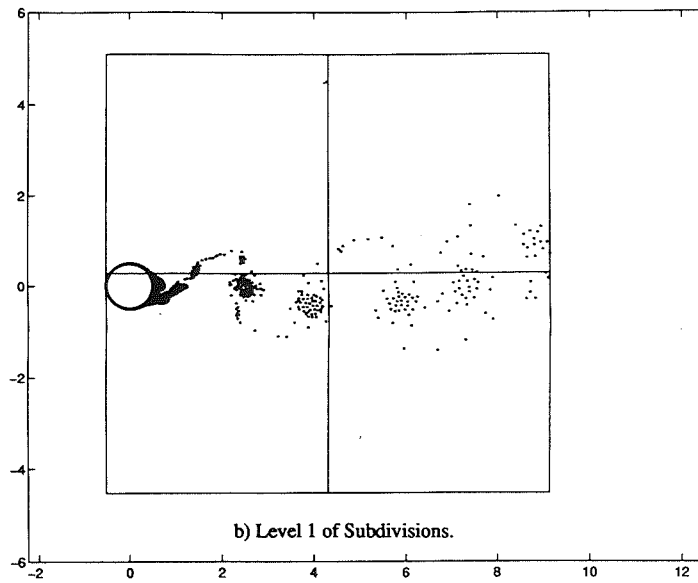
b) Level 1 of Subdivision.
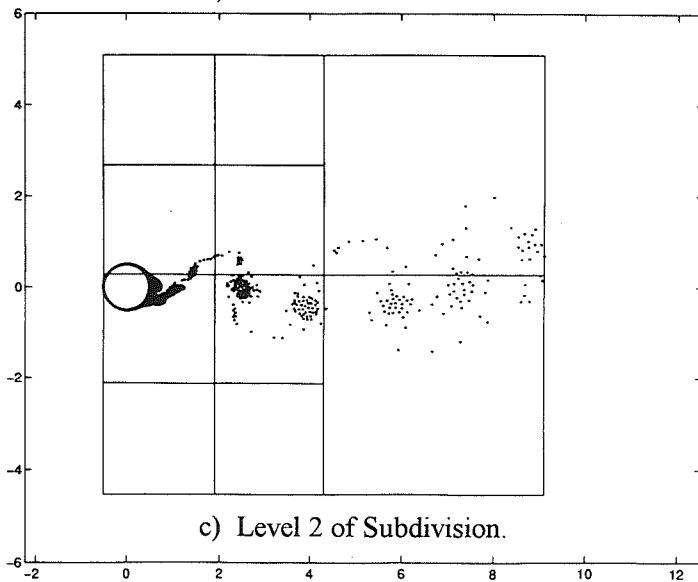
c) Level 2 of Subdivision.

Fig. 3.17 - Decomposition of Flow Field in Hierarchical Zonal Structure.
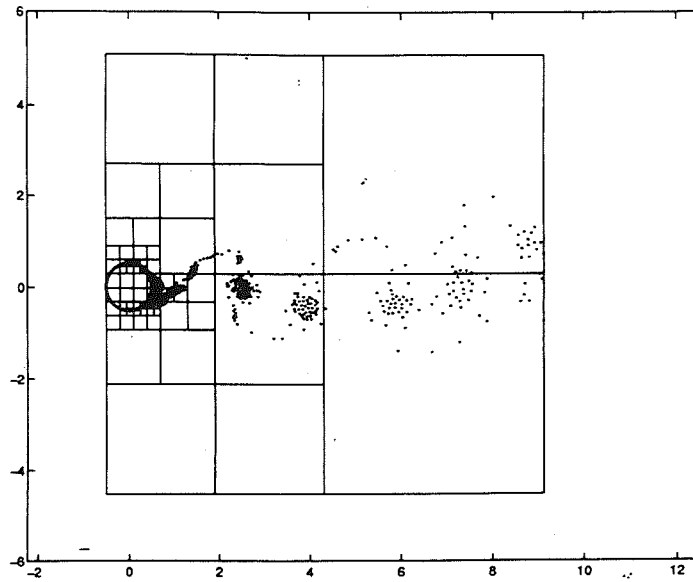
d) Resultant Zonal Decomposition of Flow Field.
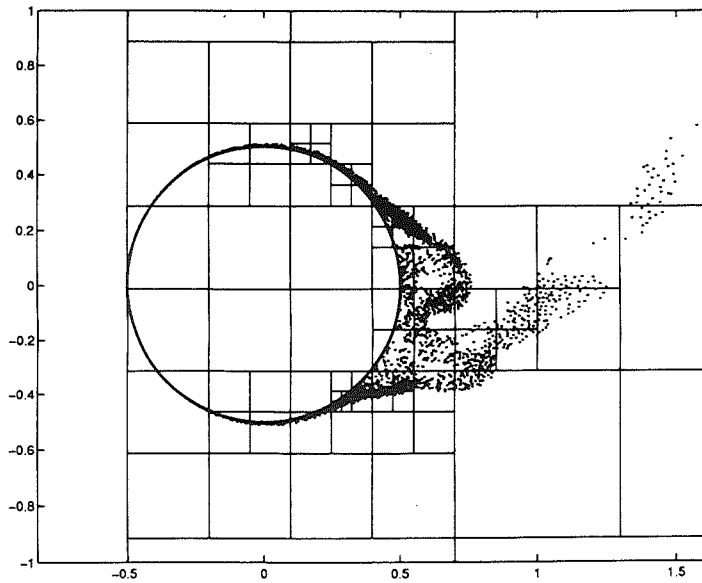
e) Close of Zonal Decomposition around Body.

Fig. 3.17 - Decomposition of Flow Field into Hierarchical Zonal Structure.

Zone A containing
Np particles.
Centre Z_c
Radius R.

Vortex at z_k
Circulation G_k

Z_c

R

2R

Z
O

Vortex at Z −
use series expansion.
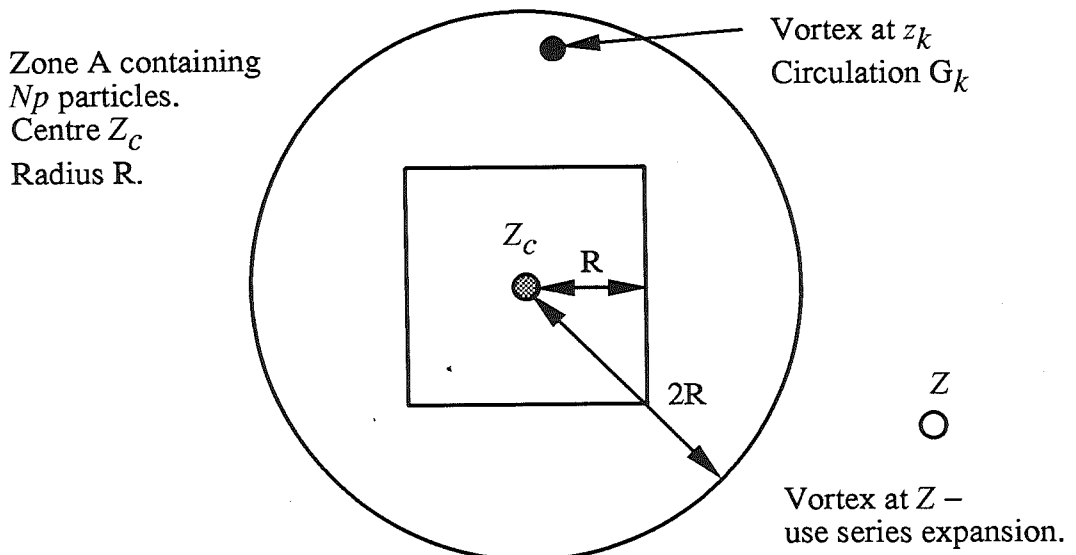
Fig. 3.18 - Nomenclature for Zone and Particles in Zonal Decomposition Algorithm.

Algorithm For Velocity Calculation using Zonal Decomposition.

Algorithm performed in a single pass over all vortex particles.

† At lowest level, contribution of other particles in zone calculated from direct summation later in algorithm.

Fig. 3.19 - Flowchart for Velocity Calculation using Series Expansion and Zonal Decomposition.

Sample Flow Field and Zonal Decomposition
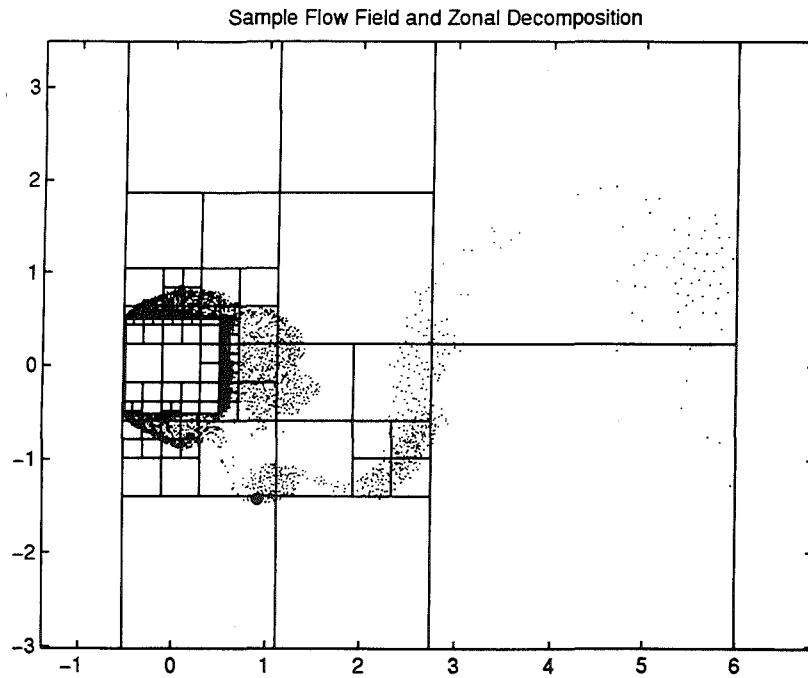
a) Sample Flow Field - Zonal Decomposition and Point at which Velocity Calculated.

= Use Series Expansion in Velocity Calculation

= Use Direct Summation in Velocity Calculation

⊙ = Point at Which Velocity is being Calculated

Use of Series Expansion in Zonal Decomposition Algorithm
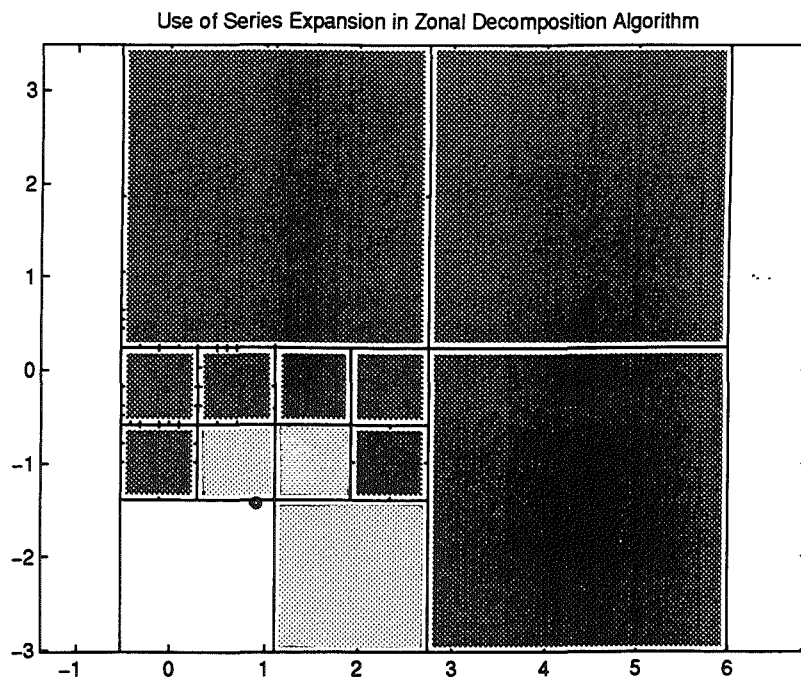
b) Illustration of Zones used in the Series Expansion part of Velocity Calculation.

Fig. 3.20 - Example Illustrating use of Series Expansion and Zonal Decomposition in Velocity Calculation.
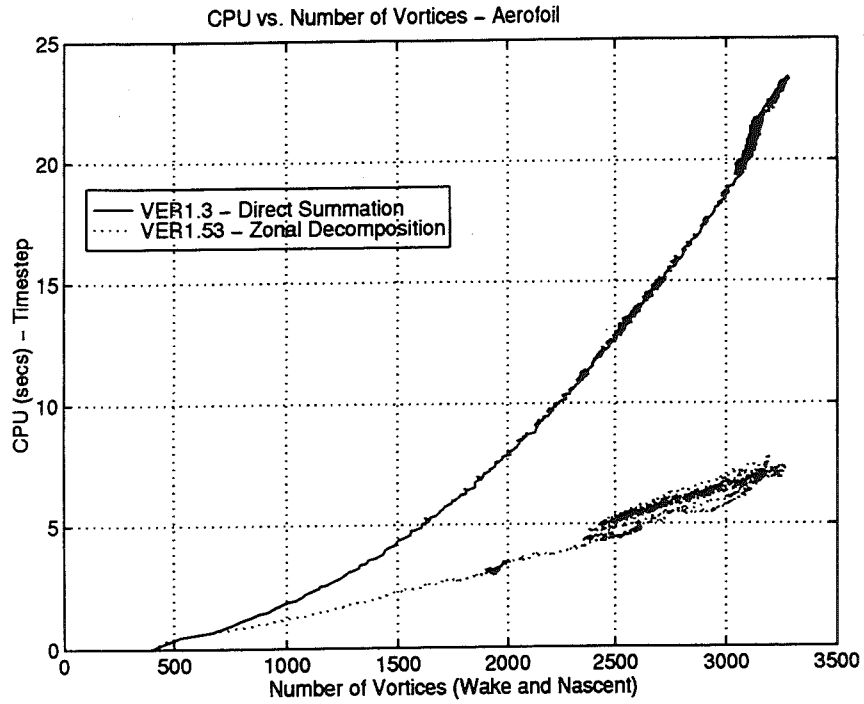
a) Full Time Step.
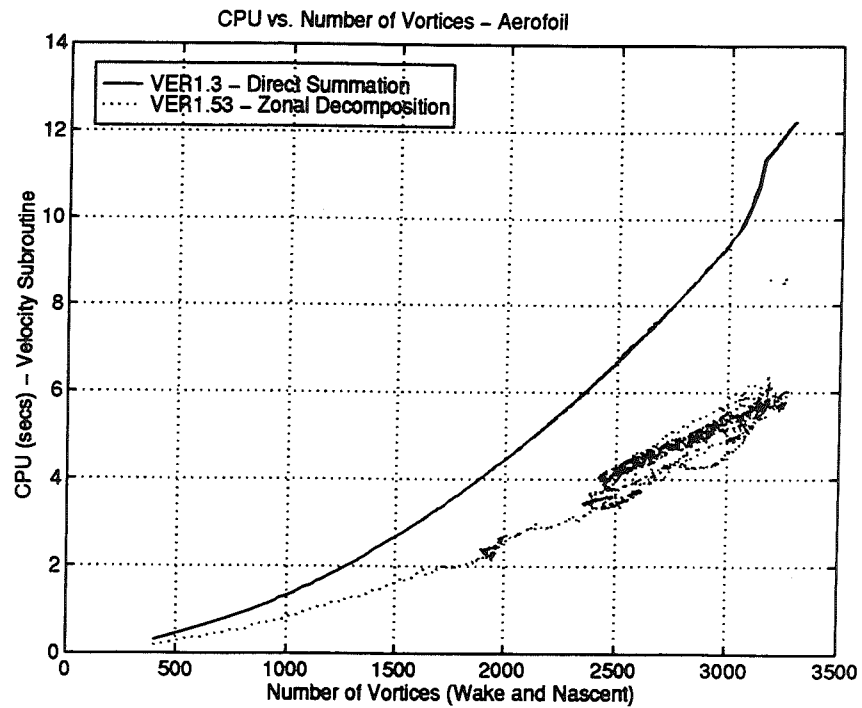
b) Velocity Calculation only.

Fig. 3.21 - Comparison of CPU Required for Direct Summation and Zonal Decomposition :
Aerofoil Test Case.
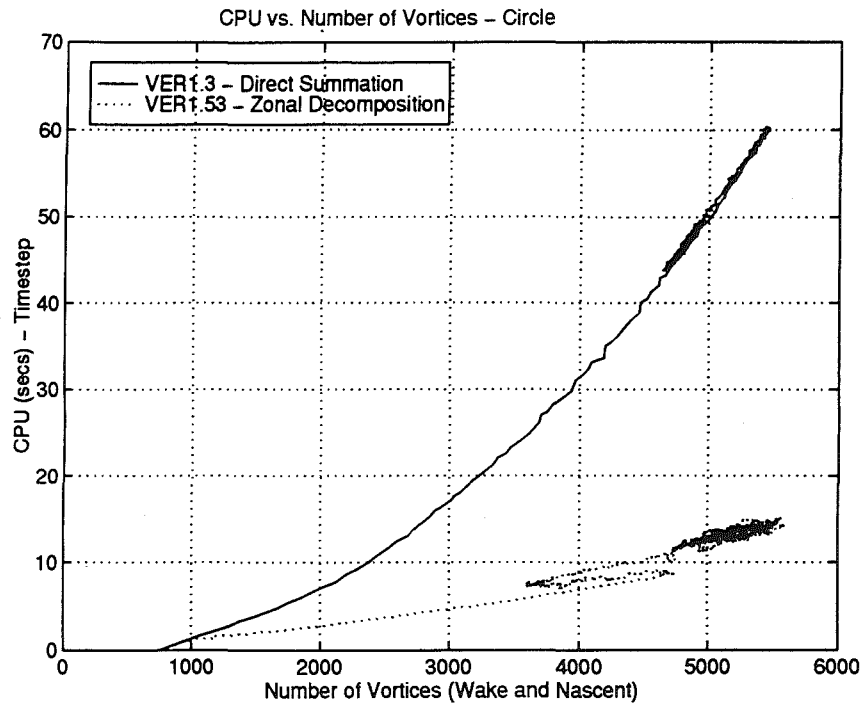
a) Full Time Step.
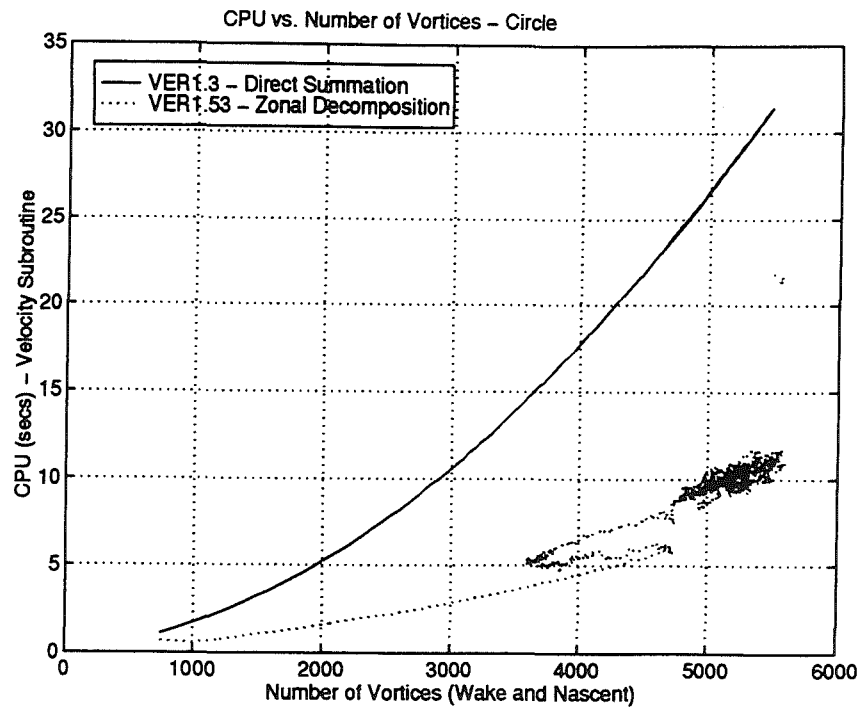
b) Velocity Calculation only.

Fig. 3.22 - Comparison of CPU Required for Direct Summation and Zonal Decomposition :

Circle Test Case.
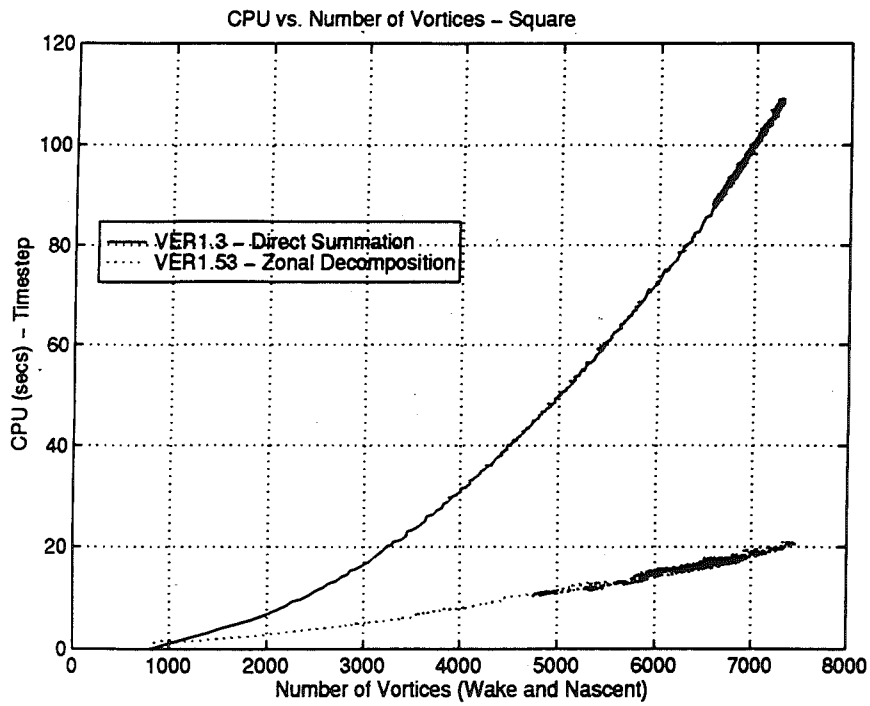
a) Full Time Step.
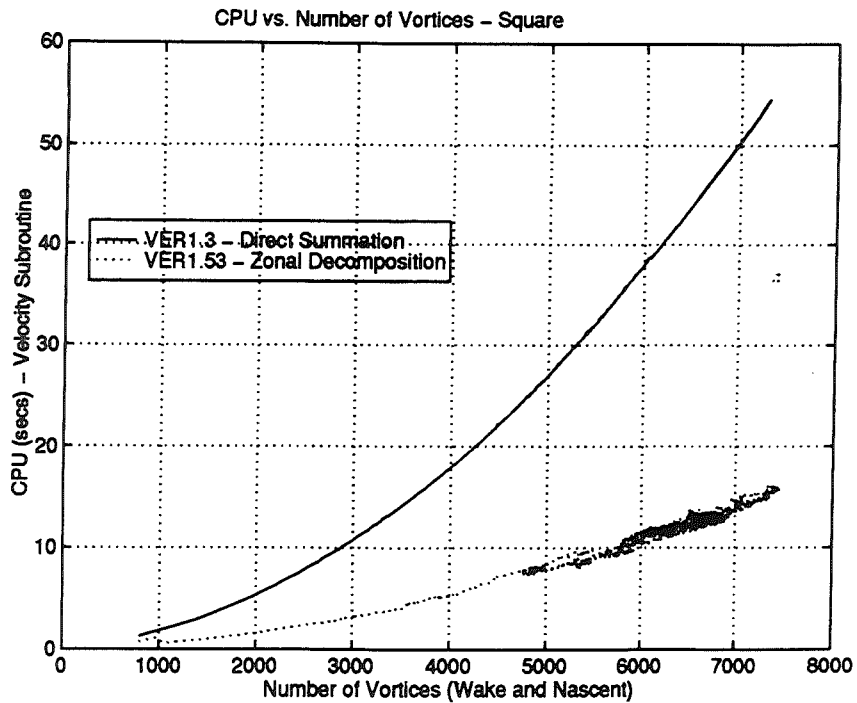
b) Velocity Calculation only.

Fig. 3.23 - Comparison of CPU Required for Direct Summation and Zonal Decomposition : Square Test Case.
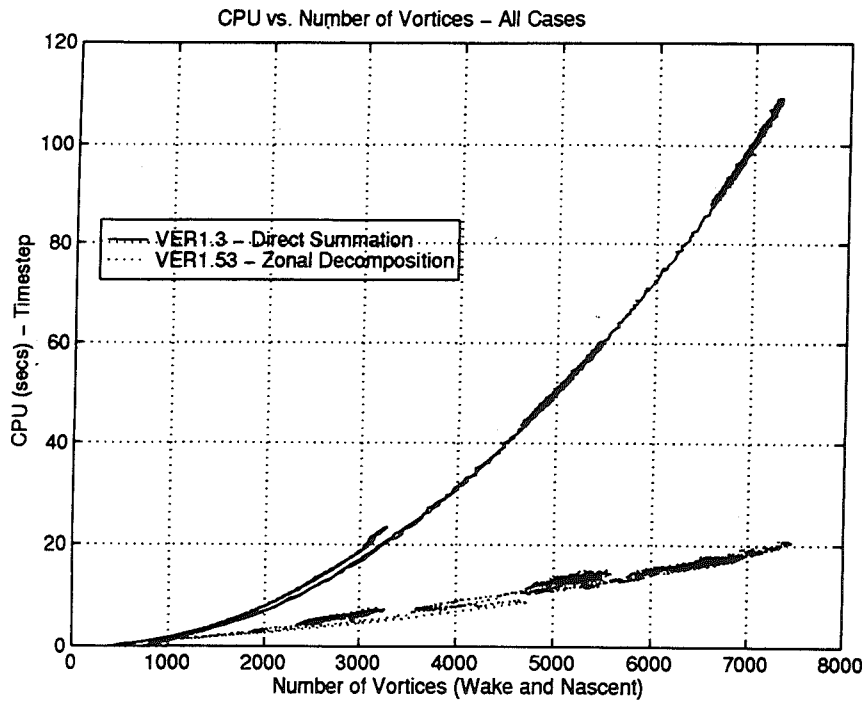
a) Full Time Step.
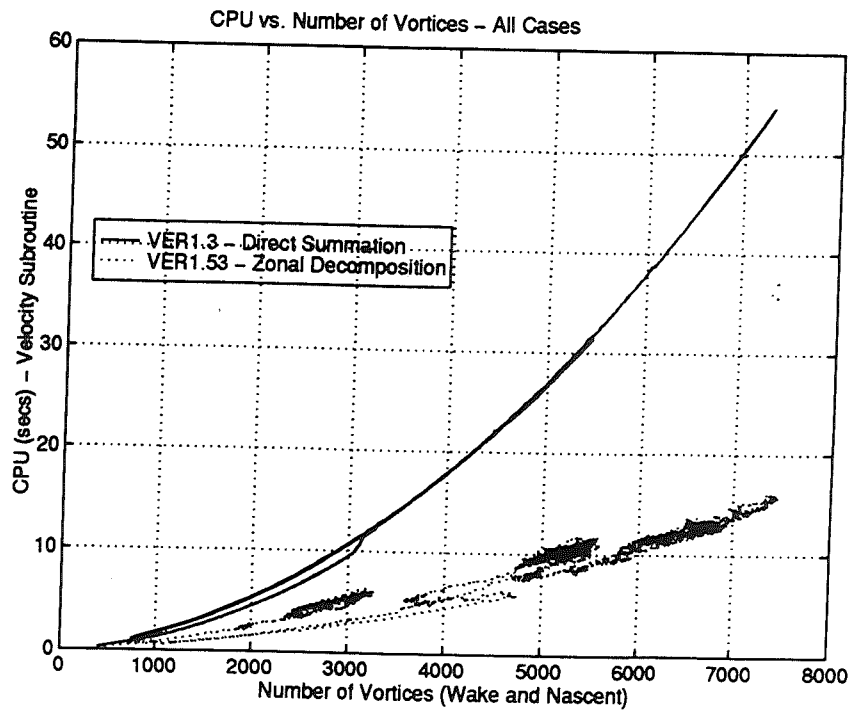
b) Velocity Calculation only.

Fig. 3.24 - Comparison of CPU Required for Direct Summation and Zonal Decomposition : All Test Cases.

Curve fit to CPU for VER1.3 (Direct Summation)

Time=cN**2   c=2.0411e-6

a) Full Time Step.

Curve fit to CPU for VER1.3 (Direct Summation)

Time=cN**2   c=1.0421e-6
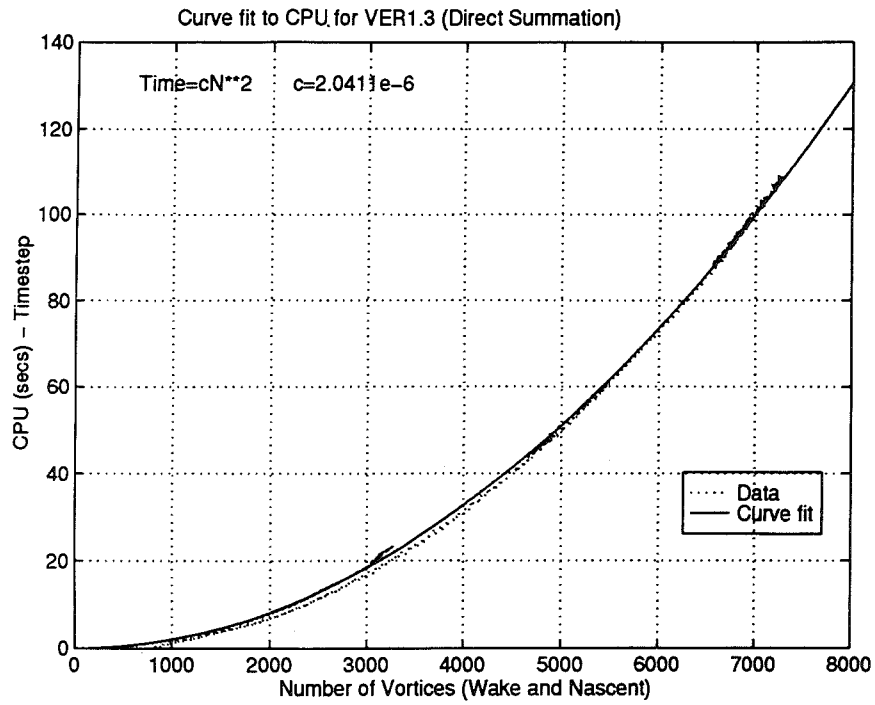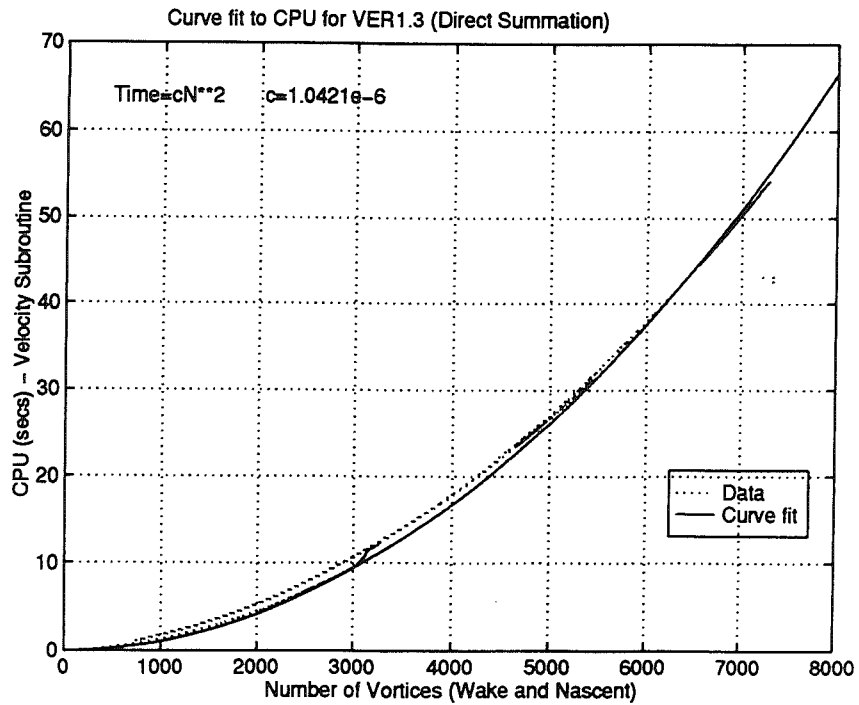
b) Velocity Calculation only.

Fig. 3.25 - Curve Fit to CPU Required for Direct Summation Method.

Time=aN+bNlogN· a=-2.9832e-3, b=1.4547e-3
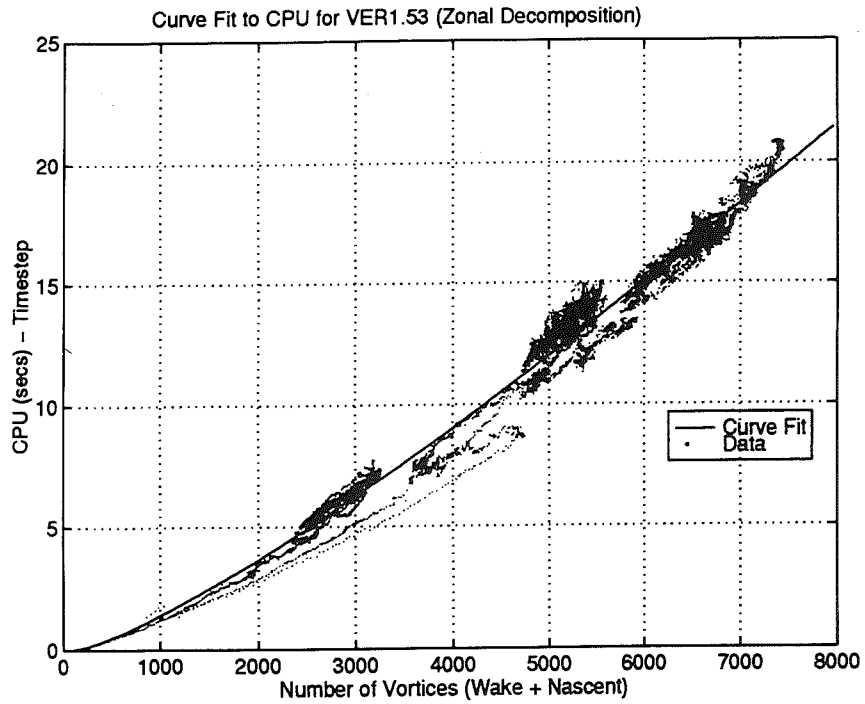
a) Full Time Step.

Time=aN+bNlogN a=-1.6905e-3, b=9.4648e-4
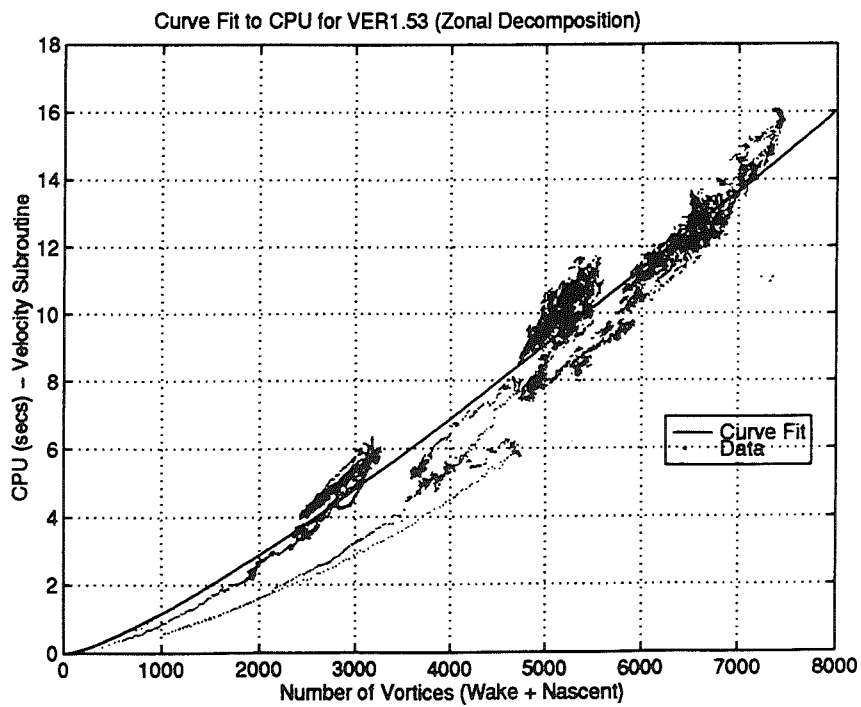
b) Velocity Calculation only.

Fig. 3.26 - Curve Fit to CPU Required for Zonal Decomposition Method.
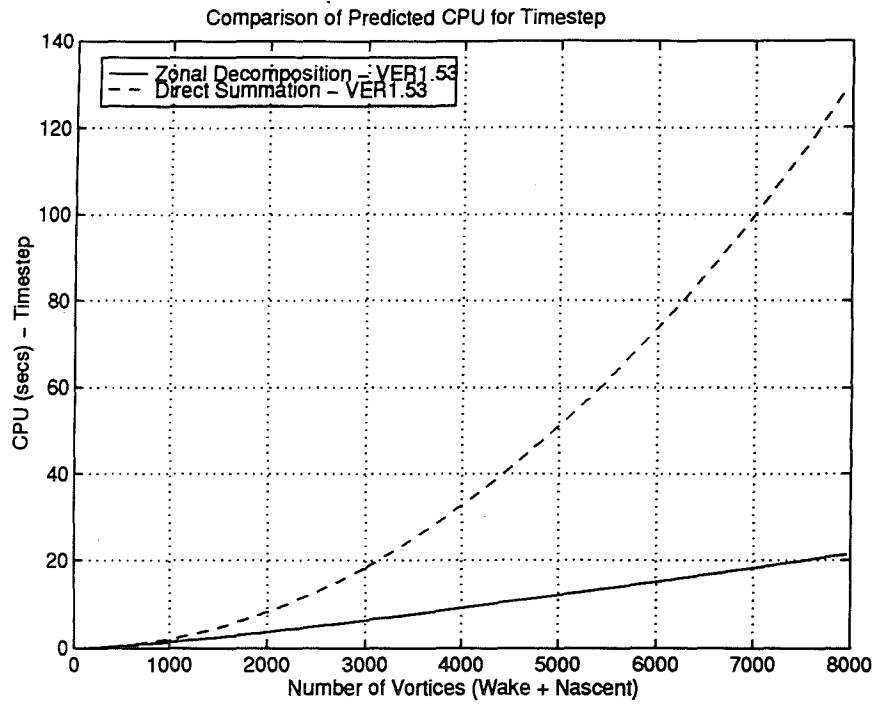
a) Comparison of Predicted CPU for each Method.
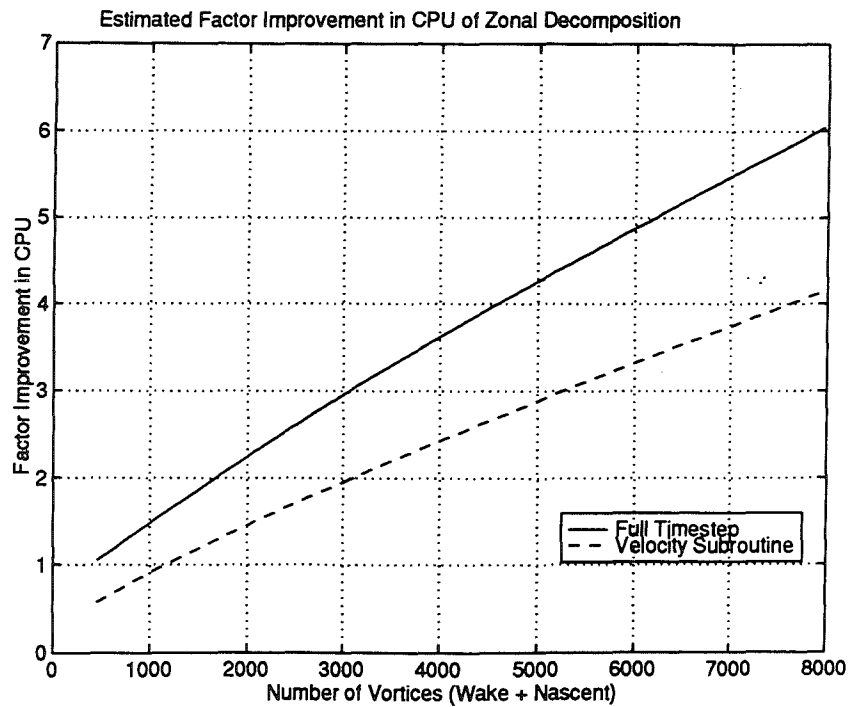
b) Factor Improvement Obtained from Zonal Decomposition Algorithm.

Fig. 3.27 - Comparison of Curve Fits to CPU Required for Direct Summation Method and Zonal Decomposition Method.
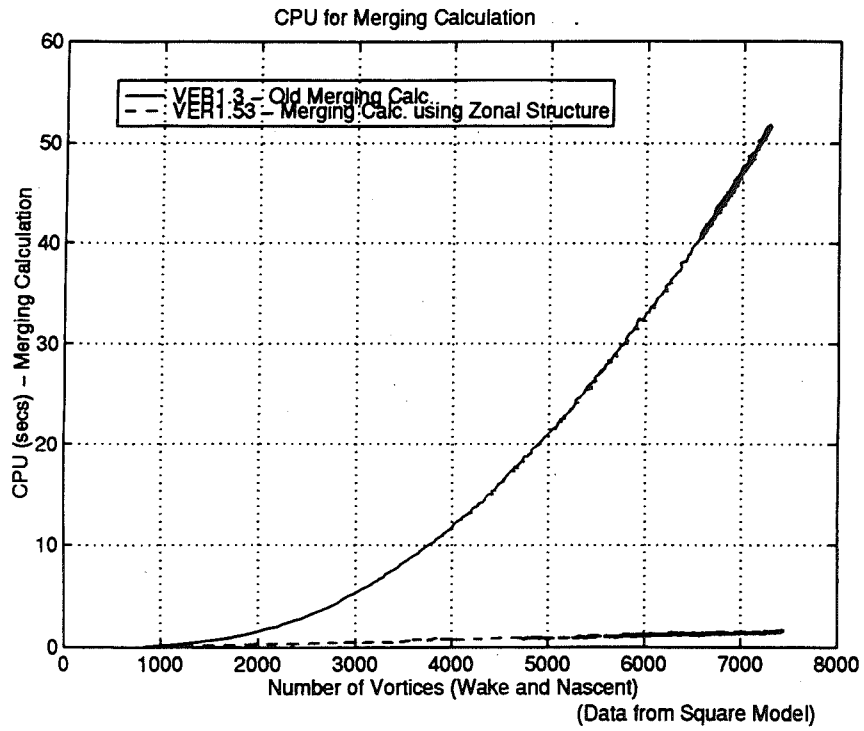
Fig. 3.28 - Comparison of CPU Required for Old and New Vortex Merging Calculation.
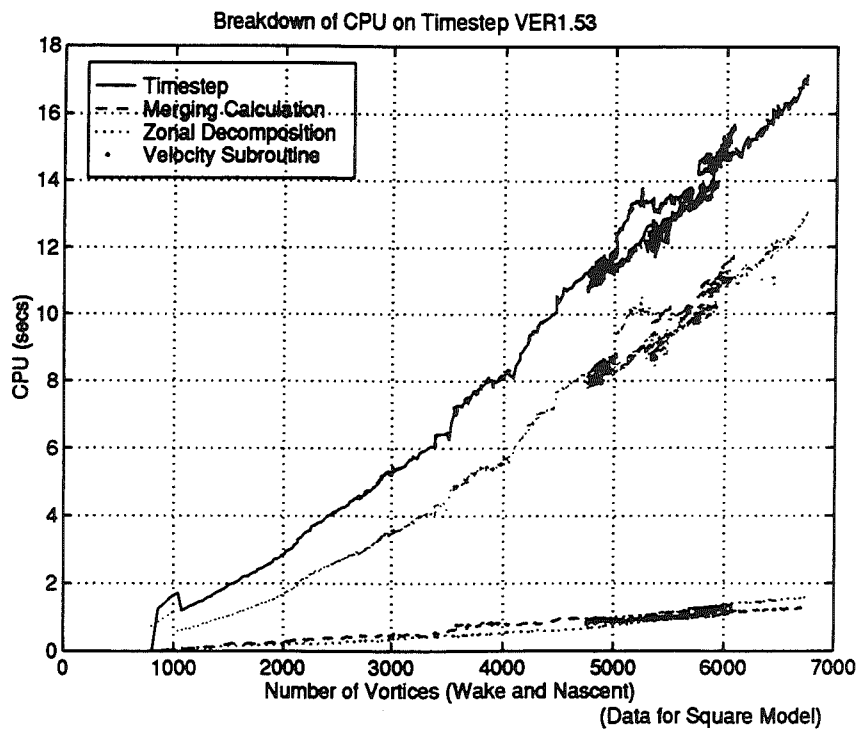
Fig. 3.29 - Analysis of CPU for Time Step in Zonal Decomposition Algorithm.

Zonal Decomposition for Square Model – VER1.53

a) Whole Flow Field.

Zonal Decomposition for Square Model – VER1.53
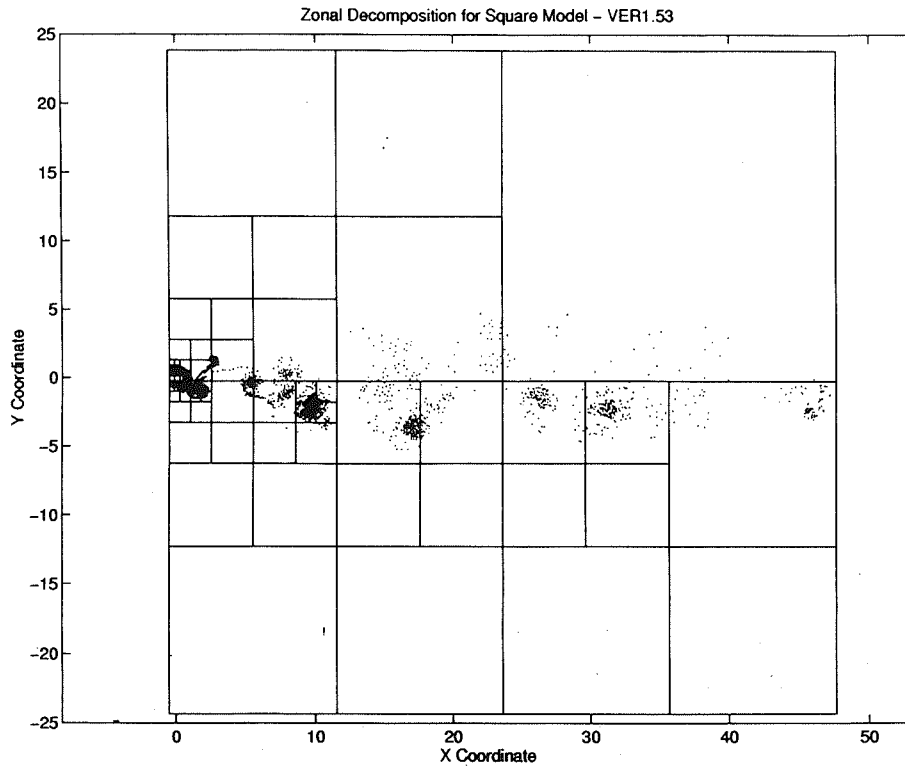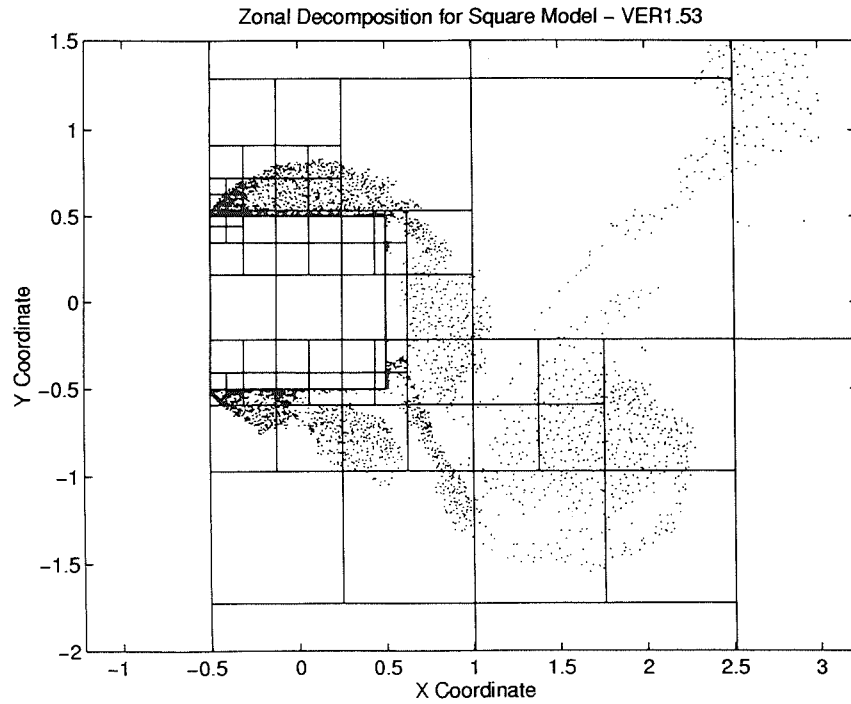
b) Close up of Zonal Decomposition around Body.

Fig. 3.30 - Sample Flow Field and Zonal Decomposition for Square Cylinder.
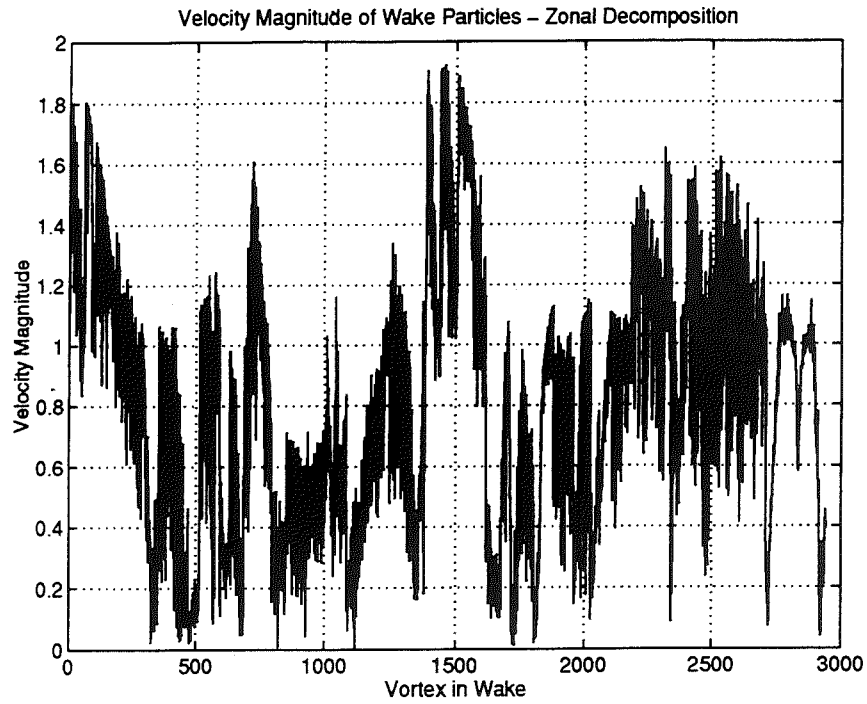
a) Velocity Magnitude.
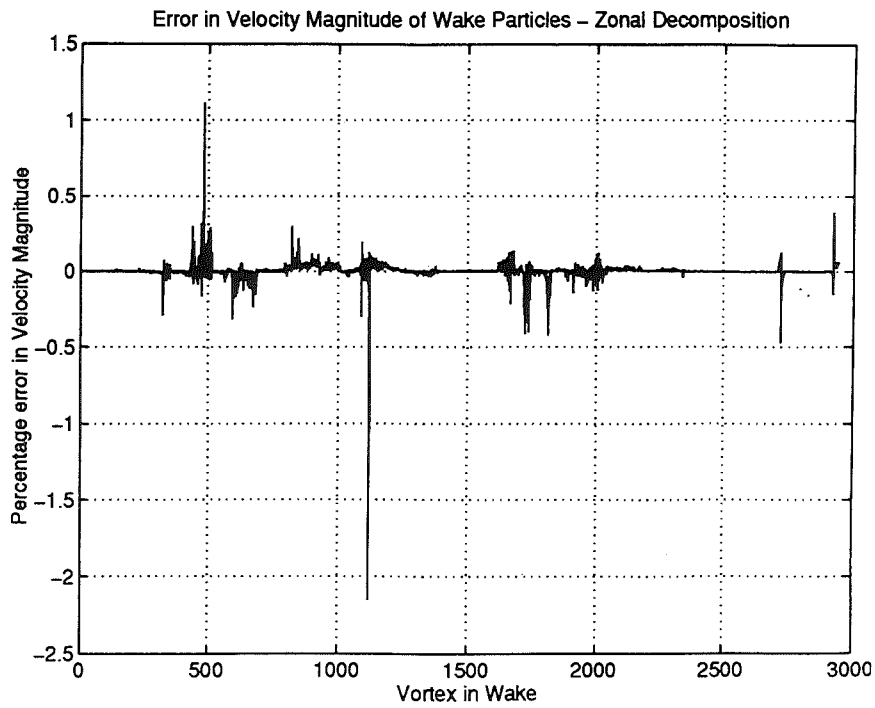
b) Percentage Error in Velocity Magnitude.

Fig. 3.31 - Analysis of Error in Velocity Magnitude Calculated by Zonal Decomposition for Wake Vortex Particles.

a) Zonal Decomposition.

b) Direct Summation
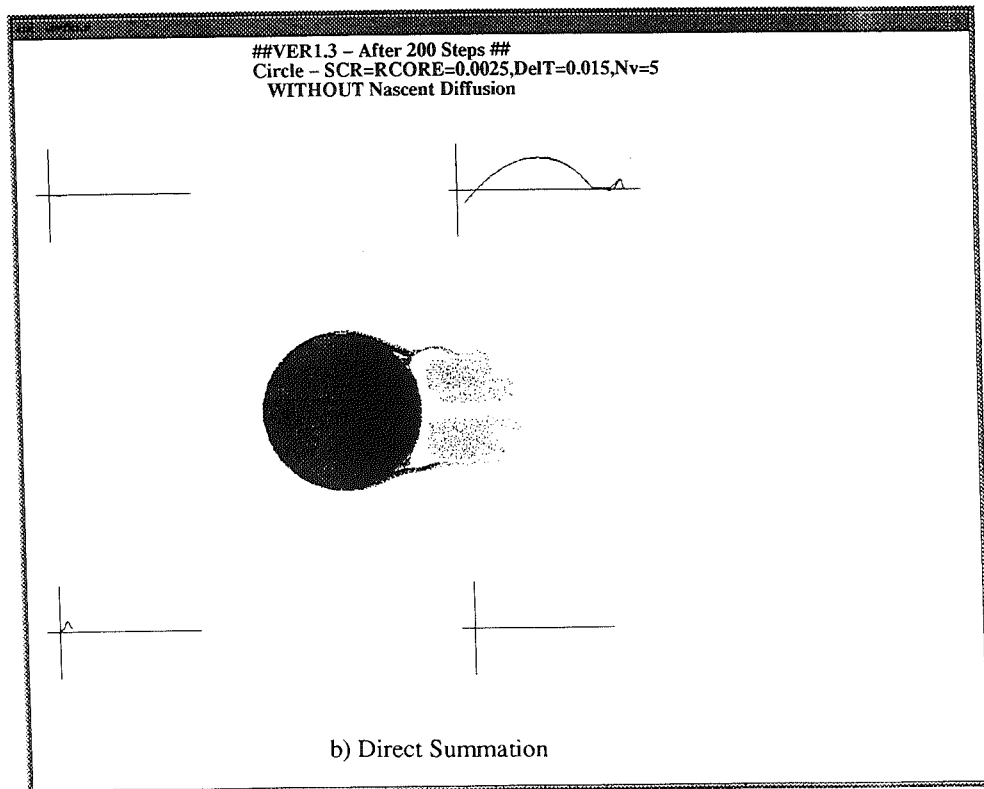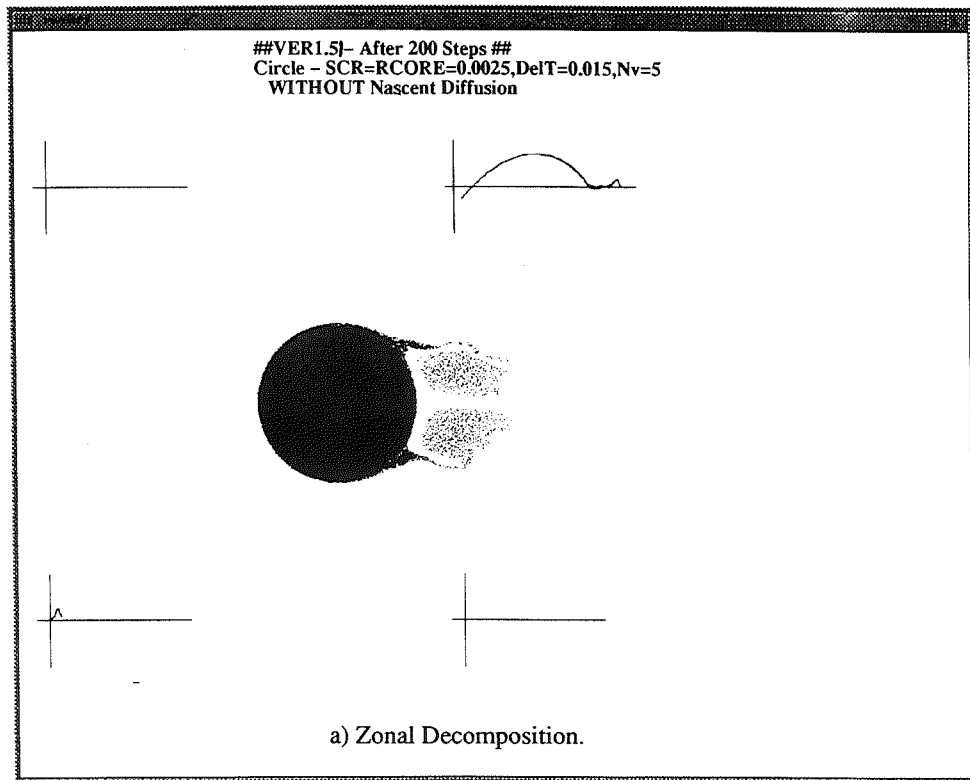
Fig. 3.32 - Comparison of Predicted Flow Field for Circular Cylinder after 200 Time Steps.
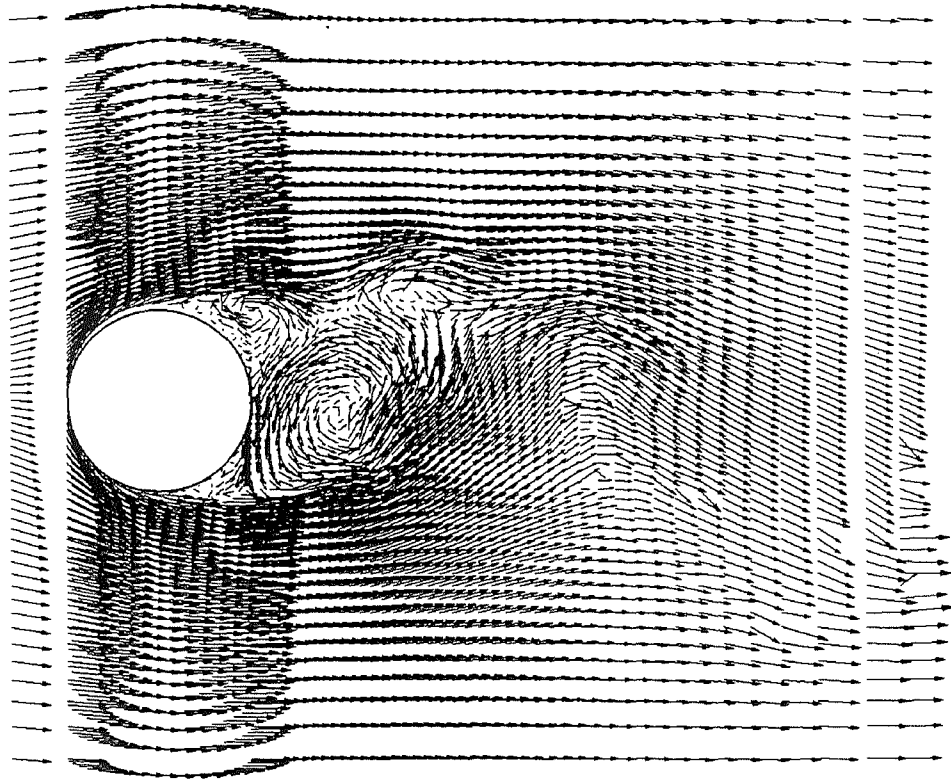
a) t*=161.0
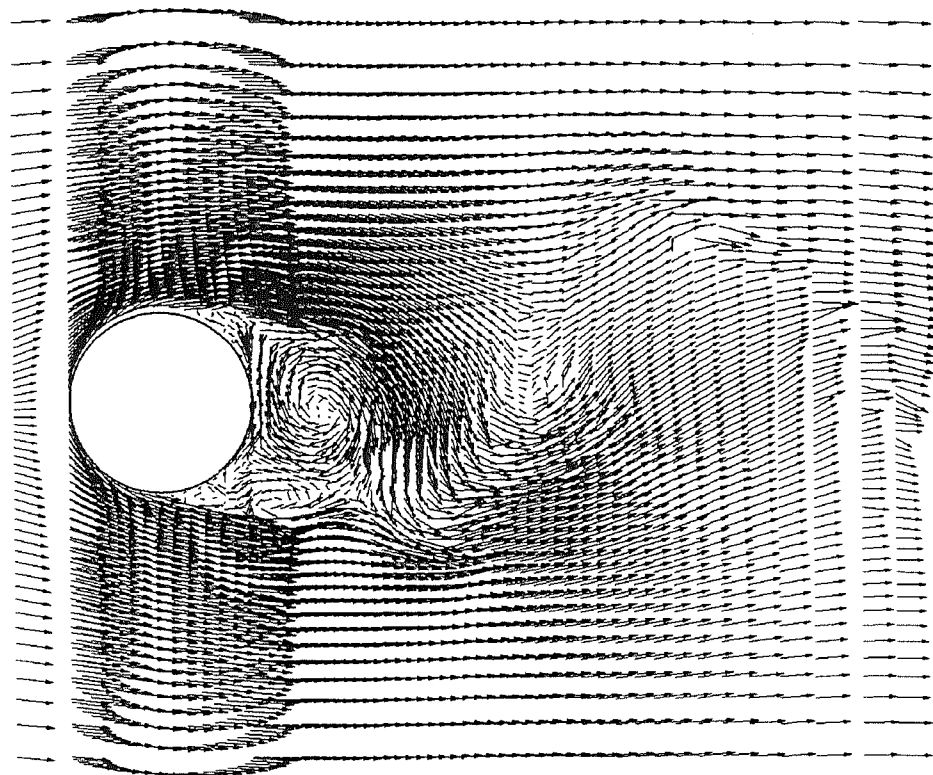
b) t*=163.0

Fig. 4.1 - Flow Field around Circular Cylinder Predicted by DVM for *Re*=20,000 : Velocity
Vectors.
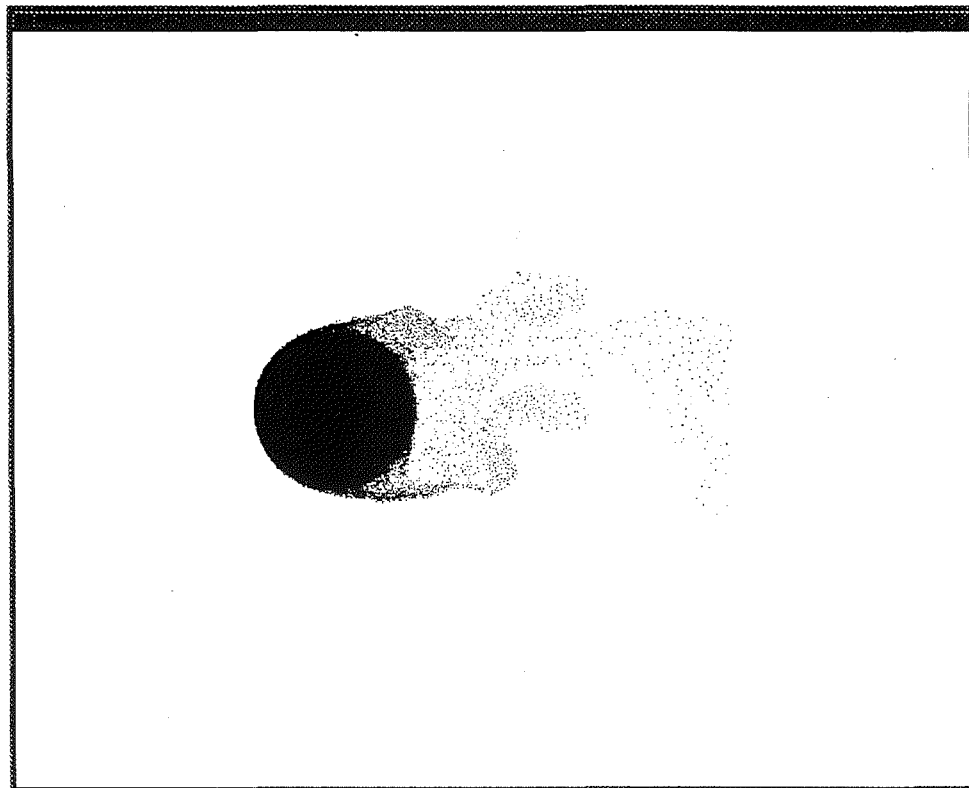
a) t*=161.0
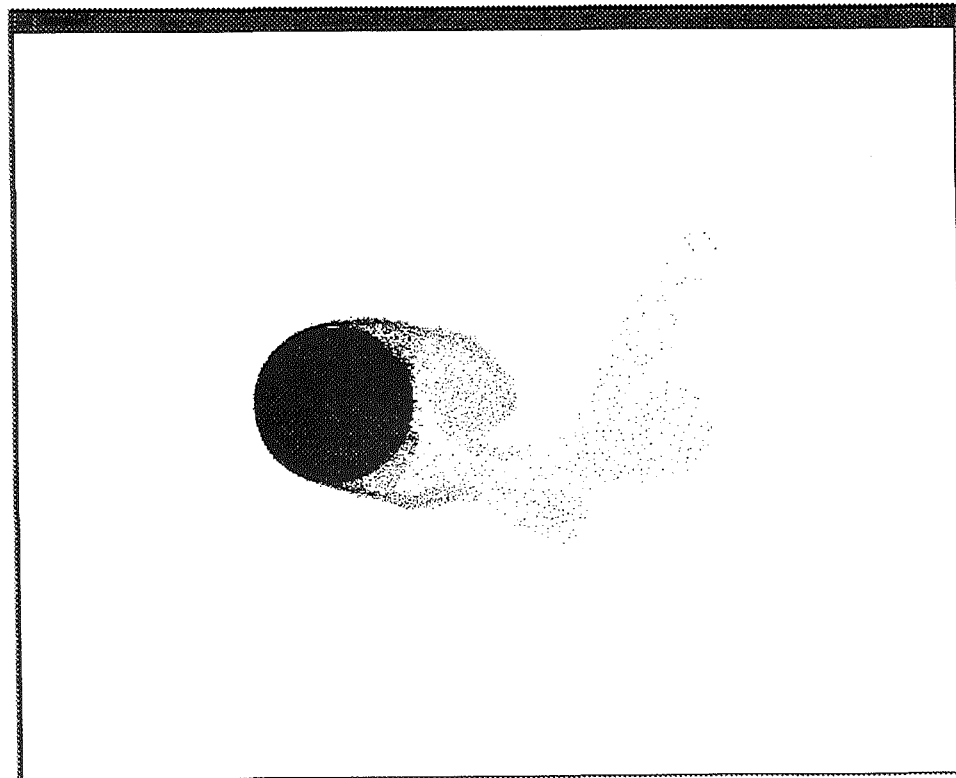
b) t*=163.0

Fig. 4.2 - Flow Field around Circular Cylinder Predicted by DVM for *Re*=20,000 : Vortex Particle Distribution.
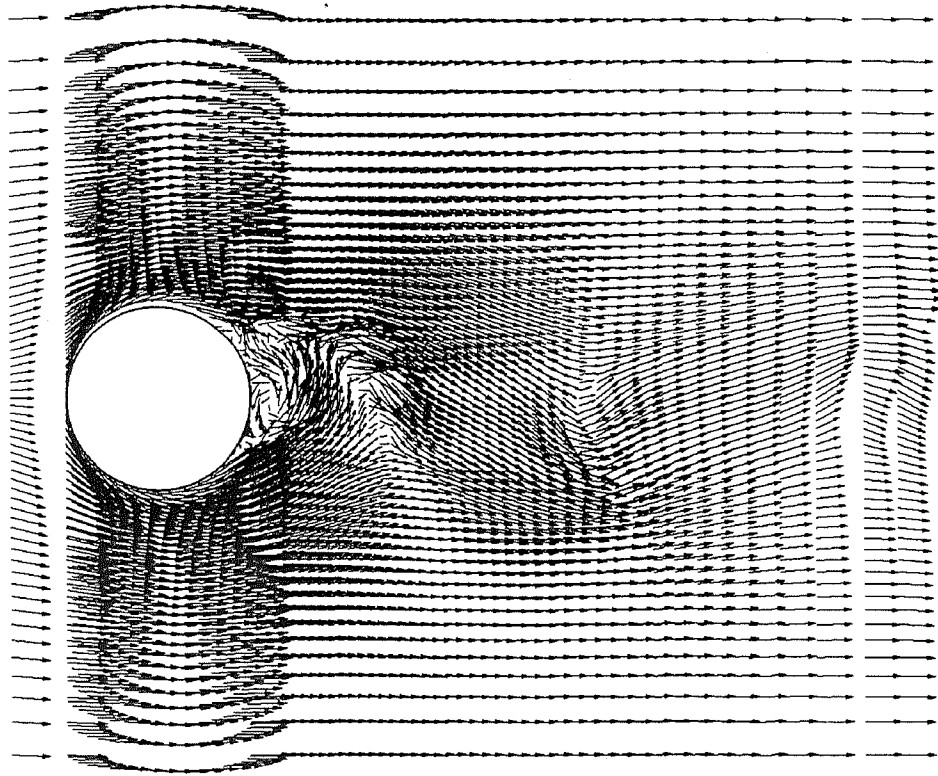
a) t*=28.0
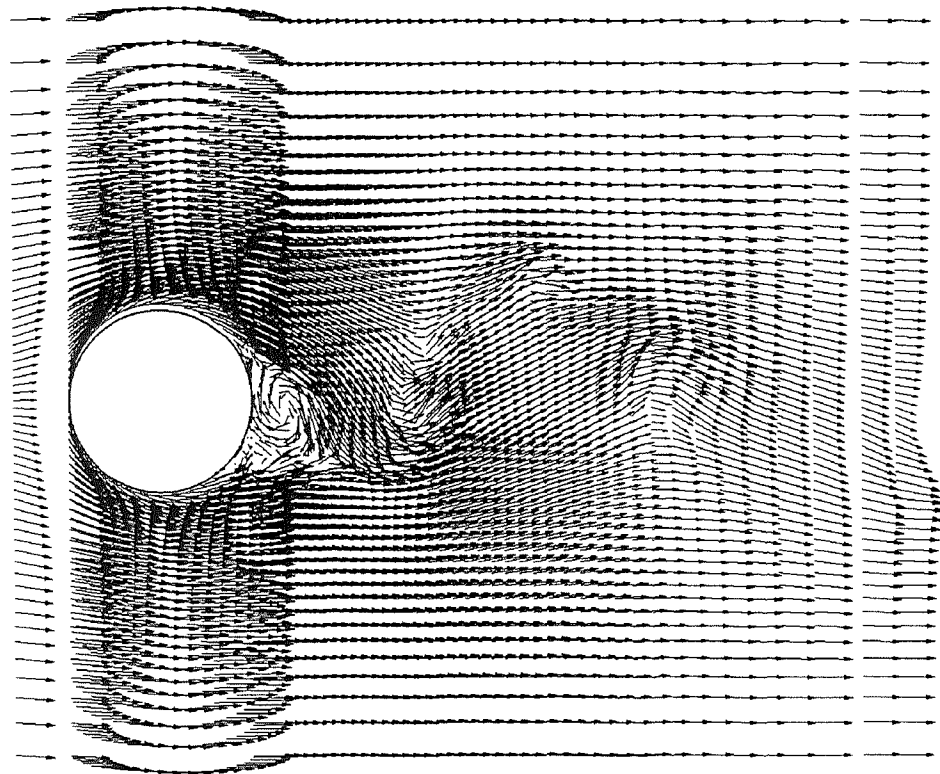
b) t*=30.0

Fig. 4.3 - Flow Field around Circular Cylinder Predicted by DVM for $Re=10^6$: Velocity Vectors.
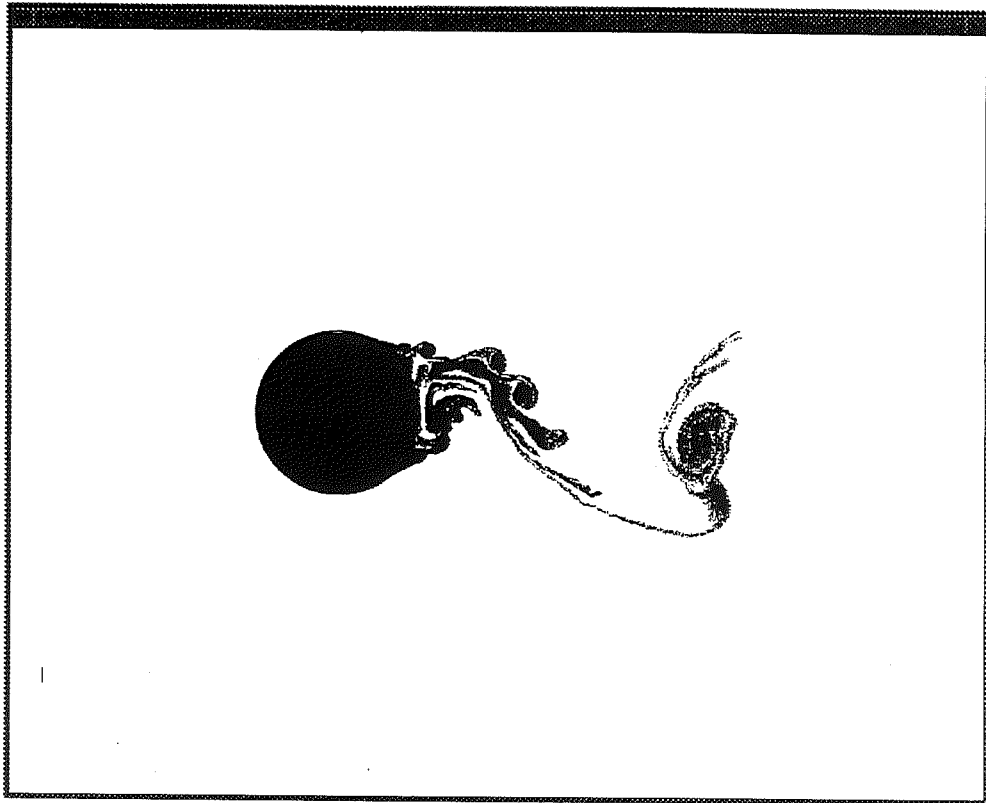
a) t*=28.0
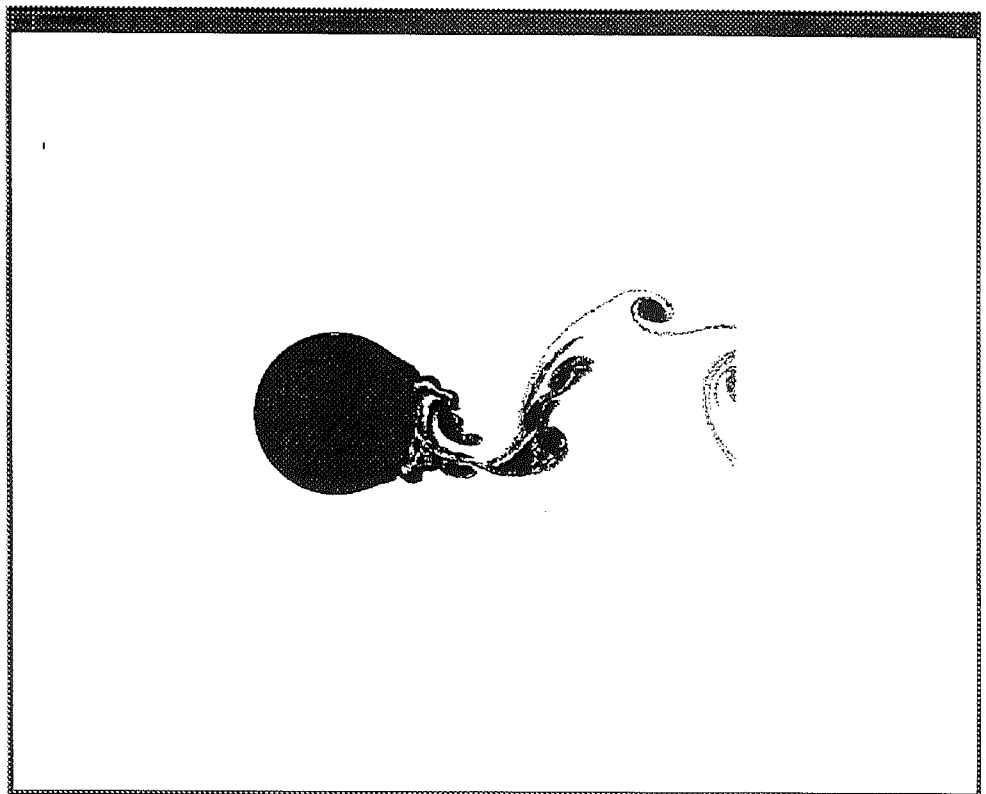
b) t*=30.0

Fig. 4.4 - Flow Field around Circular Cylinder Predicted by DVM for $Re=10^6$: Vortex Particle

Distribution.
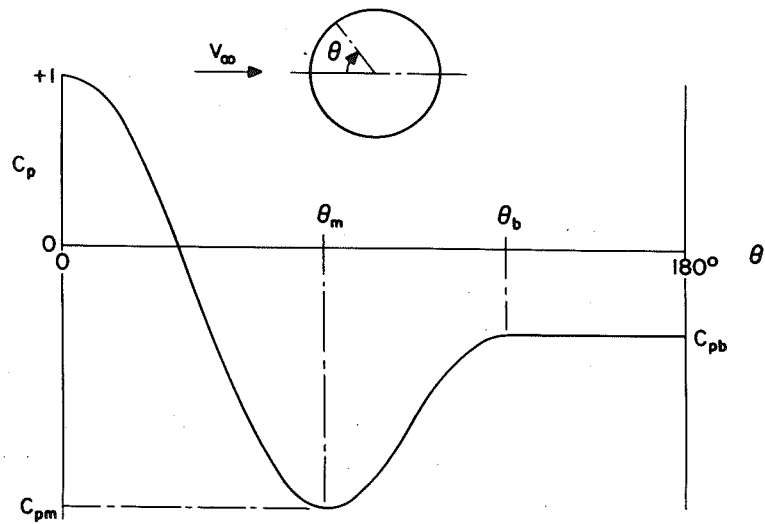
Fig. 4.5 -Mean Pressure Distribution on Circular Cylinder and Defining Parameters (from ESDU 1980 [10]).
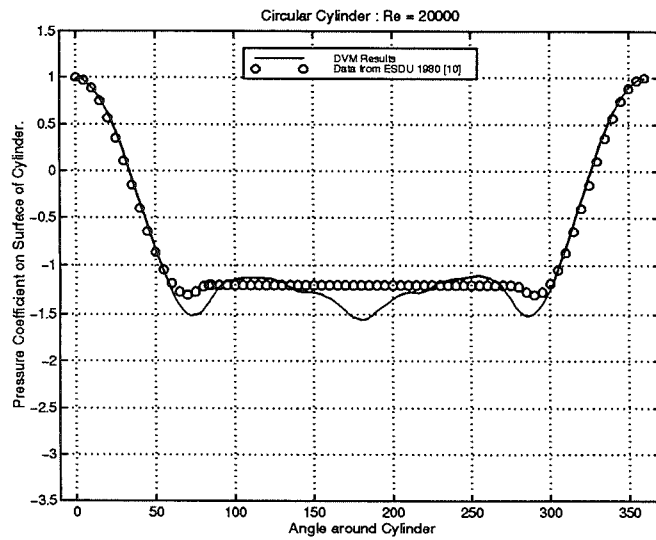
a) Re=20,000
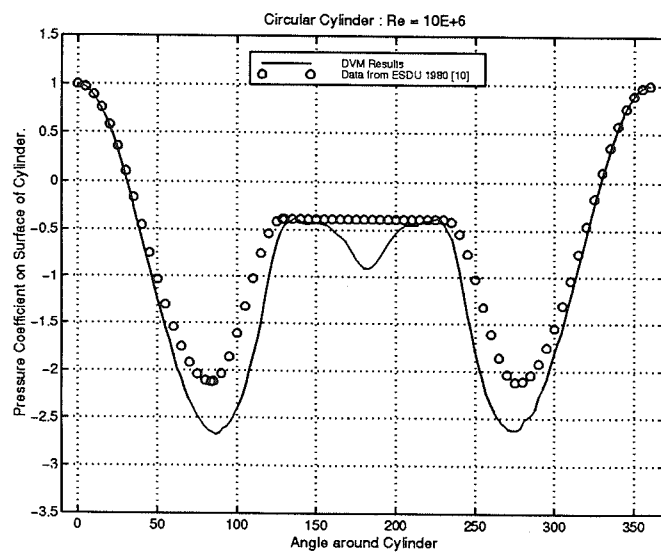
b) Re=10^6

Fig. 4.6 - Comparison of Predicted Pressure Coefficient on Circular Cylinder with Experiment.
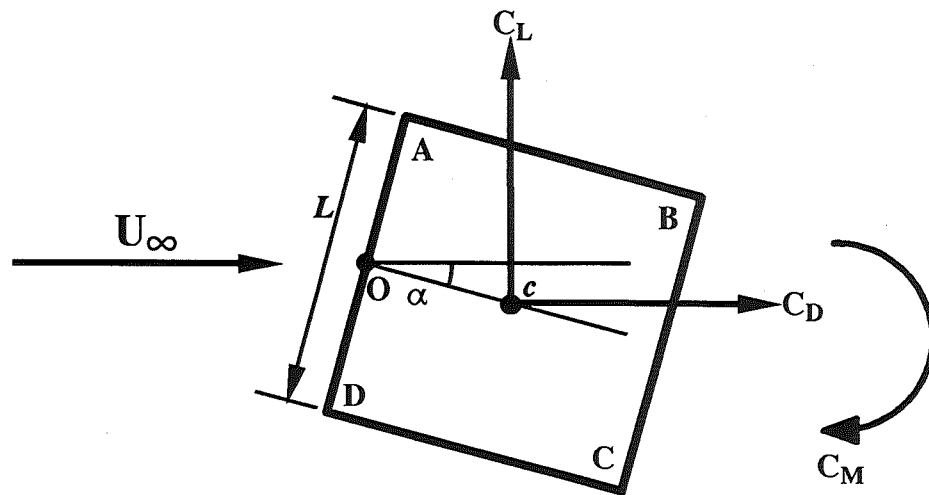
a) Static Cylinder
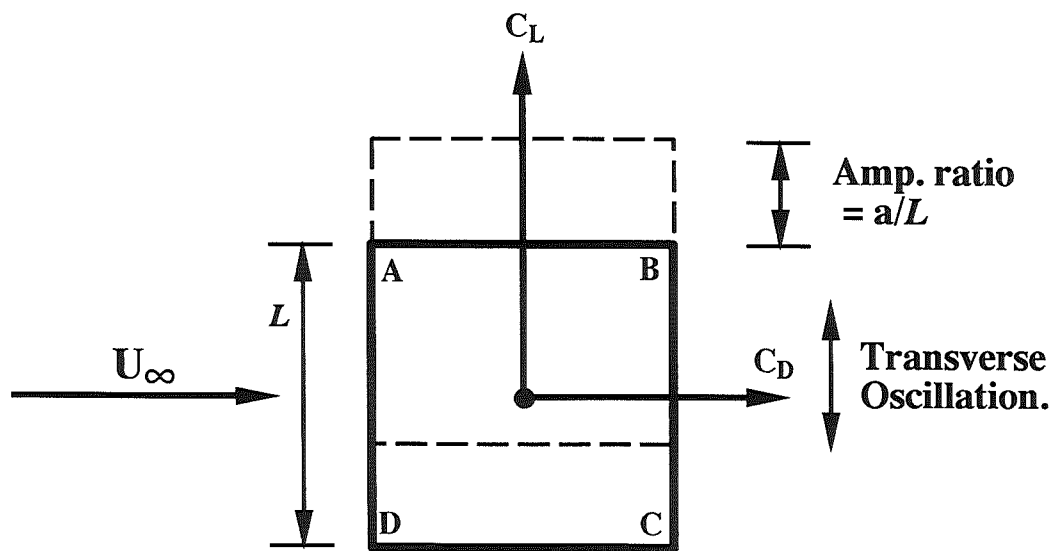
b) Transversely Oscillating Cylinder.

Fig. 4.7 - Labelling and Orientation of Square Cylinder.
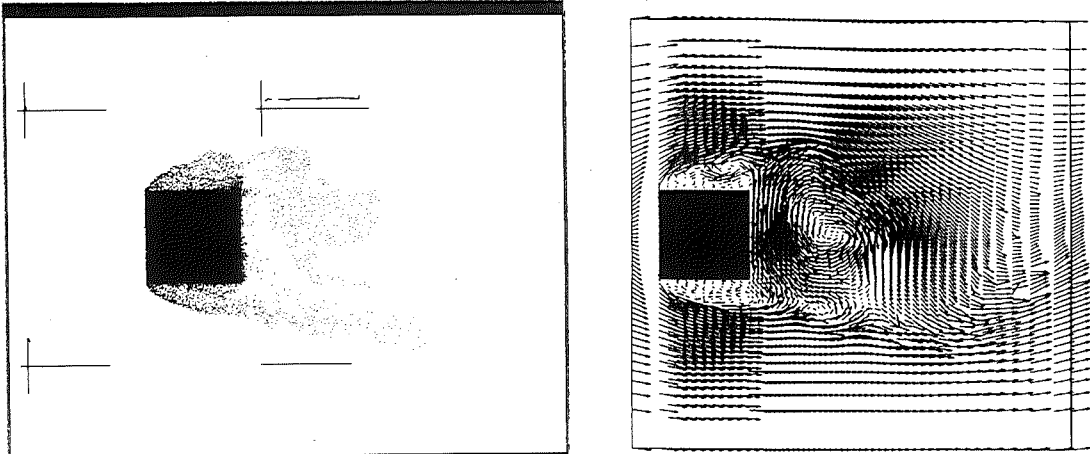
a) $t^* = 181.0$ ($t^* = tD/U$)
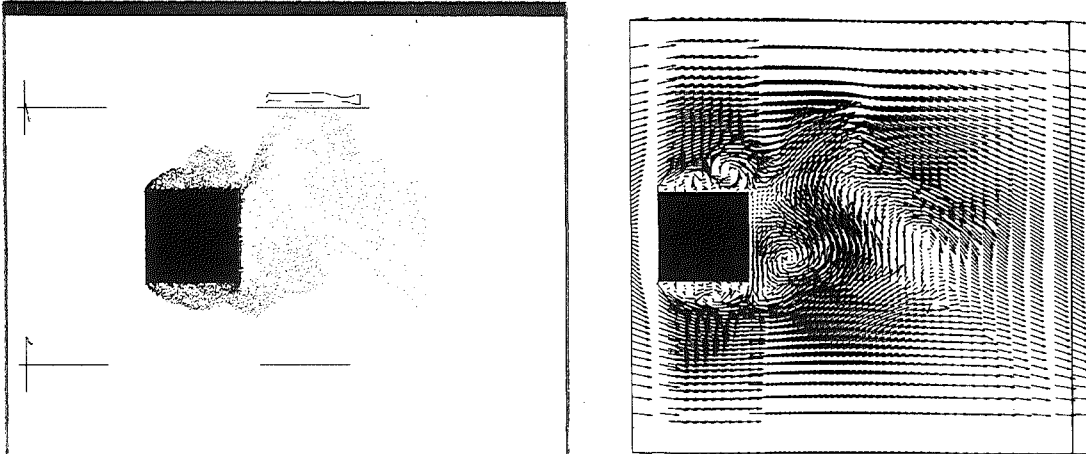
b) $t^* = 183.0$
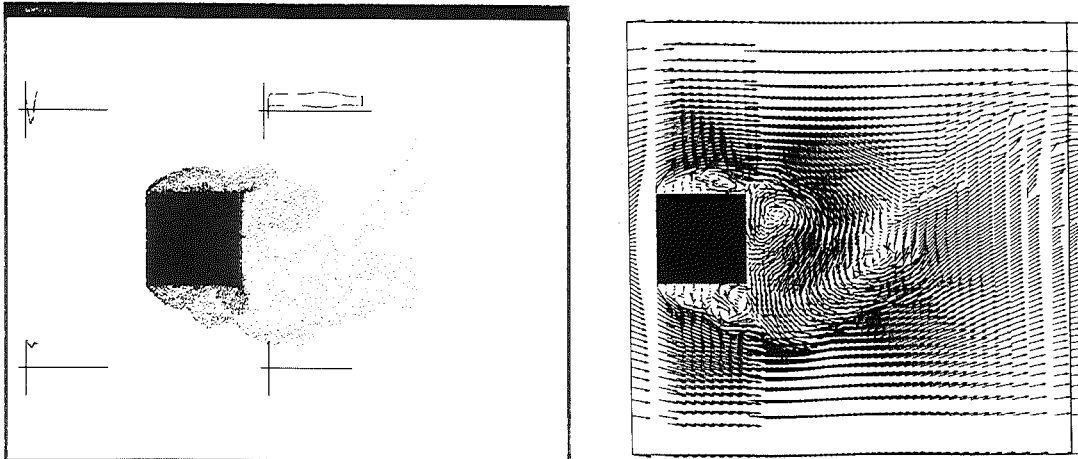
c) $t^* = 186.0$

Fig. 4.8 - Square Section Cylinder at 0° Incidence : Visualisation of Vortex Shedding.
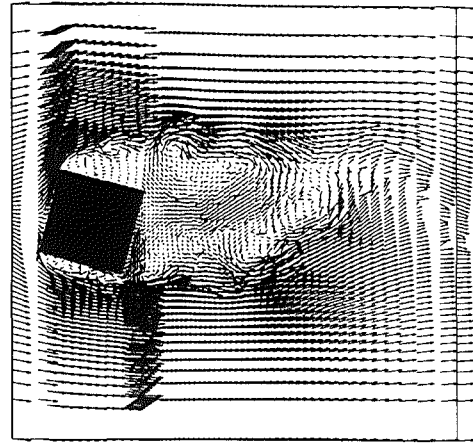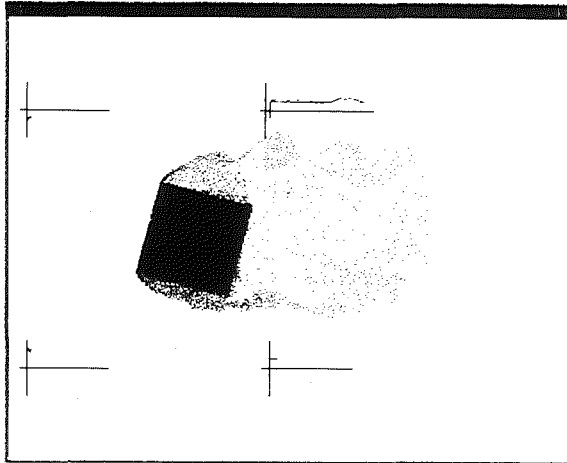
a) $t^* = 142.0$ ($t^* = tD/U$)
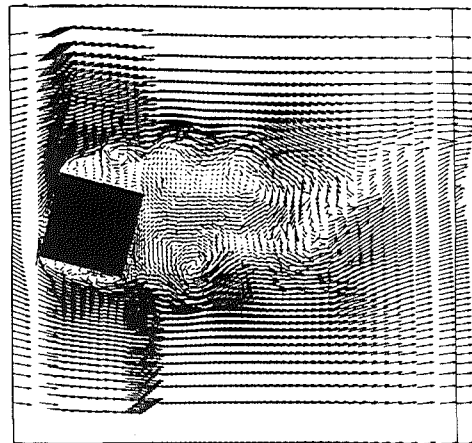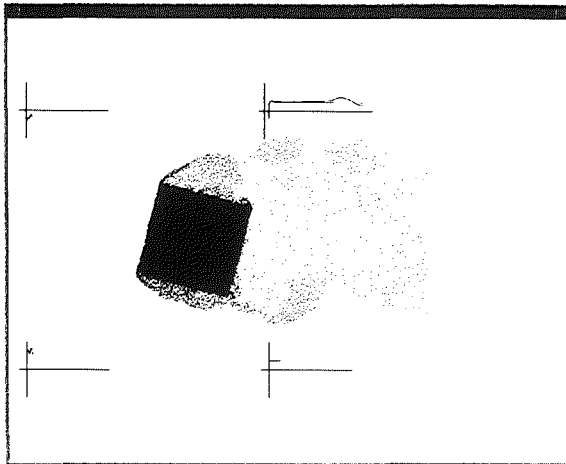
b) $t^* = 143.0$
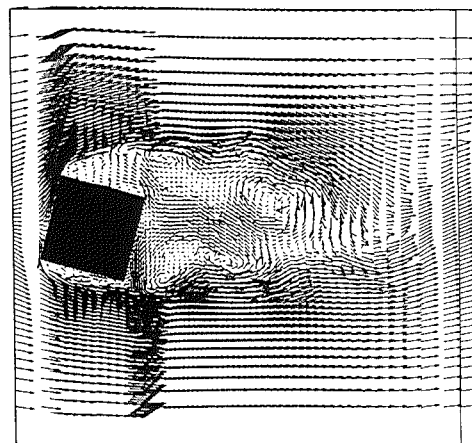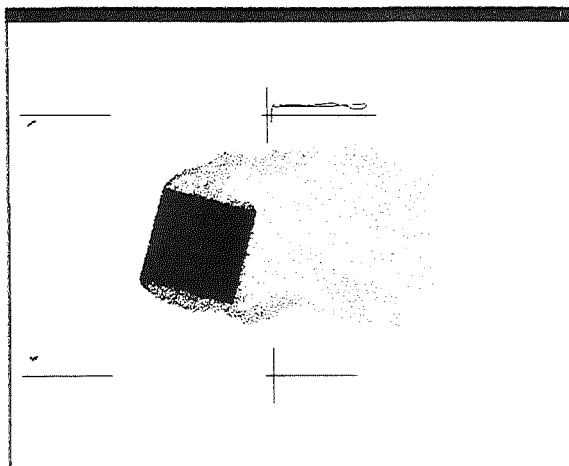
c) $t^* = 144.0$

Fig. 4.9 - Square Section Cylinder at 15° Incidence : Visualisation of Vortex Shedding.

Square at 0 Degrees Incidence

a) Lift Coefficient.

Square at 0 Degrees Incidence
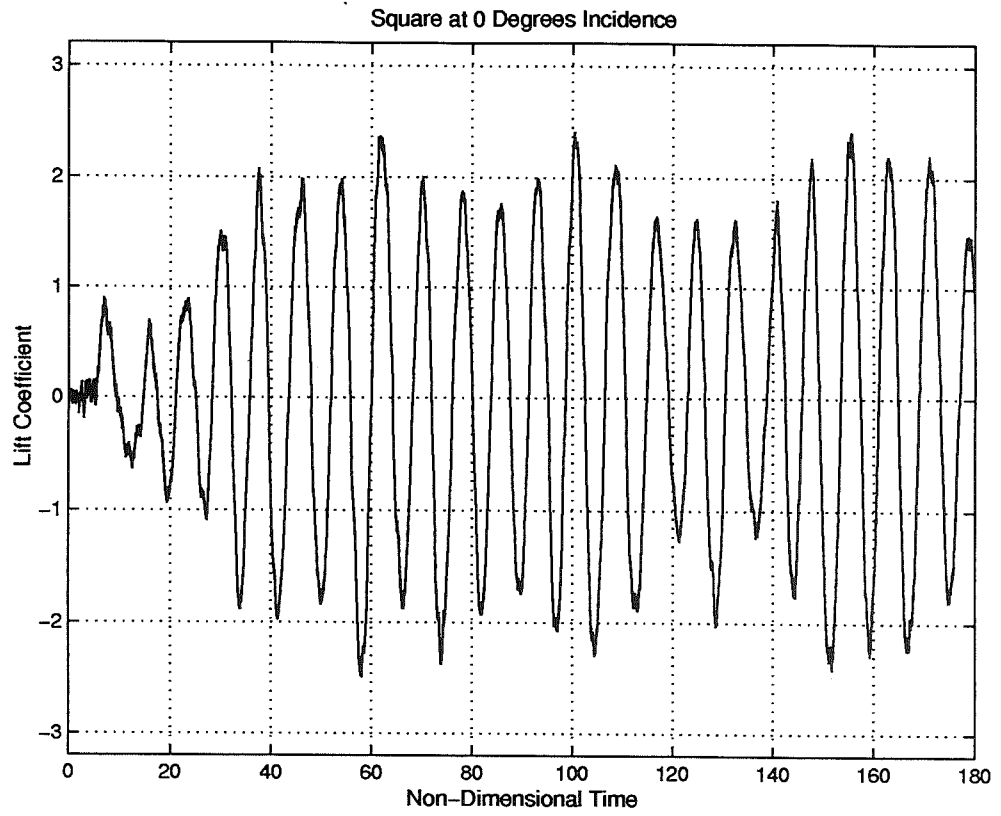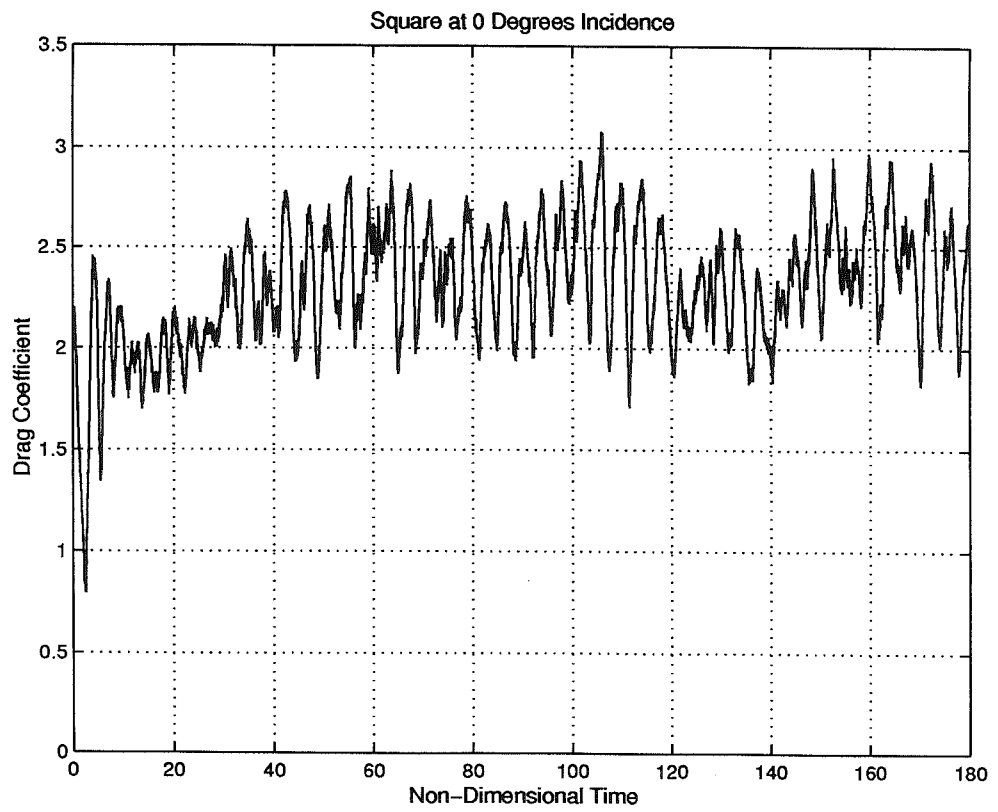
b) Drag Coefficient.

Fig. 4.10 - Static Square Cylinder : Sample Time History of Force Coefficients.
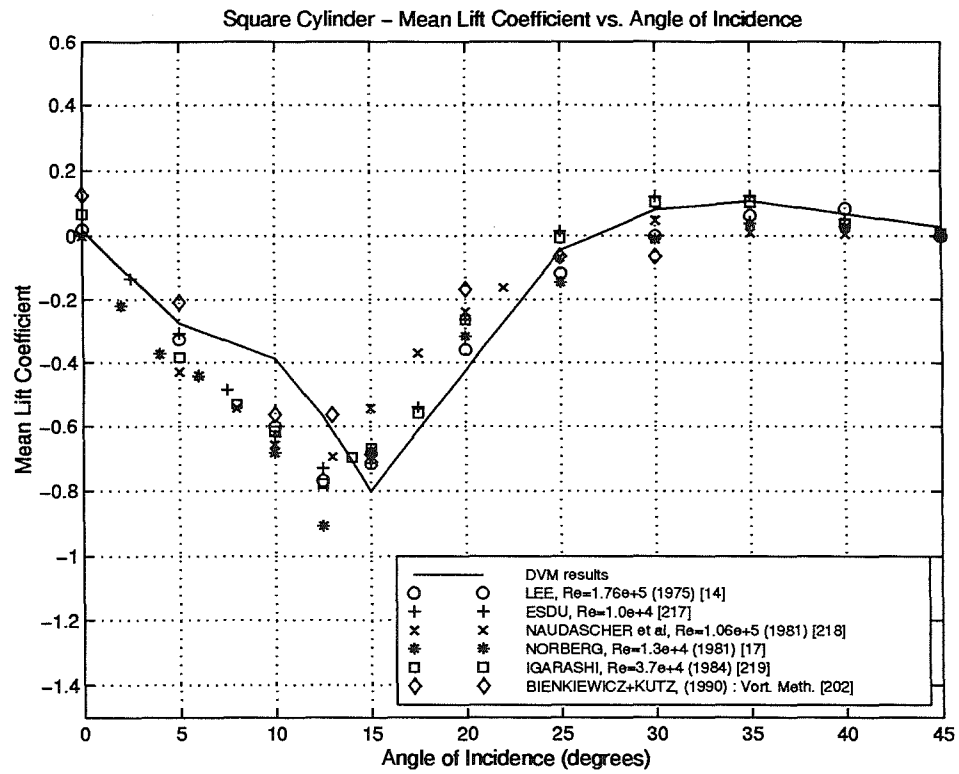
Fig. 4.11 - Static Square Cylinder : Variation of Mean Lift Coefficient with Angle of Incidence.
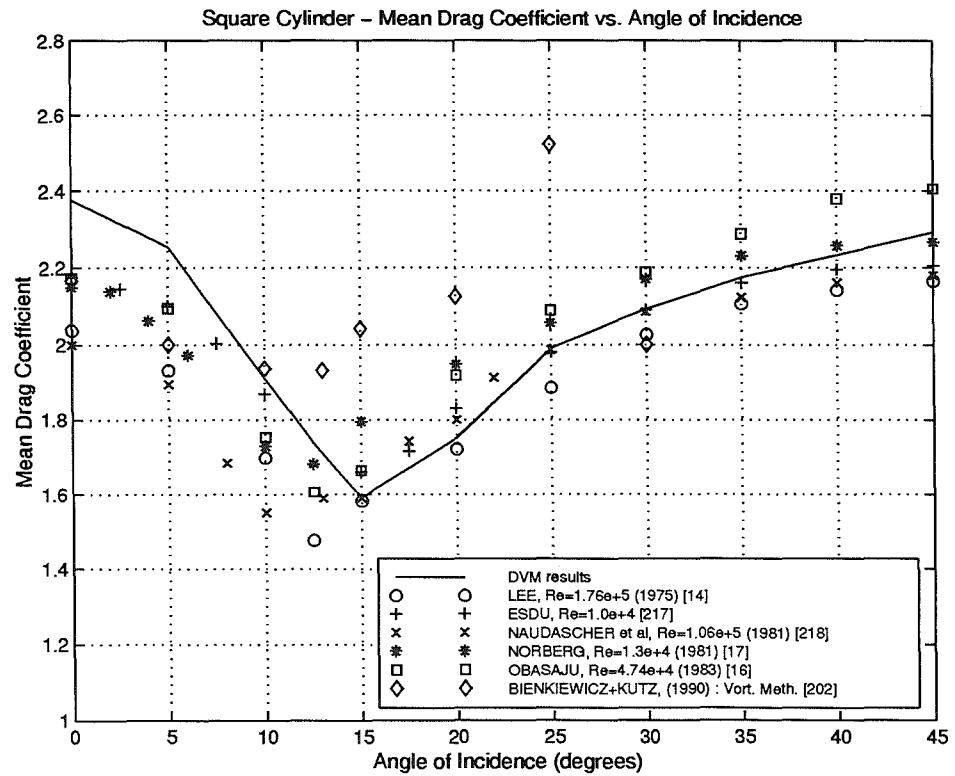
Fig. 4.12 - Static Square Cylinder : Variation of Mean Drag Coefficient with Angle of Incidence.
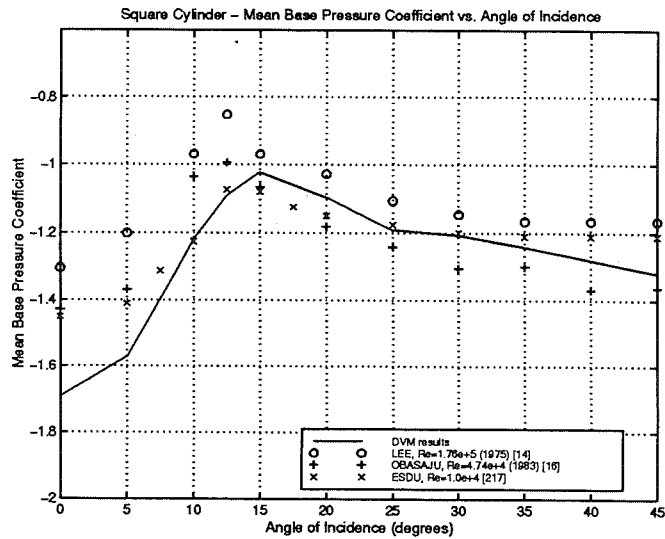
Fig. 4.13 - Static Square Cylinder : Variation of Mean Base Pressure Coefficient with Angle of Incidence.
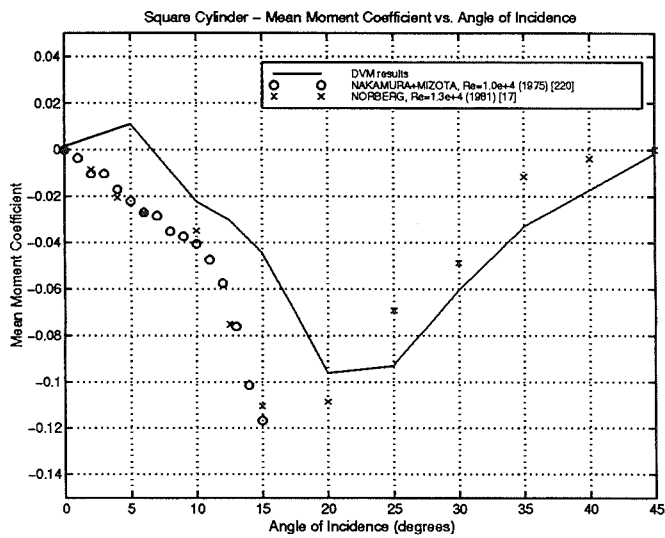
Fig. 4.14 - Static Square Cylinder : Variation of Mean Moment Coefficient with Angle of Incidence.
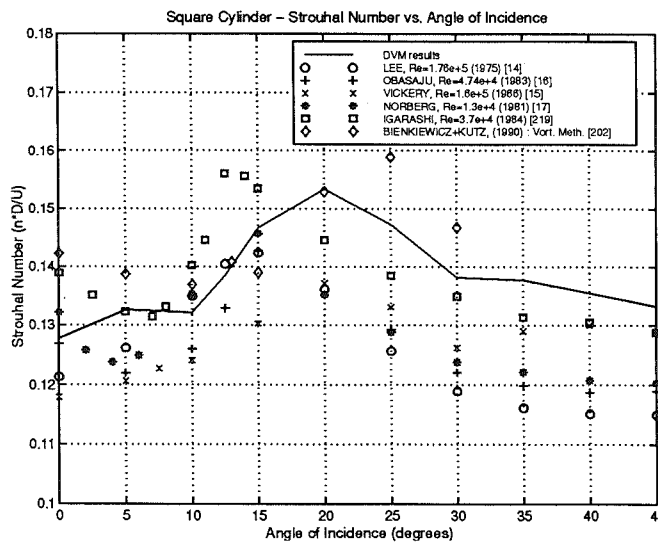
Fig. 4.15 - Static Square Cylinder : Variation of Strouhal Number with Angle of Incidence.
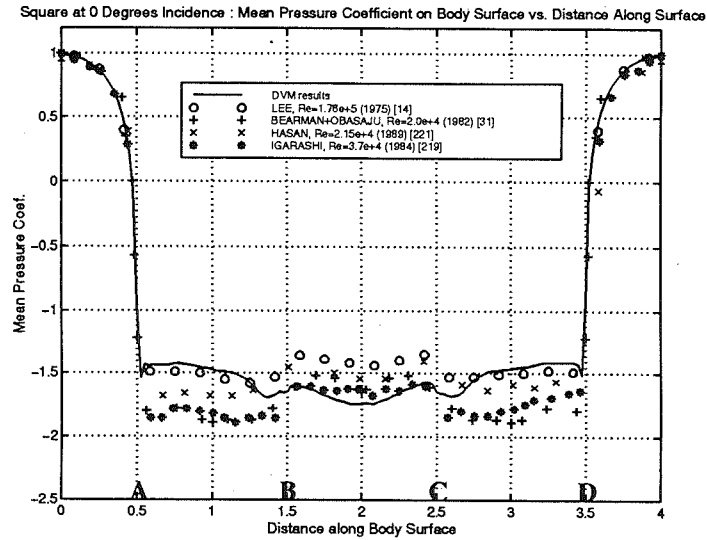
Square at 0 Degrees Incidence : Mean Pressure Coefficient on Body Surface vs. Distance Along Surface

a) Comparison with Experimental Data.

Square at 0 Degrees Incidence : Mean Pressure Coefficient on Body Surface vs. Distance Along Surface
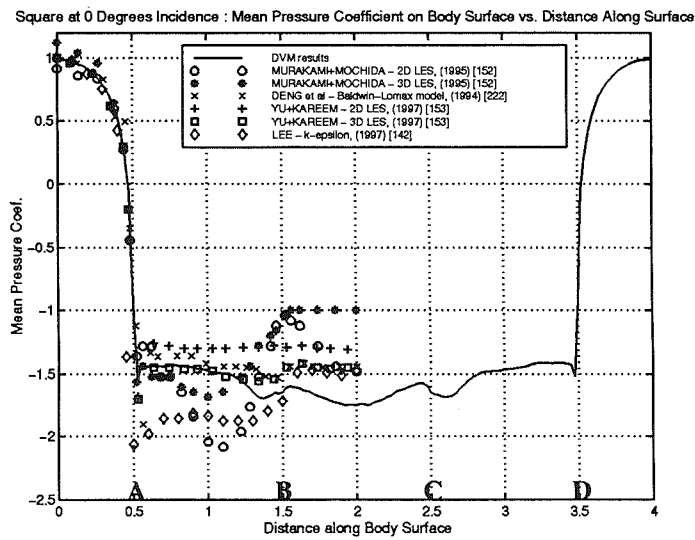
b) Comparison with Other Computational Results.

Fig. 4.16 - Static Square Cylinder at 0° Incidence : Surface Pressure Coefficient vs. Distance along Body Surface.

Square at 10 Degrees Incidence : Mean Pressure Coefficient on Body Surface vs. Distance Along Surface
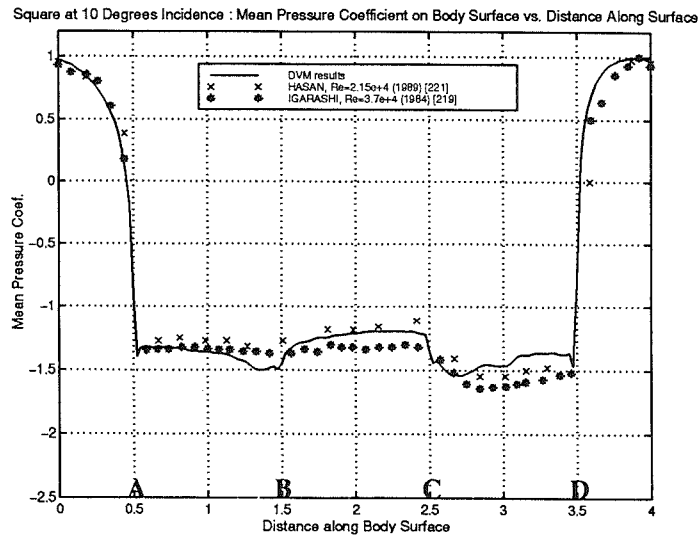
Fig. 4.17 - Static Square Cylinder at 10° Incidence : Surface Pressure Coefficient vs. Distance along Body Surface.

Square at 0 Degrees Incidence : RMS. Fluctuating Pressure Coefficient on Body Surface vs. Distance Along Surface
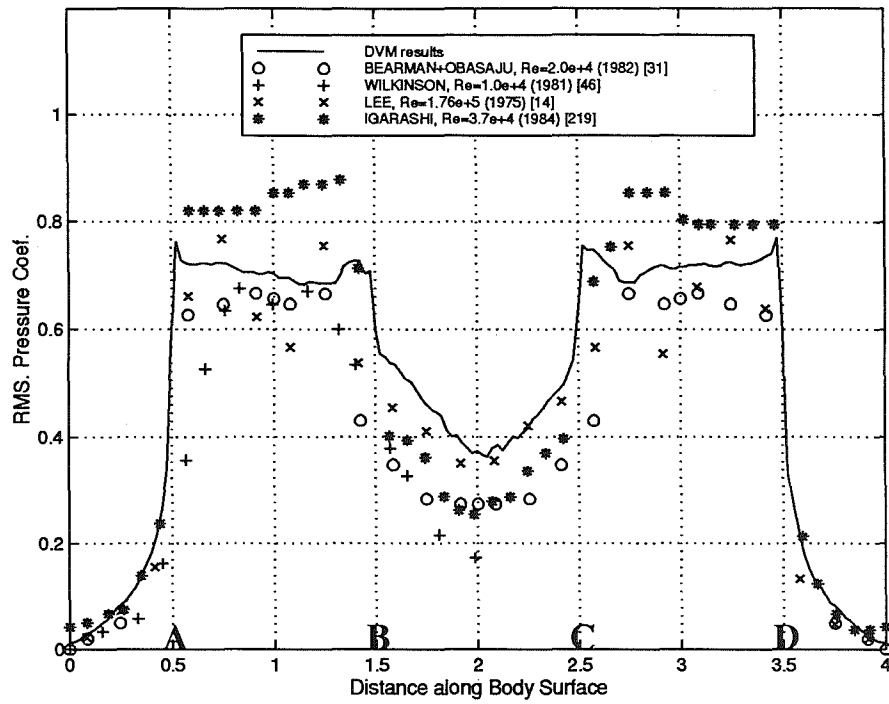
a) Comparison with Experimental Data.

Square at 0 Degrees Incidence : RMS. Fluctuating Pressure Coefficient on Body Surface vs. Distance Along Surface
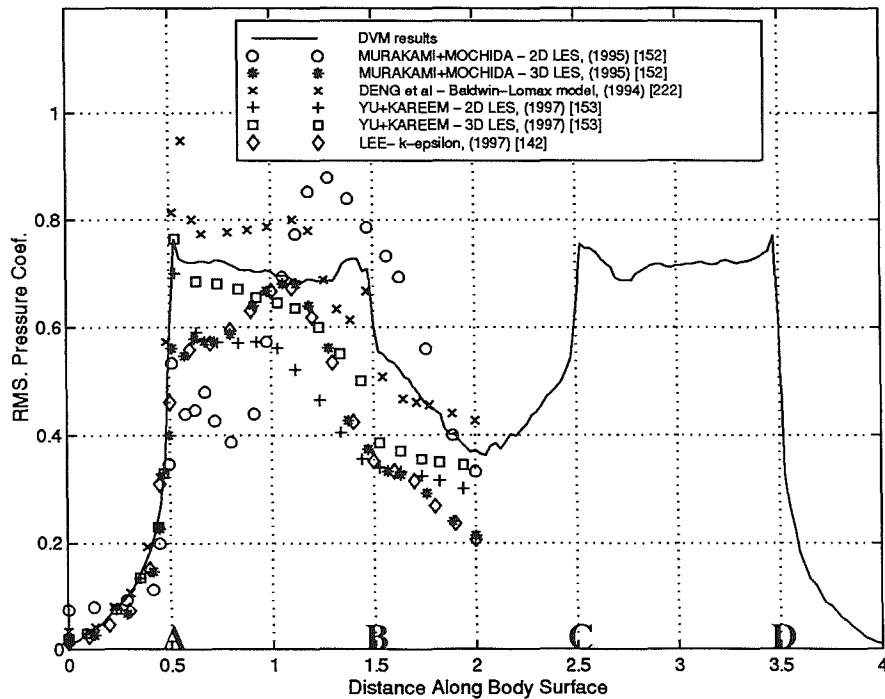
b) Comparison with Other Computational Results.

Fig. 4.18 - Static Square Cylinder at 0° Incidence : RMS Fluctuating Pressure Coefficient vs.
Distance along Body Surface.
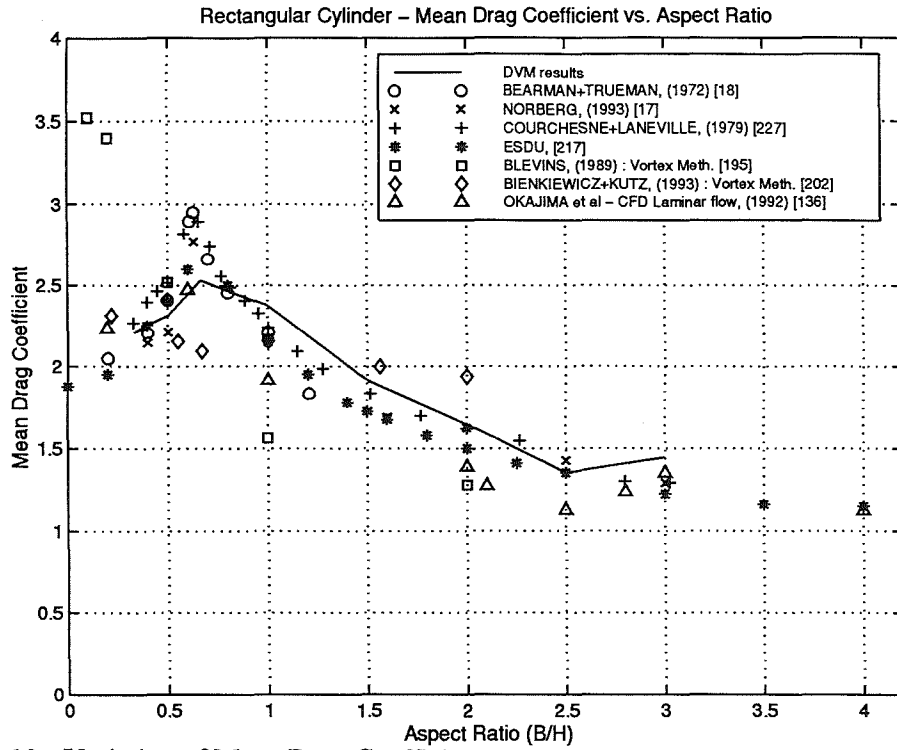
Fig. 4.19 - Variation of Mean Drag Coefficient with Aspect Ratio on Rectangular Cylinder at 0°
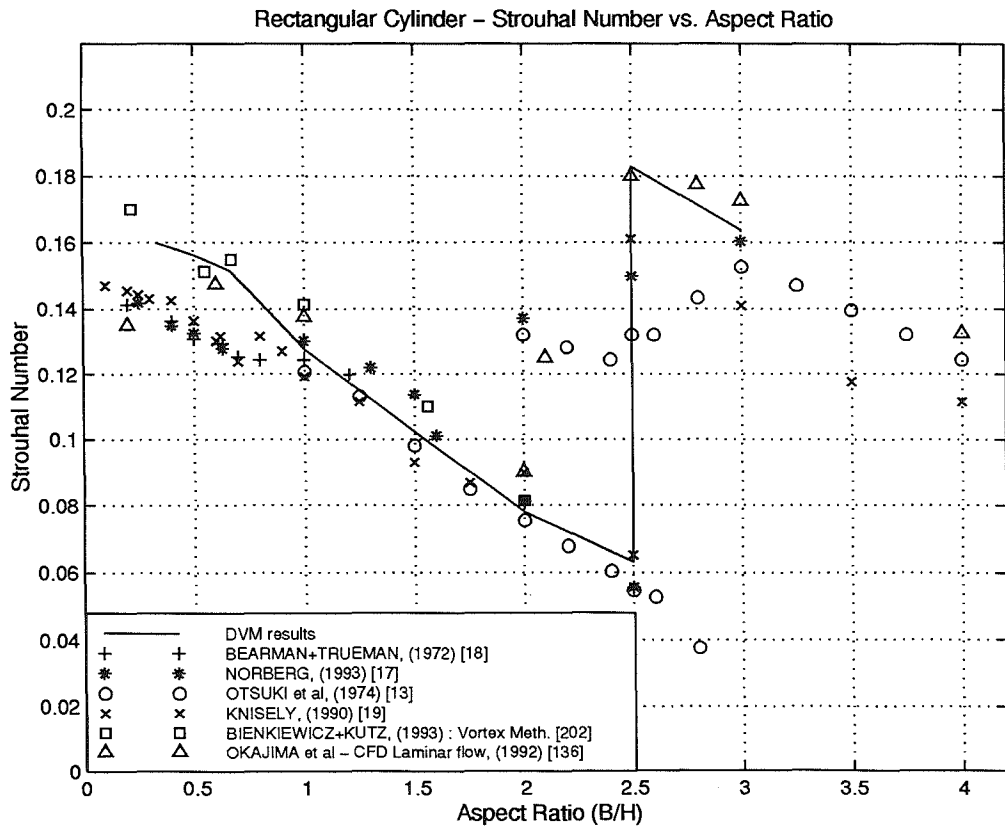
Incidence.

Fig. 4.20 - Variation of Strouhal Number with Aspect Ratio on Rectangular Cylinder at 0°

Incidence.
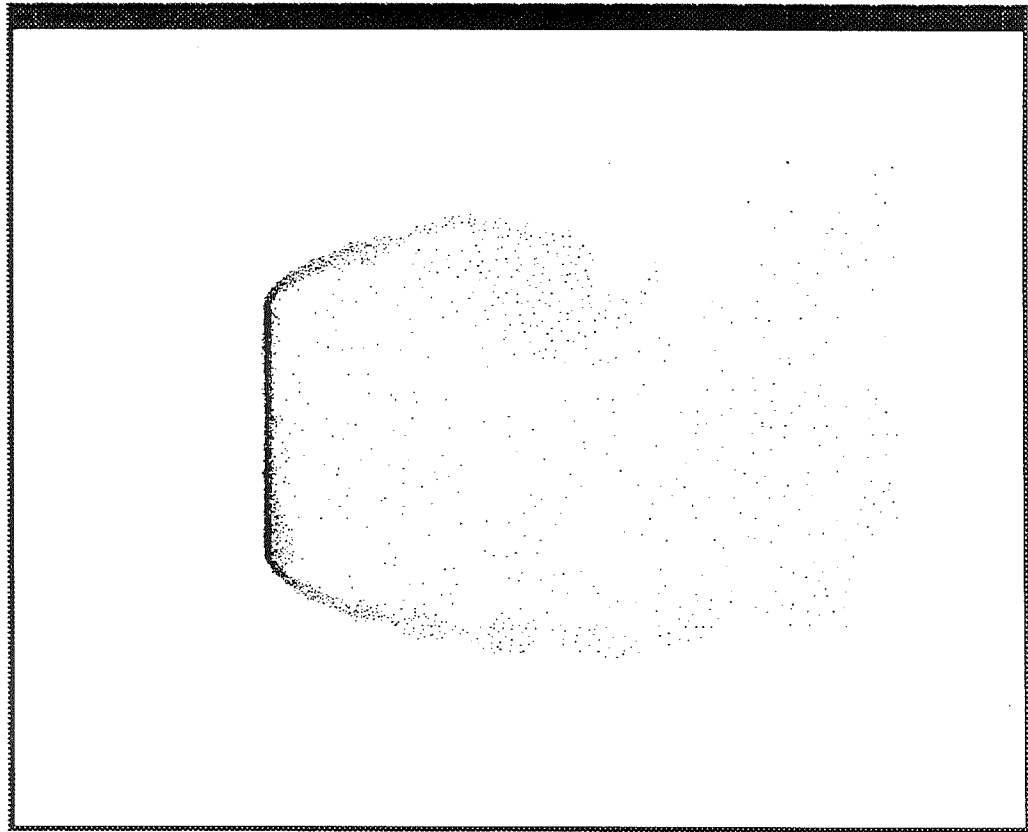
a) Particle Distributions.
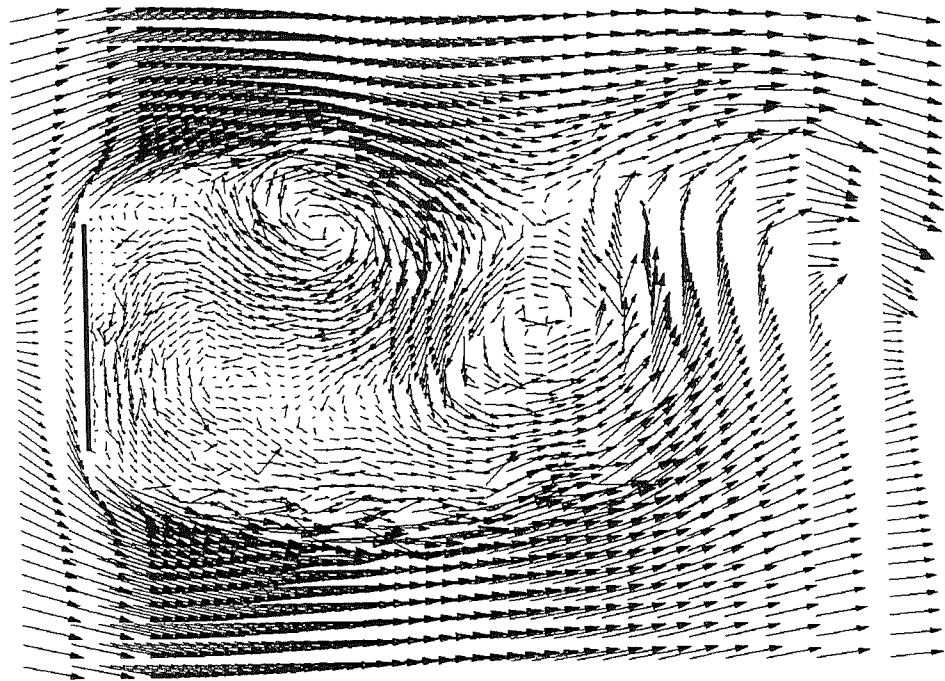
b) Velocity Vectors.

Fig. 4.21 - Predicted Flow Field around "Flat Plate" Normal to Freestream Flow : Aspect ratio = 100.
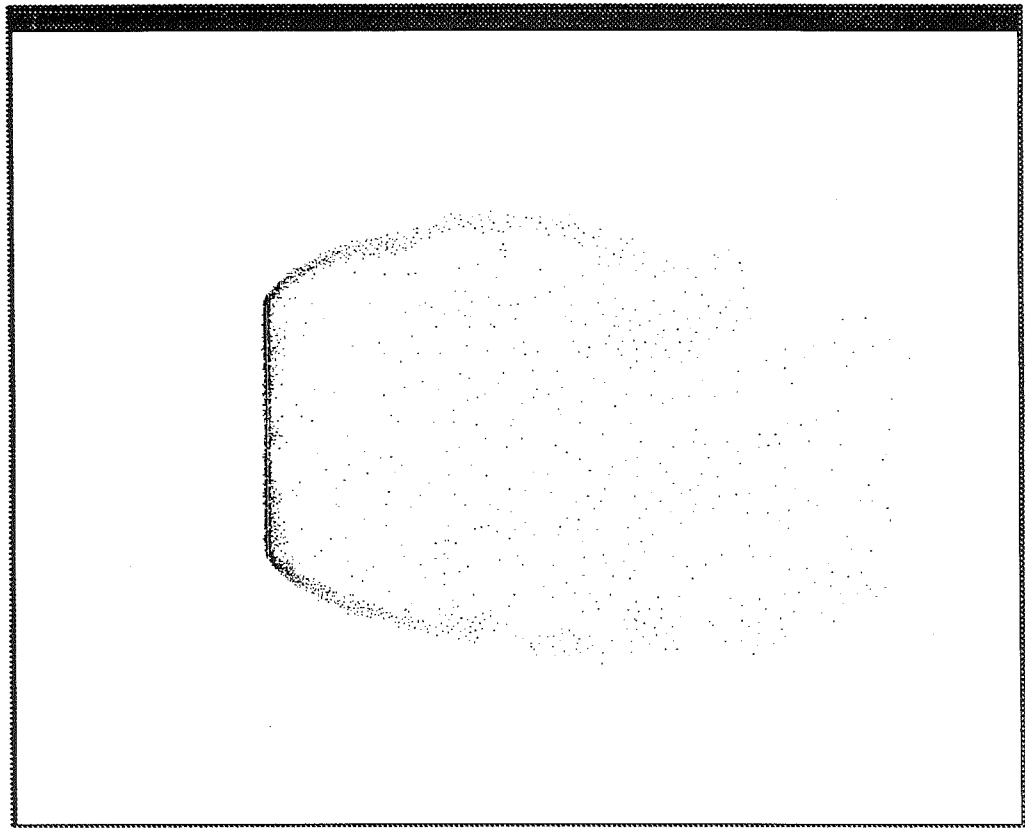
a) Particle Distributions.
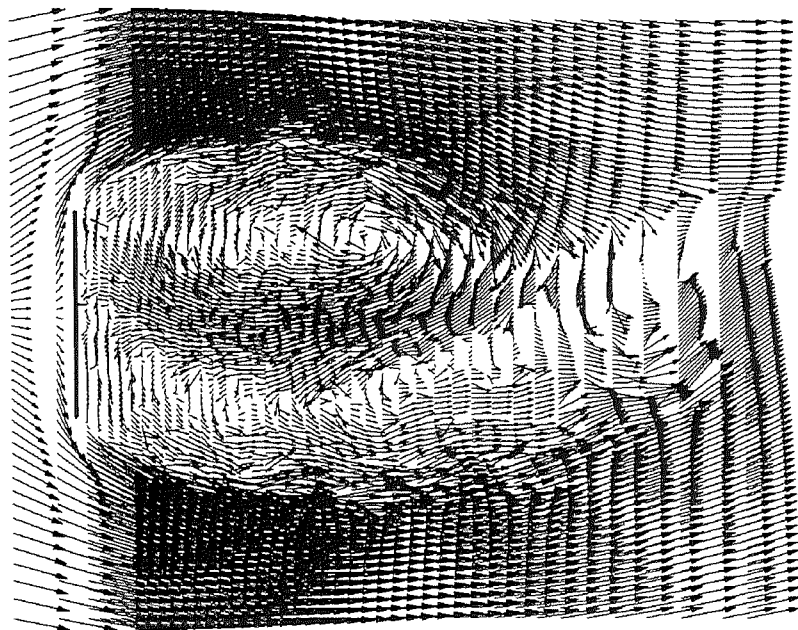
b) Velocity Vectors.

Fig. 4.22 - Predicted Flow Field around "Flat Plate" Normal to Freestream Flow : Aspect ratio = 200.
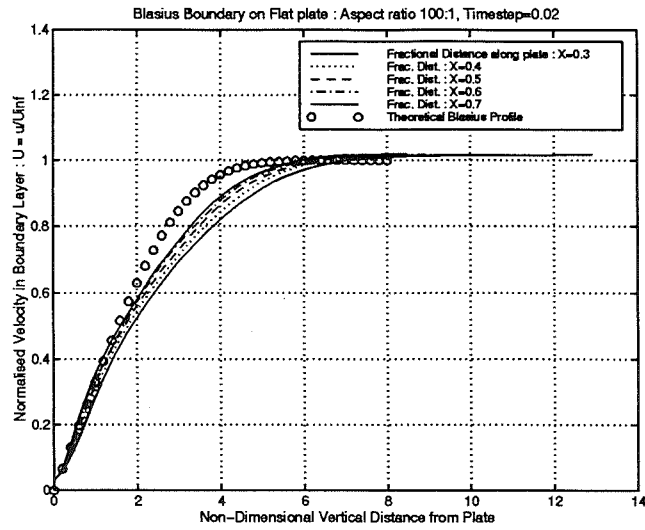
a) Aspect Ratio : 100, Time step : 0.02.
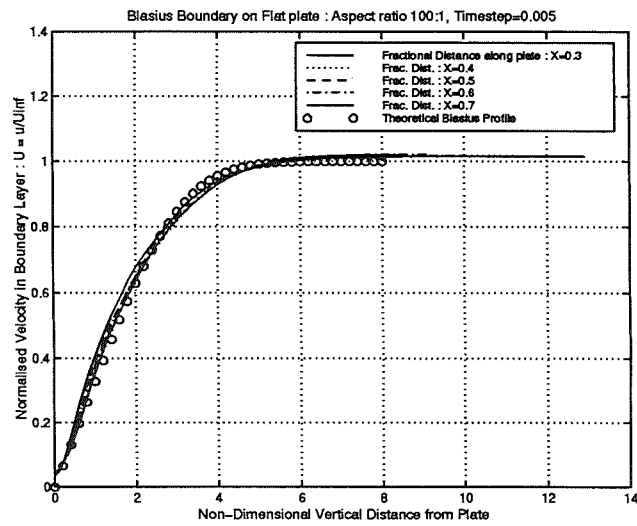
b) Aspect Ratio : 100, Time step : 0.005.
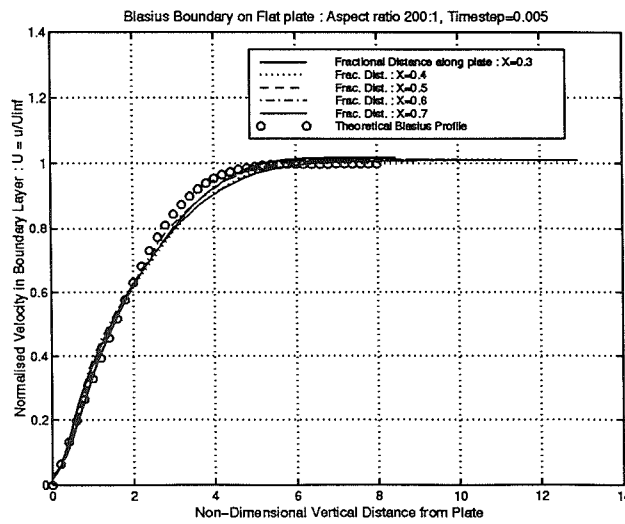
c) Aspect Ratio : 200, Time step : 0.005.

Fig. 4.23 - Comparison of Predicted and Theoretical Boundary Layer Profiles on Flat Plate at 0° Incidence.
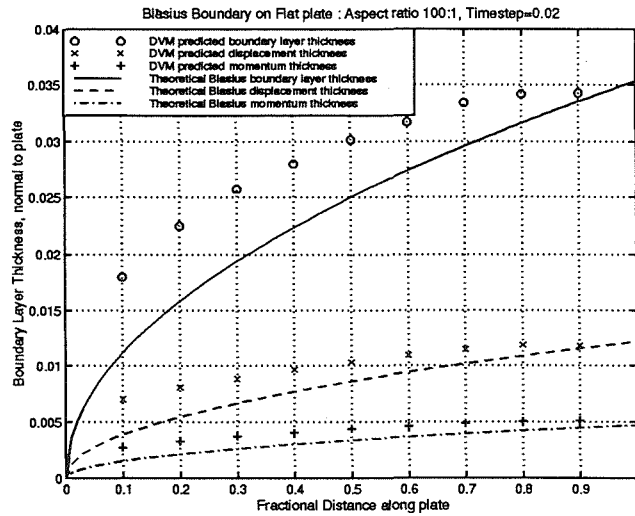
a) Aspect Ratio : 100, Time step : 0.02.
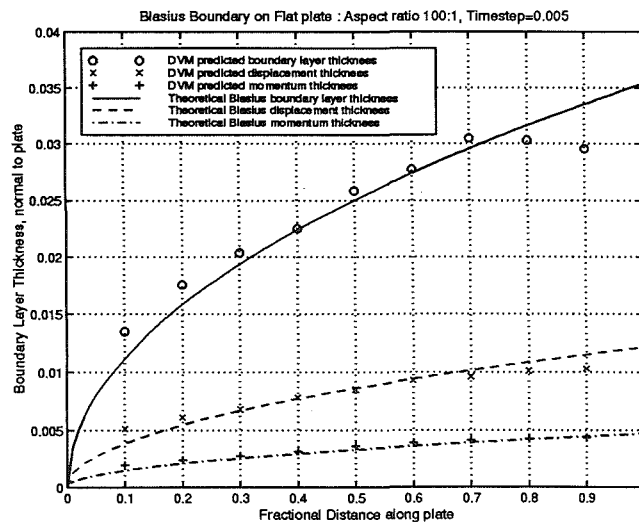
b) Aspect Ratio : 100, Time step : 0.005.
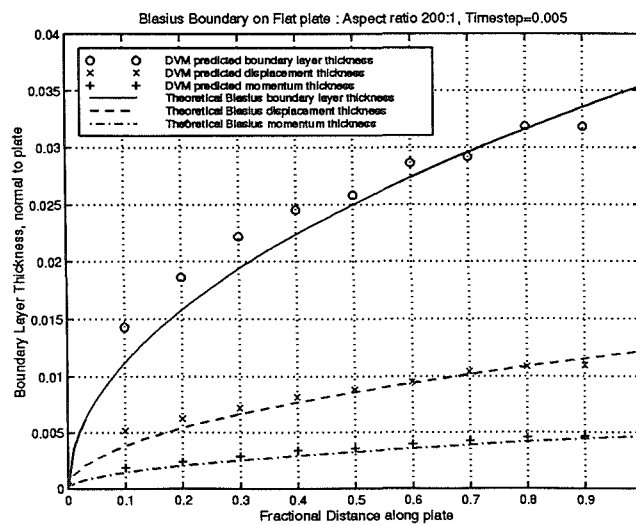
c) Aspect Ratio : 200, Time step : 0.005.

Fig. 4.24 - Comparison of Predicted and Theoretical Boundary Layer Thickness on Flat Plate at 0° Incidence.
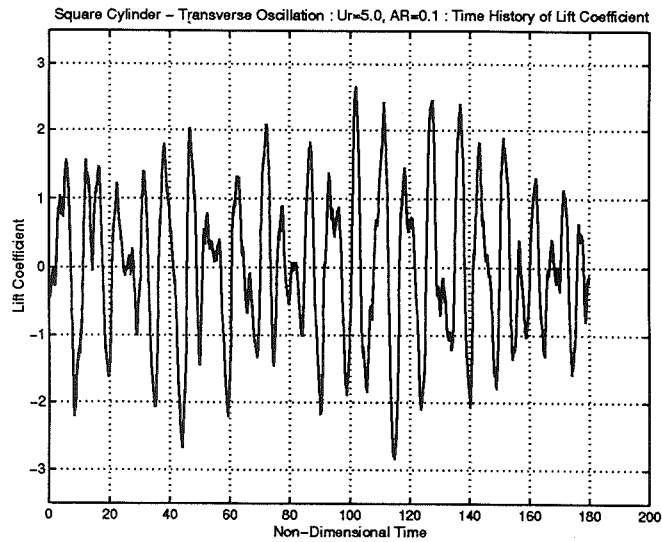
a) U_r=5.0, Amplitude Ratio = 0.1.
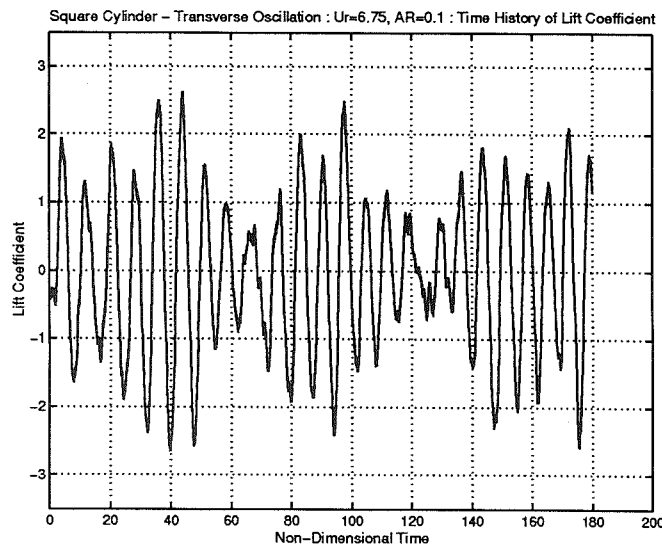
b) U_r=6.75, Amplitude Ratio = 0.1.
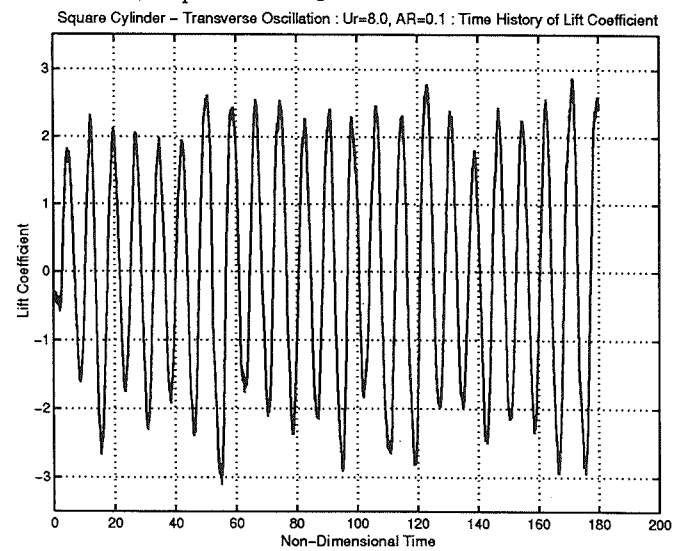
c) U_r=8.0, Amplitude Ratio = 0.1.

Fig. 4.25 - Sample Lift Histories for Square Cylinder Undergoing Forced Transverse Oscillation.

Square Cylinder – Transverse Oscillation : Ur=8.3, AR=0.1 : Time History of Lift Coefficient

d) U_r=8.3, Amplitude Ratio = 0.1.

Fig. 4.25 - Sample Lift Histories for Square Cylinder Undergoing Forced Transverse Oscillation.

Square Cylinder – Transverse Oscillation : Ur=5.0, AR=0.1 : Frequency Analysis of Lift Coefficient

Non Dimensional Frequency. (nL/U)
Vortex Shedding Frequency (Strouhal number) = 0.12093
Frequency of Forcing Oscillation = 0.2000

a) U_r=5.0, Amplitude Ratio = 0.1.

Square Cylinder – Transverse Oscillation : Ur=8.0, AR=0.1 : Frequency Analysis of Lift Coefficient

Non Dimensional Frequency. (nL/U)
Vortex Shedding Frequency (Strouhal number) = 0.124741
Frequency of Forcing Oscillation = 0.124741 (1/8.0 = 0.1250)
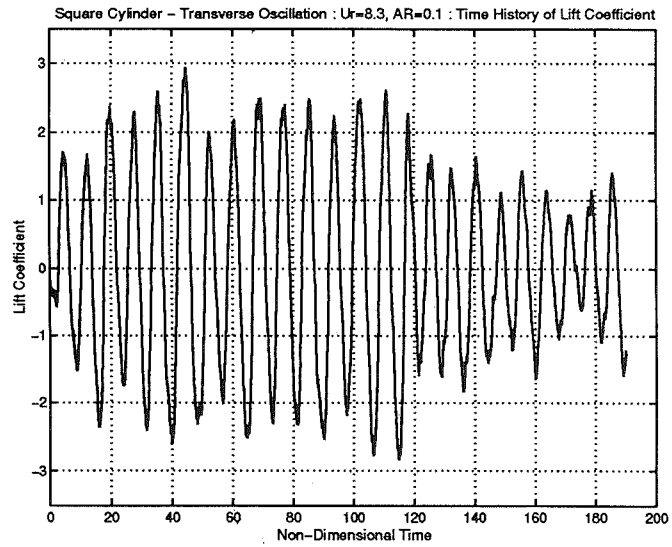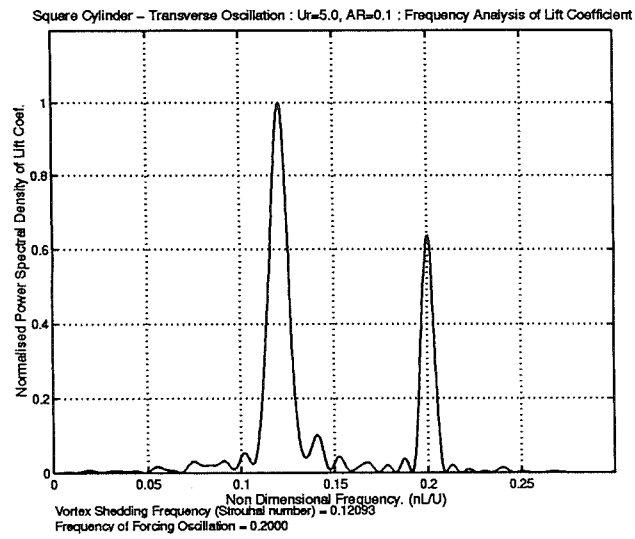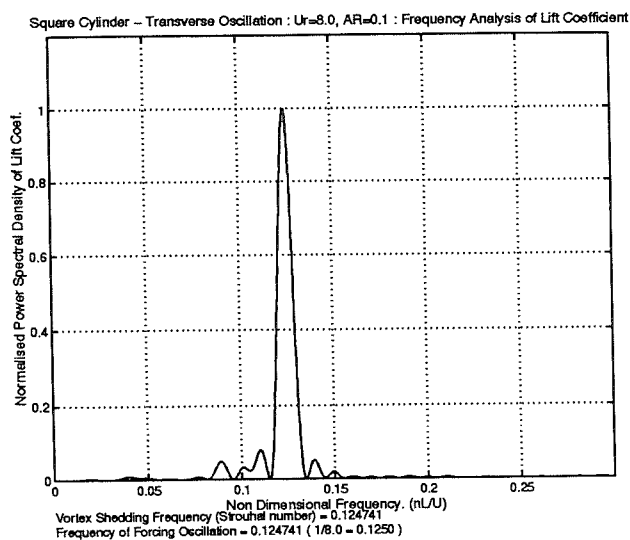
b) U_r=8.0, Amplitude Ratio = 0.1.

Fig. 4.26 - Sample Spectral Analysis for Square Cylinder Undergoing Forced Transverse
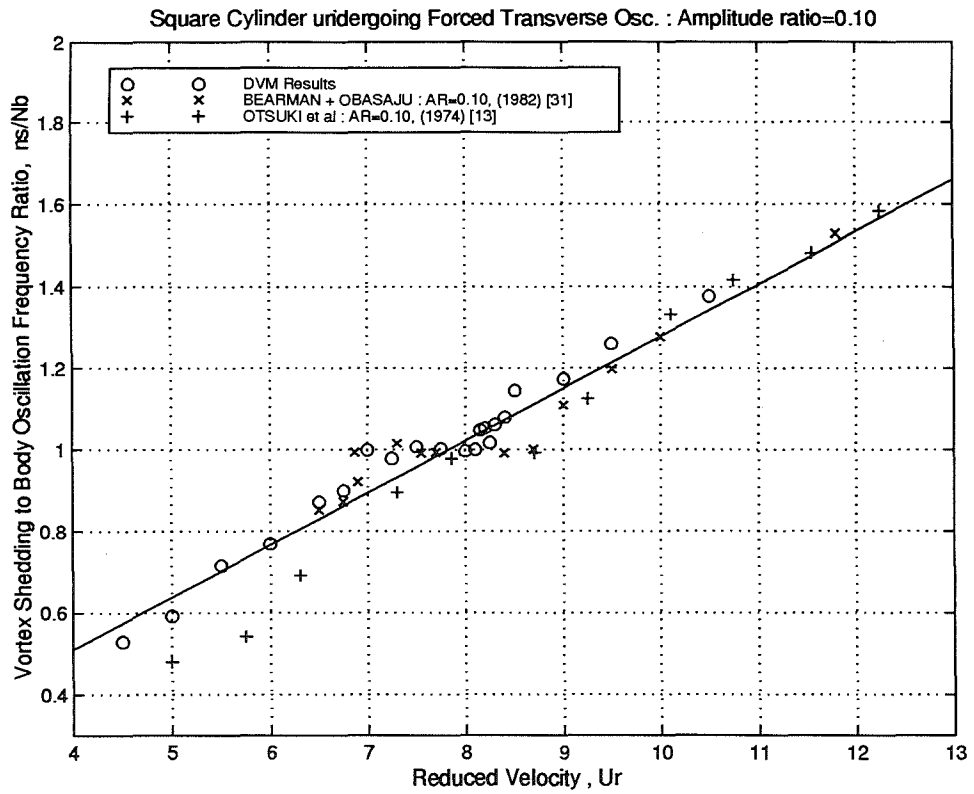
Oscillation.

a) Amplitude Ratio = 0.1.
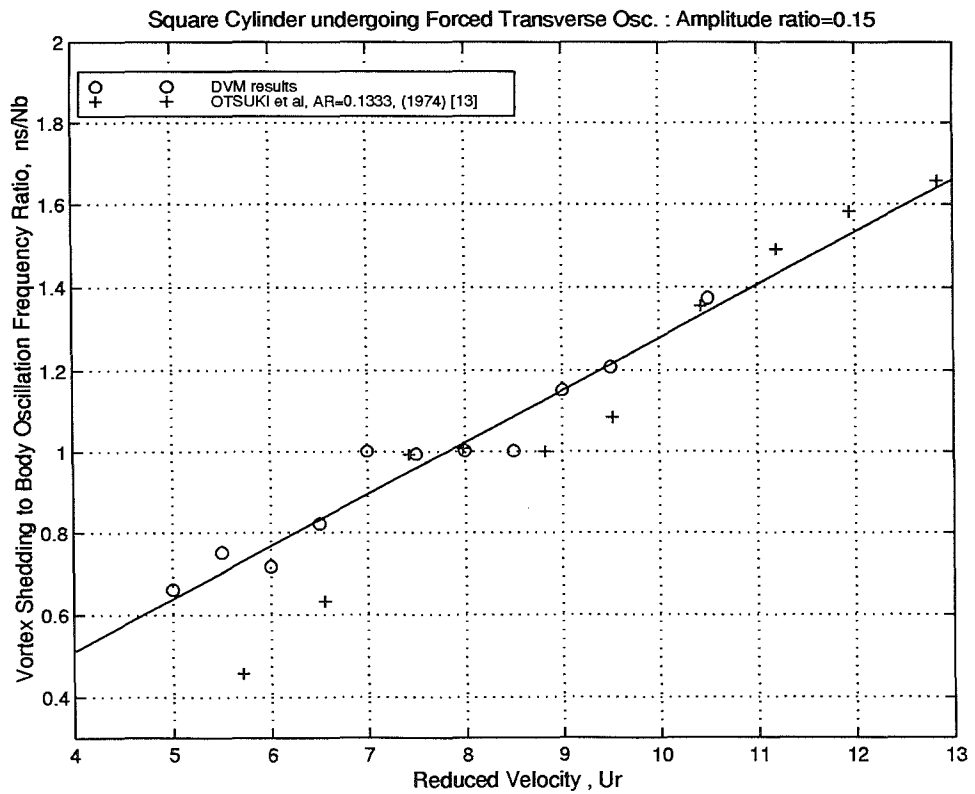
b) Amplitude Ratio = 0.15.

Fig. 4.27 - Variation of Vortex Shedding Frequency with Reduced Velocity : Demonstration of Vortex Lock-in on Square Cylinder with Transverse Oscillation.

Y=0.0
Body motion
Upwards.

a) t* = 192.0

Y=0.1
Body at max.
Positive Position.

b) t* = 193.5

Y=0.0
Body Motion
Downwards.

c) t* = 195.0

Y=-0.1
Body at min.
Negative Position.

d) t* = 196.5

Y=0.0
Body motion
Upwards.

e) t* = 198.0
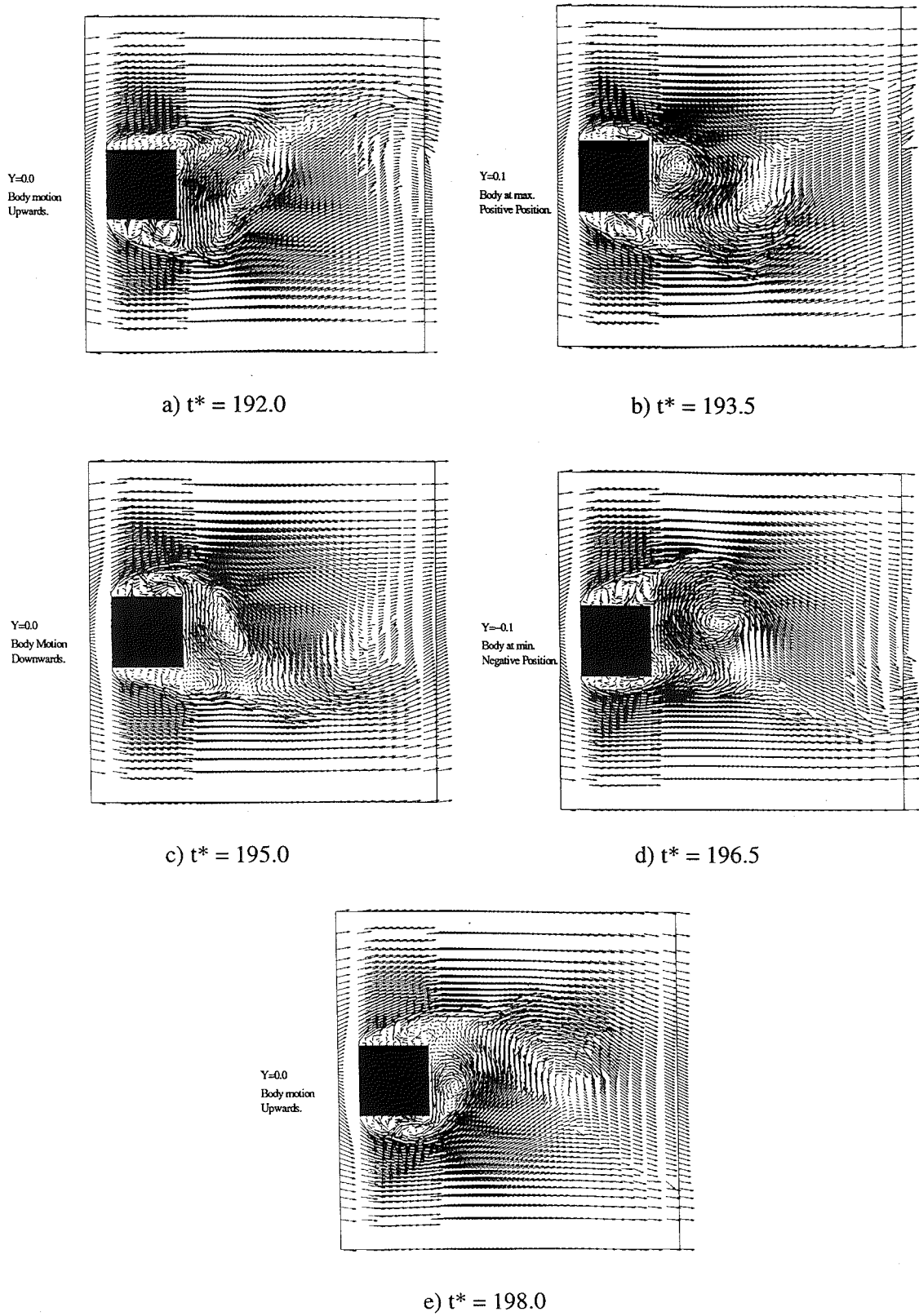
Fig. 4.28 - Square Cylinder with Transverse Oscillation, U_r=6.0 (Below lock-in) : Velocity Vectors.

Y=0.0
Body Motion
Upwards.

a) t* = 184.0

Y=0.1
Body at max.
Positive Position.

b) t* = 186.0

Y=0.0
Body motion
Downwards.

c) t* = 188.0

Y=-0.1
Body at min.
Negative Position.

d) t* = 190.0

Y=0.0
Body Motion
Upwards.

e) t* = 192.0
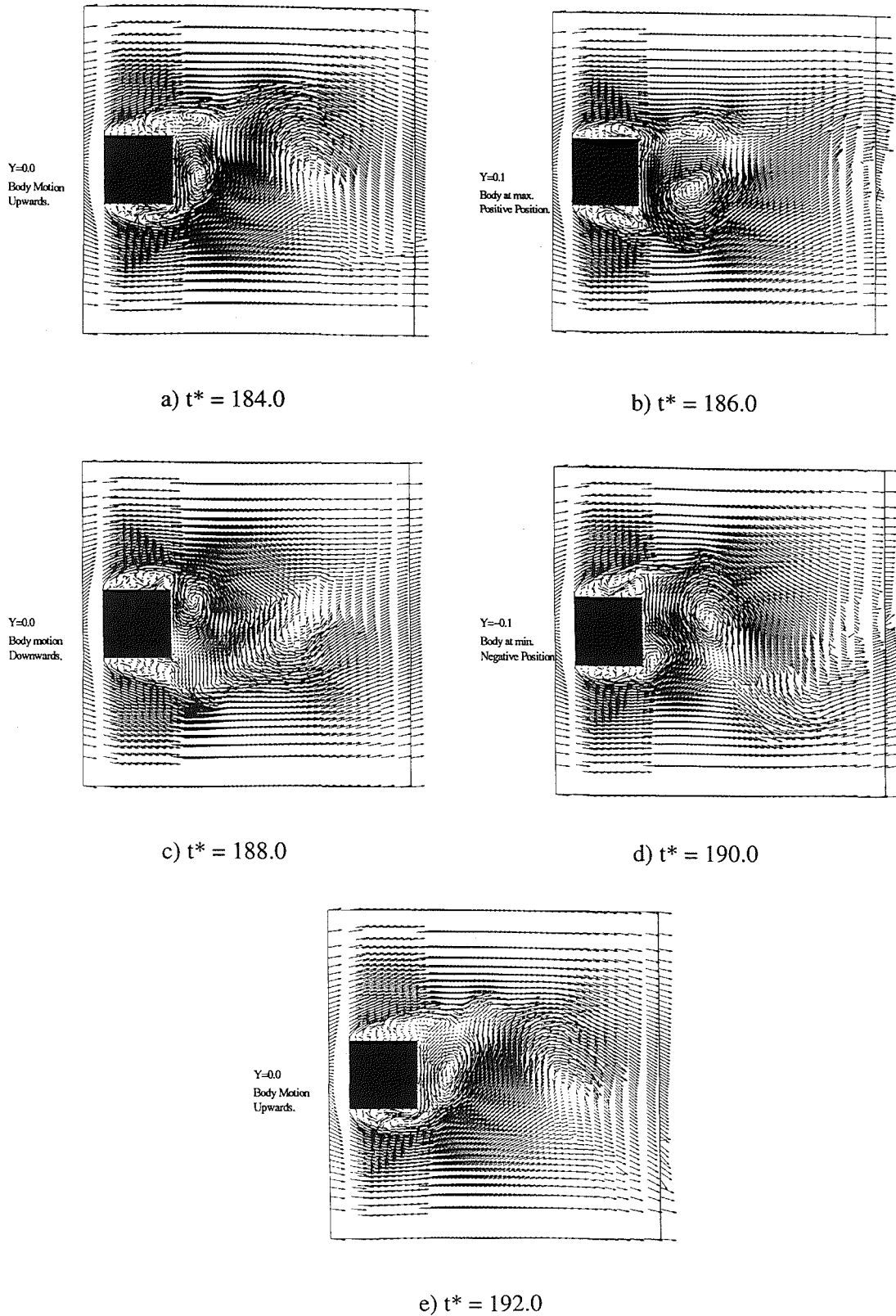
Fig. 4.29 - Square Cylinder with Transverse Oscillation, U_r=8.0 (Lock-in) : Velocity Vectors.
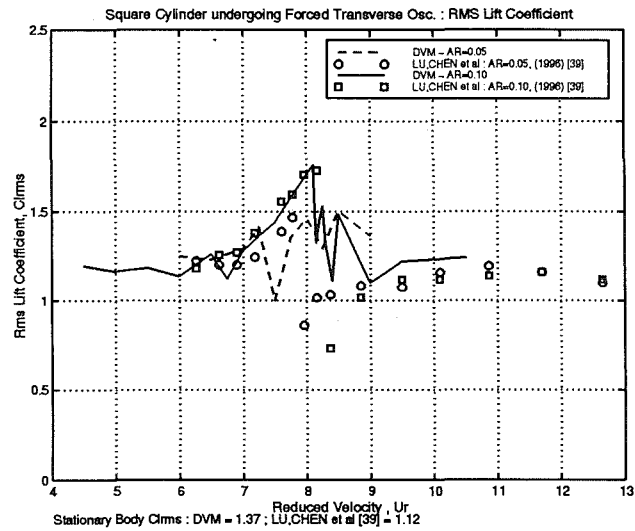
a) Amplitude Ratio = 0.05 and 0.10.
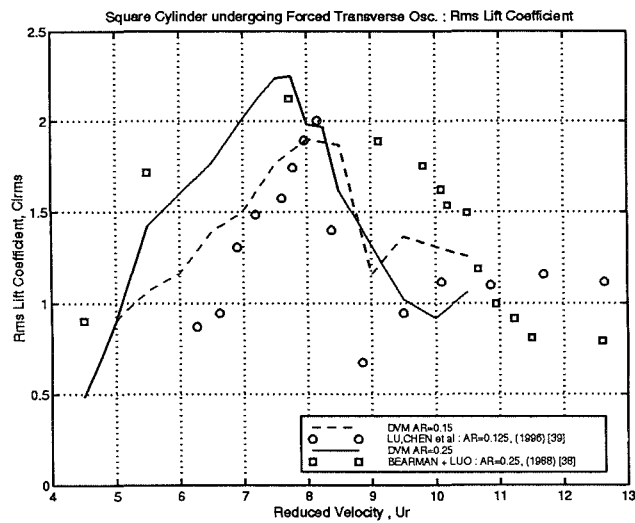
b) Amplitude Ratio = 0.15 and 0.25.

Fig. 4.30 - Variation of RMS Lift Coefficient with U_r : Square Cylinder with Transverse Oscillation.
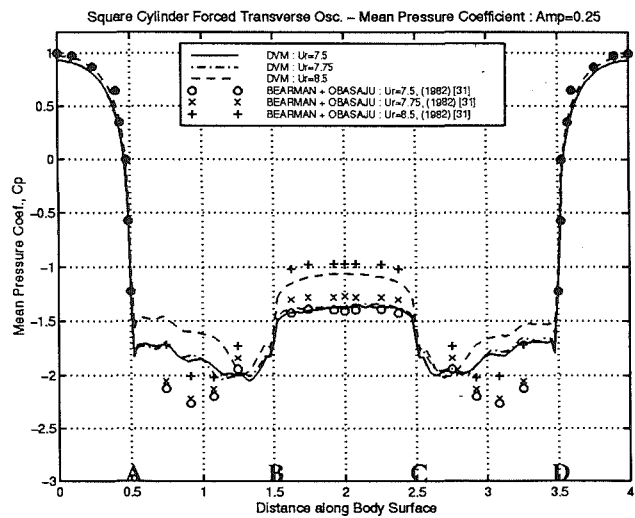
Fig. 4.31 - Mean Pressure Coefficient on Transversely Oscillating Square Cylinder : Amplitude Ratio = 0.25.
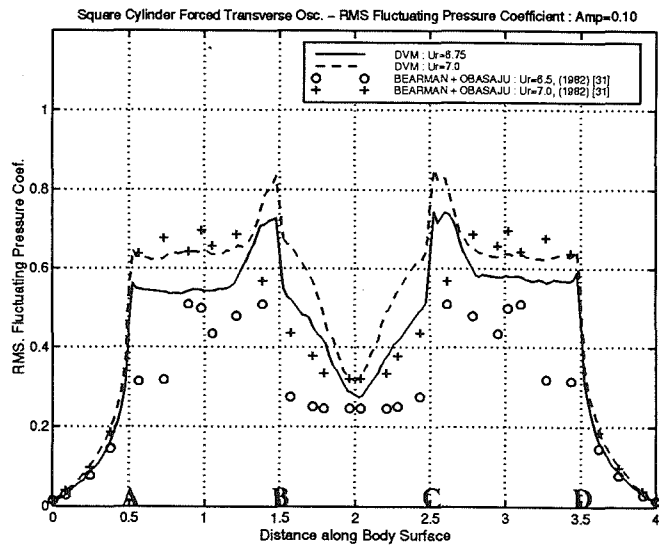
a) Reduced Velocities up to Lower end of Lock-in Region.
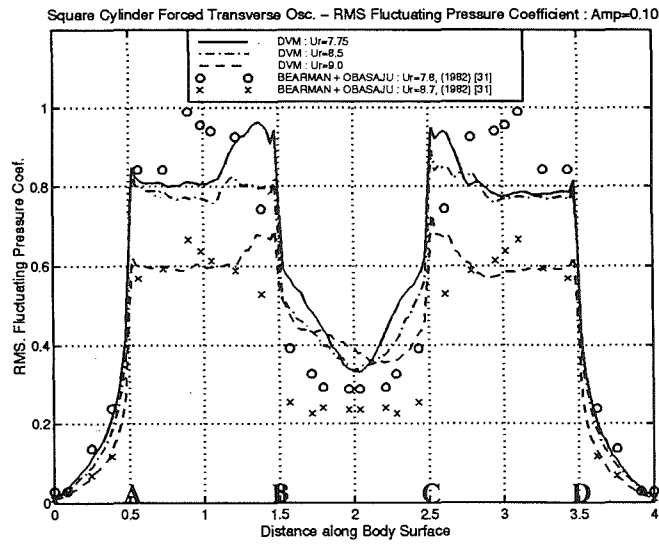
b) Reduced Velocities from Upper end of Lock-in Region.

Fig. 4.32 - RMS Fluctuating Pressure Coefficient on Transversely Oscillating Square Cylinder.
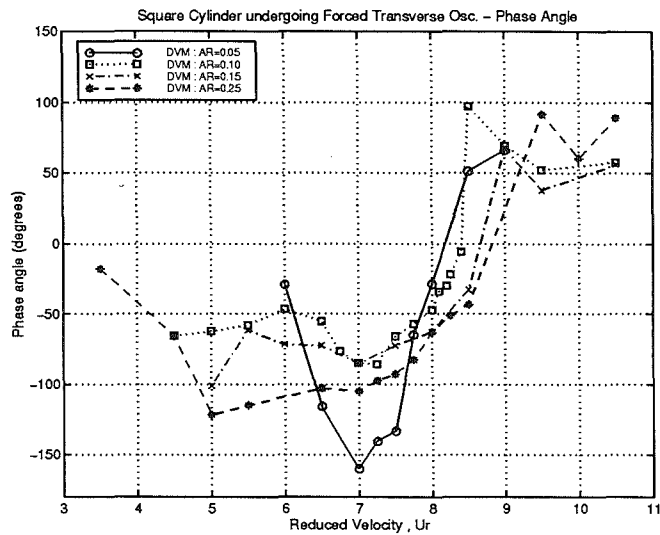
Fig. 4.33 - Phase Angle vs. Reduced Velocity : DVM Predictions on Transversely Oscillating Square Cylinder.
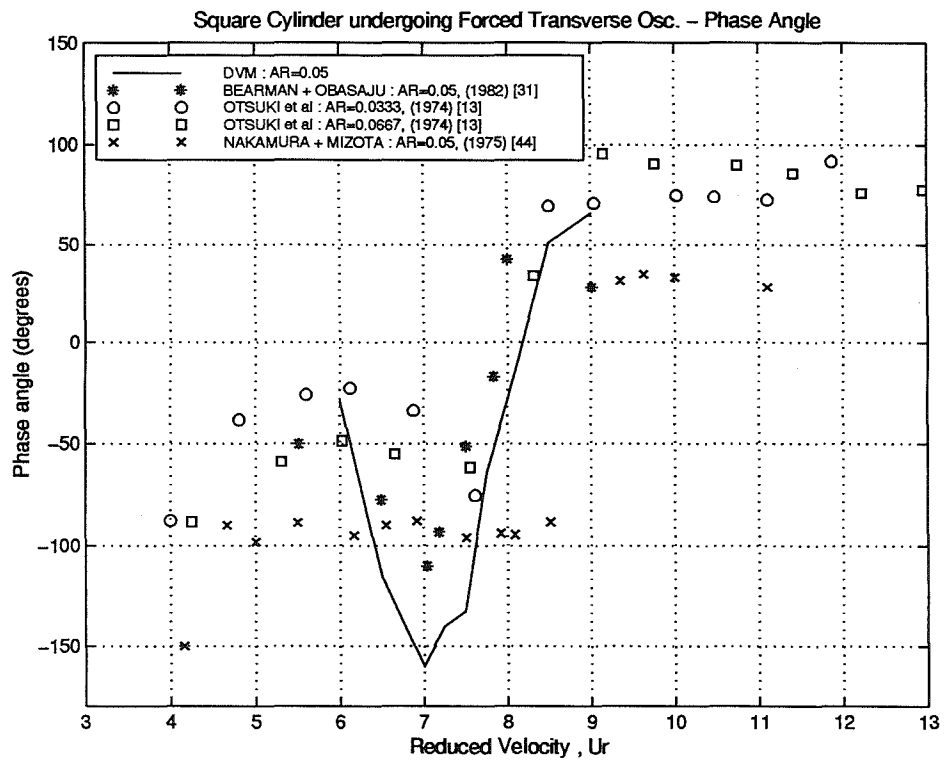
a) Amplitude Ratio = 0.05.
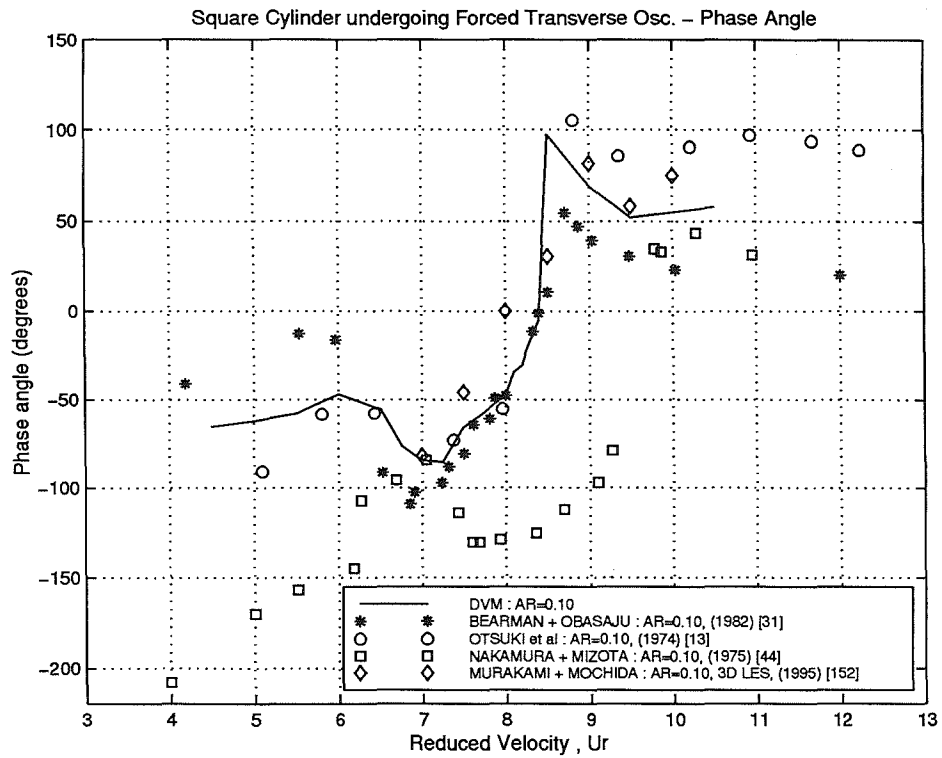
b) Amplitude Ratio = 0.10.

Fig. 4.34 - Phase Angle vs. Reduced Velocity : Square Cylinder with Transverse Oscillation.
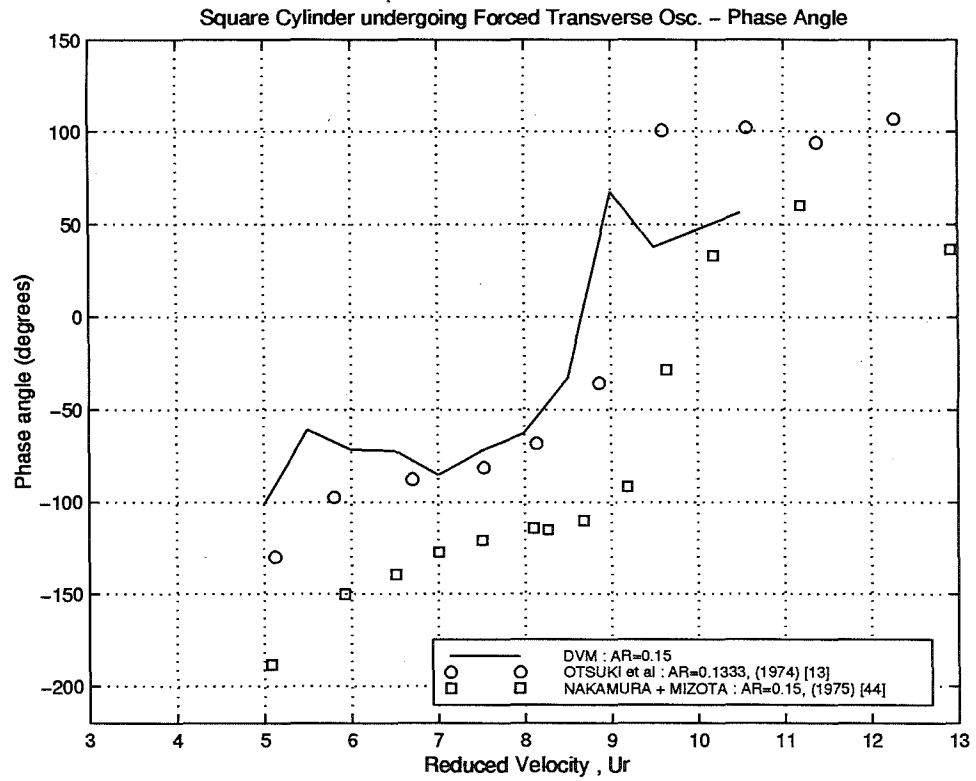
c) Amplitude Ratio = 0.15.
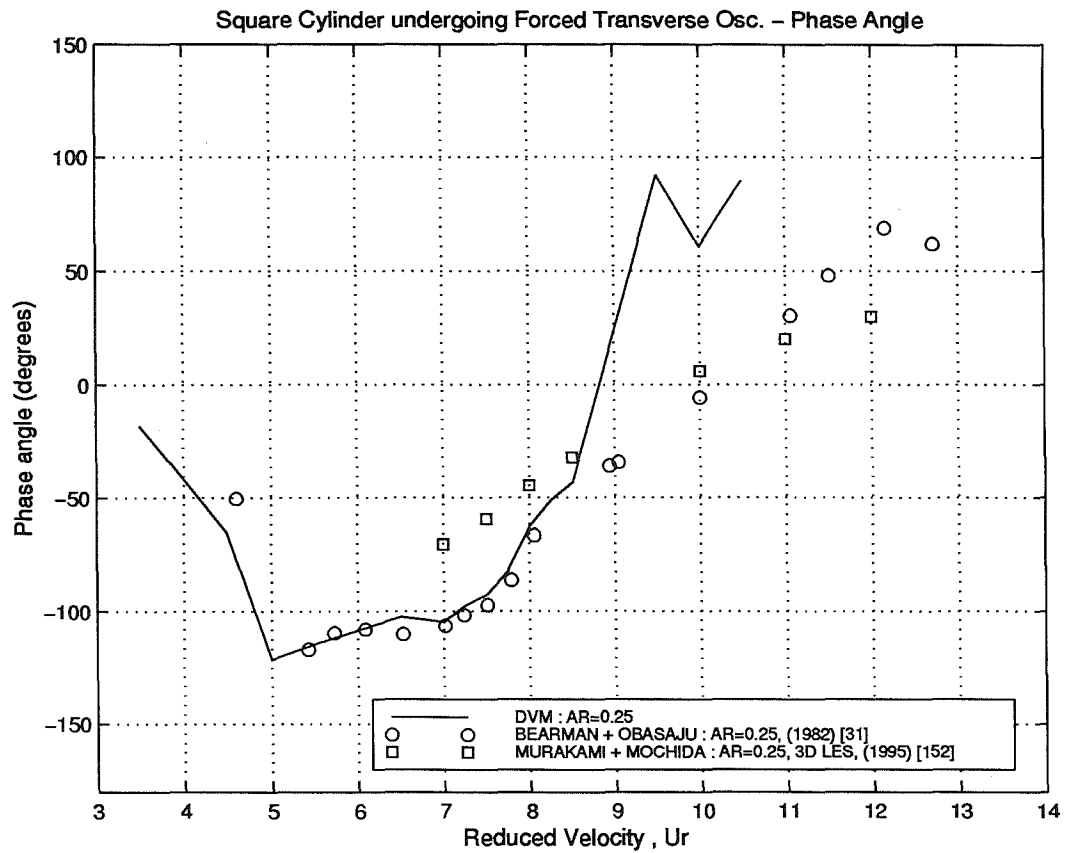
d) Amplitude Ratio = 0.25.

Fig. 4.34 - Phase Angle vs. Reduced Velocity : Square Cylinder with Transverse Oscillation.
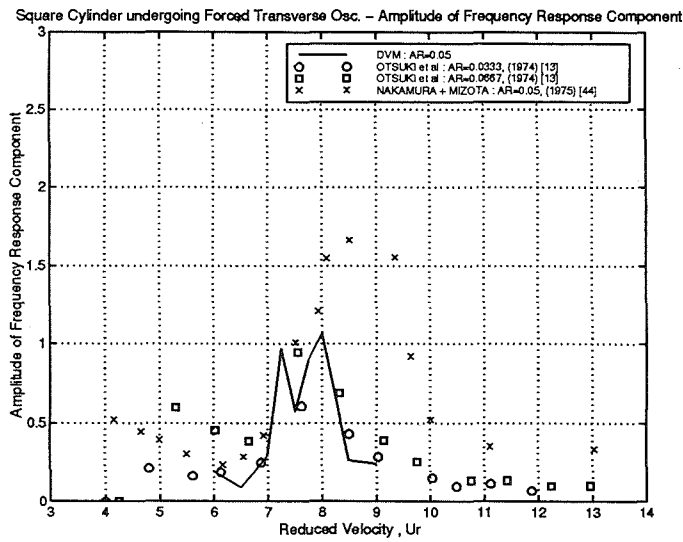
a) Amplitude Ratio = 0.05.
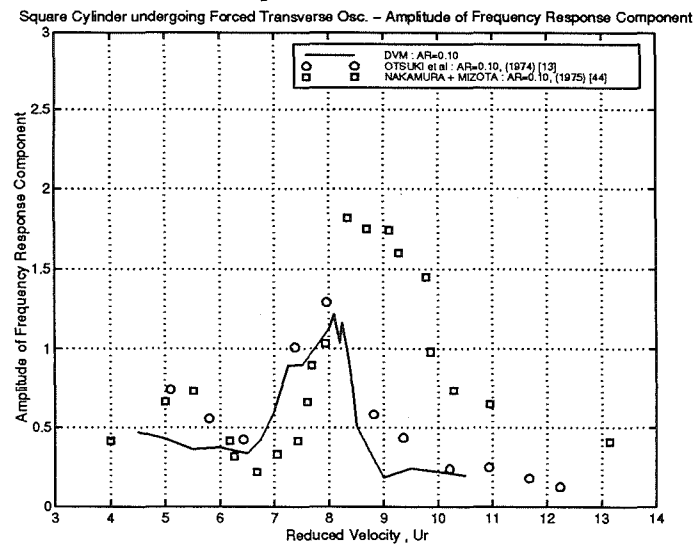
b) Amplitude Ratio = 0.10.

c) Amplitude Ratio = 0.15.

Fig. 4.35 - Amplitude of Frequency Response Component of Lift Coefficient : Square Cylinder with Transverse Oscillation.

Square Cylinder undergoing Forced Transverse Osc. – Imaginary Part of Frequency Response Component

a) Amplitude Ratio = 0.05.

Square Cylinder undergoing Forced Transverse Osc. – Imaginary Part of Frequency Response Component

b) Amplitude Ratio = 0.10.

Square Cylinder undergoing Forced Transverse Osc. – Imaginary Part of Frequency Response Component
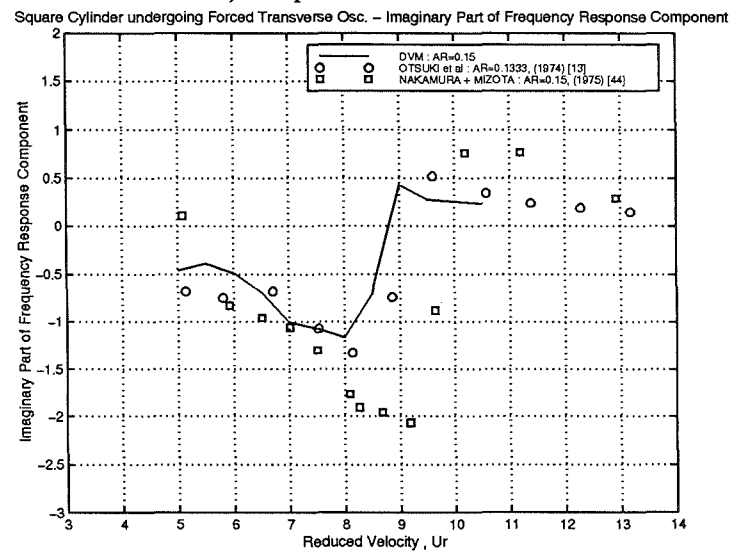
c) Amplitude Ratio = 0.15.

Fig. 4.36 - Imaginary Part of Frequency Response Component of Lift Coefficient : Square
Cylinder with Transverse Oscillation.
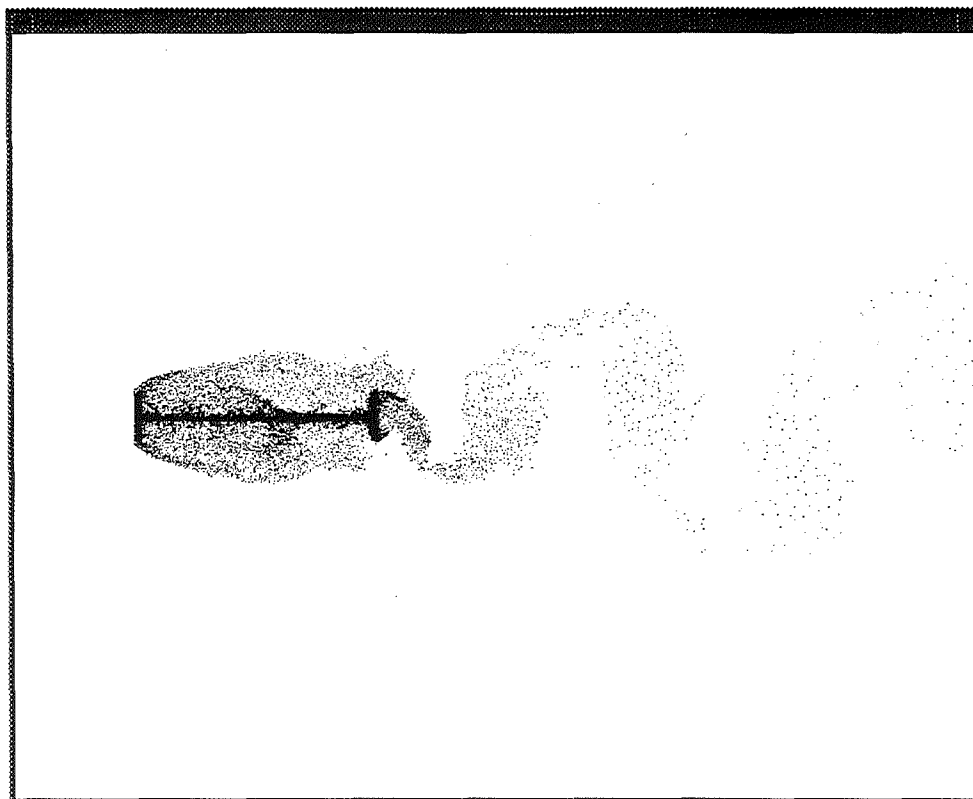
a) Particle Distributions.
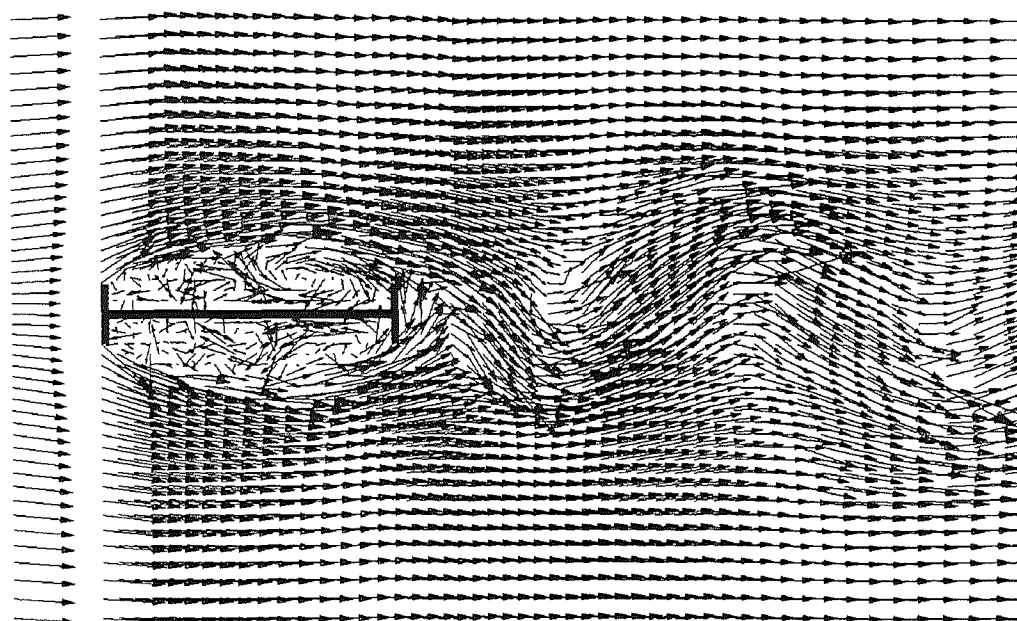
b) Velocity Vectors.

Fig. 4.37 - Predicted Flow Field around Static H-Section Cylinder at 0° Incidence.
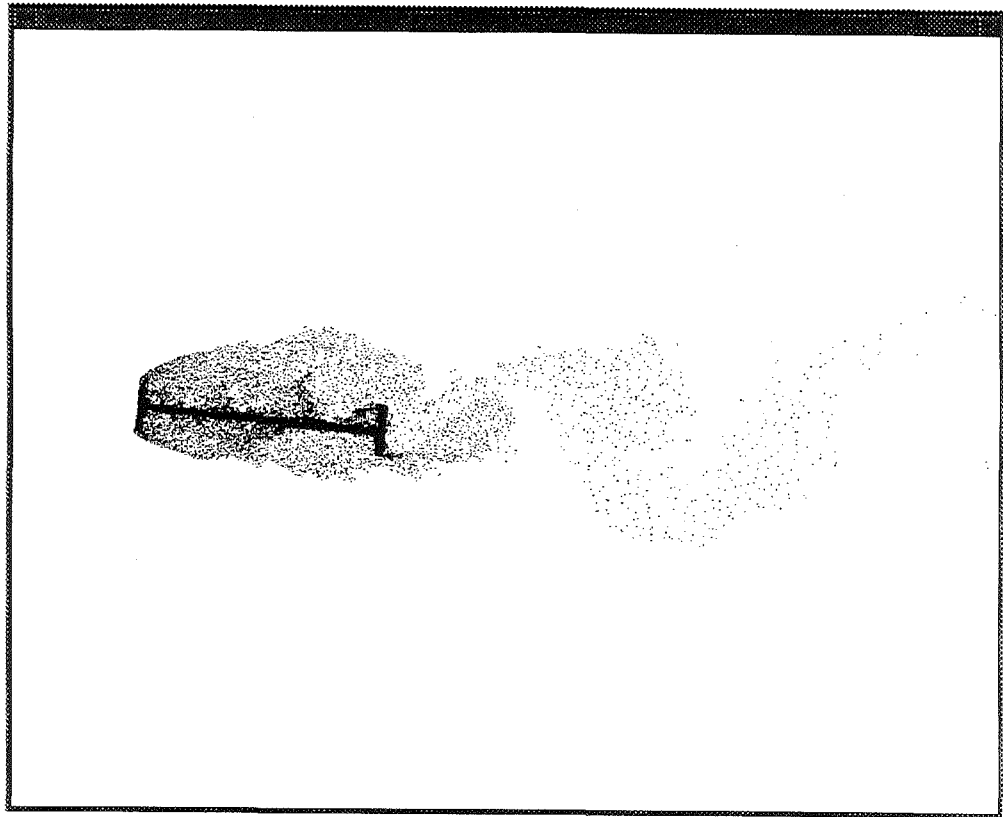
a) Particle Distributions.
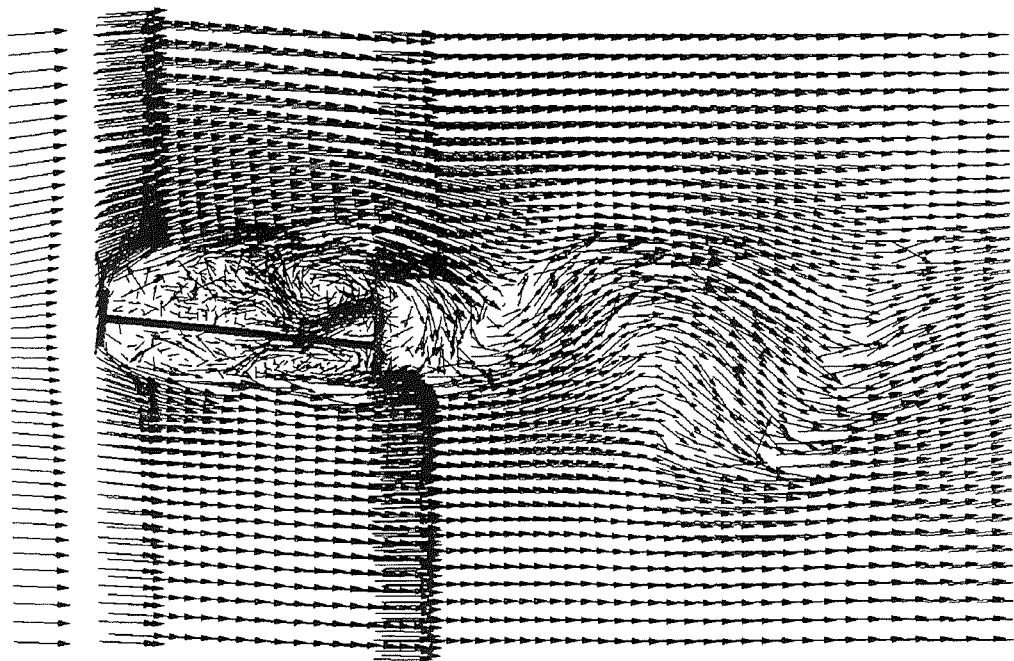
b) Velocity Vectors.

Fig. 4.38 - Predicted Flow Field around Static H-Section Cylinder at 6° Incidence.
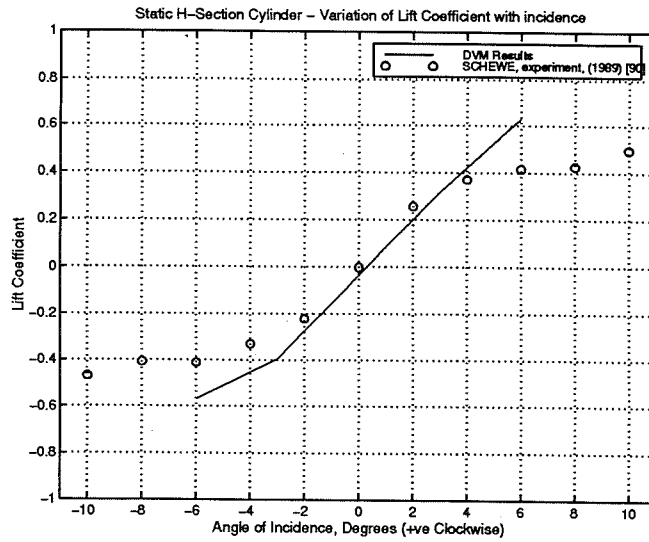
a) Lift Coefficient.
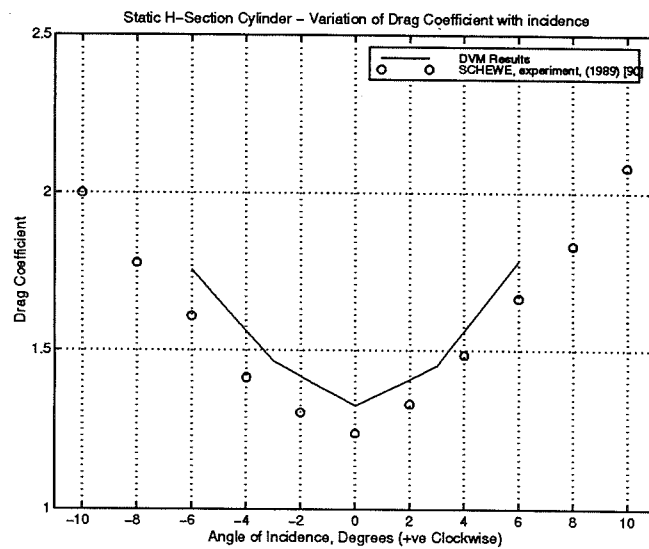
b) Drag Coefficient.
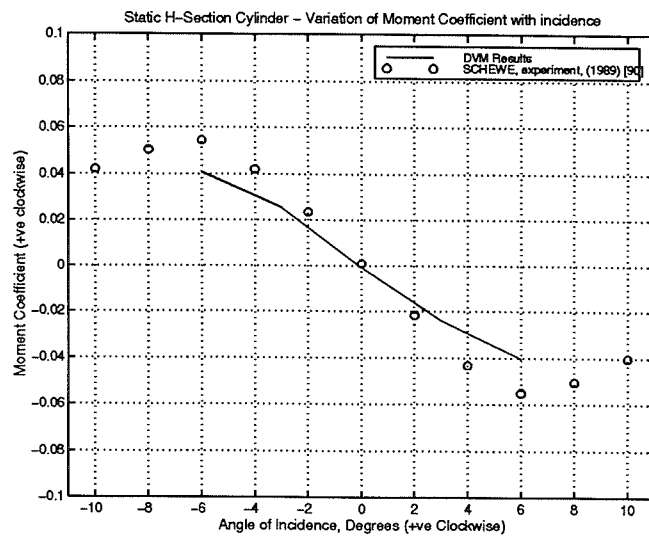
c) Moment Coefficient.

Fig. 4.39 - Static H-Section Cylinder : Variation of Aerodynamic Forces with Incidence.
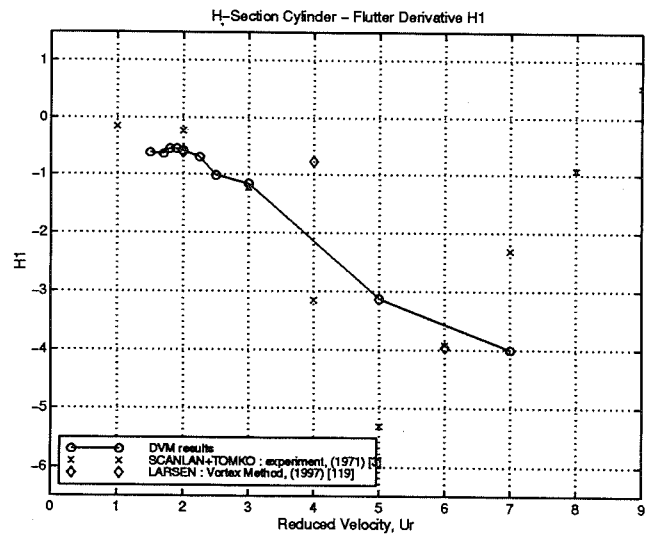
a) H_1^*.
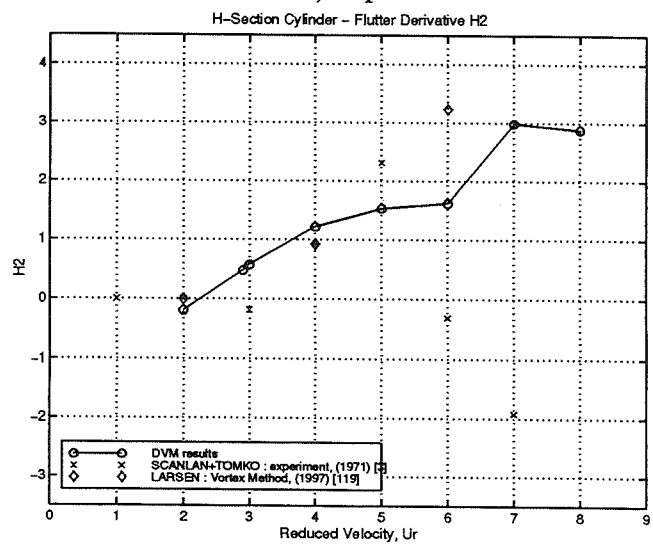
b) H_2^*.
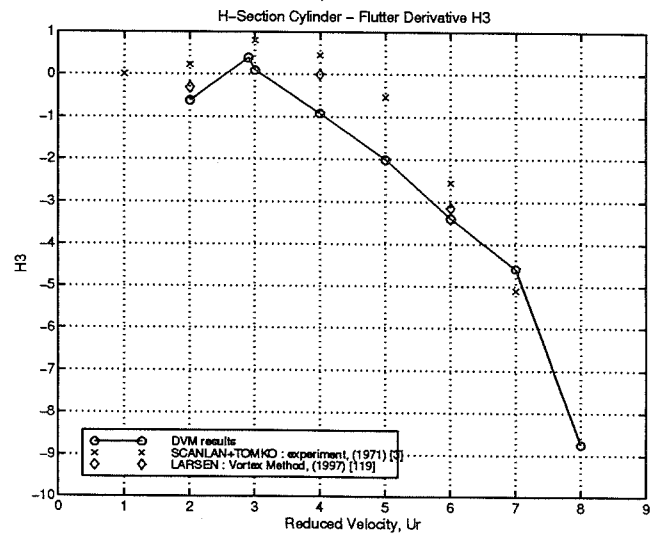
c) H_3^*.

Fig. 4.40 - Flutter Derivatives on Oscillating H-Section Cylinder : H_i^* Derivatives.
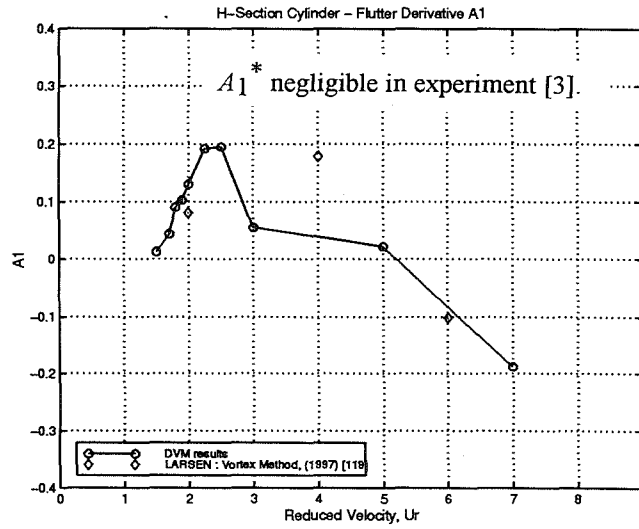
a) $A_1{}^*$.
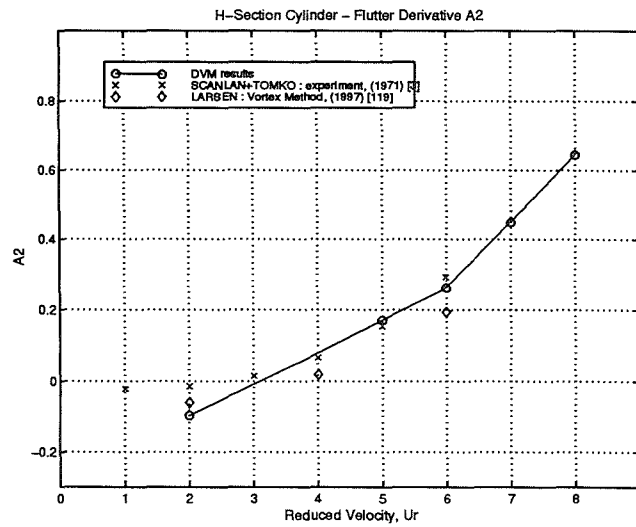
b) $A_2{}^*$.
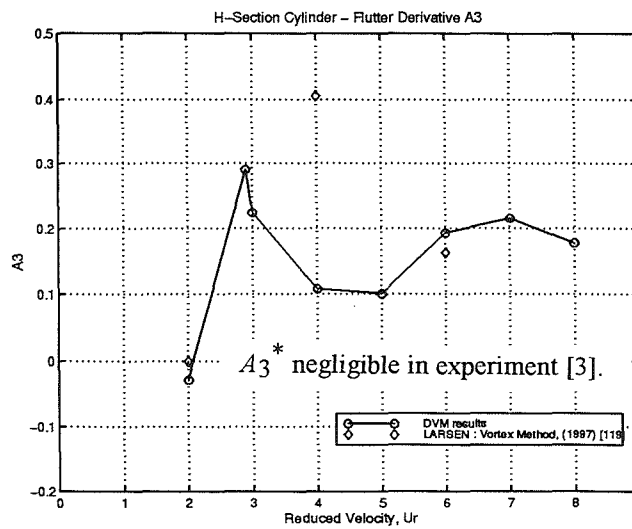
c) $A_3{}^*$.

Fig. 4.41 - Flutter Derivatives on Oscillating H-Section Cylinder : $A_i{}^*$ Derivatives.

Great Belt East Bridge

Suspended spans

4.4

B = 31.0

Pylon

254.1

Elevation

535.0 m · 1624 m · 535.0 m

General arrangement of the Great Belt East Bridge.
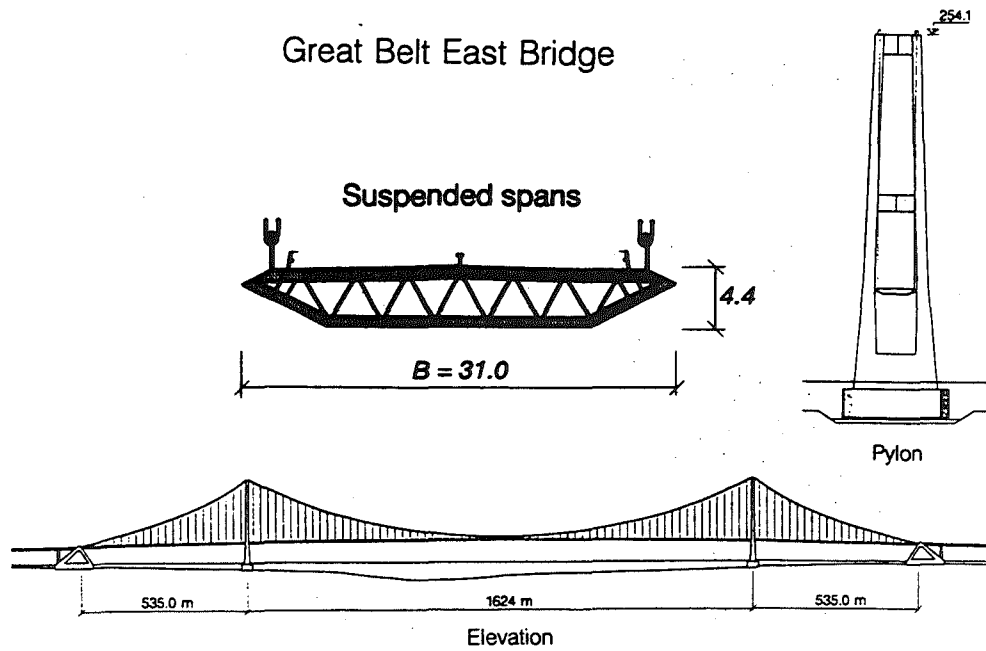
a) Full Bridge (from Larsen 1993 [133] and 1997 [119]).

25 · 21.25

H = 550 (4.40)

50.0 (4.0)

37.5

S.C.

29.4

H9.1

0

75.0 · 237.5 · 75.0

B = 387.5 (31.0)
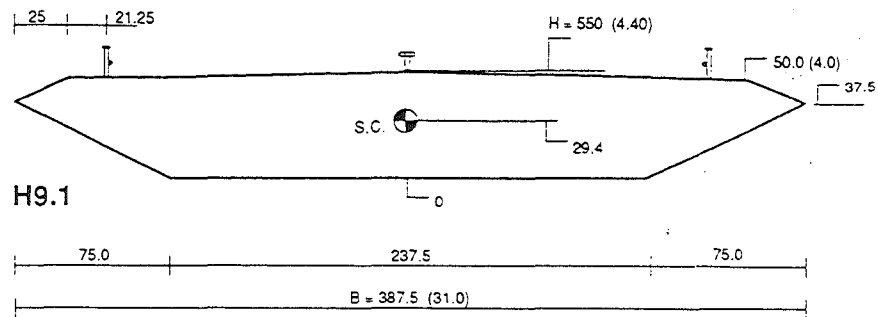
Note - Dimensions in mm for Sectional Model Test, Figures in Brackets Refer to Actual Dimensions of Bridge in m.

b) Main Suspended Section (from Poulsen et al 1992 [98]).

Fig. 4.42 - General Arrangement of the Great Belt East Bridge.
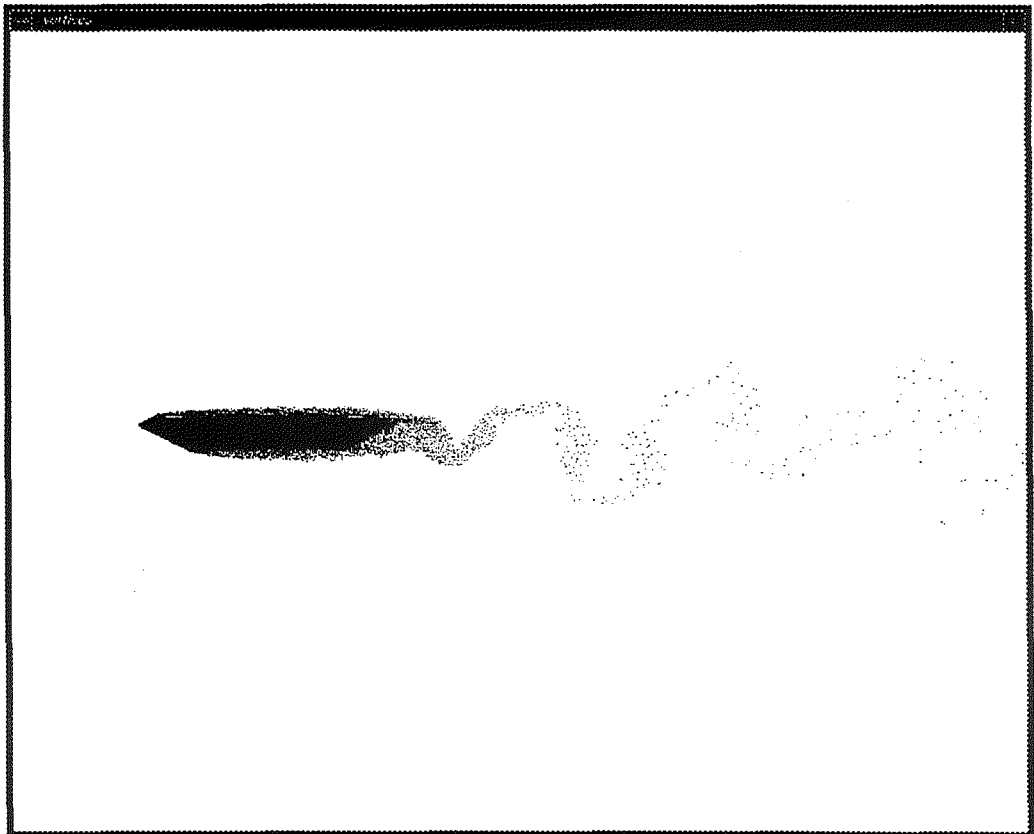
a) Particle Distributions.
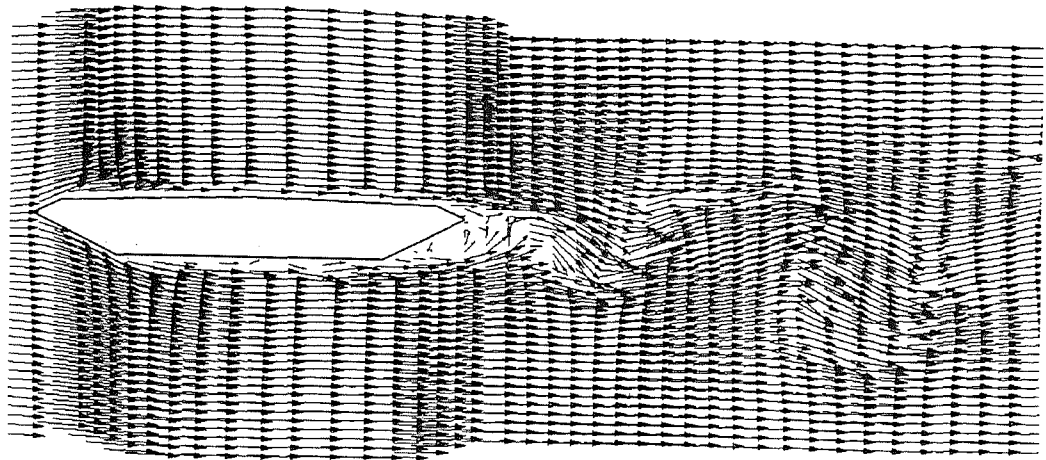
b) Velocity Vectors.

Fig. 4.43 - Predicted Flow Field around Great Belt East Main Span at 0° Incidence.
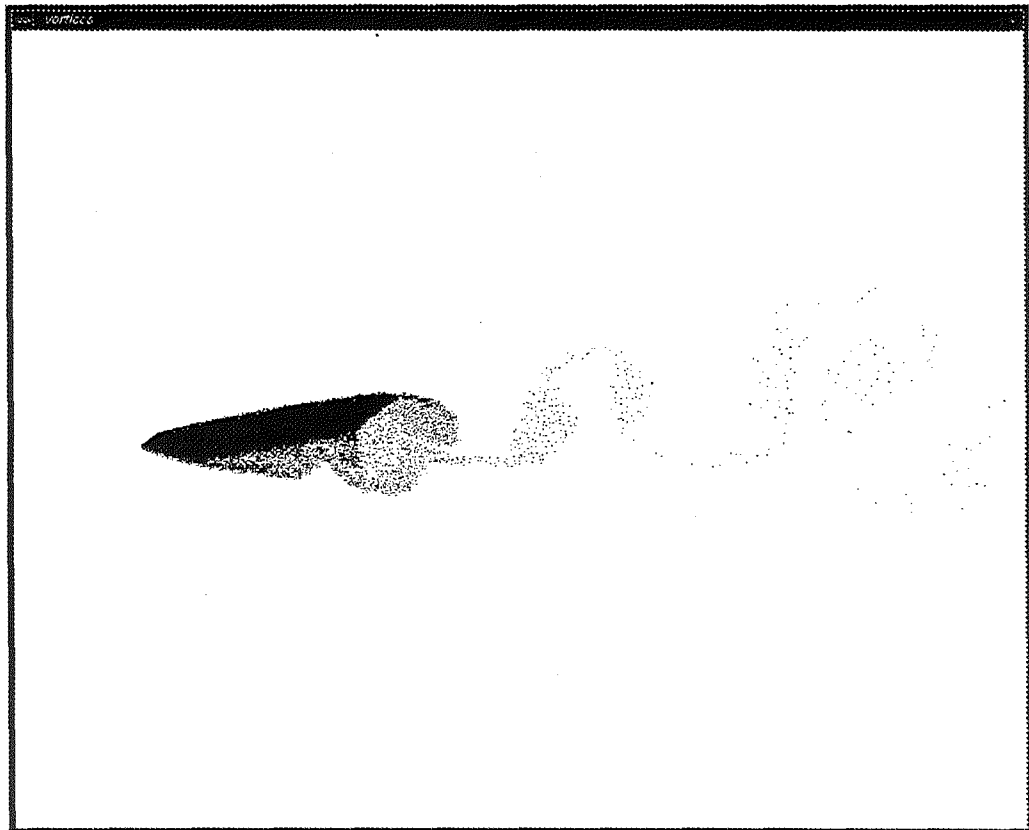
a) Particle Distributions.
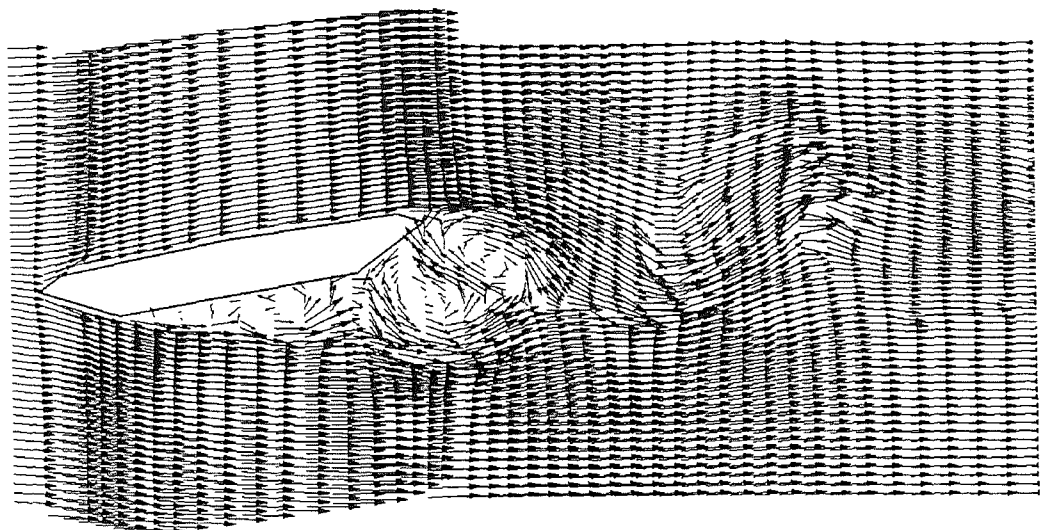
b) Velocity Vectors.

Fig. 4.44 - Predicted Flow Field around Great Belt East Main Span at 10° Incidence.
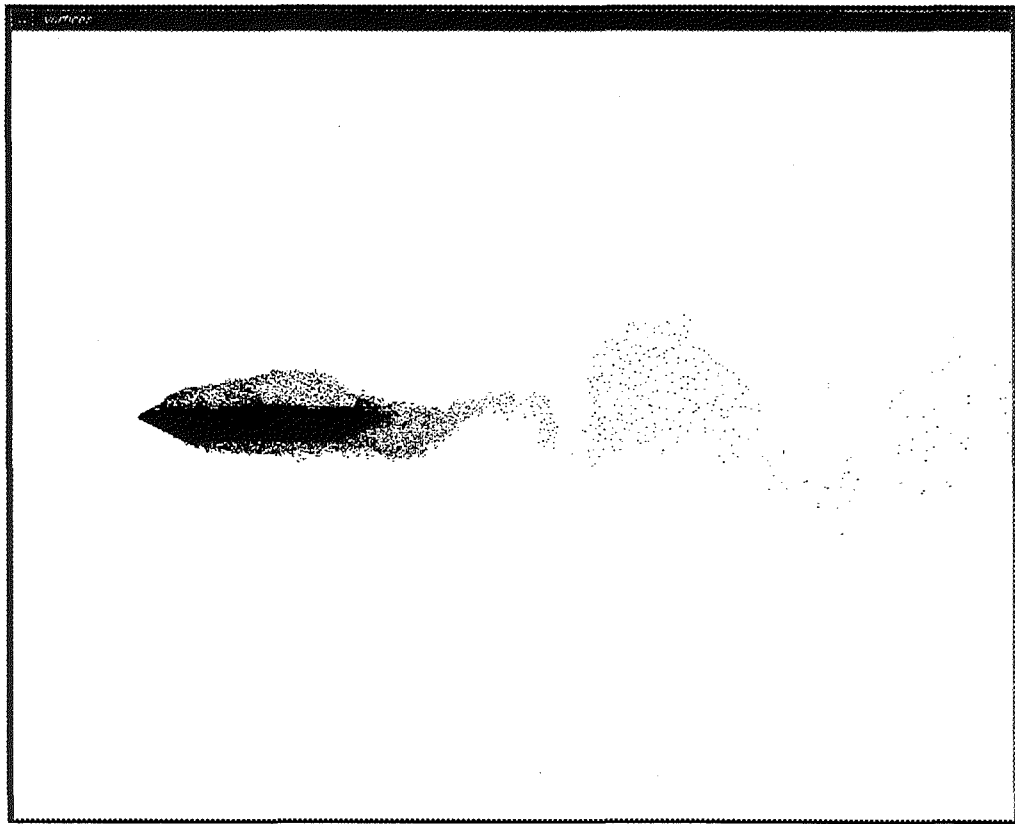
a) Particle Distributions.
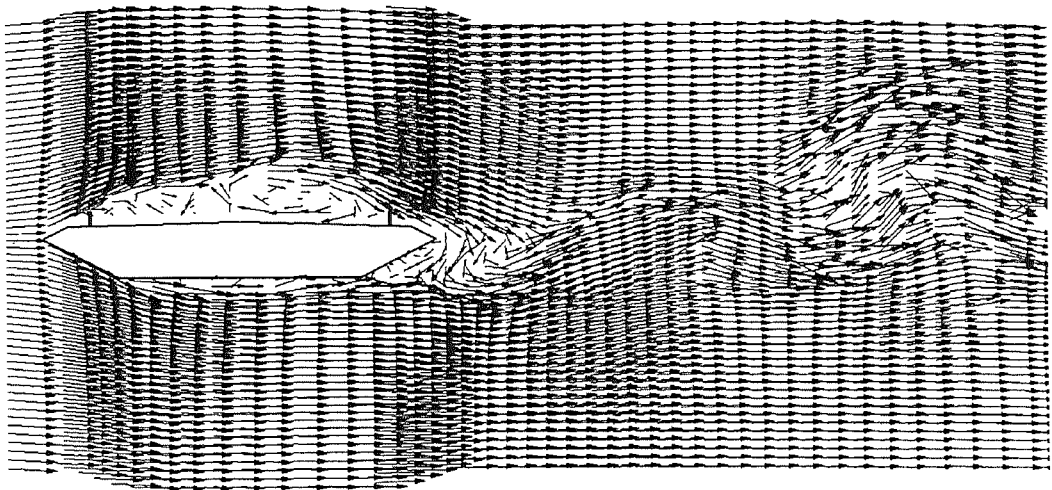
b) Velocity Vectors.

Fig. 4.45 - Predicted Flow Field around Great Belt East Main Span at 0° Incidence with Barrier Model.
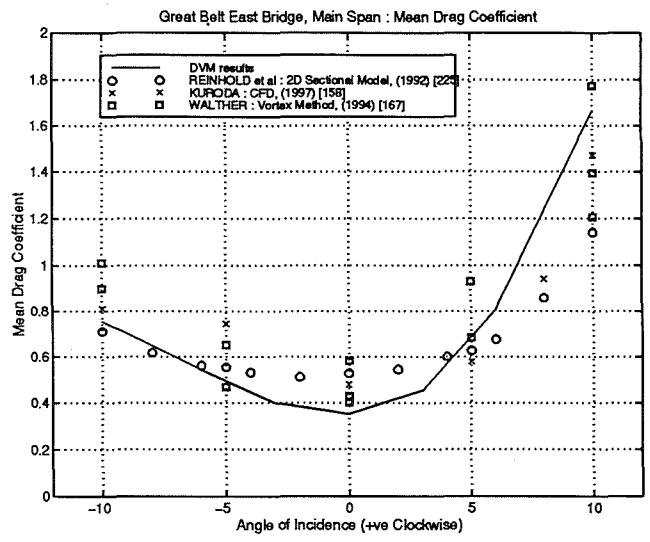
a) Drag Coefficient.
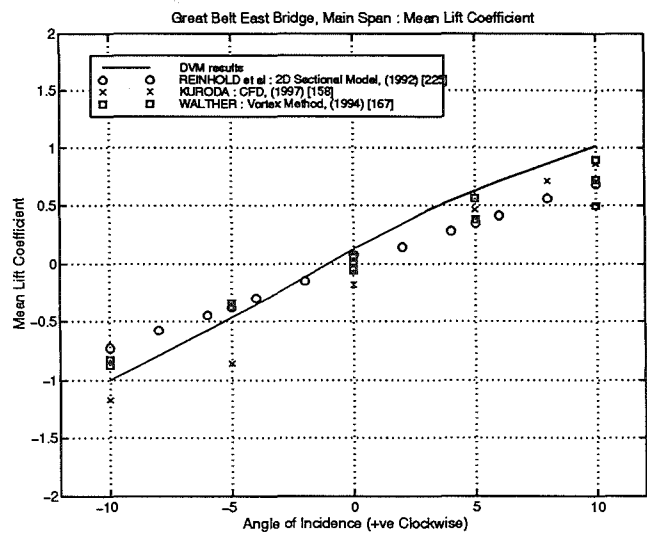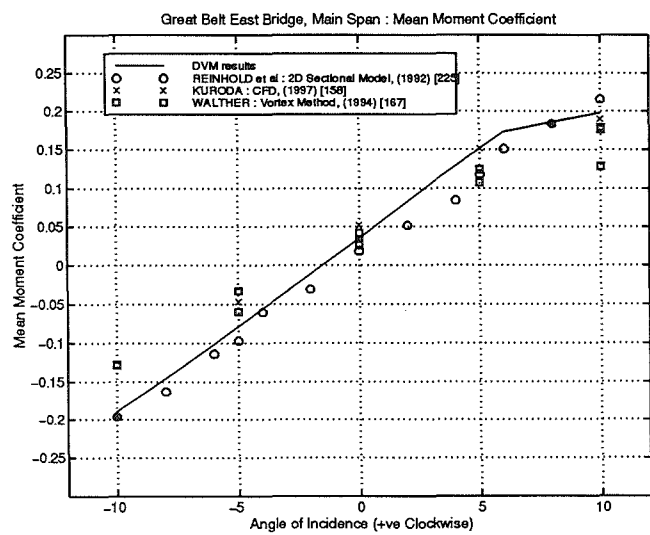
b) Lift Coefficient.

c) Moment Coefficient.

Fig. 4.46 - Great Belt East Main Span - Variation of Aerodynamic Forces with Incidence.
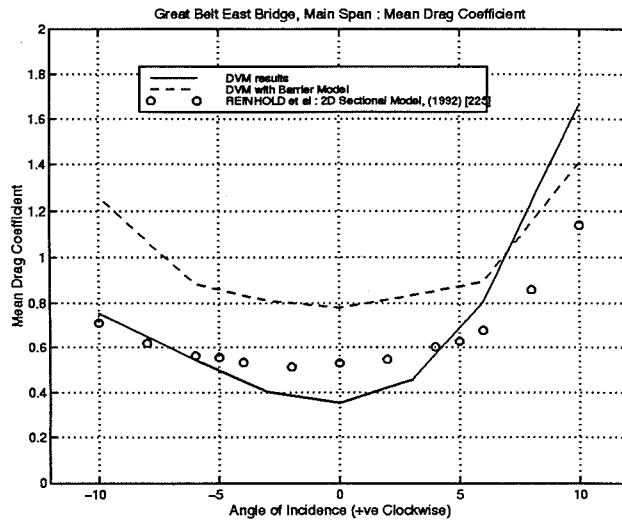
a) Drag Coefficient.
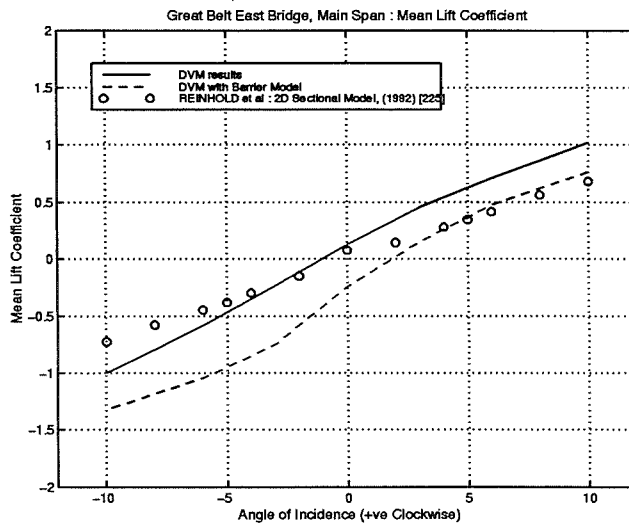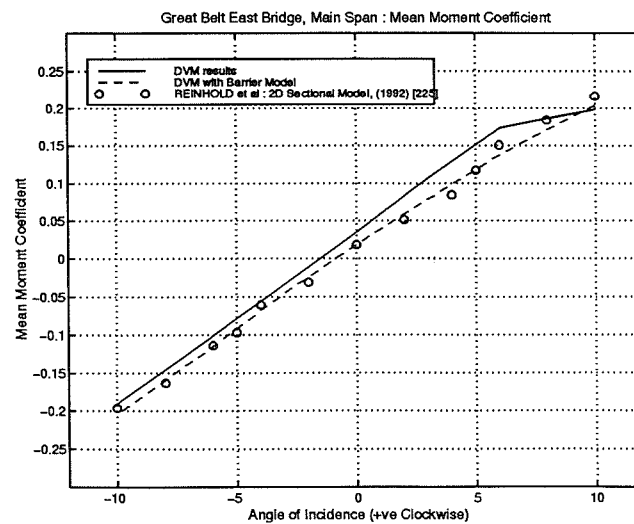
b) Lift Coefficient.

c) Moment Coefficient.

Fig. 4.47 - Great Belt East Main Span with Barrier Model - Variation of Aerodynamic Forces with Incidence.
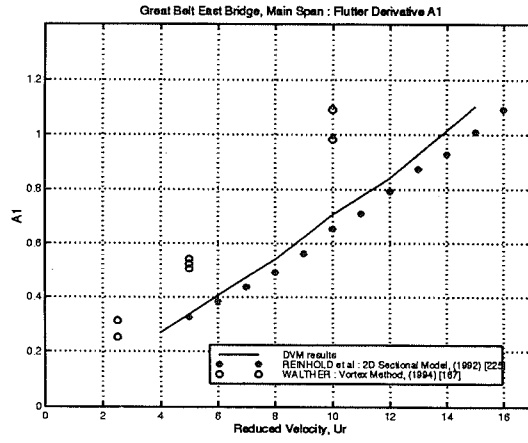
a) A_1^*.
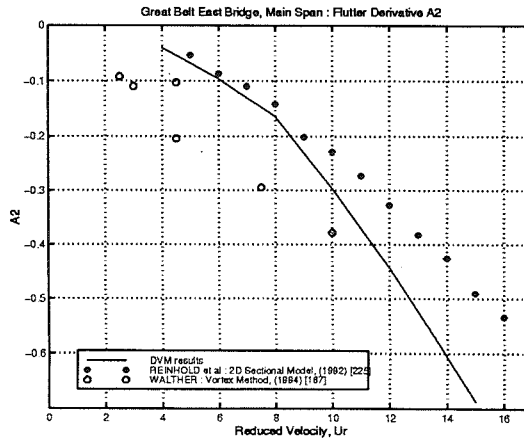
b) A_2^*.
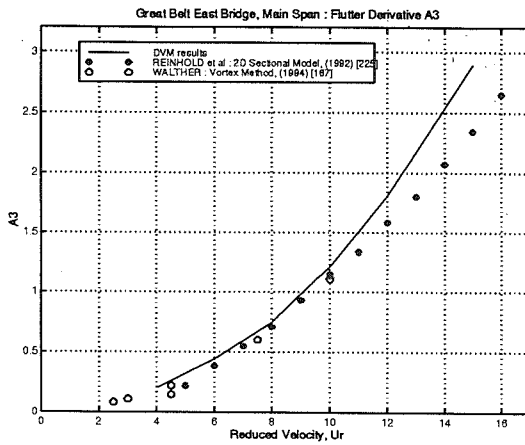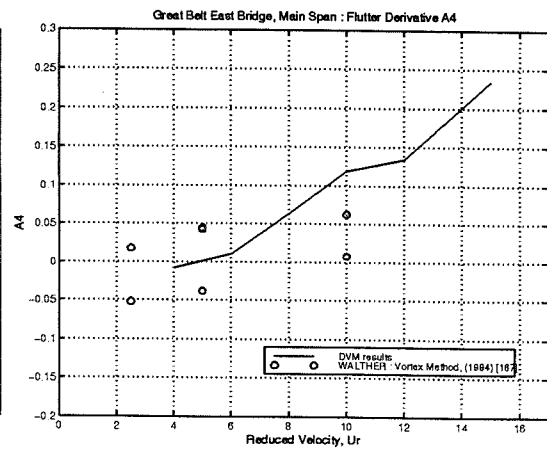
c) A_3^*.   d) A_4^*.

Fig. 4.48 - Flutter derivatives for the Great Belt East Main Span.
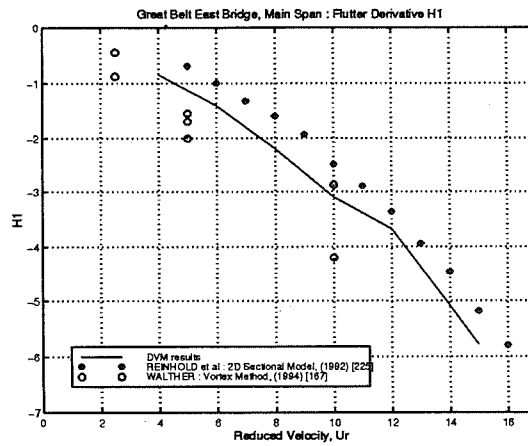
e) $H_1{}^*$.
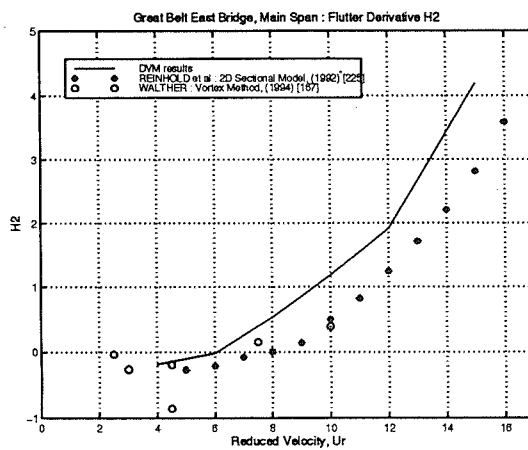
f) $H_2{}^*$.
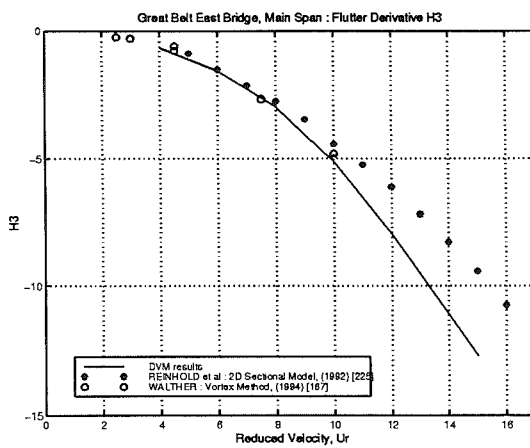
g) $H_3{}^*$.
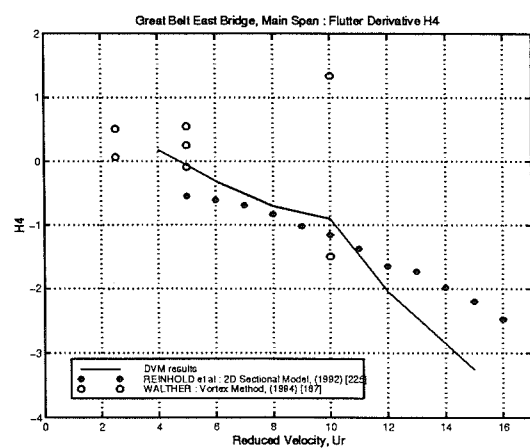
h) $H_4{}^*$.

Fig. 4.48 - Flutter Derivatives for the Great Belt East Main Span.
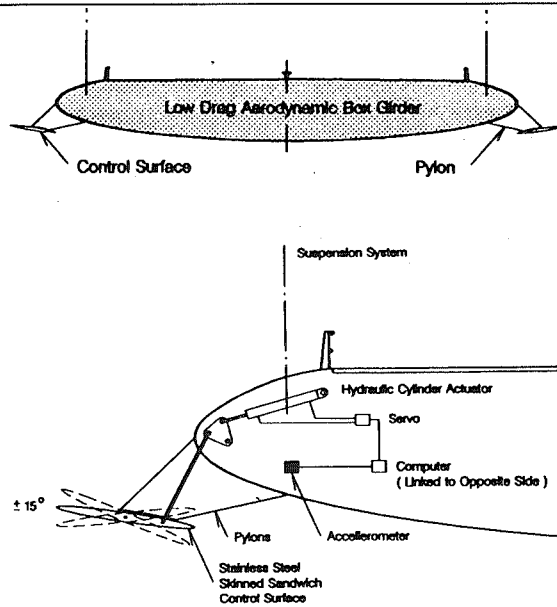
Fig. 4.49 - Suggestions for Implementation of Active Control Surface Systems on Streamlined Bridge Sections (from Ostenfeld and Larsen 1992 [132]).
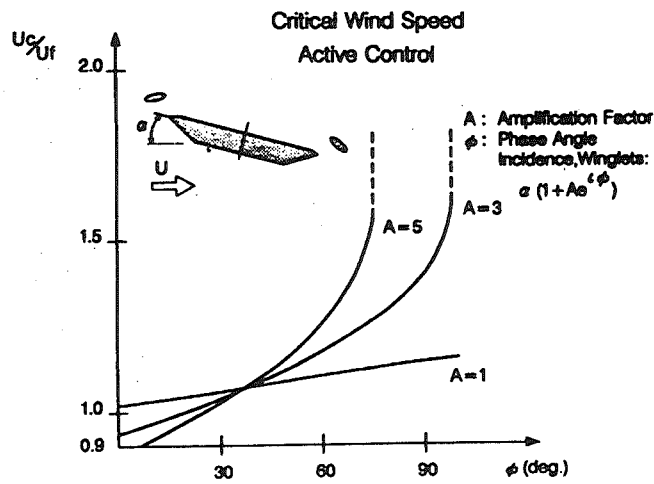
a) Theoretical Study (from Ostenfeld and Larsen 1992 [132]).
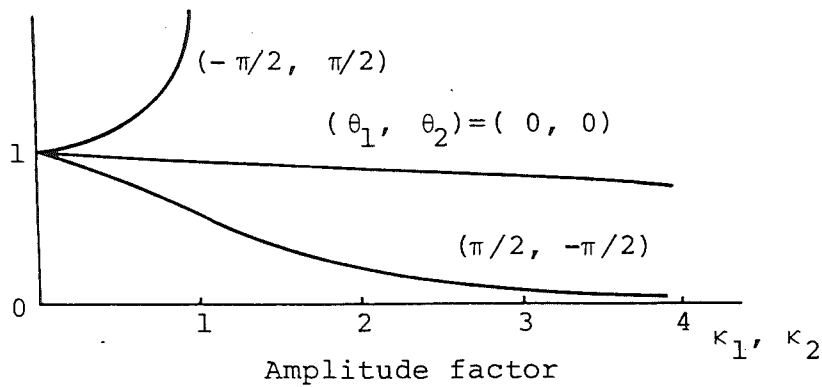
b) Experimental Study (from Kobayashi et al 1992 [131]).

Fig. 4.50 - Potential Enhancement of Aerodynamic Stability through Active Control Surfaces.
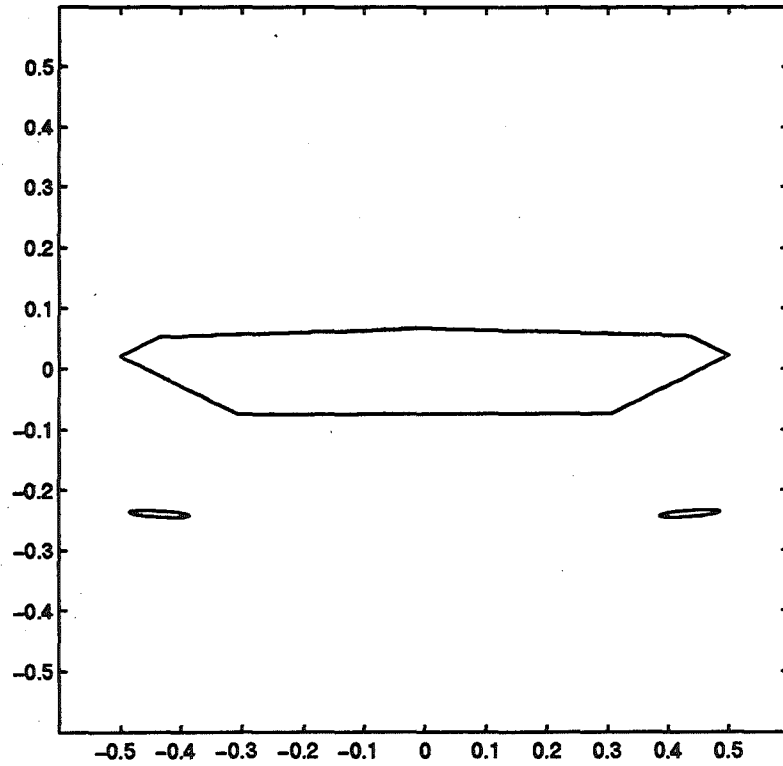
Fig. 4.51 - Great Belt East Bridge - Main Suspended Section with Flow Control Vanes.
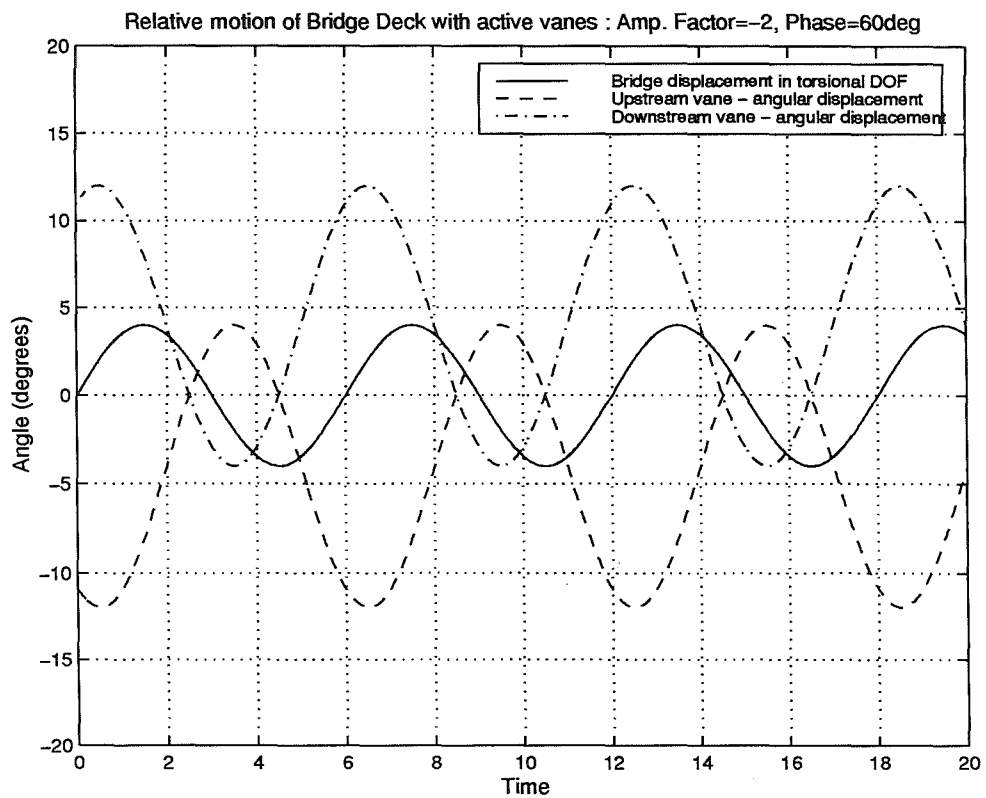
Fig. 4.52 - Relative Torsional Motion of Bridge Deck and Actively Controlled Guide Vanes.
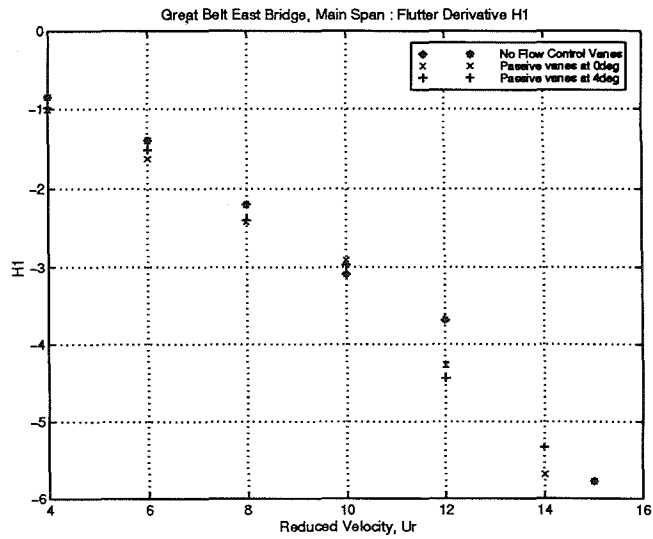
a) $H_1{}^*$.
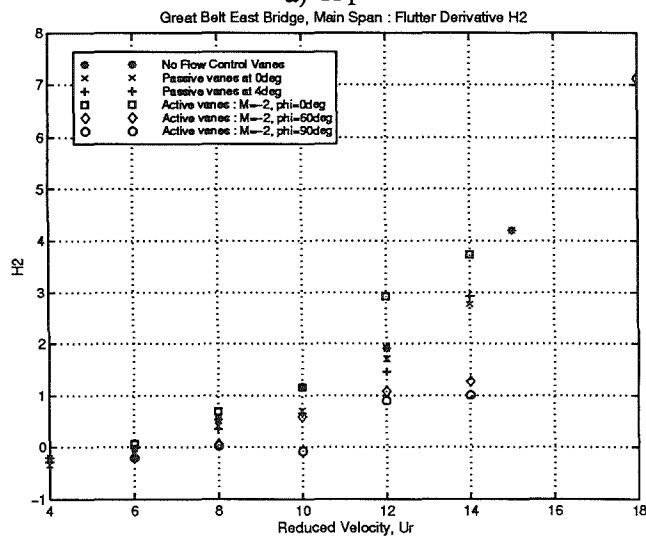
b) $H_2{}^*$.
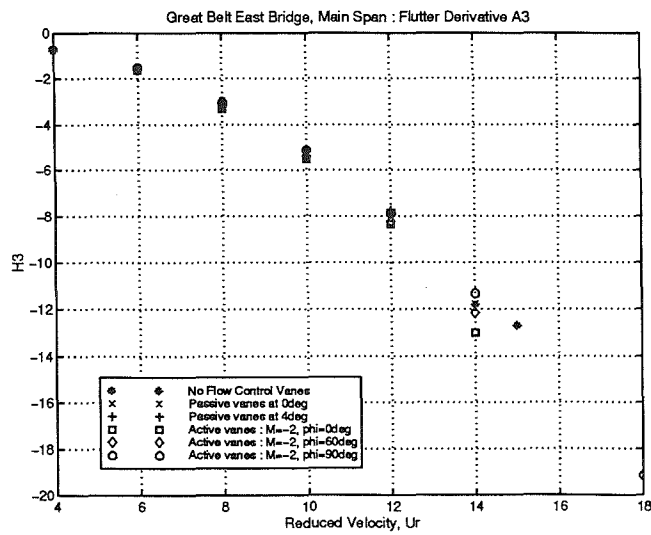
c) $H_3{}^*$.

Fig. 4.53 - $H_i{}^*$ Flutter Derivatives for Great Belt East Main Span with Active and Passive Flow Control Vanes.
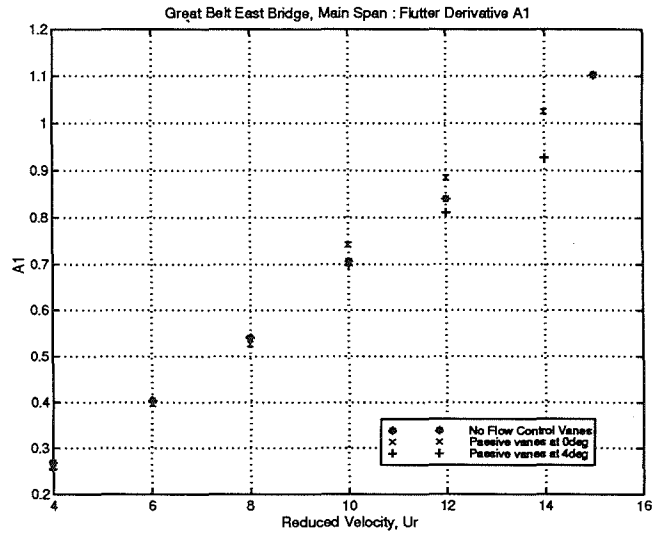
a) A_1^*.
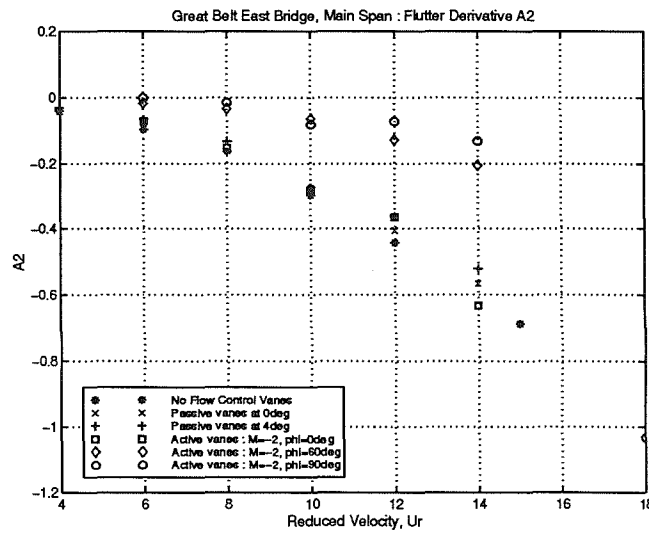
b) A_2^*.
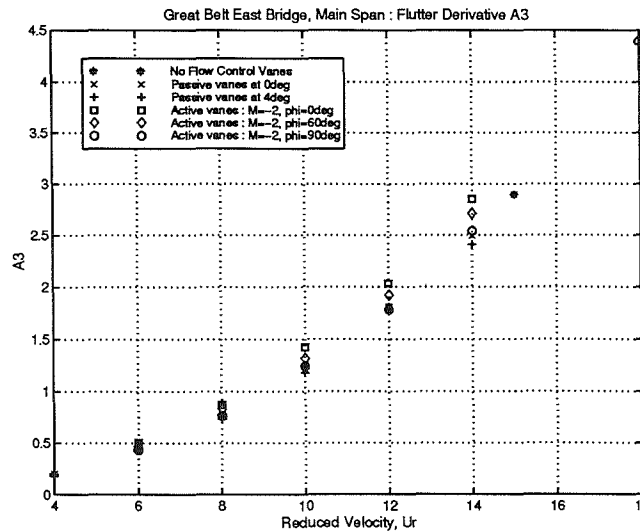
c) A_3^*.

Fig. 4.54 - A_i^* Flutter Derivatives for Great Belt East Main Span with Active and Passive Flow Control Vanes.

Level 0

Level 1

Level 2

Level 3
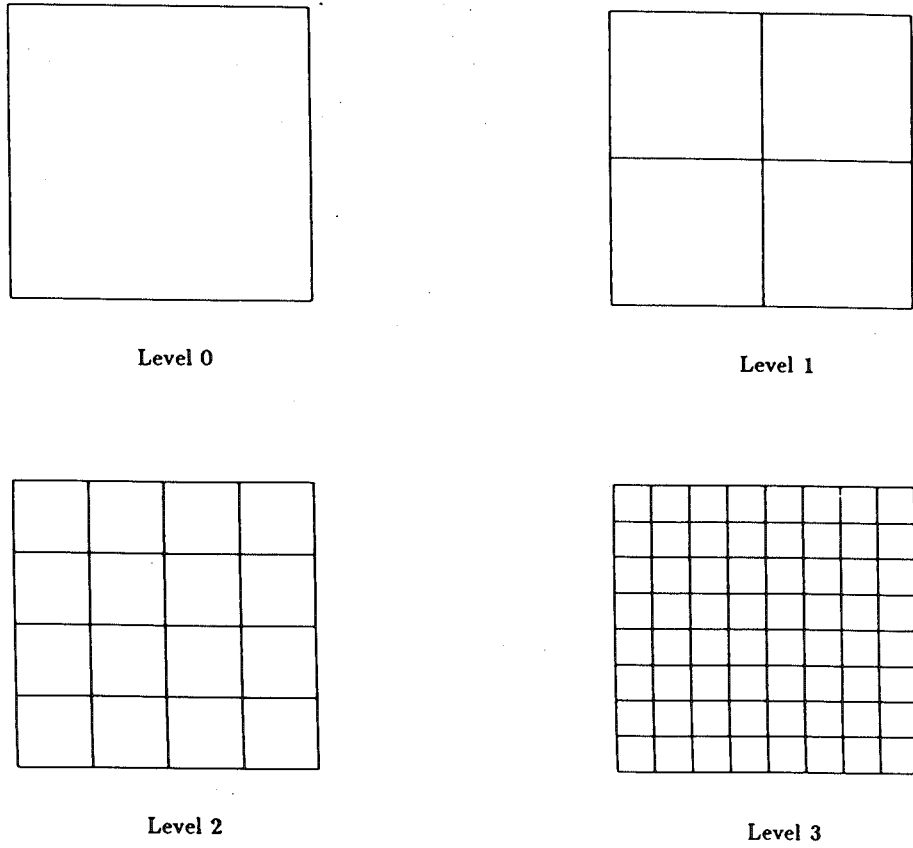
Fig. B.1 - Division of Flow Field into Uniform Square Zones.

Variation in CPU and Error with H
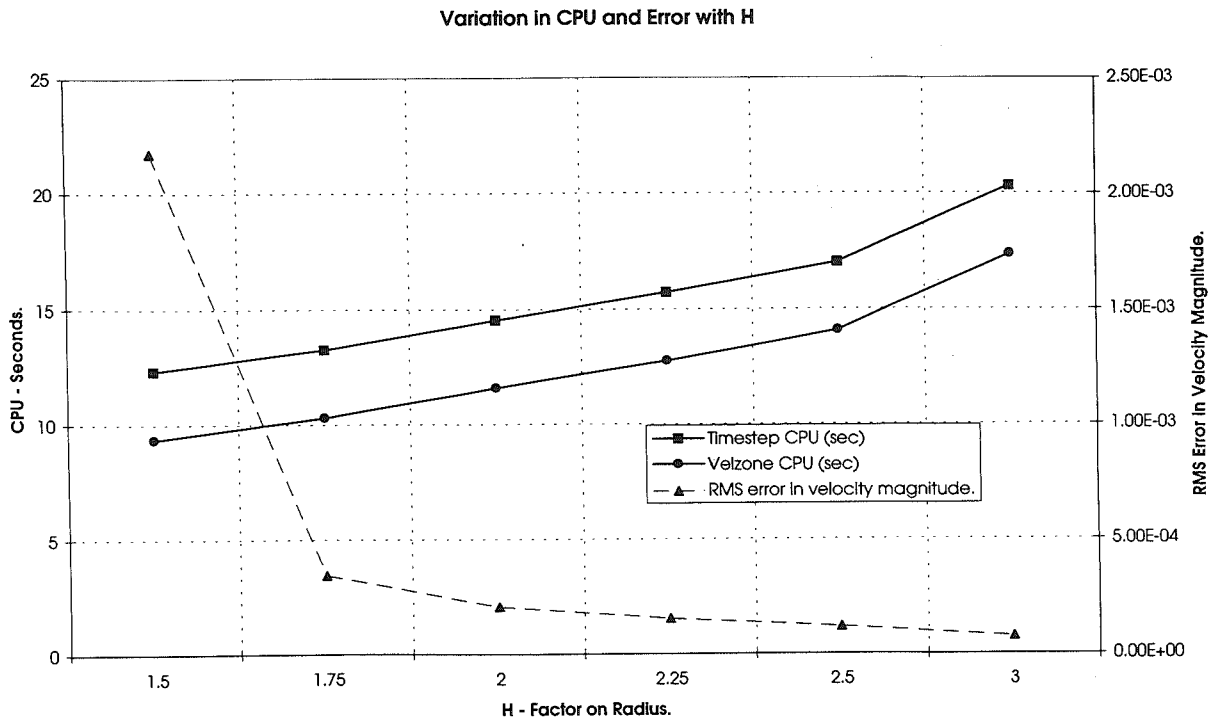
Fig. C.1 - Variation of CPU and RMS Error with Factor on Zone Radius - *H*.

Variation in CPU and Error with Nt
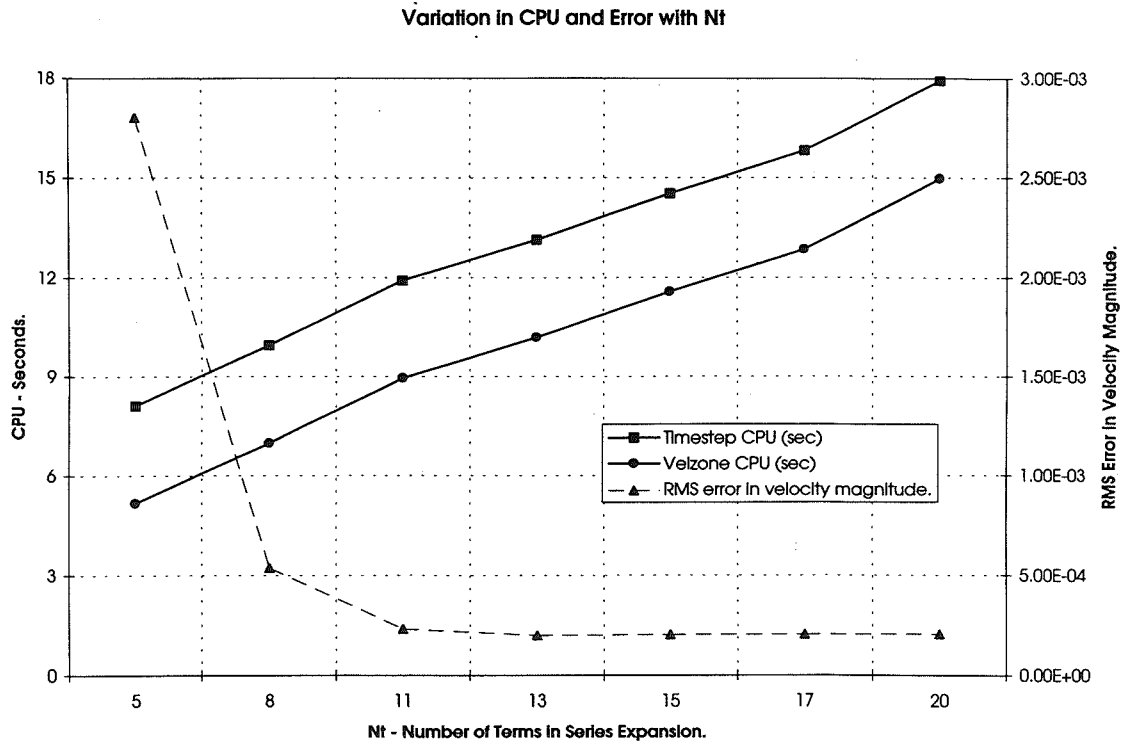
Fig. C.2 - Variation of CPU and RMS Error with Number of Terms in Series Expansion - *Nt*.

Variation in CPU and Error with Np
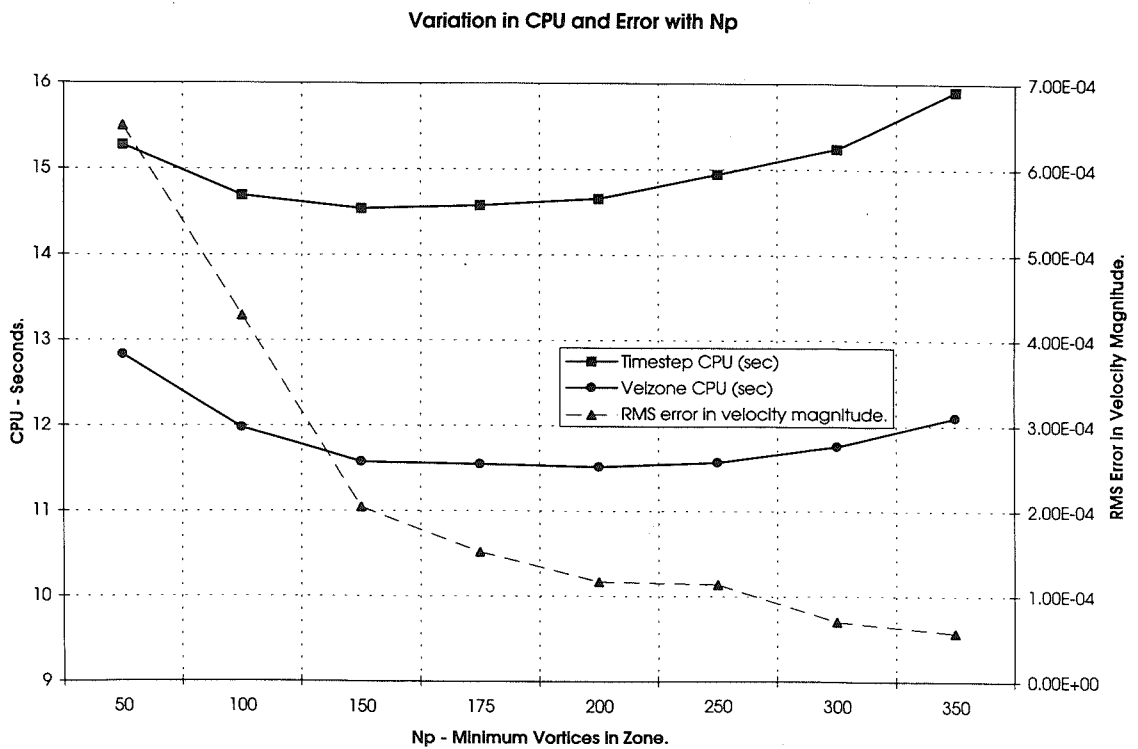
Fig. C.3 - Variation of CPU and RMS Error with Minimum Number of Vortices in Zone - *Np*.
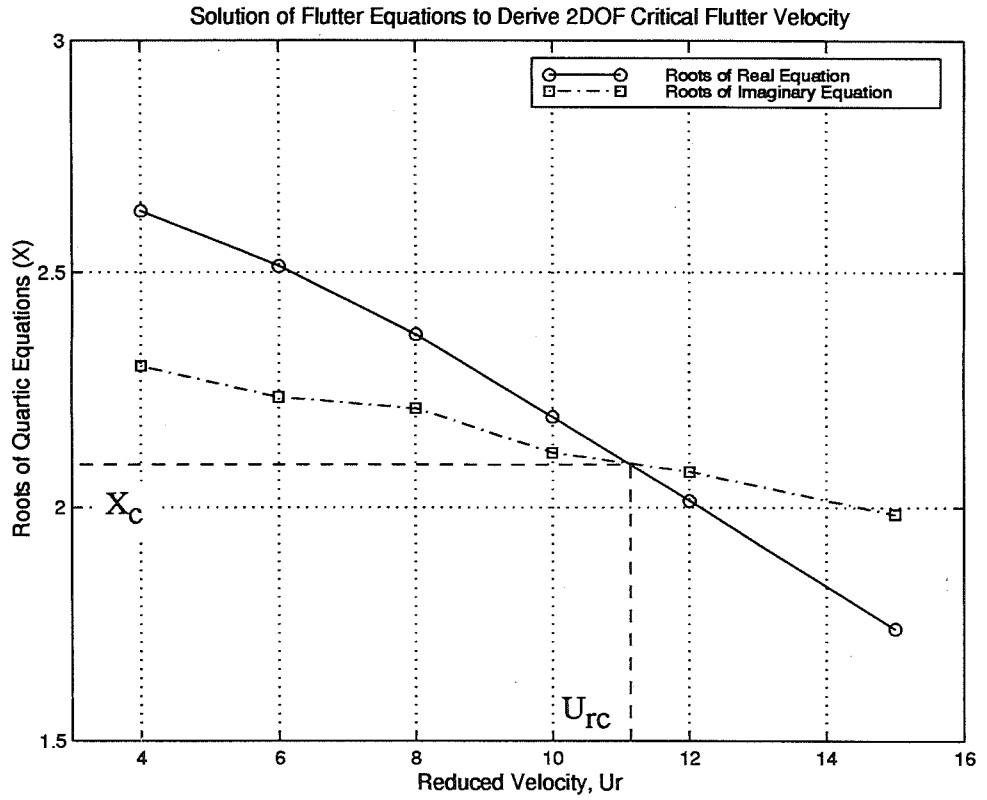
Fig. F.1 - Solution of Flutter Equations to Derive 2DOF Critical Flutter Velocity.
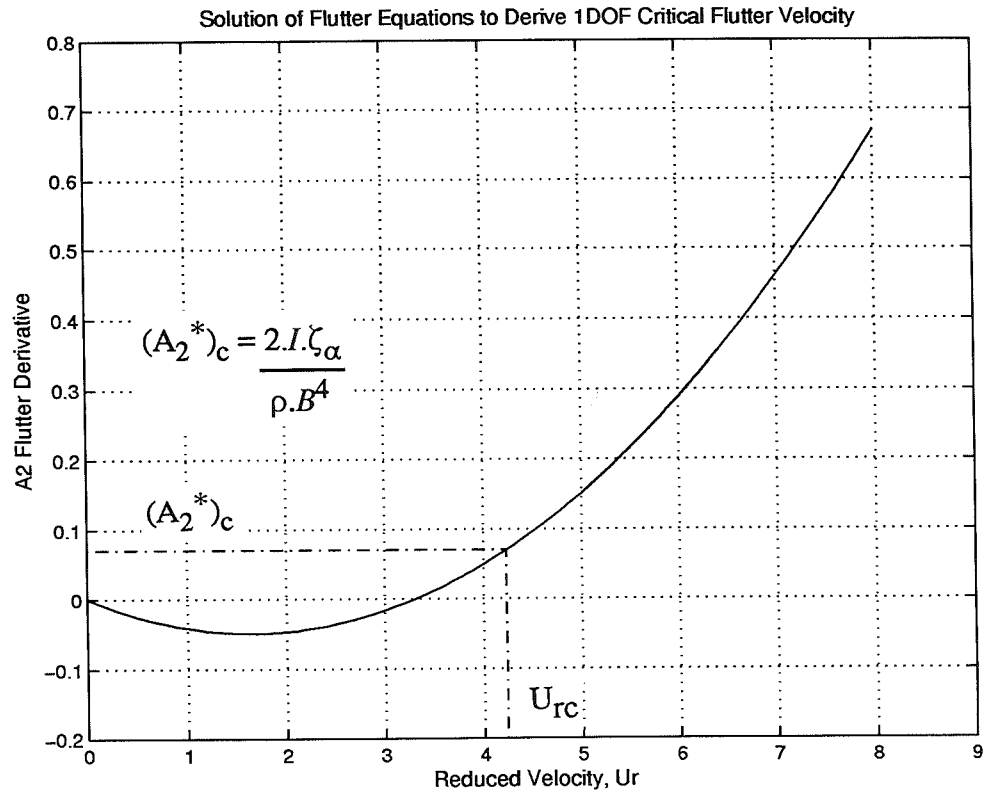

Fig. F.2 - Solution of Flutter Equations to Derive 1DOF Critical Flutter Velocity.